GaSb/Silicon-on-Insulator Heterogeneous Photonic Integrated Circuits
for the Short-Wave Infrared

Fotonische geïntegreerde circuits op GaSb/silicium-op-isolator
voor kortegolfinfrarood-toepassingen

Nannicha Hattasan

UNIVERSITEIT
GENT

GaSb/Silicon-on-Insulator Heterogeneous Photonic Integrated Circuits for the Short-Wave Infrared

Fotonische geïntegreerde circuits op GaSb/silicium -op-isolator voor kortegolfinfrarood-toepassingen

Nannicha Hattasan

Universiteit Gent
Faculteit Ingenieurswetenschappen en Architectuur
Vakgroep Informatietechnologie

Promotoren: Prof. Dr. Ir. Günther Roelkens

Examencommissie:

Prof. dr. ir. Rik Van de Walle (voorzitter)	Universiteit Gent, iMinds
Prof. dr. ir. Günther Roelkens (promotor)	Universiteit Gent, INTEC
Prof. dr. ir. Roel Baets (secretaris)	Universiteit Gent, INTEC
Prof. dr. ir. Dries van Thourhout	Universiteit Gent, INTEC
Prof. dr. ir. Jan Vanfleteren	Universiteit Gent, ELIS
Prof. dr. ir. Eric Tournié	Université Montpellier 2, IES-CNRS
Dr. ir. Danaë Delbeke	Universiteit Gent, Business Development
Dr. ir. Ronny Bockstaele	Universiteit Gent, INTEC

INTEC

Dankwoord

Six years ago, when I was a test engineer looking for a new challenge, I applied for the Erasmus Mundus Master of Photonics program. Several weeks after an interview with Irina Veretennicoff, I received an email that changed my life forever. Thanks to Irina, Dave, Bert and Erasmus Mundus committee for giving me the opportunity of a lifetime. Thanks to my Erasmus friends, Siew Jean, Pakpairin, Hamed, Andy, Adane, Alvaro, Buvana, Pierre, Aimi, Tom, Joanne for the great time in both Sweden and Belgium. Thanks to Wout, my thesis supervisor, for a great time during my Master thesis, which made me fall for Photonics. After 2 years of the Master program, I thought it is time to move back to industry. Then Roel came with his charming question "So, what is your plan? Would you like to do a PhD?"To me, PhD was a fancy word. But I thought, why not? Thanks to Roel for such a charming question that started my real adventure. Thanks to Dries for his advice on my topic selection, "whatever crap you make, it is publishable". Thanks to Geert for all the chats and advice on a free trip to Japan during his smoke break. Thanks to Wim for all the jokes, Peter Bienstman and Nicolas for creating Camfr and the chats.

Special thanks to my supervisor, Günther who has always been there whenever I needed him, never complaining on "the craps"I came up with and never discouraging my crazy ideas. Thanks to you, I had a real fun time for the past 4 years.

Special thanks to the team from University of Montpellier II, Eric Tournié, Laurent Cerutti, Jean-Baptiste Rodriguez for their support from the very beginning to the very last day of my PhD. I really appreciate it.

Thanks to the jury members, Ronny Bockstaele, Danaë Delbelke, Jan Vafleteren, Roel Baets, Eric Tournie, Dries van Thourhout for their reading and comments.

Thanks to the Glucosens team, Ronny, Geert Morron, Sandeep, Karolien, Elke, David, Kamath, Valerie, Peter, Ria, Wouter. I have learnt a lot during the project. Thanks to Prof. Peter Dubruel and Veerle Boteborg for contact angle measurement.

My PhD could never start or finish without the help of all the staff members, Thanks to Kristien for being such a great doctor of my PC, Ilse V. for all sorts of things that mattered. Ilse M. for POs, Mike for contracts, Michael for the awesome python codes, Jeroen for the practise in measurements, Eddy for the care of the books, Peter for all the great crafts from the workshop, Paratesh for the laugh,

Nok Eing, Duean, Paew, Chatchai, Nut, Am for being the same since the first day we met. Thanks for the care, wishes and laughs that lifted up my spirit for the last 20 years. I look forward for more in the future.

Life in Europe is not that simple. Thank you Tazin for being there when I needed you most, cheering me up when my days were dark and straightening me up when I was getting lazy.

Leaving your family behind and studying abroad is not an easy task. Thanks to my sister, Arparat for being the greatest sister taking good care of the parents and my businesses in Thailand during all these years. Thanks to my wonderful parents for supporting my decision. I would never be able to come this far without your love and strength that you have given and taught me.

Finally, nothing is free in this world; thanks to the European community and the Belgium taxpayers for supporting my study.

<div align="right">

Gent, 24 February 2014
Nannicha Hattasan

</div>

Table of Contents

List of Figures

List of Tables

List of Acronyms

C

CAMFR	Cavity Modeling Framework
CMOS	Complemntary Metal Oxide Semiconductor
CTE	Thermal Expansion Coefficients
CW	Continuous Wave

D

DBR	Distributed Bragg Reflector
DC	Direct Current
DFB	Distributed Feedback
DI	Deionized
DMSO	Dimethyl sulfoxide
DSA	Drop Shape Analysis
DVS-BCB	Divinylsiloxane-bis-Benzocyclobutene

F

FIB	Focused Ion Beam
FP	Fabry Perot
FCA	Free Carrier Absorption

G

GC	Grating Coupler

I

| ICL | Interband Cascade Laser |
| ICP | Inductively Coupled Plasma |

L

| LED | Light Emiting Diode |
| LPE | Liquid Phase Epitaxy |

M

MBE	Molecular Beam Epitaxy
MEMS	Micro-Electro-Mechanical System
MFD	Mode Field Diameter
MMF	Multimode fiber
MOCVD	Metalorganic Chemical Vapour Deposition
MQW	Multiple Quantum Well
MWIR	Mid-Wave Infrared

N

| NEP | Noise Equivalent Power |

O

| OSA | Optical Spectrum Analyzer |

P

| PECVD | Plasma Enhanced Chemical Vapor Deposition |

PICs   Photonic Integrated Circuits

Q

QCL   Quantum Cascade Laser
QW   Quantum Well

R

RCA   Radio Corporation of America
RF   Radio Frequency
RIE   Reactive-Ion Etching
RMS   Root Mean Square

S

SCH   Separate Confinement Heterostructure
SEM   Scanning Electron Microscope
SMF   Single Mode Fiber
SOI   Silicon-On-Insulator
SON   Silicon-On-Nitride
SOS   Silicon-On-Sapphire
SWIR   Short-Wave Infrared

T

TLM   Transmission Line Method

W

WDM   Wavelength-division Multiplexing

Nederlandse samenvatting
–Summary in Dutch–

Inleiding

Spectroscopisch meten heeft de laatste tijd aanzienlijk aan belangstelling gewonnen in biomedische en milieugerichte toepassingen. De techniek laat toe om gassen of bio-moleculen te detecteren waarvan de karakteristieke absorptielijnen in het nabij- en mid-infrarood liggen. Spectroscopie is nu al een gevestigde methode om de samenstelling en de concentratie van stoffen te bepalen door opmeting en analyse van het absorptiespectrum. Niettemin bevatten traditioneel ontworpen systemen doorgaans lichtbronnen, detectoren of passieve componenten die te groot of te duur zijn voor heel wat toepassingen, zoals implanteerbare sensoren. Fotonische geïntegreerde circuits bieden een significante miniaturisatie en zijn daardoor een interessant alternatief.

Fotonische geïntegreerde circuits op het silicium-op-isolator (SOI) platform bieden een compacte en kosteneffectieve oplossing, alsook een gevestigde en robuuste CMOS-technologie die rechtstreeks kan ingeschakeld worden voor de fabricage. Passieve SOI circuits van hoge kwaliteit kunnen op wafer-schaal geproduceerd worden met hoog rendement. Hoewel SOI als platform veel voordelen biedt, blijft het opwekken van licht een moeilijke opgave vanwege de indirecte bandkloof – of verboden zone – van het materiaal. Een heterogene integratie van actieve componenten is daarom nodig indien we circuits wensen te realiseren met volledige functionaliteit. Er bestaan diverse technieken om een dergelijke integratie tot stand te brengen, zoals moleculaire bonding, metaalbinding en adhesieve bonding. In dit werk maken we gebruik van adhesieve bonding met divinylsiloxaan-benzocyclobuteen (DVS-BCB) als bondingmateriaal. Deze aanpak biedt verschillende voordelen. Het vereist geen ultra-zuivere oppervlakken zoals bij moleculaire bonding. Bovendien behoudt DVS-BCB goede adhesie wanneer een zekere ruwheid van de oppervlakken aanwezig is, zowel op de epitaxie als op de wafer.

De uitdagingen van deze thesis bevatten onder meer het uitbreiden van het bestaand SOI platform naar operatie in het kortegolfinfrarood domein (1.4-3 μm) en de ontwikkeling van integratietechnologie voor GaSb-gebaseerde actieve componenten op dit platform. Fabricagetechnieken worden ontwikkeld die ons toelaten om de eerste geïntegreerde GaSb fotodetector en laser te demonstreren op het SOI

platform.

Onderzoek van SOI golfgeleiders voor kortegolfinfrarood licht

De ontwikkeling van fotonische componenten op SOI heeft zich tot nu toe vooral gericht op toepassingen in telecom en datacom, de voornaamste commerciële drijfveren van deze technologie. Niettemin heeft een vraag naar compacte spectroscopische systemen recentelijk geleid tot onderzoek naar SOI als een platform voor kortegolfinfrarood licht. In tegenstelling tot telecom applicaties waar de golflengte vastligt op 1.3μm of 1.55μm vereist het spectroscopisch systeem een breedbandige operatie in het kortegolfinfrarood. Bijgevolg werd een onderzoek uitgevoerd naar het gebruik van SOI golfgeleiders in dit bereik. Een state-of-the-art vezel-naar-chip roosterkoppelaar met hoge efficiëntie werd ontwikkeld en gedemonstreerd. Een maximale efficiëntie van -3.8dB wordt verkregen bij 2.1μm, met een 3dB bandbreedte van 90nm. Het ontwerp maakt gebruik van een speciale *advanced passive* fabricagestap om een 380nm dikke Si golfgeleider laag te bekomen. Verder wordt een standaard roosterkoppelaar in 220nm dik Si ontwikkeld en gedemonstreerd die compatibel is met het ePIXfab Multi-project Wafer Scheme. Voor de standaard roosterkoppelaar is de koppelingsefficiëntie beperkt tot 10% bij 2.2μm, met een 3dB bandbreedte van 300nm. De 220nm golfgeleider vertoont een laag propagatieverlies (<0.6dB/cm) bij $\sim 2\mu$m. Deze resultaten tonen aan dat SOI een veelbelovend platform is voor korte-golf infrarood toepassingen.

Ontwikkeling van integratie- en en fabricagetechnologie voor GaSb-gebaseerde componenten

De indirecte bandkloof van Si maakt het moeilijk om efficiënte lichtbronnen of fotodetectors rechtstreeks te implementeren in SOI. Heterogene integratie biedt een oplossing door materiaal met directe bandkloof te combineren met de SOI. In deze thesis wordt een adhesieve integratietechnologie ontwikkeld die gebruik maakt van DVS-BCB als bindingsagent om integratie te bekomen van SOI en epitaxie-gebaseerde GaSb fotodetectors en lasers die werken in het kortegolfinfrarood. Dit omvat een studie van de oppervlaktecompatibiliteit tussen DVS-BCB en verschillende types van substraat, gebruik makend van contacthoekmetingen. Diverse bindingstechnieken zoals manuele bonding, machinale bonding en bonding via partiële uitharding worden onderzocht. Naast de bonding worden geoptimaliseerde verwijderingstechnieken voor het GaSb substraat ontwikkeld die gebruik maken van nat etsen. De fabricageprocessen werden ontwikkeld in de cleanroom van de Photonics Research Group van Universiteit Gent. Mesa formatie via nat etsen en droog etsen werd onderzocht voor diverse GaSb-gebaseerde samenstellingen, bijvoorbeeld InGaAsSb en AlGaAsSb. Tenslotte bestudeerden we metalli-

satie op n- en p-gedoteerd GaSb. Deze studies leveren geoptimaliseerde processen op die ons toelieten om state-of-the-art GaSb-gebaseerde fotodetectors en lasers te demonstreren op SOI.

Ontwerp en demonstratie van de integratie van GaSb-gebaseerde fotodetectors op SOI

Met behulp van het ontwikkeld integratie- en fabricageproces wordt de eerste geïntegreerde GaSb fotodiode op SOI gedemonstreerd, met een cut-off golflengte van 1.7μm, gebruik makend van evanescente koppeling . Het ontwerp van deze *proof of concept* component werd vervolgens uitgebreid tot een cut-off golflengte van 2.5μm. Dit vereist InGaAsSb als absorberend materiaal in de plaats van GaSb. Voor de geïntegreerde InGaAsSb fotodiode onderzoeken we twee verschillende methodes om het licht in te koppelen vanuit de Si golfgeleider: via evanescente koppeling en via roosterkoppelaars. Componenten gebaseerd op beide methodes werden ontworpen en gefabriceerd. De InGaAsSb fotodiode met evanescente koppeling vertoont een intrinsieke responsiviteit tot 1.4A/W bij kamertemperatuur. Het ruisequivalent vermogen (NEP) van de fotodiode bedraagt 1.51×10^{-12}W/Hz$^{1/2}$ bij 25°C wat overeenstemt met een specifieke detectiviteit (D*) van 1.63×10^{9}cmHz$^{1/2}$/W.

In tegenstelling tot evanescente koppeling, welke een zeer dunne DVS-BCB bonding laag vereist, laat roosterkoppeling enige flexibiliteit toe wat betreft de dikte van de DVS-BCB laag. Dit leidt tot een verbetering van het integratierendement in vergelijking met de eerste aanpak. De gefabriceerde component vertoont een intrinsieke responsiviteit tot 0.3A/W, beperkt door de directiviteit van de gebruikte roosterkoppelaar.

Daarenboven laten de ruisprestaties vermoeden dat verdere verbeteringen mogelijk zijn om de sensitiviteit te verhogen. Een van de oorzaken van ruis is lekstroom (hagelruis). We maken daarom een gedetailleerde inschatting van de bron van de lekstroom. De lekstroom wordt grotendeels toegeschreven aan lekkage via de zijwand van de geëtste fotodetector, terwijl de intrinsieke lekstroom slechts 10mA/cm^2 bedraagt. Een passivatie met DVS-BCB reduceert het aantal *surface traps* en daardoor de lekstroom langs de zijwanden. De resultaten wijzen op potentieel tot verdere verbetering door behandeling van de zijwanden en gebruik van andere materialen voor passivatie.

Ontwerp en demonstratie van de integratie van een GaSb-gebaseerde Fabry-Perot laser op SOI met emissiegolflengte 2.01μm

Volgend op de demonstratie van de geïntegreerde fotodiode wordt een geïntegreerde laser ontworpen en gerealiseerd. De eerste generatie maakt gebruik van een standaard epitaxiaal ontwerp om de uitvoerbaarheid van de integratie aan te tonen

onder goed gekende omstandigheden. De epitaxie wordt geïntegreerd op een InP substraat. De facetten van de laser worden gevormd door klieven. Bij kamertemperatuur liggen de drempelwaarden van de stroomdichtheid bij 422 and 676A/cm^2 voor gepulste en continue operatie respectievelijk. De thermische weerstand van de laser is 323K/W. De lasers kunnen opereren in continue regime bij temperaturen tot 35°C. De tweede generatie lasers worden vervolgens ontwikkeld en gedemonstreerd door het integreren van de epitaxie op SOI. De facetten van de laser worden gevormd met behulp van een *Focused Ion Beam* systeem. Een DVS-BCB polymeer golfgeleider gevormd bovenop een geïnverteerde Si *taper* koppelt het licht vanuit de laser naar de Si golfgeleider. De laser werkt in continu regime bij temperaturen tot 10°C met drempelwaarden voor de stroomdichtheid van 1.4kA/cm^2 en 2.2kA/cm^2 voor gepulst en continu regime respectievelijk.

De ontwikkelde integratie- en fabricagetechnieken laten toe om lasers te realiseren die werken met lage drempelstroom bij kamertemperatuur. Niettemin leidt de dikte van de DVS-BCB tot een hoge thermische weerstand. Dit kan verholpen worden door toepassing van een dunnere DVS-BCB laag of door het ontwerp van een thermische shunt die instaat voor warmteafvoer. Bovendien zijn Fabry-Perot lasers minder gewenst voor sommige toepassingen zoals hoge resolutie spectroscopie omdat ze verschillende longitudinale modes vertonen wat leidt tot verschillende laser-golflengtes en een onstabiel optisch uitgangsvermogen. Het is bijgevolg van belang om het ontwerp van de laser verder te optimaliseren om single-mode werking te bekomen.

Elektrisch gepompte hybride InGaAsSb-Si laser met emissiegolflengte 2.42μm

Om een monochromatisch laserspectrum te bekomen dient een Bragg rooster geimplementeerd te worden in de III-V/silicium laserstructuur. Dit wordt bereikt door een Bragg rooster te vormen op de Si golfgeleider. De voornaamste uitdaging bestaat erin de golfgeleider dusdanig te ontwerpen dat de optische mode vooral opgesloten zit in de siliciumgolfgeleider zo dat enkel de evanescente staart van de mode overlapt met de III-V halfgeleider actieve laag. Dit zorgt terzelfdertijd voor een eenvoudige koppeling naar het passief silicium golfgeleidercircuit. Een eerste demonstratie, die gebruik maakt van een Fabry-Perot ontwerp wordt gerealiseerd als een *proof of concept* van een dergelijke hybride InGaAsSb-Si caviteit. De laser opereert met een drempelwaarde voor de stroomdichtheid van 1.75kA/cm^2 bij oneindige lengte in gepulst regime bij 10°C. Dit opent perspectieven voor verdere ontwikkeling van dit type hybride gedistribueerde feedback laser.

Conclusie

Deze thesis onderzoekt het potentieel van het SOI platform en zijn heterogene integratie voor kortegolfinfrarood-toepassingen. Ik kan state-of-the-art resultaten

voorleggen voor kortegolfinfrarood roosterkoppelaars in SOI. Ik heb integratie- en fabricagetechnieken ontwikkeld die toelaten om geïntegreerde fotonische circuits te realiseren met on-chip fotodiodes en lasers. Dit werk resulteert in de allereerste demonstratie van geïntegreerde GaSb-gebaseerde fotodiodes en Fabry-Perot lasers in SOI werkend in het kortegolfinfrarood bij kamertemperatuur. De fotodiodes vertonen een hoge responsiviteit en een cut-off golflengte van 2.5μm. De lasers hebben een lage drempelstroom en emissie bij 2.01μm en 2.4μm. Deze resultaten geven uitzicht op verdere optimalisatie op het gebied van performantie en productierendement.

English summary

Introduction

Spectroscopy-based sensing has recently gained significant attention from industrial users in the environmental and biomedical field. This is because this technique allows the detection of bio-molecules or gases with characteristic absorption lines in the near and mid-infrared wavelength region with extremely high sensitivity. Indeed, spectroscopy is now well-established for examining the composition and concentration of substances by measuring and analyzing the absorption spectrum. Nevertheless, traditionally designed systems contain one or more light sources, detectors and passive components that are bulky, expensive and unsuitable for many applications e.g. implantable sensors. Therefore, photonic integrated circuits offering significant miniaturization are an attractive alternative.

Photonic integrated circuits on the silicon-on-insulator (SOI) platform provide compact and cost effective solutions as well as an established and robust CMOS fabrication technology which can be directly used for their fabrication. High quality SOI passive circuits can be designed and fabricated on wafer scale with high yield. Moreover, the high omni-directional refractive index contrast between Si and the cladding allows the realization of miniaturized photonic integrated circuits. Although SOI, as a platform, has several advantages, light generation remains difficult due to the indirect bandgap of the material. Heterogeneous integration of active devices on SOI is therefore needed to realize fully functional integrated circuits. There are several techniques for doing such integration, such as molecular bonding, metal bonding and adhesive bonding. In this work, we employ adhesive bonding with divinylsiloxane-benzocyclobutene (DVS-BCB) as the bonding agent. This strategy offers several advantages. For example it does not require an ultra-clean surface, unlike the molecular bonding technique. Moreover, DVS-BCB maintains good adhesion when some roughness is presented on both epitaxy and SOI wafer.

In this thesis, the challenges include extending the existing SOI waveguide platform to operate in the short-wave infrared region and the development of integration technology for GaSb-based active devices on the SOI waveguide platform. Furthermore, fabrication technologies are developed which allowed us to demonstrate the first integrated GaSb-based photodetectors and lasers on the SOI platform.

Investigation of SOI waveguide circuits for the short-wave infrared

The design of photonic components on the SOI platform has thus far been focused mainly on telecom and datacom applications, the main commercial drivers for this technology. Nevertheless, in recent years, interests in compact spectroscopic systems sparked research on SOI as a platform for the short-wave infrared. In contrast to telecom applications where the operating wavelength is fixed at $1.3\mu m$ or $1.55\mu m$, spectroscopic applications require broadband operation in the short-wave infrared. Hence, an investigation into the use of SOI waveguides in this wavelength region is carried out. A state-of-the-art high efficiency fiber-to-chip grating coupler is designed and demonstrated. A maximum efficiency of -3.8dB is obtained at $2.1\mu m$, with a 3dB bandwidth of 90nm. The design employs a special advanced passive fabrication run, to achieve a 380nm thick Si waveguide layer. In addition, a standard grating with 220nm thick Si which is compatible with the ePIXfab multi-project wafer scheme is designed and demonstrated. For a standard grating coupler, only 10% coupling efficiency is achieved at $2.2\mu m$ with 300nm 3dB bandwidth. The 220nm thick single mode waveguides exhibit very low (<0.6dB/cm) propagation loss at $\sim 2\mu m$. These results prove that SOI is a promising platform for short-wave infrared applications, including sensing.

Development of integration and fabrication technology for integrated GaSb-based components

Although SOI is promising as a platform for photonic components, the indirect bandgap of Si makes it difficult to implement high efficiency light sources and photodetectors directly. Heterogeneous integration offers a solution by combining direct bandgap materials with the SOI waveguide circuit technology. In this thesis, an adhesive integration technology using DVS-BCB as a bonding agent is developed for the integration of SOI and GaSb epitaxy-based lasers and detectors. This work includes an assessment of surface compatibility between DVS-BCB and different types of substrates using contact angle measurement. Different bonding approaches such as manual bonding, machine bonding and bonding through partial curing are investigated. In addition to bonding, optimized GaSb substrate removal processes using wet etching are developed for device processing. Fabrication processes for GaSb-based photodiodes and lasers were developed in the Ghent University cleanroom. Wet etching and dry etching procedures for mesa formation have been investigated for several GaSb-based compounds, for example InGaAsSb and AlGaAsSb. Metallization is finally studied on n and p doped GaSb. These studies yield optimized processes to demonstrate state-of-the-art integrated GaSb-based photodetectors and lasers on the SOI platform.

Design and demonstration of the integration of GaSb-based photodetectors on SOI waveguide circuits

By employing the integration and fabrication process developed in this thesis, the first integrated GaSb photodiode on SOI using evanescent coupling with a cut-off wavelength up to 1.7μm is demonstrated. The design of this proof of concept device was then expanded to achieve a cut-off wavelength of 2.5μm. This involves the use of InGaAsSb intrinsic material instead of GaSb. For the InGaAsSb integrated photodiode, light is coupled from the Si waveguide to the photodiode using two different approaches: evanescent coupling and grating assisted coupling. Both approaches were designed and fabricated. The fabricated InGaAsSb photodiode with evanescent coupling exhibits an intrinsic responsivity of up to 1.4A/W at room temperature. The Johnson limited noise equivalent power (NEP) of the photodiode at room temperature is $1.51\text{x}10^{-12}$W/Hz$^{1/2}$ at 25°C corresponding to a specific detectivity (D*) of $1.63\text{x}10^{9}$cmHz$^{1/2}$/W.

Contrary to evanescent coupling, where a very thin DVS-BCB bonding layer is required, grating assisted coupling permits some flexibilities in using a thicker DVS-BCB bonding layer. This leads to an improvement in integration yield as compared to the former approach. The fabricated device exhibits an intrinsic responsivity of up to 0.3A/W, limited by the directivity of the grating coupler used in the experiment.

In addition, the noise performance suggests that the device requires further improvements to enhance its sensitivity. One of the causes of noise is leakage current (shot noise). Therefore, a detailed assessment of the source of the leakage current was carried out. The leakage current is mostly attributed to sidewall leakage whereas the intrinsic leakage is only 10mA/cm^2. A passivation with DVS-BCB reduces the amount of surface traps, thereby reducing the sidewall leakage current. The results indicate potential for further improvement by applying sidewall treatment and using different passivation materials.

Design and demonstration of the integration of a GaSb-based Fabry-Perot laser on an SOI waveguide circuit emitting at 2.01μm

Following the demonstration of the integrated photodiode, an integrated laser was designed and realized. The first generation device employs a standard epitaxy design to confirm the feasibility for integration while maintaining good laser properties. The epitaxy is first integrated on an InP substrate. The facets of the lasers are formed by cleaving. Lasers operating at room temperature exhibit threshold current densities of 422 and 676A/cm^2 for pulsed and CW operation respectively at 2.01μm. The thermal resistance of the laser is measured to be 323K/W. The lasers can operate in CW at temperatures up to 35°C. The second generation lasers were then developed and demonstrated by integrating the epitaxy on a SOI waveguide

circuit. The Fabry-Perot laser facets are formed using a Focused Ion Beam system. A DVS-BCB polymer waveguide formed on top of a Si inverted taper is used to couple light from the laser into the Si waveguide. The laser operates in CW mode at temperatures up to 10°C with threshold current densities of 1.4kA/cm^2 and 2.2kA/cm^2 for pulsed and CW mode, respectively.

The results demonstrate the optimized integration and fabrication techniques, allowing the realization of low threshold current lasers operating at room temperature. However, the DVS-BCB bonding results in high thermal resistance. This can be remedied by employing a thinner DVS-BCB layer or by a novel thermal shunt design for heat removal. In addition, Fabry-Perot lasers are undesirable for several applications such as high-resolution spectroscopy because they exhibit several longitudinal modes leading to several lasing wavelengths and unstable optical output power. Therefore, it is of interest to optimize laser designs further to obtain single mode lasing.

Electrically pumped hybrid InGaAsSb-Si laser emitting at 2.42μm

To achieve a single wavelength laser, a weak modulation between the propagating mode and a wavelength selective component must be established. This is attained by forming a Bragg grating on the Si waveguide layer. The main challenge of this task is to design an optical mode to have its main confinement in the Si waveguide such that only the evanescent field is experiencing gain from the multi-quantum well region. Having the main confinement in the Si waveguide improves the coupling efficiency between the laser and the Si waveguide. A first demonstration using a Fabry-Perot design is realized as a proof of concept of such a hybrid InGaAsSb-Si cavity. The laser operates with a threshold current density (J$_0$) of 1.75kA/cm^2 at infinite length at 10°C in pulsed regime. This opens up perspectives for the further development of hybrid distributed feedback InGaAsSb/Si lasers.

Conclusion

This thesis investigates the potential of the SOI waveguide platform and its heterogeneous integration for short-wave infrared applications. For SOI, I present state-of-the-art results for short-wave infrared grating couplers. I developed integration and fabrication techniques to realize integrated phonics circuits with on-chip photodiodes and lasers. This work has resulted in the world's first realization of integrated GaSb-based photodiodes and Fabry-Perot lasers on SOI operating in the short-wave infrared ($\sim$2μm wavelength). The devices operate at room temperature with high responsivity and a cut-off wavelength of 2.5μm for the photodiodes and low threshold currents for lasers emitting at 2.01μm and 2.4μm. These results

open up new possibilities for further optimization in terms of processing yield and device performance, in view of large scale manufacturing.

1

Introduction

The goal of this thesis is to demonstrate integrated lasers and photodetectors on a silicon-on-insulator waveguide circuit, operating in the short-wave infrared wavelength range. The work is part of the Glucosens project [1] which aims to develop the photonics technology required for an implantable integrated absorption spectrometer for blood glucose sensing.

1.1 Introduction

Absorption spectroscopy is an important technique to analyze material composition especially in the infrared wavelength range. The infrared wavelength region refers to wavelengths in a range of 0.75 to 30μm which can be divided into different sub-group. In this thesis, it is divided into 5 subsections [2]: near-infrared (NIR, 0.7-1.0μm), short-wave infrared (SWIR, 1.0-3μm), mid-wave infrared (MWIR, 3-5μm), long-wave infrared (LWIR, 8-12μm), very-long wave infrared (FIR, 12-30μm). The definitions are not strict and the wavelength boundaries can vary slightly. Absorption spectroscopy of blood glucose in the 2-3μm wavelength region has been of substantial interest. This is because the combination band of the vibrational-rotational state of glucose is located in this wavelength region, where the interference from water absorption remains relatively low [3–5]. Moreover, in this wavelength range, several gases of industrial interest such as HF and CH_4 also have strong absorption signatures [6, 7]. These two considerations make a spectroscopic system operating in the short-wave infrared very attractive.

In addition, the interest in extending telecommunication applications to the 2μm wavelength region has strongly increased. This is due to the shortage of bandwidth in the 1.55μm wavelength range, leading to an extension into the short-wave infrared where thulium-doped fiber amplifiers can be used [8]. However, typical system requirements for these applications are high sensitivity, compactness and low cost. To fulfil these requirements, further development of the conventional sources and detectors is required. On-chip integration of these devices can help further to reduce the cost and improve compactness. GaSb-based semiconductors have been proven an ideal material for compact active devices in the short-wave infrared. Indeed, several groups have successfully reported high efficiency lasers and high responsivity detectors at room temperature [9–11]. Silicon-On-Insulator (SOI) is now a well-studied passive photonics platform for telecommunication applications. This platform provides several advantages such as CMOS processing compatibility which allows mass production at low cost [12]. Although SOI is a good passive platform for the short-wave to mid-wave infrared wavelength range [13, 14], the indirect bandgap of silicon hampers efficient light emission. Thus, it is highly desirable to integrate a gain material onto SOI waveguide circuits to enable a fully functional integrated circuit operating in the short-wave infrared. Several examples on different platforms operating at 1.55μm have thus far been reported, including the hybrid Si-InP platform [15, 16]. Despite its huge potential, there are only few reports on hybrid Si-GaSb optical devices [17] because of its early stage of development.

This thesis deals with the challenges of extending the existing SOI passive platform from the telecommunication wavelength range to the short-wave infrared. In a first stage, I investigated which active material to integrate on SOI waveguide circuit. The second stage involved the exploration, design and development of the integration and fabrication procedures.

In the next sections, I elaborate on applications where short-wave infrared and mid-wave infrared photonic integrated circuits are applicable. It is followed by a review of the currently available choices in passive photonic integrated circuit platforms for long wavelength. I discuss the selection of active materials used for heterogeneously integrated photodiodes and lasers. Finally, various heterogeneous integration techniques are discussed. I conclude the chapter with my rationale of the choice of materials and integration methodology.

1.2 Photonic applications in the short-wave infrared

Photonics refers to the science and technology of generation, manipulation, and detection of light and its interaction with different substances [18]. Photonics covers wavelengths from the ultraviolet to the far-infrared range. Thus far, the main applications, such as displays, medical devices and telecommunication, are
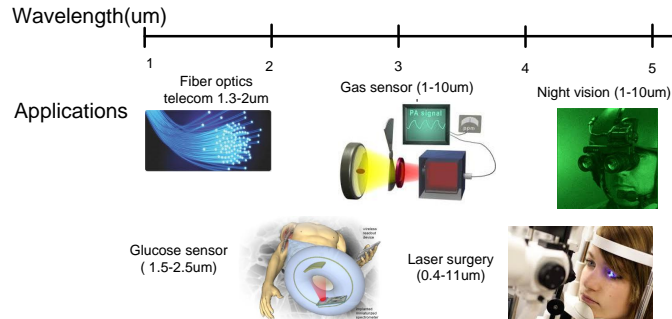
Figure 1.1: Summary of applications from the near to mid-wave infrared wavelength range

implemented in the visible and near-infrared range. Nevertheless, several important applications in the short-wave and mid-wave infrared have recently emerged including thermal imaging [19, 20], gas sensing [21], non-invasive medical devices [5, 22], laser surgery [23] and telecommunication [24]. Fig. 1.1 illustrates examples of the current potential applications available in the near to mid-wave infrared.

In the following section, I review the application of optical devices in the field of absorption spectroscopy, biomedical devices and telecommunication as they are directly relevant to this thesis.

1.2.1 Gas sensors using absorption spectroscopy

Absorption spectroscopy is the most common technique to differentiate molecules. The interaction of light and matter is observed via the change in absorption of photons at different energy. A spectroscopic system needs a light source, which can be a broadband light source [25] or a tunable laser [4, 26]. In the first case the light is sent through a dispersive element such as a grating to obtain a narrow bandwidth. This narrow bandwidth is important to detect gas molecules, because of their very narrow absorption lines. By detecting the changes in the transmission spectrum at different wavelengths, molecules can be differentiated. Fig. 1.2 shows absorption spectra of different gas molecules. As can be seen, in the SWIR wavelength range, the effect from water and CO_2 absorption is minimized. Therefore, this wavelength range is interesting for spectroscopic sensing. Several absorption lines of interesting gases such as CO, HF and CH_4 are also located in the SWIR range. A typical spectroscopic system with a dispersive element has a limit on resolution due to the grating technology. Also, the signal to noise ratio is relatively low due to the inefficiency of the typical light source, for instance, a tungsten-halogen lamp. To achieve a good signal to noise ratio, the system requires a very powerful light source and a high sensitivity detector, preferably with a cryogenic cooling system.
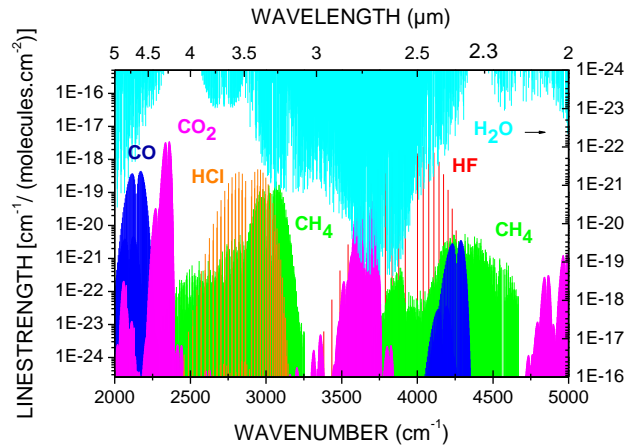
Figure 1.2: Atmospheric transparency window and absorption signatures in the 2-5µm wavelength range

These requirements lead to a bulky system with high power consumption. Such spectroscopic systems are thus unsuitable when portability and power efficiency are prime requirements.

A second class of spectroscopic systems employs a tunable laser diode as a light source. This system allows wavelength tuning by changing the current injection and temperature of the laser diode or by using an external cavity. The power spectral density in laser systems is much higher than in conventional dispersive systems relaxing the requirements on the photodetector. Without the requirements of a powerful broadband source, a grating component and a high sensitivity photodiode, it is possible to implement a compact spectroscopic system. This gives us an access to several applications such as gas detection in hazardous environments where compactness and low power consumption are desirable [7, 26].

1.2.2 Biomedical applications

Photonics has rapidly found its application in medical technology. Optical imaging and monitoring such as optical coherence tomography [27], breath analysis [28] and glucose monitoring [3, 29] give doctors an alternative perspective to diagnose and treat patients. Photonic devices offer fast and effective ways to image or sense biological molecules noninvasively. Moreover, early disease or abnormal symptom detection can improve the patient condition and treatment planning.

Similar to gas sensing applications, medical applications exploit the interaction of light and matter, for example, water absorption and the corresponding penetration depth in tissue. Human tissue consists more than 70% of water [30]. Fig. 1.3
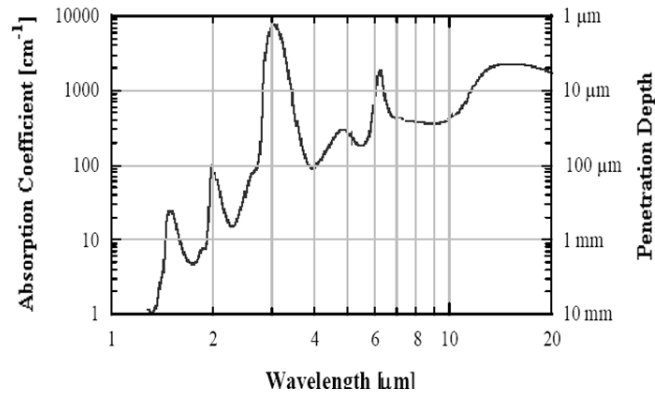
Figure 1.3: Absorption spectrum of water and the penetration depth in the 1-20μm infrared range [33]

shows the water absorption as a function of wavelength in the infrared wavelength range. This absorption is an inverse function of the penetration depth, typically in the range of a few μm to a mm. These properties are very important for tissue ablation [23].

On the other hand, similar to what is done in gas sensing applications, molecule specific detection also provides great benefits in medical fields such as in breath analysis [31] and glucose sensors [3]. For breath analysis, the standard technique involves collecting the breath samples and is followed by analysis of the samples with a highly sensitive instrument [32]. Mass spectrometry is typically used to analyze breath samples. The sample is first ionized. Then the ions are accelerated and passed through a magnetic field which sorts the ions based on mass/charge ratio. This makes the system complex and bulky and prevents real time measurement. On the other hand, an optical instrument would enable real time sampling. Real time measurement provides advantages such as eliminating the complexity of storing the breath sample and allowing the measurement of the change in breath composition over time.

Another example, in the SWIR, is the sensing of the blood glucose level as optical absorption from glucose is strong compared to that of water in the overtone (1.6-1.8μm) and combination band (2.0-2.3μm) [33]. This provides the opportunity to develop a minimally invasive glucose monitoring system. Moreover, by combining glucose sensing and breath analysis, a better diagnosis and recommendation to the patients can be given [31].

1.2.3   Telecommunication applications

The main driver of the development in telecommunication components over the last couple of decades has been the low loss in optical fibers at around 1.55μm. However, with the tremendous increase of demand for information bandwidth, the available bandwidth is becoming insufficient. Several approaches have been taken to alleviate this problem, such as novel modulation schemes. Alternatively, extending the working wavelength bandwidth from 1.55μm to around 2μm is also of great interest [34]. Such technology is currently being developed in the European Mode-gap project [8, 24, 35].

1.3   Passive waveguide platform for the short-wave infrared

A photonic waveguide platform is an essential component for the realization of Photonic Integrated Circuits (PICs). PICs allow complete functionality in one single chip, resulting in a compact, high efficiency and reliable device [36, 37]. PICs were developed originally to serve demands in telecommunication applications. Over the last decade, several photonic components such as multiplexers, polarization rotators, grating couplers and waveguides have been developed and realized on different platforms, especially SOI [36, 38–40].

Recently, spectroscopy has emerged as an interesting application that could benefit from the advantages of PICs. However, spectroscopic applications require a broad range of operating wavelengths while many materials used on common photonic waveguide platforms such as Si and SiO_2 have limited transparency [34, 41]. In theory, several materials such as SiO_2, Ge, Al_2O_3, SiN_x are transparent in the SWIR [34]. Soref et al. [34] discusses the compatibility of different waveguide platforms for different wavelength ranges as shown in Table 1.1. An extensive review of different waveguide structures and materials can be found in [34].

Following a proposal from Soref et al. in 2006, component design and fabrication on several platforms such as SOS (Silicon-On-Sapphire) [42], Ge on Si [43–45], suspended Si membrane [46] and SOI [14] have been investigated and realized that support different infrared wavelength regions.

SOS employs sapphire as a substrate and Si as a waveguide. The Si layer is epitaxially grown on the sapphire. Typical waveguide losses are 4.5dB/cm at 4.5μm wavelength [42].

Ge-on-Si hetero-waveguides show losses as low as 3-4dB/cm in the 5μm wavelength [44, 45, 47].

Suspended Si membranes [46] are proposed as an alternative approach when absorption loss in SiO_2 or Al_2O_3 is a limiting factor. The structure proposed by [34] consists of a suspended Si rib waveguide membrane surrounded by an

Waveguide type	Wavelength ranges of operation
Si/SiO$_2$/Si (SOI)	1.2-2.6μm and 2.9-3.7μm and 100-200μm
Si/Al$_2$O$_3$(SOS)	1.2-4.4μm
Si/Si$_3$N$_4$/Si (SON)	1.2-6.7μm
Si membrane	1.2-8.0μm and 24-200μm
Si nano-slotted membrane	1.2-9.2μm and 23-200μm
SiGe/Si	1.6-12μm and 100-200μm
Ge/Si	1.9-16.8μm and 140-200μm
GeSn/Si	2.2-19μm
Hollow core (Bragg, SiO$_2$/Si cladding)	1.2-3.9μm
Hollow core (Bragg, SiGe/Si cladding)	1.2-200μm
Hollow core (Anti-Res., SiGe/Si cladding)	1.2-200μm
Porous-Si/Si	1.2-9.0μm and 23-200 μm
Si PhC-line membrane	1.2-8.0 μm and 24-200μm
Si PhC self-coll. membrane	1.2-8.0 μm and 24-200 μm
Si nano-crystal/Si membrane	1.2-8.0μm and 24-200μm
Si Arrow (SiGe/Si cladding)	1.2-8.0μm and 24-200 μm

Table 1.1: Summary of waveguide platforms covering the infrared wavelength range (reproduced from [34])

air cladding. The advantage of this structure is that the suspended membrane is formed by using an SOI substrate where the bottom air cladding is obtained by under-etching the oxide. Therefore, it is a CMOS compatible process.

Among these proposed waveguide structures, the SOI platform has been the most widely studied due to the availability of mature CMOS fabrication processes and well developed basic component design know-how [12, 48]. Ghent University together with imec are pioneering the development of PICs on the SOI platform for communication applications. This makes the SOI platform the first choice to examine the possibility of accommodating longer wavelengths in this thesis. The discussion on SOI waveguides and grating couplers is presented in Chapter 2. A waveguide propagation loss as low as 0.6 dB/cm at 2.2μm is reported [13].

1.4 Light sources and detectors for the short-wave infrared

Different types of light sources (such as lasers and LEDs), and detectors (thermal and photon) are available in the short-wave and mid-wave infrared. I limit the review of light sources to lasers only, due to their relevance to this thesis. The discussion on photodetector is limited to semiconductor photodiodes for the same reason.
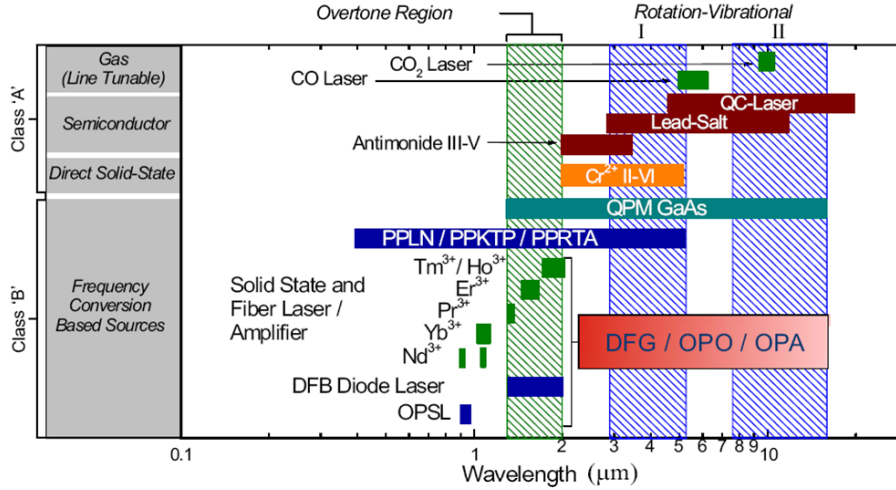
Figure 1.4: Summary of lasers available for the short-wave and mid-wave infrared (reproduced from [57])

1.4.1 Light sources

In general, an ideal light source offers 1) a wide tuning range and 2) a narrow linewidth for high sensitivity and selectivity, 3) high output power 4) reliable performance over a long period 5) compactness and 6) low temperature and current sensitivity. It is challenging to meet all these requirements. Fig.1.4 summarizes the lasers available for infrared wavelengths, ranging from 1 to 11μm. In the SWIR to the MWIR, several types are available such as antimonide (Sb) based III-V lasers [49–51], direct solid state (Cr^{2+} II-VI) laser [52, 53] and frequency conversion based sources based on solid state and rare-earth element doped fiber operating in the NIR to the SWIR [54, 55]. Typically, frequency conversion based sources and direct solid state Cr^{2+} II-VI lasers offer very high output power (>Watt) with wide tunability [53, 56]. However, these systems require very powerful pump light sources. The typical power conversion efficiency is only ~25% [53, 56]. This limits their potential in applications where compactness is a critical requirement.

In contrast, in the past decade, several groups have reported high performance semiconductor III-V lasers and detectors in the short-wave and mid-wave infrared based on several compounds [58–63]. For example InP based lasers and detectors currently operate at room temperature at wavelengths to up to 2.6μm [58, 59]. Unfortunately, this material has reached its limit due to a high lattice mismatch between the quantum well and the substrate [64]. GaSb has recently emerged [60–62] as an alternative to extend the wavelength range of III-V semiconductor
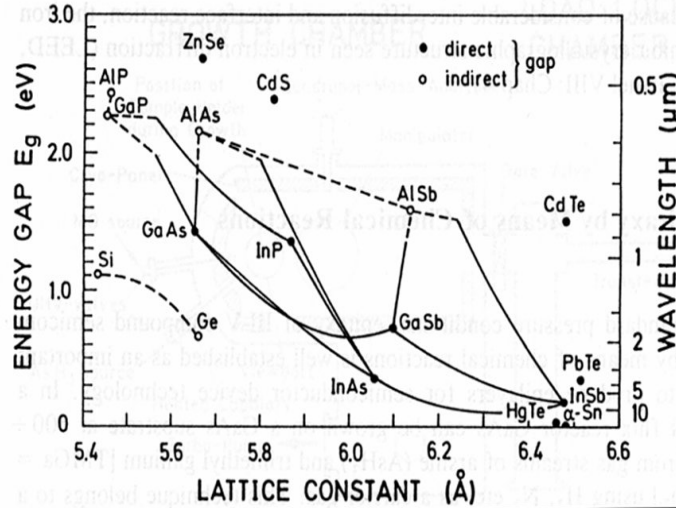
Figure 1.5: Bandgap positions of selected binary alloys [65]
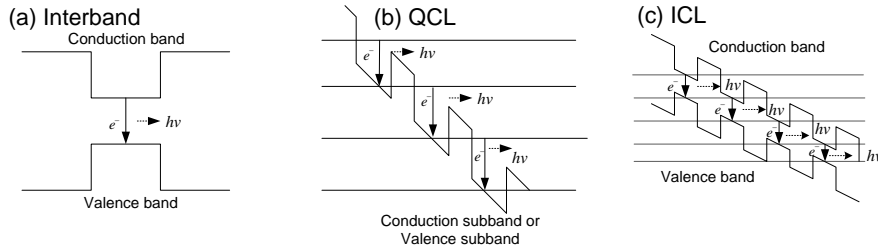
Figure 1.6: Light emission mechanism for different types of lasers a) Interband transition b) QCL c) ICL

laser into the mid-wave infrared regime.

As shown in Fig. 1.5, the GaSb, AlSb and InAs compounds have very similar lattice constants ($\sim$6.1 Å). That makes them suitable for the epitaxial growth of several types of lasers, including interband transition (Type I) [60–62] and intersubband quantum cascade lasers (QCL) where the carrier transition involves only one type of carrier such as the electron. In a QCL, the electrons make a transition within the conduction band, thereby emitting a photon and tunnel though to another period to restart the process again [56]. The interband cascade laser (ICL) is similar to a QCL in that the electron is recycled periodically. However, the radiative recombination occurs between valence and conduction band, similar to what is seen in Type I lasers. A schematic of the energy transitions of different laser schemes is presented in Fig. 1.6.

For wavelengths in the range of 2-2.5μm, Type I lasers exhibit the best performance in terms of power consumption and output power. Therefore, in this work, Type I lasers are selected.

An overview of demonstrated Multiple-Quantum-Well (MQW) Type I GaSb based lasers starting from the early 1990s is presented in Fig. 1.7. The first highly strained MQW laser operated at room temperature in pulsed regime with 143A/cm^2 threshold current density [63]. This device suffered from high internal loss. The internal loss could be further reduced by reducing the overlap of the optical mode with the cladding, resulting in a reduction in the free carrier absorption loss. This was implemented by adding separate confinement layers into the laser waveguide [66]. The threshold current density in continuous wave was further improved to 300A/cm^2 [66], and subsequently reduced to 115A/cm^2 [67]. Additional improvements of the epitaxial growth, allowing higher strain by increasing In concentration in QW and the incorporation of Al in the barrier to create a quinternary compound has further advanced this type of laser to lase up to 3.7μm [68–70]. Due to the tremendous design efforts over the last decade, the Type I GaSb laser is considered to be reaching maturity. The device is commercially available, operating with Watt-level output power at room temperature [71, 72]. While the laser performances are well investigated [68, 70–72], only a few works are focused on designs for specific applications. In 2006, Rattunde et al. [73] designed a laser with a smaller fast axis beam divergence (from 67° to 44°) to support coupling with standard optical components. Such a laser is mainly utilized in free space coupling systems. In this thesis, to serve our purpose inside a fully integrated compact spectroscopic system, our laser is designed to accommodate a waveguide coupling system. This topic will be discussed in detail in following chapters.

1.4.2 Photodetectors

Semiconductor photodetectors are commonly available for SWIR detection. The detection mechanism is based on the interaction of photons and the absorbing material, generating a photo current. In the last decade, HgCdTe has been developed intensively as an infrared photon detector [81, 82]. HgCdTe offers several advantages over others materials due to several reasons: 1) It can accommodate wide wavelength range detection in the infrared wavelength range with almost no lattice mismatch constraint [81]. 2) It offers better absorption/thermal generation ratio than other materials at long wavelength ($> 10\mu$m) at temperatures above 70K. However, devices based on HgCdTe have drawbacks such as instability of the surface and interfaces due to the weak Hg-Te bond [83], inferior material uniformity [82] and therefore low yield [82].

Photodiodes utilizing quantum well structures (such as Type-II superlattice InAs/GaAsSb quantum wells) have received much attention as an alternative to
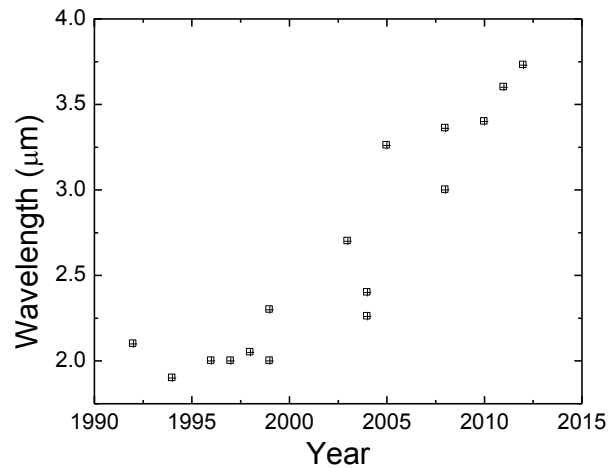
Figure 1.7: The development evolution of GaSb type I laser diodes in the spectral range of
2-3.8μm [49, 51, 60, 63, 66, 67, 70, 74–80]

HgCdTe in the MWIR spectral range [84, 85]. Nevertheless, the overall performance of these devices is not yet satisfactory for practical applications compared to HgCdTe photodiodes [84].

For the NIR and SWIR wavelength range, InGaAs photodetectors with a lattice constant matched to InP are well developed for optical communications. The devices offer low noise, high speed, and high sensitivity operating at room temperature [86, 87]. By incorporating more In into the alloy, increasing the lattice mismatch between the InP substrate and the absorbing layer, the cutoff wavelength of this photodetector can be extended up to 2.6μm [86, 87]. However, the increasing lattice mismatching between the InP and InGaAs layers considerably degrades the material quality due to an increase in dislocation density [88]. This leads to a larger dark current and a higher noise level in the photodetectors. This type of photodiode is commercially available [87]. The specific detectivity (D*) is a typical figure of merit for comparing photodetectors. D* is defined as the ratio of square root of the area of the photodetector and the noise equivalent power (the input optical power that give rise to a signal to noise ratio of 1). The details on this parameter can be found in Chapter 4. Fig. 1.8 summarizes the specific detectivity (D*) of different types of photodiodes from Hamamatsu [87]. InGaAs exhibits a minimal noise level (maximum specific detectivity) compared to other types of photodetectors in the SWIR wavelength range.

The quaternary alloy InGaAsSb epitaxially grown on GaSb substrate is a very promising candidate to extend the wavelength further and cover both SWIR and MWIR at room temperature [89–92]. From Fig. 1.5, it can be seen that the
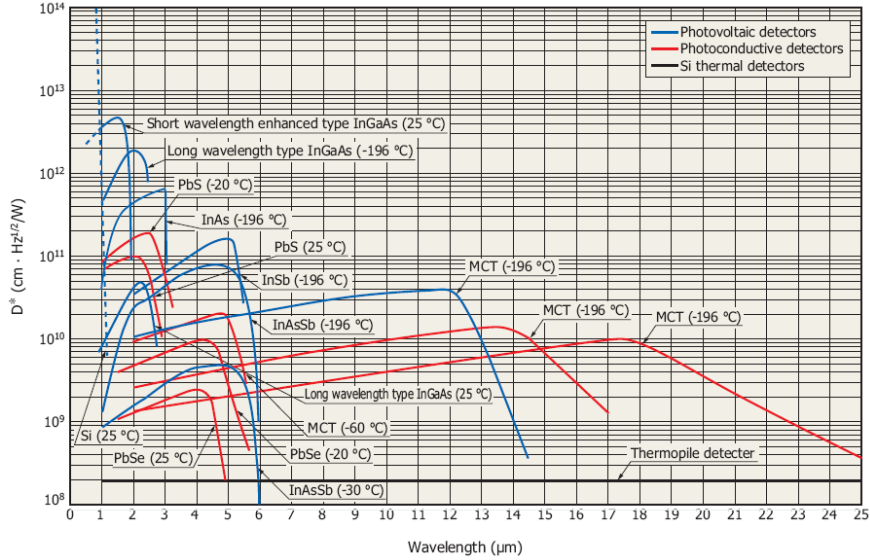
Figure 1.8: The summary of specific detectivity (D*) of different types of photodetectors (reproduced from [87])

bandgap of the absorbing layer can be varied from 1.7 to 4.9μm by increasing the lattice mismatch of the absorbing layer to the GaSb substrate [91]. During the past few years, InGaAsSb photodetectors on GaSb substrate have been reported using different device structures and growth methods, such as molecular beam epitaxy (MBE), liquid phase epitaxy (LPE) and metalorganic chemical vapour deposition (MOCVD) [92–94]. Among different growth methods, MBE has several advantages such as lower substrate temperature and precise control leading to better quality. Nevertheless, commercial photodetectors are grown using LPE and MOCVD due to its maturity [95]. The photodetectors exhibit higher noise than their InGaAs counterparts due to higher dark current at room temperature operation [89–92]. Therefore, depending on the system design, trade-offs between parameters such as noise, peak wavelength responsivity and bandwidth are made and suitable materials are selected accordingly. In this thesis, the InGaAsSb system is selected due to its broad wavelength coverage. Moreover, it is highly desirable to obtain both photodetectors and lasers in one system, in this case, grown on a GaSb substrate. Thereby, the complexity of implementing a photonic integrated circuit with both lasers and detectors operating in the short-wave infrared is minimized.

1.5 Integration technology for the short-wave infrared

Integration technology has been extensively developed for several applications such as PICs, microelectromechanical systems (MEMS) and electronics. The need to create a system with new functionality by including new materials has accelerated the development in this field. In this section, we limit ourselves to only technology development for PIC applications based on SOI, which is relevant to this thesis.

When developing PIC applications on the SOI platform, the two main development steps involve 1) advanced passive circuit design as discussed earlier in Section 1.3 and 2) the heterogeneous integration of active components such as lasers and detectors onto the passive circuit.

The two most common approaches to incorporate other materials onto SOI are epitaxial growth and die-to-wafer bonding. The success of epitaxial growth is very material dependent. For example, for the case of Si and InP, the difference in lattice mismatch and thermal expansion coefficient between the substrate (Si) and active layer (InP) results in a high dislocation density when grown in sheets [96]. It should be noted that this problem was recently overcome by using selective area growth [97] which makes InP epitaxial growth on Si substrate possible. However, the research is still at an early stage.

In addition, GaSb shows potential for direct epitaxial growth on a Si substrate [98]. With proper growth conditions during molecular beam epitaxy (MBE), it is possible to release the high strain by formation of Lomer-type dislocations which propagate at the Si/III-V interface. This results in minimal dislocations in the vertical direction [99]. Since 2009, epitaxial grown multiple quantum well (MQW) lasers on Si substrate, lasing at 1.55 and 2.2μm have been demonstrated by two separate groups [17, 99–102]. The devices operate in both pulsed and continuous wave at room temperature. This approach appears to be the most promising technology for GaSb/Si integration. However, due to the requirement of a thick buffer layer between a Si substrate and GaSb to avoid dislocations, this results in no coupling mechanism between these two materials. This problem is possible to overcome by using localize epitaxial growth so that the Si passive platform can be fabricated on the same side as epitaxy. Nevertheless, research in this field is still at very early stage. Moreover, the Si substrate used in this work is 7 $^\circ$ miscut which is not commonly used in CMOS process [102].

Another material system that shows potential for direct epitaxial growth on Si, is Ge/GeSn/SiGeSn. GeSn is supposed to exhibit a direct bandgap when the Sn concentration is increased to more than 10% [103, 104]. By adding Sn to the Ge matrix, the bandgap reduces, pushing the emission into the 2μm wavelength range [105]. An electrically pumped Ge laser lasing at 1.55-1.7μm has recently been demonstrated [106]. Despite of this recent progress, research on this topic is

still at an early stage and requires extensive material engineering and device design in order to obtain efficient devices.

Although the epitaxial growth approach shows promise as a future platform, an intensive optimization on material properties is still required to obtain comparable performance to the existing systems.

Alternatively, heterogeneous integration can be developed as a short term solution. Several techniques are available for this, such as fusion bonding [107], plasma assisted direct bonding [108], DVS-Benzocyclobutene (DVS-BCB) adhesive bonding [109], metallic bonding [110], anodic bonding [110] etc. Different techniques have different advantages and disadvantages, depending on the materials to be bonded. An extensive review of these techniques can be found in [111, 112].

The most common techniques used for Si-based photonic integrated circuits are molecular bonding [108, 113, 114] and adhesive bonding using DVS-BCB [109, 115, 116].

Molecular bonding or direct bonding was introduced in 1992 [117]. This approach employs the covalent bond of OH groups on both the SOI and the epitaxy surface [108]. The typical process flow of this bonding technique is schematized in Fig. 1.9.

A thin layer of SiO_2 is deposited on both SOI and epitaxy to adsorb by-products which are the result of previous chemical reactions. The process requires an extensive cleaning process using HF acid mixed followed by a NH_4OH solution to remove native oxide and contamination. It is followed by plasma activation to activate the surfaces by growing a thin layer of a highly reactive native oxide. The substrates are brought in contact at room temperature and then loaded into the bonding chamber. Under pressure and at an elevated temperature of up to 300°C, the hydrogen bonds transform into covalent bonds, resulting in the bonding [108, 111]. Several highly efficient active devices including hybrid lasers [119–121] and detectors [119, 122, 123] have been demonstrated by several groups. These demonstrations, however, are limited to InP lasers operating at telecommunication wavelengths. Also, the bonding involves intensive cleaning procedures, which require an expensive cleanroom facility.

The adhesive bonding technique using DVS-Benzocyclobutene (DVS-BCB) as an adhesive agent was introduced in 2002 as an alternative wafer bonding approach [109]. DVS-BCB is employed as an interfacial layer which conforms to deeps-submicron-level irregular surface topography. Therefore, cleanliness of the bonding surface is less critical compared to the molecular bonding technique. Moreover, since this technique is based on the adhesive property of the bonding agent, it simplifies the integration process and offers high compatibility with different material systems [124–127]. Several demonstrations of InP/SOI devices using this technique have been reported by different groups [109, 116, 128]. Wafer scale
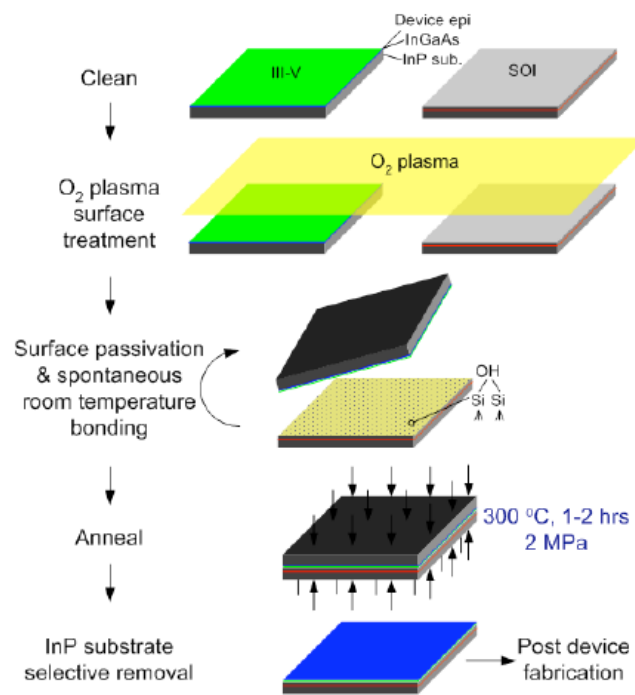
Figure 1.9: Schematic of O_2 plasma assisted low-temperature III-V-to-Si bonding process flow (reproduced from [118])
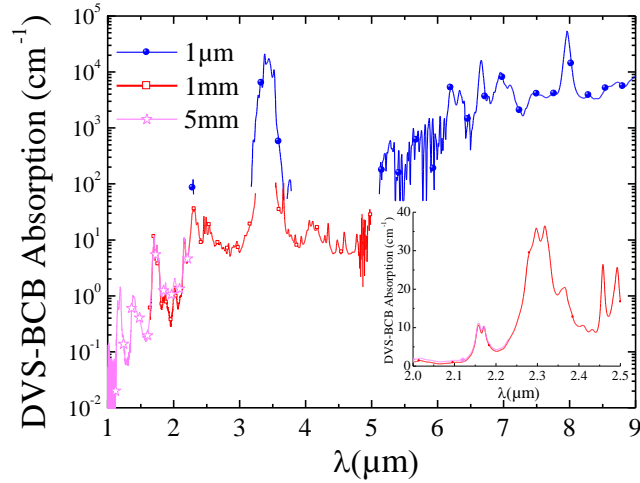
Figure 1.10: Absorption of DVS-BCB measured using different film thicknesses as a function of wavelength. The inset presents the zoom in the 2-2.5μm wavelength range

fabrication capability is also reported for InP-based systems [109, 129]. However, the transparency window of DVS-BCB is limited. Fig. 1.10 presents the optical absorption of DVS-BCB as a function of wavelength. The DVS-BCB layer has a loss lower than 12/cm below 2.26μm and around 2.4μm. However, at longer wavelengths, the losses are much higher. Therefore, DVS-BCB is definitely not ideal for the integration of wide band infrared devices. However, in the scope of this thesis I focus on active devices operating in the 2 to 2.4μm wavelength range, where DVS-BCB is still reasonably transparent. Therefore, integration using DVS-BCB is certainly an interesting alternative platform.

In summary, the SOI waveguide platform shows potential to serve as a good passive platform for the SWIR. Given its advantages such as compactness and CMOS compatible processing, the SOI platform certainly surpass other possible technologies such as Si-on-SiN$_x$, Si-on-sapphire and Si membrane. However, the Si indirect bandgap precludes it from forming good photodetector or laser components in the SWIR. Therefore, integration of direct band gap material is required to achieve fully functional PICs. GaSb and its compounds present a promising platform for SWIR lasers and detectors. This raised my interest in investigating the heterogeneous integration of GaSb-based compounds on SOI waveguide circuits. The integration approach selected is adhesive bonding, using DVS-BCB as a bonding agent. Combining SOI and GaSb optoelectronic components could thus yield a compact, yet efficient spectroscopic system.

1.6   Organization of this dissertation

This thesis investigates the design of passive SOI components, integrated photodetectors and lasers operating in the SWIR, and the development of the integration and fabrication technology of these GaSb integrated devices on passive SOI photonic devices. The study includes component design, the integration technology and the processing development. Chapter 1 (this chapter) presents a brief overview of materials and the technologies involved in this thesis. Chapter 2 presents the state-of-the-art of the short-wave infrared passive devices developed during this thesis. This includes the design and measurement of SOI waveguides and fiber-to-chip grating couplers. Chapter 3 presents the integration and fabrication technology developed in this thesis. Chapter 4 presents design, fabrication and measurement results of the integrated InGaAsSb photodiodes. In Chapter 5, details on the design, fabrication and measurement of thin film GaSb-based Fabry-Perot lasers lasing at 2.01μm are presented. The results include the demonstration of an integrated GaSb based Fabry-Perot laser on an SOI waveguide circuit coupled to a Si waveguide. Chapter 6 presents hybrid integrated Fabry-Perot lasers lasing at 2.4μm. The chapter discusses design, integration, fabrication and measurement results. Future device designs including an integrated hybrid DFB GaSb based laser are presented in this chapter as well. Chapter 7 concludes the thesis with a discussion on possible ways to further improve the performance of the devices.

1.7   Publications

1.7.1   Publications in international journals

1. G. Roelkens, U.D. Dave, A. Gassenq, N. Hattasan, C. Hu, B. Kuyken, F. Leo, A. Malik, M. Muneeb, E.M.P. Ryckeboer, S. Uvin, Z. Hens, R. Baets, *silicon-based heterogeneous photonic integrated circuits for the mid-infrared*, Optical Materials Express (invited), 3(9), p.1523-1536 (2013)

2. E.M.P. Ryckeboer, A. Gassenq, M. Muneeb, N. Hattasan, S. Pathak, L. Cerutti, J-B Rodriguez, E. Tournié, W. Bogaerts, R. Baets, G. Roelkens, *Silicon-on-insulator spectrometers with integrated GaInAsSb photodiodes for wide-band spectroscopy from 1510 to 2300 nm*, Optics Express, 21(5), p. 6101-6108 (2013)

3. N. Hattasan, B. Kuyken, F. Leo, E.M.P. Ryckeboer, D. Vermeulen, G. Roelkens, *High-efficiency SOI fiber-to-chip grating couplers and low-loss waveguides for the short-wave infrared*, IEEE Photonics Technology Letters, 24(17), p.1536-1538 (2012)

4. A. Gassenq, N. Hattasan, E.M.P. Ryckeboer, J.B. Rodriguez, L. Cerutti, E. Tournié, G. Roelkens, *Study of evanescently-coupled and grating-assisted GaInAsSb photodiodes integrated on a silicon photonic chip*, Optics Express, 20(11), p.11665-11672 (2012)

5. G. Roelkens, W. M. J, Green, B. Kuyken, X. Liu, N. Hattasan, A. Gassenq, L. Cerutti, J.B. Rodriguez, R. M. Osgood, E. Tournié, R. Baets, *III-V/silicon photonics for short-wave infrared spectroscopy*, Journal of quantum electronics (invited), 48(2), p. 292-298 (2012)

6. N. Hattasan, A. Gassenq, L. Cerutti, J. B. Rodriguez, E. Tournié, G. Roelkens, *Heterogeneous integration of GaInAsSb p-i-n photodiodes on a silicon-on-insulator waveguide circuit* , IEEE Photonics Technology Letters, 23(23), p.1760 (2011)

1.7.2   Publications in international conferences

1. G. Roelkens, B. Kuyken, F. Leo, N. Hattasan, E.M.P. Ryckeboer, M. Muneeb, C. Hu, A. Malik, Z. Hens, R. Baets, Y. Shimura, F. Gencarelli, B. Vincent, R. Loo, P. Verheyen, G. Lepage , J. Van Campenhout, L. Cerutti, J.B. Rodriguez, E. Tournié, X. Chen, M. Nedeljkovic, G. Mashanovich, X. Liu, W. Green, *Long-wavelength III-V/silicon photonic integrated circuits*, Advanced Photonics - OSA Optics & Photonics Congress (invited), United States, p. IT2A.1 (2013)

2. E.M.P. Ryckeboer, A. Gassenq, N. Hattasan, Cerutti, Laurent, Rodriguez, J.B., Tournié, Eric, R. Baets, G. Roelkens, *Silicon-on-insulator spectrometers with integrated GaInAsSb photodiode array for wideband operation from 1500 to 2300 nm*, CLEO, United States, p. JW2A.69, (2013)

3. N. Hattasan, A. Gassenq, L. Cerutti, J.B. Rodriguez, E. Tournié, G. Roelkens, *Integrated thin-film GaSb-based Fabry-Perot lasers: towards a fully integrated spectrometer on a SOI waveguide circuit*, 2013 SPIE-Photonics West Conference, 8631, United States, p. 8631-35 (2013)

4. N. Hattasan, A. Gassenq, L. Cerutti, J.B. Rodriguez, E. Tournié, G. Roelkens, *GaSb-based integrated lasers and photodetectors on a Silicon-On-Insulator waveguide circuit for sensing applications in the shortwave infrared*, Photonics Global Conference 2012, Singapore, p.1-4 (2012)

5. N. Hattasan, A. Gassenq, L. Cerutti, J.B. Rodriguez, E. Tournié, G. Roelkens, *InGaAsSb/GaSb lasers and photodetectors integrated on a Silicon-On-Insulator waveguide circuit for spectroscopic applications*, International Workshop on Opportunities and Challenges in Mid-infrared Laser-based Gas Sensing (MIRSENS2), Poland, p.16 (2012)

6. N. Hattasan, A. Gassenq, L. Cerutti, J.B. Rodriguez, E. Tournié, G. Roelkens, *The study of integrated thin film GaSb-based Fabry Perot lasers: towards a fully integrated spectrometer on a Silicon-On-Insulator waveguide circuit*, 2012 SPIE-Photonics West, United states, p.8631-5 (2012)

7. A. Gassenq, N. Hattasan, L. Cerutti, JB Rodriguez, E Tournié, G. Roelkens, *Laser and photodetector integration on silicon-on-insulator waveguide circuits: towards a fully integrated SWIR spectrometer*, MIOMD-XI, United States, (2012)

8. E.M.P. Ryckeboer, A. Gassenq, N. Hattasan, B. Kuyken, L. Cerutti, J. B. Rodriguez,E. Tournié, G. Roelkens, W. Bogaerts, R. Baets, *Integrated spectrometer and integrated detectors on Silicon-on-Insulator for short-wave infrared applications*, CLEO, United States, p.CTu1A.3 (2012)

9. F. Leo, B. Kuyken, N. Hattasan, R. Baets, G. Roelkens, *Passive SOI devices for the short-wave infrared*, 16th European Conference on Integrated Optics (ECIO 2012), Spain, p.156 (2012)

10. G. Roelkens, S. Keyvaninia, S. Stankovic, M. Tassaert, N. Hattasan, A. Gassenq, P. De Heyn, Y. De Koninck, P. Mechet, R. Kumar, M. Muneeb, D. Vermeulen, G. Morthier, R. Baets, D. Van Thourhout, *III-V-on-silicon membrane photonics for near-infrared and mid-infrared applications*, 16th European Conference on Integrated Optics (ECIO 2012) (invited), Spain, (2012)

11. N. Hattasan, A. Gassenq, B. Kuyken, L. Cerutti, J.B. Rodriguez, E. Tournié, D. Van Thourhout, G. Roelkens, *Heterogeneously integrated InGaAsSb detectors on SOI waveguide circuits for short-wave infrared applications*,Integrated Photonics Research, Silicon and Nano-Photonics (IPR), Canada, p.IWC5 (2011)

12. B. Kuyken, N. Hattasan, D. Vermeulen, S. Selvaraja, W. Bogaerts, W. M. J. Green, R. Baets, G. Roelkens, *Highly efficient broadband silicon-on-insulator grating couplers for the short wave infrared wavelength range*,Integrated Photonics Research, Silicon and Nano-Photonics (IPR), Canada, p.IMB6 (2011)

13. N. Hattasan, L. Cerutti, J.B. Rodriguez, E. Tournié, D. Van Thourhout, G. Roelkens, *Heterogeneous GaSb/SOI mid-infrared photonic integrated circuit for spectroscopic applications*, 2011 SPIE Photonics West (invited), United states, vol. 7945, p.79451K-6, (2011)

14. E.M.P. Ryckeboer, N. Hattasan, G. Morren, D. Delbeke, W. Bogaerts, R. Baets, *Power budget considerations for in vivo continuous glucose monitoring using absorption spectroscopy*, Proceedings of the 2010 Annual Symposium of the IEEE Photonics Benelux Chapter, Netherlands, p.253-256 (2010)

15. N. Hattasan, L. Cerutti, J.B. Rodriguez, E. Tournié, D. Van Thourhout, G. Roelkens, *Heterogeneous integration of GaSb based photodetector on Silicon-on Insulator waveguide circuits for shortwave-infrared sensing applications*, 15th Annual Symposium of the IEEE Photonics Benelux Chapter, The Netherlands, p.105-108 (2010)

16. G. Roelkens, N. Hattasan, E.M.P. Ryckeboer, D. Delbeke, D. Van Thourhout, R. Baets, *Lab-on-a-chip approach based on heterogeneous III-V/silicon photonic integrated circuits for bio-medical applications*, European Optical Society topical meeting on biophotonics, France, (2010)

17. G. Roelkens, N. Hattasan, E.M.P. Ryckeboer, D. Delbeke, D. Van Thourhout, R. Baets, *Integrated III-V semiconductor/silicon photonic integrated circuits for bio-medical applications*, Optics within Life Sciences, Canada, p.S7-p4 (2010)

18. N. Hattasan, L. Cerutti, J.B. Rodriguez, E. Tournié, D. Van Thourhout, G. Roelkens, *Heterogeneous Integration of GaSb-based epitaxy on silicon-on-insulator: towards mid-infrared photonic integrated circuits for environmental and bio-medical applications*, 10th International Conference on Mid-Infrared Optoelectronics: Materials and Devices, China, p.90-91 (2010)

19. W.A.D. De Cort, N. Hattasan, J. Beeckman, K. Neyts, R. Baets, *Tuning SOI filter structures with liquid crystals*, Proceedings of the 2009 Annual Symposium of the IEEE Photononics Benelux Chapter, Belgium, p.57-60 (2009)

20. N. Hattasan, W.A.D. De Cort, J. Beeckman, K. Neyts, R. Baets, *Tunable Silicon-on-Insulator based integrated optical filters with liquid crystal cladding*, The 22nd Annual Meeting of the IEEE Photonics Society, Turkey, p.189-190 (2009)

1.7.3   Publications in national conferences

1. N. Hattasan, G. Roelkens, *Can we measure gases from our mobile phone? Or knowing our glucose level in our body real time?*, 11th UGent-FirW Phd Symposium, Belgium, (2012)

2. N. Hattasan, G. Roelkens, D. Van Thourhout, *Integration of GaSb photodetectors on SOI: Towards mid-infrared photonic integrated circuits*, 9th UGent-FirW PhD Symposium, Belgium, (2010)

References

[1] Glucosens, *Glucosens*, *http://www.glucosens.be/node/1*.

[2] J. S. Byrnes. *Unexploded Ordnance Detection and Mitigation.* Springer Science+Business Media, 2009.

[3] C. Vrančić, A. Fomichova, N. Gretz, C. Herrmann, S. Neudecker, A. Pucci, and W. Petrich. *Continuous glucose monitoring by means of mid-infrared transmission laser spectroscopy in vitro.* Analyst, 136(6):1192–8, March 2011.

[4] A. Bauer, K. Röß ner, T. Lehnhardt, M. Kamp, S. Höfling, L. Worschech, and a. Forchel. *Mid-infrared semiconductor heterostructure lasers for gas sensing applications.* Semicond. Sci. Technol., 26(1):014032, January 2011.

[5] K. Xu, Q. Qiu, J. Jiang, and X. Yang. *Non-invasive glucose sensing with near-infrared spectroscopy enhanced by optical measurement conditions reproduction technique.* Opt. Lasers Eng., 43(10):1096–1106, October 2005.

[6] W. Volland, *Organic compound Identification using Infrared Spectroscopy*, *www.zenitech.com*.

[7] M. Lackner. *Gas sensing in industry by tunable diode laser spectroscopy (TDLS).* ProcessEng Engineering GmbH, 2008.

[8] N. Ophir, R. K. W. Lau, M. Menard, X. Zhu, K. Padmaraju, Y. Okawachi, R. Salem, M. Lipson, A. L. Gaeta, and K. Bergman. *Wavelength conversion and unicast of 10-Gb/s data spanning up to 700nm using a silicon nanowaveguide.* Opt. Express, 20(6):6488–6495, 2012.

[9] S. Arafin, A. Bachmann, K. Kashani-Shirazi, and M.-C. Amann. *Electrically pumped continuous-wave vertical-cavity surface-emitting lasers at 2.6μm.* Appl. Phys. Lett., 95(13):131120, 2009.

[10] J. P. Prineas, J. Yager, S. Seyedmohamadi, and J. T. Olesberg. *Leakage mechanisms and potential performance of molecular-beam epitaxially grown GaInAsSb 2.4 μm photodiode detectors.* J. Appl. Phys., 103:104511, 2008.

[11] A. Ducanchez, L. Cerutti, A. Gassenq, and P. Grech. *Fabrication and Characterization of GaSb-Based Emitting Around 2.3μm and Including a Tunnel Junction.* IEEE J. Quantum Electron., 14(4):1014–1021, 2008.

[12] W. Bogaerts, P. Dumon, D. V. Thourhout, D. Taillaert, P. Jaenen, J. Wouters, S. Beckx, V. Wiaux, and R. G. Baets. *Compact Wavelength-Selective Functions in Silicon-on-Insulator Photonic Wires*. IEEE J. Sel. Top. Quantum Electron., 12(6):1394–1401, 2006.

[13] N. Hattasan, B. Kuyken, F. Leo, E. M. P. Ryckeboer, D. Vermeulen, and G. Roelkens. *High-Efficiency SOI Fiber-to-Chip Grating for the Short-Wave Infrared*. IEEE Photonics Technol. Lett., 24(17):1536–1538, 2012.

[14] G. Z. Mashanovich, M. M. Milošević, M. Nedeljkovic, N. Owens, B. Xiong, E. J. Teo, and Y. Hu. *Low loss silicon waveguides for the mid-infrared.* Opt. Express, 19(8):7112–9, April 2011.

[15] A. W. Fang, E. Lively, Y.-H. Kuo, D. Liang, and J. E. Bowers. *A distributed feedback silicon evanescent laser.* Opt. Express, 16(7):4413–9, March 2008.

[16] S. Stankovic, R. Jones, M. N. Sysak, J. M. Heck, G. Roelkens, and D. V. Thourhout. *Hybrid III-V/Si Distributed-Feedback Laser*. IEEE Photonics Technol. Lett., 24(23):2155–2158, 2012.

[17] J. B. Rodriguez, L. Cerutti, P. Grech, and E. Tournie. *Room-temperature operation of a 2.25μm electrically pumped laser fabricated on a silicon substrate*. Appl. Phys. Lett., 94(6):061124, 2009.

[18] F. Trager. *Handbook of lasers and optics.* Springer Science+Business Media, 1 edition, 2007.

[19] *Uncooled Shortwave Infrared (SWIR) Cameras, Sensors Unlimited Inc., http://utcaerospacesystems.com/.*

[20] *Thermal Imaging for Process Control Applications, Infrared Cameras Inc., http://www.infraredcamerasinc.com/index.html.*

[21] M. Peach, *Gas sensor based on mid-infrared MEMS design, http://optics.org/news/4/2/37.*

[22] O. S. Khalil. *Spectroscopic and clinical aspects of noninvasive glucose measurements.* Clin. Chem., 45(2):165–77, February 1999.

[23] Q. Ren, V. Venugopalan, K. Schomacker, T. F. Deutsch, T. J. Flotte, C. A. Puliafito, and R. Birngruber. *Mid-Infrared laser ablation of the cornea: A comparative study.* Lasers Surg. Med., 12(3):274–281, 1992.

[24] N. Ophir, R. K. W. , Lau, M. Ménard, R. Salem, K. Padmaraju, Y. Okawachi, S. Member, M. Lipson, and A. L. Gaeta. *First Demonstration of a 10-Gb/s RZ End-to-End Four-Wave-Mixing Based Link at 1884nm*

Using Silicon Nanowaveguides. Photonics Technol. Lett., 24(4):276–278, 2012.

[25] *DigiTect detectors for Bruker Optics*, *http://www.bruker.com/*.

[26] P. B. Frish, Mickey, D. Wehnert and P. D. Wehnert. *Tunable Diode Laser Absorption Spectroscopy (TLDAS) Technology For Leak Detection in the Natural gas Industry, Portable, Mobile and Aerial Application*. In Int. Gas Union Res. Conf., 2008.

[27] R. O. Esenaliev, K. V. Larin, I. V. Larina, and M. Motamedi. *Noninvasive monitoring of glucose concentration with optical coherence tomography*. Opt. Lett., 26(13):992–4, July 2001.

[28] Y.-J. Kim, S. Hahn, and G. Yoon. *Determination of glucose in whole blood samples by mid-infrared spectroscopy*. Appl. Opt., 42(4):745–9, February 2003.

[29] M. Mueller, M. Grunze, E. H. Leiter, P. C. Reifsnyder, U. Klueh, and D. Kreutzer. *Non-invasive glucose measurements in mice using mid-infrared emission spectroscopy*. Sensors Actuators B Chem., 142(2):502–508, November 2009.

[30] H. Q. Woodard and D. R. White. *The composition of body tissues*. Br. J. Radiol., 56(December):1209–1218, 1986.

[31] T. H. Risby and S. F. Solga. *Current status of clinical breath analysis*. Appl. Phys. B, 85(2-3):421–426, May 2006.

[32] K. M. Dubowski. *Breath analysis as a technique in clinical chemistry*. Clin. Chem., 20(8):966–72, August 1974.

[33] A. Krier. *Mid-Infrared Semiconductor Optoelectronics*. Springer, 2006.

[34] R. A. Soref, S. J. Emelett, and W. R. Buchwald. *Silicon waveguided components for the long-wave infrared region*. J. Opt. A Pure Appl. Opt., 8(10):840–848, October 2006.

[35] *Mode-Gap project*, *http://modegap.eu/*.

[36] W. Bogaerts, P. Dumon, D. V. Thourhout, D. Taillaert, P. Jaenen, J. Wouters, S. Beckx, V. Wiaux, R. G. Baets, and S. Member. *Compact Wavelength-Selective Functions in Silicon-On-Insulator Photonics wires*. IEEE J. Sel. Top. Quantum Electron., 12(6):1394–1401, 2006.

[37] G. T. Reed and A. P. Knights. *Silicon Photonics: An Introduction*. John wiley & Sons Ltd., 2004.

[38] J. H. Schmid, P. Cheben, S. Janz, J. Lapointe, E. Post, a. Delâge, a. Densmore, B. Lamontagne, P. Waldron, and D.-X. Xu. *Subwavelength Grating Structures in Silicon-on-Insulator Waveguides*. Adv. Opt. Technol., 2008(October):1–8, 2008.

[39] A. Mekis, S. Gloeckner, G. Masini, A. Narasimha, T. Pinguet, S. Sahni, and P. D. Dobbelaere. *A Grating-Coupler-Enabled CMOS Photonics Platform*. J. Sel. Top. Quantum Electron., 17(3):1–12, 2010.

[40] Y. Zhou, M. C. Y. Huang, C. Chase, V. Karagodsky, M. Moewe, B. Pesala, F. G. Sedgwick, and C. J. Chang-hasnain. *High-Index-Contrast Grating (HCG) and Its Applications in Optoelectronic Devices*. IEEE J. Sel. Top. Quantum Electron., 15(5):1–15, 2009.

[41] E. D. Palik. *Handbook of Optical Constants*. Academic press, 1 edition, 1985.

[42] T. Baehr-Jones, A. A. Spott, R. Ilic, B. Penkov, W. W. Asher, and M. Hochberg. *Silicon-on-sapphire integrated waveguides for the mid-infrared*. Opt. Express, 18(12):12127–35, June 2010.

[43] R. Soref. *Mid-infrared photonics in silicon and germanium*. Nat. Photonics, 4(8):495–497, August 2010.

[44] A. Malik, M. Muneeb, Y. Shimura, J. Van Campenhout, R. Loo, and G. Roelkens. *Germanium-on-silicon planar concave grating wavelength (de)multiplexers in the mid-infrared*. Appl. Phys. Lett., 103(16):161119, 2013.

[45] A. Malik, M. Muneeb, S. Pathak, S. Member, Y. Shimura, J. V. Campenhout, R. Loo, and G. Roelkens. *Germanium-on-Silicon Mid-Infrared Arrayed Waveguide Grating Multiplexers*. Photonics Technol. Lett., 25(18):1805–1808, 2013.

[46] Z. Cheng, X. Chen, C. Y. Wong, K. Xu, and H. K. Tsang. *Broadband focusing grating couplers for suspended-membrane waveguides*. Opt. Lett., 37(24):5181–3, December 2012.

[47] Y.-C. Chang. *Design, Fabrication and Characterization of Mid-Infrared Strip Waveguide for Laser Spectroscopy in Liquid Environments*. PhD thesis, 2012.

[48] P. Cheben, A. Delâge, A. Densmore, S. Janz, B. Lamontagne, J. Lapointe, E. Post, J. Schmid, P. Waldron, and D. Xu. *Recent advances in silicon microphotonic devices*. Rev. Cuba. Fis., 25(2):75–80, 2008.

[49] H. K. Choi and S. J. Eglash. *High-power multiple-quantum-well GaInAsS-b/AIGaAsSb emitting at 2.1μm with low threshold current density diode lasers.* Appl. Phys. Lett., pages 1154–1156, 1992.

[50] D. Donetsky, J. Chen, L. Shterengas, G. Kipshidze, and D. Westerfeld. *2.3μm High-Power Type I Quantum-Well GaInAsSb/AlGaAsSb/GaSb Laser Diode Arrays with Increased Fill Factor.* J. Electron. Mater., 37(12):1770–1773, June 2008.

[51] D. Z. Garbuzov, H. Lee, V. Khalfin, R. Martinelli, J. C. Connolly, and G. L. Belenky. *2.3-2.7μm Room Temperature CW Operation of InGaAsSbAl-GaAsSb Broad Waveguide SCH-QW Diode Lasers.* IEEE Photonics Technol. Lett., 11(7):794–796, 1999.

[52] A. Sennaroglu, A. O. Konca, and C. R. Pollock. *Continuous-Wave Power Performance of a 2.47μm Cr^{2+} : ZnSe Laser : Experiment and Modeling.* IEEE J. Quantum Electron., 36(10):1199–1205, 2000.

[53] I. T. Sorokina, E. Sorokin, S. Mirov, V. Fedorov, V. Badikov, V. Panyutin, and K. I. Schaffers. *Broadly tunable compact continuous-wave Cr^{2+}:ZnS laser.* Opt. Lett., 27(12):1040–2, June 2002.

[54] L. Goldberg, J. Koplow, D. G. Lancaster, R. F. Curl, and F. K. Tittel. *Mid-infrared difference-frequency generation source pumped by a 1.1-1.5μm dual-wavelength fiber amplifier for trace-gas detection.* Opt. Lett., 23(19):1517–1519, 1998.

[55] D. G. Lancaster, D. Richter, and F. K. Tittel. *Portable fiber-coupled diode-laser-based sensor for multiple trace gas detection.* Appl. Phys. B., 69:459–65, 1999.

[56] A. Godard. *Infrared (2-12μm) solid-state laser sources: a review.* Comptes Rendus Phys., 8(10):1100–1128, December 2007.

[57] I. T. Sorokina and K. L. Vodopyanov. *Solid-State Mid-Infrared Laser Sources.* SPRINGER, 2003.

[58] S. Sprengel, A. Andrejew, K. Vizbaras, T. Gruendl, K. Geiger, G. Boehm, C. Grasse, and M.-C. Amann. *Type-II InP-based lasers emitting at 2.55μm.* Appl. Phys. Lett., 100(4):041109, 2012.

[59] R. Sidhu, S. Member, N. Duan, J. C. Campbell, and A. L. Holmes. *A Long-Wavelength Photodiode on InP Using Type-II Quantum Wells.* IEEE Photonics Technol. Lett., 17(12):2715–2717, 2005.

[60] G. W. Turner, H. K. Choi, and M. J. Manfra. *AlGaAsSb lasers emitting at 2.05μm*. Appl. Phys. Lett., 72(8):876–878, 1998.

[61] M. Grau, C. Lin, O. Dier, C. Lauer, and M.-C. Amann. *Room-temperature operation of 3.26μm GaSb-based type-I lasers with quinternary AlGaInAsSb barriers*. Appl. Phys. Lett., 87(24):241104, 2005.

[62] H. Lee, P. K. York, R. J. Menna, R. U. Martinelli, D. Z. Garbuzov, S. Y. Narayan, and J. C. Connolly. *Room-temperature 2.78μm AlGaAsSb/In-GaAsSb quantum-well lasers*. Appl. Phys. Lett., 66(15):1942–1944, 1995.

[63] J. Choi, H. K., Turner, G. W., Eglash. *High-Power GaInAsSb-AlGaAsSb Multiple- Quantum-Well Diode Lasers Emitting at 1.9μm*. IEEE Photonics Technol. Lett., 6(1):7–9, 1994.

[64] H. K. Choi. *Long-Wavelength Infrared Semiconductor Lasers*. Jonhn Wiley& Sons, 2004.

[65] J. Piprek. *Semiconductor Optoelectronic Devices*. Elsevier Science B. V., 2003.

[66] D. Z. Garbuzov, R. U. Martinelli, H. Lee, P. K. York, R. J. Menna, J. C. Connolly, and S. Y. Narayan. *Ultralow-loss broadened-waveguide high-power 2μm AlGaAsSb/InGaAsSb/GaSb separate-confinement quantum-well lasers*. Appl. Phys. Lett., 69(14), 1996.

[67] D. Z. Garbuzov, R. U. Martinelli, H. Lee, R. J. Menna, P. K. York, L. A. Dimarco, M. G. Harvey, R. J. Matarese, S. Y. Narayan, and J. C. Connolly. *4W quasi-continuous-wave output power from 2μm AlGaAsSb/InGaAsSb single-quantum-well broadened waveguide laser diodes*. Appl. Phys. Lett., 70(22):2931–2933, 1997.

[68] T. Hosoda, G. Kipshidze, L. Shterengas, S. Suchalkin, and G. Belenky. *200 mW type I GaSb-based laser diodes operating at 3μm: Role of waveguide width*. Appl. Phys. Lett., 94(26):261104, 2009.

[69] K. Vizbaras, A. Vizbaras, A. Andrejew, C. Grasse, and M.-C. Amann. *Room-temperature type-I GaSb based lasers in the 3-3.7μm wavelength range*. Proc. SPIE, 8277(June):82771B–7, 2012.

[70] K. Vizbaras and M.-C. Amann. *Room-temperature 3.73μm GaSb-based type-I quantum-well lasers with quinternary barriers*. Semicond. Sci. Technol., 27(3):032001, March 2012.

[71] *Welcome to Nanoplus, http://www.nanoplus.com/*.

[72] VERTILAS, *VERTILAS*, *http://www.vertilas.com/*.

[73] M. Rattunde, J. Schmitz, G. Kaufel, M. Kelemen, J. Weber, and J. Wagner. *GaSb-based 2.X μm quantum-well diode lasers with low beam divergence and high output power*. Appl. Phys. Lett., 88(8):081115, 2006.

[74] T. Newell, X. Wu, A. Gray, S. Dorato, H. Lee, and L. Lester. *The effect of increased valence band offset on the operation of 2μm GaInAsSb-AlGaAsSb lasers*. IEEE Photonics Technol. Lett., 11(1):30–32, January 1999.

[75] J. G. Kim, L. Shterengas, R. U. Martinelli, and G. L. Belenky. *High-power room-temperature continuous wave operation of 2.7 and 2.8μm In(Al)GaAsSb/GaSb diode lasers*. Appl. Phys. Lett., 83(10):1926, 2003.

[76] M. Garcia, A. Salhi, P. A., Y. Rouillard, C. Sirtori, X. Marcadet, and C. Alibert. *Low Threshold High-Power Room-Temperature Emitting at 2.264μm*. IEEE Photonics Technol. Lett., 16(5):1253–1255, 2004.

[77] A. Salhi, Y. Rouillard, J. Angellier, and M. Garcia. *Very Low Threshold 2.4μm GaInAsSb-AlGaAsSbLaser Diodes Operating at Room Temperature in the Continuous-Wave Regime*. IEEE Photonics Technol. Lett., 16(11):2424–2426, 2004.

[78] L. Shterengas, G. Belenky, T. Hosoda, G. Kipshidze, and S. Suchalkin. *Continuous wave operation of diode lasers at 3.36μm at 12°C*. Appl. Phys. Lett., 93(1):011103, 2008.

[79] T. Hosoda, G. Belenky, L. Shterengas, G. Kipshidze, and M. V. Kisin. *Continuous-wave room temperature operated 3.0μm type I GaSb-based lasers with quinternary AlInGaAsSb barriers*. Appl. Phys. Lett., 92:091106, 2008.

[80] K. Vizbaras, M. Törpe, S. Arafin, and M.-C. Amann. *Ultra-low resistive GaSb/InAs tunnel junctions*. Semicond. Sci. Technol., 26(7):075021, July 2011.

[81] P. Norton. *HgCdTe infrared detectors*. Opto-Electronics Rev., 10(3):159–174, 2002.

[82] A. Rogalski. *HgCdTe infrared detector material: history, status and outlook*. Reports Prog. Phys., 68(10):2267–2336, October 2005.

[83] A. Rogalski. *Infrared detectors : an overview*. Infrared Phys. Technol., 43:187–210, 2002.

[84] A. Rogalski and P. Martyniuk. *InAs/GaInSb superlattices as a promising material system for third generation infrared detectors*. Infrared Phys. Technol., 48(1):39–52, April 2006.

[85] Y. Wei, a. Hood, H. Yau, V. Yazdanpanah, M. Razeghi, M. Z. Tidrow, and V. Nathan. *High-performance type-II InAs/GaSb superlattice photodiodes with cutoff wavelength around 7 μm*. Appl. Phys. Lett., 86(9):091109, 2005.

[86] Thorlab, *Thorlabs*, *http://www.thorlabs.de/index.cfm?*

[87] *Infrared   detectors,   Hamamatsu   Photonics*, *http://www.hamamatsu.com/jp/en/product/alpha/I/4007/index.html*.

[88] G. H. Olsen, M. J. Lange, M. J. Cohen, D.-S. Kim, and S. R. Forrest. *Three-Band 1-2.5μm Near-Infrared InGaAs Detector Array*. Proc. SPIE, 2225:151–159, 1994.

[89] M. H. M. Reddy, J. T. Olesberg, C. Cao, and J. P. Prineas. *MBE-grown high-efficiency GaInAsSb mid-infrared detectors operating under back illumination*. Semicond. Sci. Technol., 21(3):267–272, March 2006.

[90] J. P. Prineas, J. T. Olesberg, J. R. Yager, C. Cao, C. Coretsopoulos, and M. H. M. Reddy. *Cascaded active regions in 2.4μm GaInAsSb light-emitting diodes for improved current efficiency*. Appl. Phys. Lett., 89(21):211108, 2006.

[91] A. Yildirim and J. P. Prineas. *Suppressed phase separation in thick GaInAsSb layers across the compositional range grown by molecular beam epitaxy for 1.7-4.9μm infrared materials*. J. Vac. Sci. Technol. B, 30(2):02B104, 2012.

[92] H. Shao, a. Torfi, W. Li, D. Moscicka, and W. Wang. *High detectivity AlGaAsSb/InGaAsSb photodetectors grown by molecular beam epitaxy with cutoff wavelength up to 2.6μm*. J. Cryst. Growth, 311(7):1893–1896, March 2009.

[93] C. Lin, Y. L. Zheng, and A. Z. Li. *Mid-infrared GaInAsSb photodetector grown by solid source molecular beam epitaxy*. J. Cryst. Growth, 228:605–608, 2001.

[94] A. P. Astakhova, B. E. Zhurtanov, A. N. Imenkov, M. P. Mikhailova, M. a. Sipovskaya, N. D. Stoyanov, and Y. P. Yakovlev. *Improving parameters of GaSb/GaInAsSb/AlGaAsSb photodiode structures with thin active regions for the 1.0-2.5μm wavelength range*. Tech. Phys. Lett., 33(10):809–812, October 2007.

[95] *Roithner Lasertechnik, http://www.roithner-laser.com/*.

[96] T. E. Crumbaker, H. Y. Lee, M. J. Hafich, and G. Y. Robinson. *Growth of InP on Si substrates by molecular beam epitaxy*. Appl. Phys. Lett., 54(2), 1989.

[97] S. Hasegawa, T. Shimoi, and H. Asahi. *Mechanism of selective area growth of InP on Si(001) substrates using SiO$_2$ mask by gas-source molecular beam epitaxy*. J. Cryst. Growth, 378:47–49, September 2013.

[98] G. Balakrishnan, S. Huang, L. R. Dawson, Y.-C. Xin, P. Conlin, and D. L. Huffaker. *Growth mechanisms of highly mismatched AlSb on a Si substrate*. Appl. Phys. Lett., 86(3):034105, 2005.

[99] L. Cerutti, J. B. Rodriguez, and E. Tournie. *GaSb-Based Laser, Monolithically Grown on Silicon Substrate, Emitting at 1.55μm at Room Temperature*. IEEE Photonics Technol. Lett., 22(8):553–555, 2010.

[100] S. Lourdudoss. *Heteroepitaxy and selective area heteroepitaxy for silicon photonics*. Curr. Opin. Solid State Mater. Sci., 16(2):91–99, April 2012.

[101] G. Balakrishnan, A. Jallipalli, P. Rotella, S. Huang, A. Khoshakhlagh, A. Amtout, S. Krishna, L. R. Dawson, and D. L. Huffaker. *Room-Temperature Optically Pumped (Al) GaSb Vertical-Cavity Surface-Emitting Laser Monolithically Grown on an Si(1 0 0) Substrate*. IEEE J. Sel. Top. Quantum Electron., 12(6):1636–1641, 2006.

[102] J. R. Reboul, L. Cerutti, J. B. Rodriguez, P. Grech, and E. Tournie. *Continuous-wave operation above room temperature of GaSb-based laser diodes grown on Si*. Appl. Phys. Lett., 99(12):121113, 2011.

[103] A. A. Tonkikh, C. Eisenschmidt, V. G. Talalaev, N. D. Zakharov, J. Schilling, G. Schmidt, and P. Werner. *Pseudomorphic GeSn/Ge(001) quantum wells: Examining indirect band gap bowing*. Appl. Phys. Lett., 103(3):032106, 2013.

[104] J. Liu, X. Sun, D. Pan, X. Wang, L. C. Kimerling, T. L. Koch, and J. Michel. *Tensile-strained, n-type Ge as a gain medium for monolithic laser integration on Si*. Opt. Express, 15(18):11272–7, September 2007.

[105] A. R. Soref, J. Kouvetakis, J. Tolle, J. Menendez, and V. D. Costa. *Advances in SiGeSn Technology*. J. Mater. Res., 22:3281–3291, 2007.

[106] R. E. Camacho-aguilera, Y. Cai, N. Patel, J. T. Bessette, M. Romagnoli, L. C. Kimerling, and J. Michel. *An electrically pumped germanium laser*. Opt. Express, 20(10):11316, 2012.

[107] K. Tanabe, K. Watanabe, and Y. Arakawa. *III-V/Si hybrid photonic devices by direct fusion bonding.* Sci. Rep., 2:349, January 2012.

[108] D. Liang, A. W. Fang, H. Park, T. E. Reynolds, K. Warner, D. C. Oakley, and J. E. Bowers. *Low-Temperature, Strong SiO_2-SiO_2 Covalent Wafer Bonding for III-V Compound Semiconductors-to-Silicon Photonic Integrated Circuits.* J. Electron. Mater., 37(10):1552–1559, June 2008.

[109] F. Niklaus. *Adhesive Wafer Bonding for Microelectronic and Microelectromechanical Systems.* PhD thesis, Royal Institute of Technology, 2002.

[110] P. Ramm, J. Jian-Qiang, and M. M. V. Taklo. *Handbook of Wafer Bonding.* Jonhn Wiley& Sons, 1 edition, 2012.

[111] G. Roelkens. *Heterogeneous III/V Silicon Photonics: Bonding Technology and Integrated Devices.* PhD thesis, Ghent University, 2006.

[112] S. Stankovic. *Hybrid III-V/Si DFB lasers based on Polymer Bonding Technology.* PhD thesis, Ghent University, 2013.

[113] R. H. Esser, K. D. Hobart, and F. J. Kub. *Improved Low-Temperature Si-Si Hydrophilic Wafer Bonding.* J. Electrochem. Soc., 150(3):G228, 2003.

[114] Q.-Y. Tong, Q. Gan, G. Hudson, G. Fountain, P. Enquist, R. Scholz, and U. Gosele. *Low-temperature hydrophobic silicon wafer bonding.* Appl. Phys. Lett., 83(23):4767, 2003.

[115] R. J. Hohlfelder, D. A. Maidenberg, and R. H. Dauskardt. *Adhesion of benzocyclobutene-passivated silicon in epoxy layered structures.* J. Mater. Res., 16(1):243–255, 2001.

[116] M. Grzesik, S. R. Vangala, and W. D. Goodhue. *Indirect Wafer Bonding and Epitaxial Transfer of GaSb-Based Materials.* J. Electron. Mater., 42(4):679–683, January 2013.

[117] A. S. Ylva Backlund, Karin Ljunberg. *A suggested mechanism for silicon direct bonding from studying hydrophilic and hydrophobic surfaces.* J. microelectromechanics Microengineering, 2:157–160, 1992.

[118] G. Roelkens, L. Liu, D. Liang, R. Jones, A. Fang, B. Koch, and J. Bowers. *III-V/silicon photonics for on-chip and intra-chip optical interconnects.* Laser Photon. Rev., 4(6):751–779, November 2010.

[119] H. Park, A. W. Fang, D. Liang, Y.-H. Kuo, H.-H. Chang, B. R. Koch, H.-W. Chen, M. N. Sysak, R. Jones, and J. E. Bowers. *Photonic Integration on the Hybrid Silicon Evanescent Device Platform.* Adv. Opt. Technol., 2008:1–17, 2008.

[120] A. W. Fang, H. Park, O. Cohen, R. Jones, M. J. Paniccia, and J. E. Bowers. *Electrically pumped hybrid AlGaInAs-silicon evanescent laser.* Opt. Express, 14(20):9203–10, October 2006.

[121] H. Park. *Silicon Evanescent Devices for Optical Networks and Buffers.* PhD thesis, University of California, Santa Barbara, 2008.

[122] Z. Sheng, L. Liu, J. Brouckaert, S. He, and D. Van Thourhout. *InGaAs PIN photodetectors integrated on silicon-on-insulator waveguides.* Opt. Express, 18(2):1756–61, January 2010.

[123] J. Brouckaert. *Heterogeneous integration of photodetectors on silicon photonic ICs.* PhD thesis, Ghent University, 2010.

[124] F. Niklaus, G. Stemme, J. Q. Lu, and R. J. Gutmann. *Adhesive wafer bonding.* J. Appl. Phys., 99(3):031101, 2006.

[125] G. Roelkens, D. Van Thourhout, and R. Baets. *High efficiency Silicon-on-Insulator grating coupler based on a poly-Silicon overlay.* Opt. Express, 14(24):11622–30, November 2006.

[126] N. Hattasan, A. Gassenq, L. Cerutti, J.-b. Rodriguez, E. Tournié, and G. Roelkens. *Heterogeneous Integration of GaInAsSb p-i-n Photodiodes on a Silicon-on-Insulator Waveguide Circuit.* Photonics Technol. Lett. IEEE, 23(23):1760–1762, 2011.

[127] S. Ghosh, S. Keyvaninia, Y. Shirato, T. Mizumoto, G. Roelkens, and R. Baets. *Optical Isolator for TE Polarized Light Realized by Adhesive Bonding of Ce : YIG on Silicon-on-Insulator Waveguide Circuits.* IEEE Photonics J., 5(3), 2013.

[128] G. Roelkens, J. Brouckaert, D. Taillaert, P. Dumon, W. Bogaerts, D. Van Thourhout, R. Baets, R. Nötzel, and M. Smit. *Integration of InP/InGaAsP photodetectors onto silicon-on-insulator waveguide circuits.* Opt. Express, 13(25):10102–8, December 2005.

[129] S. Keyvaninia, M. Muneeb, S. Stanković, P. J. V. Veldhoven, D. V. Thourhout, and G. Roelkens. *Ultra-thin DVS-BCB adhesive bonding of III-V wafers , dies and multiple dies to a patterned silicon-on-insulator substrate.* Opt. Mater. Express, 3(1):1047–1056, 2013.

2

Silicon-on-Insulator platform for the short-wave infrared

In this chapter, I discuss the possibility of using SOI waveguides in the short-wave infrared (SWIR). This includes the design of a Bragg grating to couple light between an integrated photonics circuit and an optical fiber. Waveguide loss measurements in the SWIR are presented. The results form the basis for the design of a high efficiency grating coupler for the integrated photodiode in Chapter 4 and the distributed Bragg reflector used in the laser diode described in Chapter 6. The work presented in this chapter was carried out in collaboration with dr. Bart Kuyken (loss measurement in Si waveguides) and dr. Diedrik Vermeulen (help in the design of the grating coupler).

2.1 Introduction

As discussed in Chapter 1, Si photonics is rapidly emerging as a potential integration platform for applications covering a wide wavelength range. This is particularly true for spectroscopic sensing applications as well as nonlinear optics on the Si platform, moving towards the SWIR ($>2\mu$m) [1–4]. For spectroscopic sensing systems, this is driven by the fact that the characteristic absorption lines of molecules of interest become much stronger at longer wavelengths, increasing the sensitivity of the sensing system while lowering the device footprint [3]. For nonlinear optical applications on the Si platform, moving towards longer wavelengths
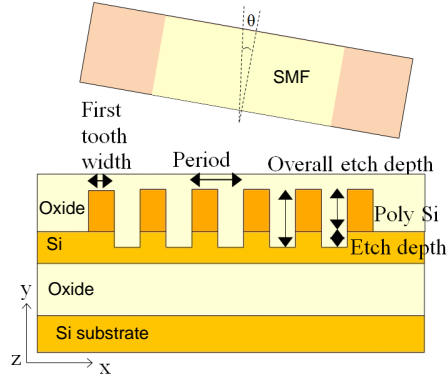
Figure 2.1: Schematic of the SWIR fiber-to-chip grating coupler structure

is driven by the absence of parasitic two-photon absorption in Si for wavelengths >2.2μm, given its 1.12eV band gap [2]. For both applications there is a need to develop photonic integrated components for the SWIR range. While several state-of-the-art Si-based passive components at telecommunication wavelengths have been reported in the past few years [5, 6], only very few have been studied in the SWIR and MWIR wavelength range [7–9]. In this chapter, I discuss the design, fabrication and a comprehensive study of grating coupler characteristics over a broad parameter range, leading to a state-of-the-art fiber-to-chip coupling efficiency of -3.8dB at 2.1μm. I also demonstrate single mode waveguides for the SWIR range with losses <0.6dB/cm at 2.2μm which is very low compared to the 2.4dB/cm of a standard Si waveguide at 1.55μm [10].

2.2 High efficiency grating coupler

2.2.1 Design and simulation

The grating coupler structure consists of a 220nm thick crystalline Si layer as the waveguide layer with a 160nm poly-Si overlay on top of the waveguide. A 2μm buried oxide layer is used. A SiO$_2$ top-cladding (1.0μm thick) is deposited and polished. The total etch depth of the Si waveguide is fixed to 240nm in order to be compatible with the CMOS fabrication process used to fabricate these devices. Fig. 2.1 shows the schematic of the grating coupler structure.

The period of the grating coupler for a given wavelength (λ) is calculated using Bragg condition. It describes the relation of the incident and diffracted waves as:

$$k_z = \beta - mK \ with \ m = \cdots, -2, -1, 0, 1, 2, \cdots \qquad (2.1)$$
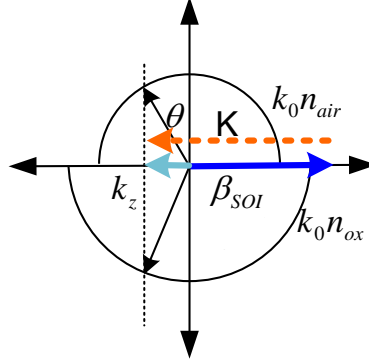
Figure 2.2: A wavevector diagram representing the Bragg condition for a grating coupler formed on SOI

where $\beta = \frac{2\pi}{\lambda} n_{eff}$ is the propagation constant of the guided mode and $K = \frac{2\pi}{\Lambda}$ with Λ the period of the grating. $k_z = \frac{2n_{air}\pi}{\lambda} sin\theta$ is the projected diffracted wave vector. θ is the angle of the phase fronts of the diffracted field with respect to the Si surface (and hence the angle of the optical fiber with respect to the surface normal for optimal fiber coupling). n_{eff} is the average effective index of the grating structure. A wavevector diagram representing the Bragg condition in Equation 2.1 is depicted in Fig. 2.2

The coupling efficiency to single mode fiber is assessed by evaluating the overlap integral as follows:

$$\eta = \left| \int E_z H_{fib,x} dx \right|^2 \qquad (2.2)$$

where E_z is the diffracted electrical field from the grating towards the superstrate, when the TE waveguide mode is launched, and $H_{fib,x}$ is the fiber mode magnetic field distribution, which is assumed to be Gaussian. The integration is carried out along a horizontal line in the superstrate.

Simulations are carried out using 2D Finite-Difference-Time-Domain (FDTD) software. The 3D nature of the problem is taken into account by analytically calculating the lateral overlap integral between the Gaussian fiber mode and the cosine-shaped Si waveguide mode. The fiber is positioned at the optimum position along the x-direction. A $10°$ tilt from the vertical direction is used to avoid substantial second order Bragg reflection back into the waveguide when coupling to the optical fiber. 20 grating periods are used for the simulation. Note that the 20-period of grating is chosen initially to ensure that the light is completely diffracted from the waveguide. The simulation in Fig. 2.3 shows that light is completely diffracted above 10 grating periods at 2.1μm wavelength.
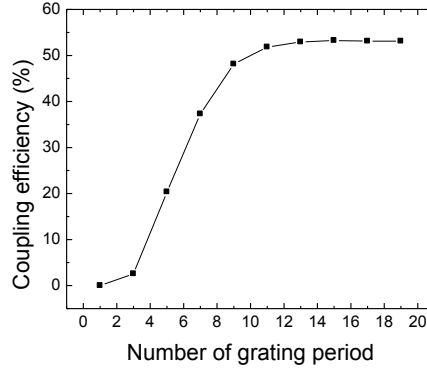
Figure 2.3: Simulation of coupling efficiency as a function of number of grating period at 2.1μm

The optical mode in the standard single mode fiber (SMF-28) with a core of 9μm diameter is approximated by a Gaussian beam with a mode field diameter (MFD) of 13.3, 13.9 and 14.5μm at 2.1, 2.2, and 2.3μm respectively as calculated by a fully-vectorial finite element method. Fig. 2.4a illustrates the simulated fiber-to-chip coupling efficiency as a function of wavelength for 4 different grating periods (0.98μm, 1μm, 1.02μm, and 1.04μm, respectively) with a 0.25 fill factor, defined as the Si tooth width to the period ratio. The gratings are etched 80nm into the crystalline Si waveguide layer (240nm overall etch depth). The center of the coupling spectrum shifts to longer wavelengths with increased period, in accordance to the Bragg condition. However, the coupling efficiency decreases due to the increased mode mismatch between the diffracted field profile and the fiber mode. Fig. 2.4b shows a grating coupler spectrum with a period of 0.98μm and 80nm etch depth into the crystalline Si layer and varying grating fill factor. The optimum fill factor is ∼0.3. The efficiency decreases substantially for fill factors > 0.4. Another parameter that affects grating coupler performance is the grating-etch depth. In Fig. 2.5a, a peak wavelength shift with varying etching depth in the crystalline Si layer is shown. The coupling efficiency decreases slowly when the etch depth is less than 80nm. In practice, due to the fabrication process, the etch depth in the crystalline waveguide layer was fixed to 80nm.

As mentioned earlier, the MFD of a standard single mode fiber increases significantly with an increasing operation wavelength. Therefore, broader waveguides are required when operating further into the SWIR range. This is illustrated in Fig. 2.5b, where the overlap integral of the transversal mode profile in the Si waveguide (cosine-shaped) and the Gaussian profile of the fiber mode is plotted.

According to [11], for 1.55μm wavelength, the width of the first tooth of the grating plays an important role in the attainable coupling efficiency. This is due to
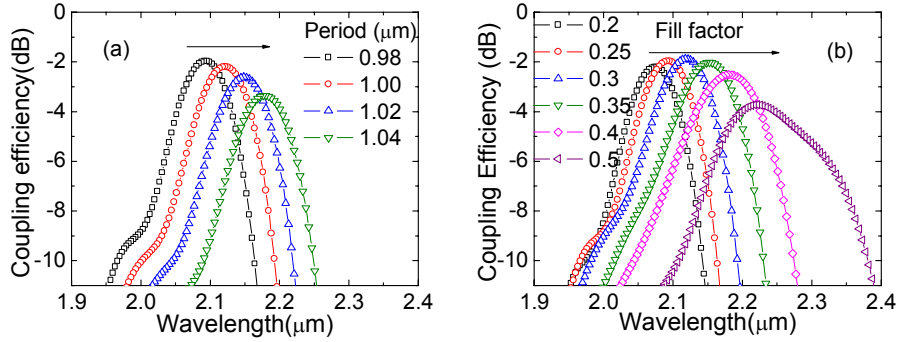
Figure 2.4: Simulated coupling efficiency for different grating parameters: a) coupling efficiency as a function of the grating period with fill factor 0.25; b) simulated coupling efficiency as a function of the fill factor (0.98μm period, 80nm etch depth)
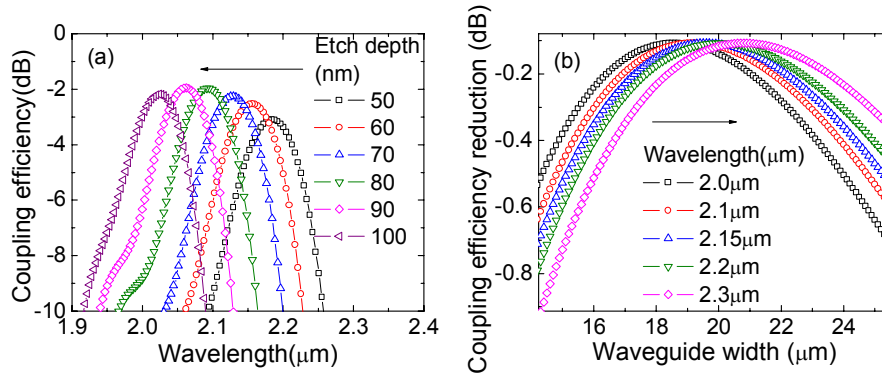
Figure 2.5: a) Simulated coupling efficiency with different grating etch depths into the crystalline Si layer (period=0.98μm; fill factor=0.25) b) coupling efficiency reduction due to the lateral mode mismatch between the Si waveguide mode and the fiber mode for various wavelengths as a function of Si waveguide width (period=0.98μm; fill factor=0.25; etch depth 240nm)
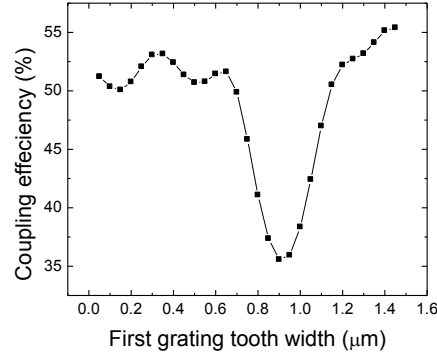
Figure 2.6: Simulation of the impact of first grating tooth width on coupling efficiency

the interference of the waveguide modes, which results in a constructive interference at only certain length or width of the grating tooth. Therefore, it is necessary to keep its size smaller than the subsequent teeth (in our case, it is 300nm) to achieve high coupling efficiency. For 2.1μm wavelength, the width of the first grating tooth shows similar impact on the coupling efficiency as seen at 1.55μm. The simulated coupling efficiency at 2.1μm wavelength as a function of the first grating tooth width is shown in Fig. 2.6. The result presents a significant decrease in the coupling efficiency when the first grating tooth width is wider than 600nm.

2.2.2   Fabrication

The fabrication of these grating couplers is carried out in imec with 193nm deep UV lithography and dry etching in a 200mm pilot line, through the multi-project wafer service ePIXfab [12]. The fabrication process is illustrated in Fig. 2.7. The base wafer consists of a 220nm crystalline Si layer on top of 2μm buried oxide on a Si substrate. A 10nm thick oxide layer is deposited, after which 160nm poly-Si is deposited on top of the crystalline Si shown in Fig. 2.7a. The oxide layer is used as an etch stop layer to accurately define the 220nm thick crystalline Si waveguides. The thin oxide layer does not influence the performance of the grating coupler when the TE optical mode is launched in the Si waveguide. The grating 240nm deep slits are formed by an Inductively Coupled Plasma (ICP) etching process (chlorine/fluorine-based and bromine-based chemistry) (Fig. 2.7b). After etching the grating slits, the poly-Si is removed, except in the grating area, by ICP etching, using the oxide layer as an etch stop (Fig. 2.7c). After the grating structure is formed, oxide is deposited as a top cladding (Fig. 2.7d). A photoresist mask was used for all processing steps.

The reproducibility of Si etching is controlled by using a thin SiO_2 as an etch
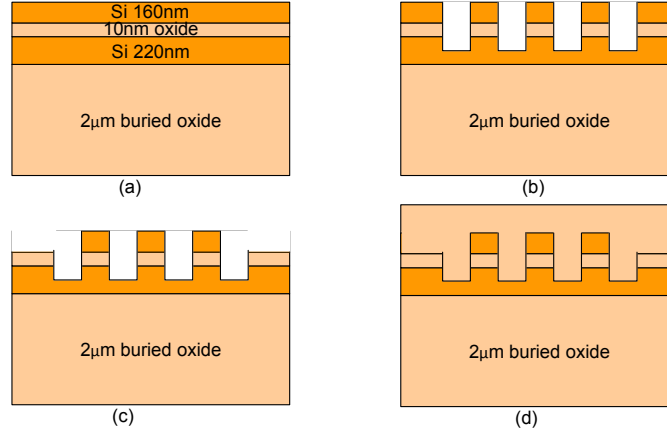
Figure 2.7: Schematic of the grating fabrication process; a) the SOI stack after deposition of 10nm oxide and 160nm of poly-Si; b) after etching 240nm c) after etching the poly- Si layer d) and after deposition and polishing of a 1μm-thick top oxide

stop layer for the first 160nm; see Fig. 2.7. A more precise control of the etching is required for the last 70nm. This is possible with the 5-10nm tolerance with slow etching rate recipe. The intensive study on this process control is well described in [13]. In this thesis, uniformity of the process has not been performed extensively. However, corresponding to [13], the Si process from imec yields a relatively good uniformity with a 5nm tolerance.

A scanning-electron-microscope (SEM) image of such a grating coupler after removing the top oxide cladding is shown in Fig. 2.8. Fig. 2.8a represents a top-view SEM image of the fabricated devices. The SEM image of the cross-section of such a grating, indicating a fill-factor of 0.3, a grating period of 1.0μm and a grating etch depth of 239nm, and a first tooth width of 175nm is shown in Fig. 2.8b. In this work, a 12μm wide waveguide was used.

Note that, this size of the waveguide in this demonstration is chosen initially to match with MFD of the single mode fiber at 1.55μm wavelength without taking wavelength dependence of MFD of the single mode fiber into account.

2.2.3 Measurement results

The setup to characterize the grating coupler structures consists of a continuous-wave mid-infrared tunable laser (IPG Cr:ZnSe tunable laser) operating below its threshold. The generated amplified spontaneous emission is coupled to an SMF-28 optical fiber, after which it passes a polarization controller, and is injected in the fundamental TE-polarized mode of the Si waveguide circuit. The light is then collected by an identical grating coupler/SMF-28 combination and is coupled to a
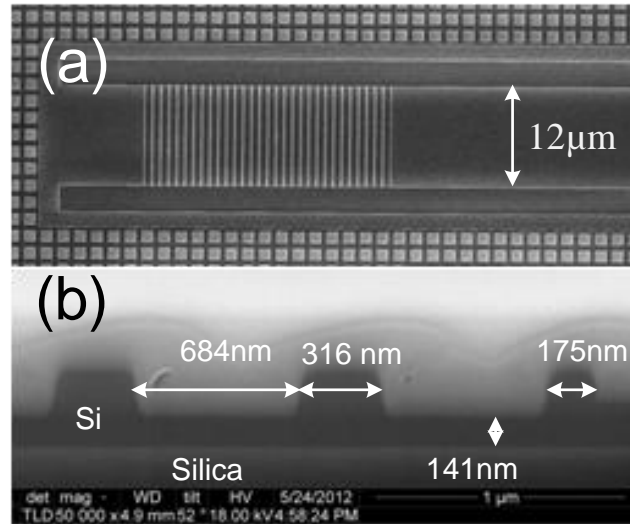
*Figure 2.8: SEM image of the fabricated SWIR fiber-to-chip grating couplers: a) top view
b) cross-section*

SWIR optical spectrum analyzer (Yokogawa AQ6375).
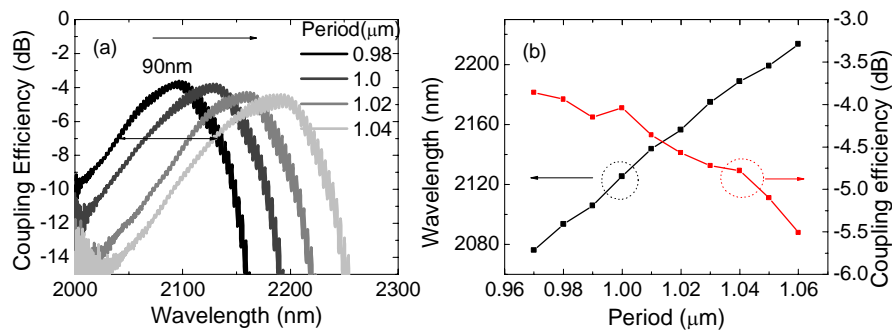
*Figure 2.9: a) Coupling efficiency as a function of wavelength for different grating periods
(fill factor ≈0.3) b) peak wavelength and coupling efficiency as a function of the grating
period*

Fig. 2.9a shows the coupling efficiency of the grating couplers as a function
of wavelength for different grating periods. The grating coupler with a period of
0.98μm and a fill factor of 0.3 shows -3.8dB coupling efficiency at a peak wave-
length of 2.1μm with a 3dB bandwidth of 90nm. The fringes observed are Fabry-
Perot interference fringes, resulting from parasitic reflections from the grating cou-
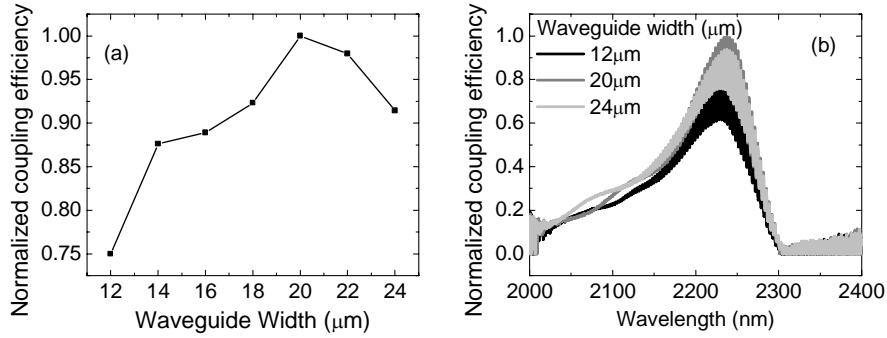
Figure 2.10: a) Normalized coupling efficiency as a function of waveguide width and b) the corresponding normalized coupling spectra

plers. From the fringe depth, the parasitic reflection from the grating couplers can be assessed. As can be seen in Fig. 2.9a, the fringe depth varies from 0.5dB at shorter wavelengths to 1.5dB at longer wavelengths, resulting in a reflection ranging from 2.8% at shorter wavelengths to 8.5% at longer wavelengths. This is consistent with the fact that for longer wavelengths the out-coupling is closer to the surface normal. Thus, stronger second order Bragg reflection can be expected. Fig. 2.9b summarizes the experimentally measured increase of peak wavelength and the decrease of coupling efficiency as a function of the grating period, for a fixed fill factor of 0.3. The decrease in efficiency when going to longer wavelengths is attributed to (a) the increase in the loss in SMF at longer wavelengths (i.e. the fiber loss increased from 0.008dB/m at 2μm to 2.3dB/m at 2.5μm), which cannot be completely calibrated out in the measurement system and (b) the increasing mode mismatch between the Si waveguide mode and that of the single mode fiber at longer wavelengths.

As predicted from the simulation, the fiber-to-chip coupling efficiency can be improved by increasing the Si waveguide width to an optimum value. In Fig.2.10a, the normalized coupling efficiency of a grating coupler with a 1.05μm period (2.225μm peak coupling wavelength) is plotted as a function of waveguide width. An optimum coupling efficiency is obtained for a waveguide width of 20μm. Fig. 2.10b shows the corresponding normalized coupling spectra.

2.3 Standard grating coupler

Although the raised grating from Section 2.2 offers highly efficient light coupling (-3.8dB), the fabrication process is complex, leading to an increase in production cost. On the other hand, it is possible to fabricate lower efficiency grating couplers

on a standard 220nm thick SOI waveguide platform. The structure of the grating coupler consists of a 220nm thick crystalline Si layer as a waveguide layer on 2μm buried oxide layer. The 220nm deep etched grating is formed in the Si waveguide layer followed by a 70nm shallow etch. This gives rise to grating teeth with a height of 150nm. Fig. 2.11 shows the schematic of this type of grating coupler. Fig. 2.12 shows the FDTD-simulated coupling efficiency for this type of grating coupler for different grating periods with fill factor of 0.5. This fill factor is chosen in this work as a standard design parameter. Further optimization of this parameter might improve the design further. About 10% maximum coupling efficiency can be obtained over a broad wavelength region. By increasing the grating period, the directivity increases for longer wavelengths, thereby increasing coupling efficiency. The -3dB bandwidth is approximately 300nm for the 1.64μm grating period and increases according to the peak wavelength.
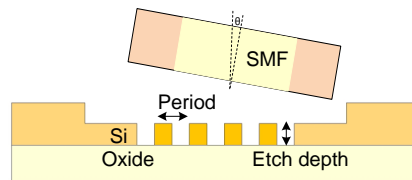
Figure 2.11: Schematic of the SWIR fiber-to-chip grating coupler structure fabricated on standard SOI
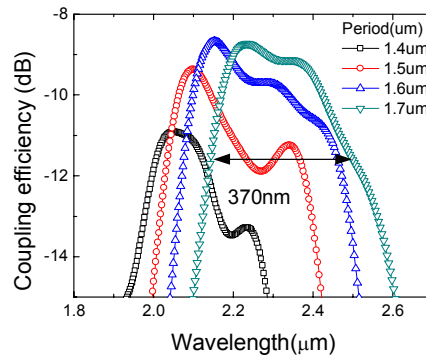
Figure 2.12: Simulated coupling efficiency for different grating periods

The measurement of these gratings is performed using the same set up which is utilized to characterize the high efficiency grating coupler (Section 2.2.3). Fig. 2.13 represents the measurement results of the grating. The directivity and the peak wavelength increase as the grating period increases corresponding to the simula-
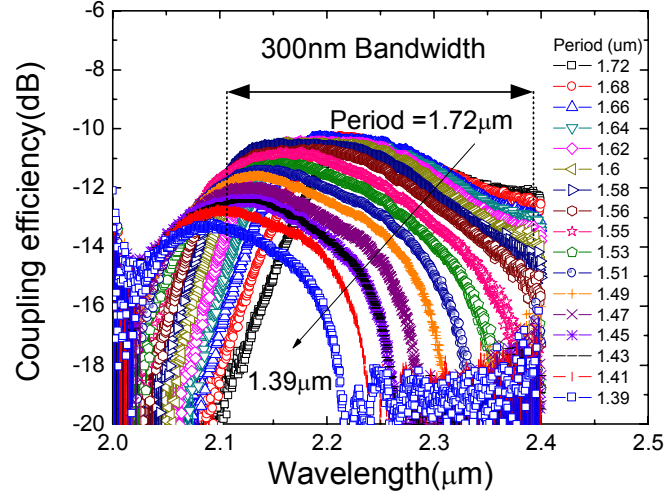
Figure 2.13: Coupling efficiency as a function of wavelength for different grating periods (fill factor =∼0.5)

tion results in Fig. 2.12. A maximum coupling efficiency of 10% is obtained. The small difference between simulation and measurement is attributed to fabrication errors.

2.4 Silicon-on-Insulator waveguides

Low-loss waveguides are of paramount importance for integration platforms for SWIR applications. The waveguides considered in this work are 900nm wide and etched completely through the 220nm crystalline Si guiding layer. There is no poly-Si on top of the waveguides. The waveguide loss was assessed by cut-back measurements on 1cm, 2cm, 4cm and 7cm long waveguides. The resulting propagation loss (TE-polarization) is plotted in Fig. 2.14, showing losses <0.6dB/cm in the SWIR range. These low losses are of the utmost importance both in spectroscopic applications and in nonlinear optics applications, since it enhances the effective interaction length in both cases.

2.5 Summary and outlook

In summary, I propose SOI as a passive platform for operating in the SWIR range. The SOI waveguides have low losses in the range of 0.6dB/cm. I demonstrate the first, high efficiency (-3.8dB) grating coupler at 2.1μm. These results open exciting opportunities for employing SOI as a platform for high density integrated
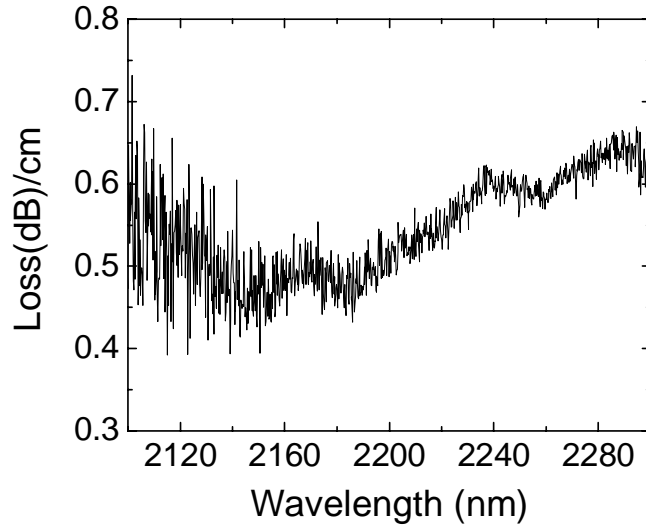
Figure 2.14: Si-on-insulator single mode waveguide losses (220nm by 900nm waveguides-TE polarization) in the SWIR

Type of grating	Wavelength (μm)	Coupling efficiency (%)
Raised grating, UGent, [17]	2.1	41.6
Grating coupler for Si on sapphire [14]	2.75	32.6
Focused grating coupler for suspended-membrane waveguide [7]	2.75	28
Standard grating, UGent	2.2	10

Table 2.1: State-of-the-art grating couplers for the SWIR range

circuits in the SWIR.

Table 2.1 is a comparison of state-of-the-art grating couplers using different technologies and designs operating in the SWIR range. Our design provides the maximum coupling efficiency at 2.1μm. Similar designs can be extended to operate at 2.75μm on a Si-on-Sapphire platform, as reported by Cheng et al. [14]. Focused sub-wavelength gratings provide flexibility in design to accommodate different operating wavelengths with only one etch step [15]. However, further optimization on both designs and their fabrication is still required [16].

References

[1] X. Liu, B. Kuyken, G. Roelkens, R. Baets, R. M. O. Jr, and W. M. J. Green. *Bridging the mid-infrared-to-telecom gap with silicon nanophotonic spectral translation*. Nat. Photonics, 6(October):667–671, 2012.

[2] R. Soref. *Mid-infrared photonics in silicon and germanium*. Nat. Photonics, 4(8):495–497, August 2010.

[3] M. Ortsiefer, C. Neumeyr, J. Rosskopf, S. Arafin, G. Böhm, A. Hangauer, J. Chen, R. Strzoda, and M. C. Amann. *GaSb and InP-based VCSELs at 2.3μm emission wavelength for tunable diode laser spectroscopy of carbon monoxide*. Proc. SPIE, 7945(794509):7, 2007.

[4] B. Kuyken, X. Liu, R. M. Osgood, R. Baets, G. Roelkens, and W. M. J. Green. *A silicon-based widely tunable short-wave infrared optical parametric oscillator*. Opt. Express, 21(5):5931–40, March 2013.

[5] W. Bogaerts, P. Dumon, D. V. Thourhout, D. Taillaert, P. Jaenen, J. Wouters, S. Beckx, V. Wiaux, and R. G. Baets. *Compact Wavelength-Selective Functions in Silicon-on-Insulator Photonic Wires*. IEEE J. Sel. Top. Quantum Electron., 12(6):1394–1401, 2006.

[6] P. Cheben, A. Delâge, A. Densmore, S. Janz, B. Lamontagne, J. Lapointe, E. Post, J. Schmid, P. Waldron, and D. Xu. *Recent advances in silicon microphotonic devices*. Rev. Cuba. Fis., 25(2):75–80, 2008.

[7] Z. Cheng, X. Chen, C. Y. Wong, K. Xu, and H. K. Tsang. *Broadband focusing grating couplers for suspended-membrane waveguides*. Opt. Lett., 37(24):5181–3, December 2012.

[8] Z. Cheng, X. Chen, C. Y. Wong, K. Xu, C. K. Y. Fung, Y. M. Chen, and H. K. Tsang. *Focusing subwavelength grating coupler for mid-infrared suspended membrane waveguide*. Opt. Lett., 37(7):1217–9, April 2012.

[9] T. Baehr-Jones, A. A. Spott, R. Ilic, B. Penkov, W. W. Asher, and M. Hochberg. *Silicon-on-sapphire integrated waveguides for the mid-infrared*. Opt. Express, 18(12):12127–35, June 2010.

[10] P. Dumon. *Ultra-Compact Integrated Optical Filters in Silicon-on-insulator by Means of Wafer-Scale Technology*. PhD thesis, Ghent University, 2007.

[11] G. Roelkens, D. Van Thourhout, and R. Baets. *High efficiency Silicon-on-Insulator grating coupler based on a poly-Silicon overlay*. Opt. Express, 14(24):11622–30, November 2006.

[12] *ePIXfab*, *http://www.epixfab.eu/*.

[13] S. K. Selvaraja. *Wafer-Scale Fabrication Technology for Silicon Photonic Integrated Circuits*. PhD thesis, Ghent University, 2011.

[14] C. Y. Wong, C. K. Y. Fung, and Y. M. Chen. *Mid-Infrared Grating Couplers for Silicon-on-Sapphire Waveguides*. IEEE Photonics J., 4(1):104–113, February 2012.

[15] P. Cheben, D.-x. Xu, S. Janz, and A. Densmore. *Subwavelength Waveguide Grating Coupler*. Proc. IEEE, pages 143–145, 2006.

[16] J. H. Schmid, P. Cheben, S. Janz, J. Lapointe, E. Post, a. Delâge, a. Densmore, B. Lamontagne, P. Waldron, and D.-X. Xu. *Subwavelength Grating Structures in Silicon-on-Insulator Waveguides*. Adv. Opt. Technol., 2008(October):1–8, 2008.

[17] N. Hattasan, B. Kuyken, F. Leo, E. M. P. Ryckeboer, D. Vermeulen, and G. Roelkens. *High-Efficiency SOI Fiber-to-Chip Grating for the Short-Wave Infrared*. IEEE Photonics Technol. Lett., 24(17):1536–1538, 2012.

3

Heterogeneous Integration and Fabrication Technology

In the previous chapter, I proposed to use SOI as a passive platform for SWIR applications. I demonstrated low loss waveguides and a high coupling efficiency grating coupler as basic building blocks. In order to obtain a fully integrated spectrometer, integration of active material onto the passive platform is required. In this chapter, the technology used to integrate GaSb-based epitaxy onto an SOI waveguide circuit is described. Fabrication techniques used to realize integrated GaSb-based detectors and lasers are developed. Contact angle measurement presented in this chapter was carried out in collaboration with Veerle Boterberg from Polymer Chemistry and Biomaterials Group, Ghent University.

3.1   Introduction

Although the SOI waveguide platform has emerged as a promising passive platform for the SWIR, the indirect band gap of Si prevents it from being used as an efficient SWIR emitting and absorbing material. Several works have been undertaken to remedy this problem, including the incorporating of direct bandgap material onto Si using different techniques such as epitaxial growth (GaSb on Si, InP on Si, SiGe) [1–4], rare earth doping [5, 6], and light generation and amplification in Si using non-linear optics [7]. Nevertheless, the efficiency of these devices is still quite low. On the other hand, heterogeneous integration of alien materials

onto Si using bonding is a viable approach [8]. Several works have demonstrated the successful integration of InP-based material on SOI [9, 10]. While the heterogeneous integration of InP on Si is mainly driven by applications for telecom, GaSb-based devices have recently received attention for sensing applications since the absorption lines of several gases and biological molecules are located in the SWIR to MWIR range [11]. However, at the start of this work, there was no report on the integration of GaSb-based devices on SOI waveguide circuits. Only a few works on molecular bonding based integration of GaSb on GaAs were reported to achieve semi-insulating substrates for photovoltaic applications [12, 13]. In this work, I study the feasibility of integrating GaSb and its compounds on SOI waveguide circuits employing an adhesive bonding technique with the aim of realizing a fully integrated spectroscopic system.

In this chapter, I describe the technologies utilized in this thesis. This includes the adhesive bonding technique based on DVS-Benzocyclobutene (DVS-BCB) and the fabrication processes developed for GaSb-based photodetectors and lasers. In the first part, the discussion covers basic properties of DVS-BCB and its bonding mechanism. The compatibility of the bonding technique with different surfaces is analysed using contact angle measurement. Different bonding procedures are also presented and evaluated here. In the second part, GaSb device fabrication techniques are presented. Here, I investigate the etching properties of several GaSb compounds with different etching solutions. The results on dry etching are also presented. Metallization on p- and n-doped GaSb is explored and assessed. From the results in this chapter, specific fabrication processes are derived for different active devices. A brief explanation of the specific processes for different device generations will be given in the subsequent chapters (4-6).

3.2   Adhesive bonding

Bonding one material onto another has been an important process in microelectronics industry [14–16]. For example, SOI wafers themselves are realized through bonding and offer electronic circuits with superior performance (low power consumption, high speed operation) over a standard Si platform [15]. Several bonding techniques have been briefly discussed in Section 1.5. A comprehensive review can be found in [8]. Among these bonding techniques, adhesive bonding offers several advantages such as low bonding temperature (typically below 450 °C depending on the polymer) and insensitivity to surface topography. This technique employs an interfacial layer which can conform to the surfaces to form an intimate contact between two substrates such that macroscopic bonding occurs [17, 18]. The tolerance of this technique to particles and imperfection of the bonding surface is better than the other commonly used techniques such as direct bonding [14].

Therefore, less intensive cleaning procedures are required. The bonding mechanism between polymer and substrate also depends on the type of surfaces to be bonded. Adsorption theory is commonly used to explain this phenomenon [19].

3.2.1 Adsorption theory

This theory describes optimum adhesion, which involves wettability, interfacial defects and work of adhesion [19]. Wettability refers to the capability of a liquid to spread on a substrate. Wettability is the first condition to obtain optimum adhesion. Good wettability requires the surface tension of the liquid (γ_L) to be lower than that of the substrate (γ_S). Good wettability minimizes the formation of interfacial defects and allows to establish an intimate interaction between molecules. However, good wettability alone does not guarantee the optimum adhesion in the view of work of adhesion (W_A). W_A is defined in Equation 3.1 as the work which is required to separate two substrates [19].

$$W_A = 2\sqrt{\gamma_S \gamma_L} \tag{3.1}$$

where γ_S is the surface tension of the substrate and γ_L is the surface tension of the liquid. From Equation 3.1, the W_A is maximized for a particular substrate when γ_L is maximum. However, from above discussion, we can see that γ_S should be greater than γ_L [19]. Therefore, we can approximate that

$$\gamma_S = \gamma_L \tag{3.2}$$

These two conditions are general for dispersive bonding when only van der Waals interaction/dipole-dipole bonds are present. However, in many cases, the polarities of both surface and liquid play an important role where covalent bonding is established. The third condition is under the assumption that W_A consists of both dispersive and polar parts [19]:

$$W_A = W_d + W_p = 2\sqrt{\gamma_{Sd} \gamma_{Ld}} + 2\sqrt{\gamma_{Sp} \gamma_{Lp}} \tag{3.3}$$

where
W_d is the work of adhesion for the dispersive part
W_p is the work of adhesion for the polar part
γ_{Sd} is the dispersive part of the surface tension of the substrate
γ_{Sp} is the polar part of the surface tension of the substrate
γ_{Ld} is the dispersive part of the surface tension of the liquid
γ_{Lp} is the polar part of the surface tension of the liquid

Given that $W_d = 2\sqrt{\gamma_{Sd} \gamma_{Ld}}$ and $W_p = 2\sqrt{\gamma_{Sp} \gamma_{Lp}}$, and according to Equation 3.2, we can write $\sqrt{\gamma_{Sd}} = \sqrt{\gamma_{Ld}}$ and $\sqrt{\gamma_{Sp}} = \sqrt{\gamma_{Lp}}$. Thus, for maximised values
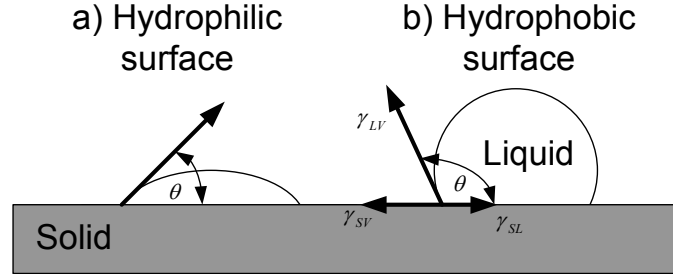
Figure 3.1: Schematic representing wettability of the liquid on the solid surface

(Equation 3.2) of W_d and W_p, simple deduction suggests that the ratio between γ_{Sp} and γ_{Sd} equals to the ratio between γ_{Lp} and γ_{Ld} i.e.

$$\frac{\gamma_{Sp}}{\gamma_{Sd}} = \frac{\gamma_{Lp}}{\gamma_{Ld}} \tag{3.4}$$

As can be seen, the third condition suggests that the optimum adhesion is obtained when the surface tension in both polar and dispersive parts of liquid and solid are comparable with each other. In conclusion, optimum adhesion between the substrate and the liquid is achieved when 2 conditions are satisfied: good wettability as in Equation 3.2 and comparable values of the polar and dispersive part of both substrate and liquid surface tension as in Equation 3.4.

To measure surface tension experimentally, a commonly used method is a contact angle measurement.

3.2.2   Contact Angle Measurement

Contact angle measurement is used to quantify wettability and thereby surface tension. Fig. 3.1 shows a schematic of two drops forming different contact angles depending on the surface tension of the substrate. Young's Equation (3.5) describes the relationship of surface interfacial tensions [19, 20].

$$\gamma_{SV} = \gamma_{LS} + \gamma_{LV} cos\theta \tag{3.5}$$

where
γ_{SV} is the solid/air surface tension
γ_{LS} is the solid/liquid interfacial surface tension
γ_{LV} is the liquid/air surface tension
θ is the contact angle.

Contact angle measurements are used to assess different surface conditions in this thesis. The measurement are performed using a Drop Shape Analysis instrument (DSA). Three different liquids (water, Diiodomethane, DMSO) are dropped on the substrate of interest. The Owens, Wendt, Rabel and Kaelble method is used to determine surface tension with distinction of polar and dispersive part. The details on the calculation used to obtain the surface tension can be found in [19]. The experimental results for different substrates and surface treatments are shown in Table 3.1. As can be seen, a SOI substrate with deposited oxide and a SOI substrate after RCA clean ($NH_4OH:H_2O_2:H_2O$ 1:1:5v/v) exhibits a high polar component to its surface tension. These values are expected because the RCA solution oxidizes the surface, which eases the formation of hydrogen bonds, increasing surface tension and thereby reducing the contact angle.

GaSb, InAs, p-i-n epitaxy (Table 4.2) and SOI, after cleaning with acetone and isopropanol, exhibit very similar surface tension to DVS-BCB. Therefore, theoretically, bonding on this surface would yield better results compared to oxide, SiN_x deposited surfaces, p-i-n epitaxy after removing InAsSb layer (Table 4.2) and SOI with RCA cleaning. However, these results contradict those obtained from InP-based bonding where a thin oxide layer is deposited on III-V die to achieve good bonding [21]. This is likely because the oxide layer prevents the etchant from penetrating underneath the die, avoiding damage to the bonding layer.
Fig. 3.2 represents experimental results of bonding on different substrates. The p-i-n epitaxy reveals the best bonding quality as shown in Fig. 3.2e. Small bonding defects are found in the GaSb bonding as shown in Fig. 3.2a. This difference is partly caused by the substrate removal etchant (see Section 3.3.3.1). The etchant can etch oxide and GaSb at a very fast etching rate while it almost does not etch InAsSb (see Section 3.3.3.1). On the GaSb sample, the etchant penetrates through bonding defects as shown in Fig. 3.2a. On the other hand, the etchant does not attack the InAsSb layer resulting in a good remaining bonded epitaxial die, as shown in Fig. 3.2e. A similar explanation applies to Fig. 3.2c and d where thin layers ($\sim$ 10nm) of oxide and SiN_x respectively are deposited on p-i-n epitaxy after removing the InAsSb layer (Table 4.2), using Plasma Enhanced Chemical Vapor Deposition (PECVD). These SiN_x and oxide layers are used as the surface for bonding instead of GaSb. The chemical penetrates through bonding or epitaxy defects etching the oxide and SiN_x layer resulting in blisters or detachment of the epitaxial die from the substrate. It is important to note that PECVD deposition can induce stress on the thin film [22]. This stress is the result of a mismatch between the thermal expansion coefficients (CTE) of GaSb and oxide/SiN (deposition at 250°C). Therefore, after substrate removal, stress generated in the thin film during oxide deposition or curing could start to bend the epitaxial thin film, causing cracks in the epitaxial die (see Fig. 3.2d). Fig. 3.2c shows the detachment of the die as a result of an absence of adherence between DVS-BCB and the p-i-n
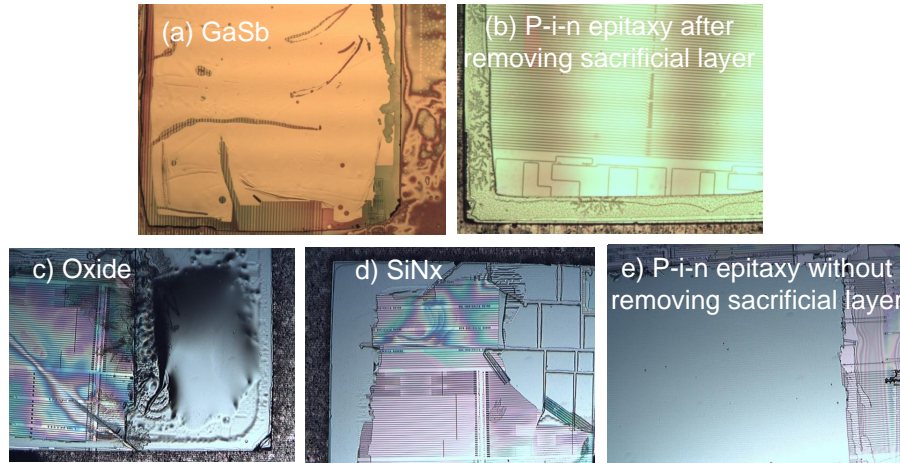
Figure 3.2: Bonding results using different samples a) GaSb b) p-i-n expitaxy after removing the InAsSb layer c) Oxide deposition on p-i-n expitaxy after removing the InAsSb layer d) SiN deposition on p-i-n expitaxy after removing the InAsSb layer e) p-i-n epitaxy with the InAsSb layer

epitaxy with the InAsSb layer removed prior to bonding. Note that a number of bonding experiment with AP3000 spin coated on III-V were carried out. However, no significant improvement in bonding quality is observed. Hence, from this assessment I conclude that the experimental results agree well with the optimum adhesion condition where polar and dispersive surface tension ratios of polymer and substrate are similar. Nevertheless, this is not the only factor to attain good bonding. Several factors such as epitaxy defects, cleanliness of both substrates and the selection of the bonding agent are also important and may strongly influence the bonding quality. In the next section, the properties of DVS-BCB, the polymer used as a bonding agent in this thesis, will be discussed.

3.2.3   DVS-Benzocyclobutene Properties

One criterion for a good adhesive material is that it should release minimum by-products to avoid void formation during the curing process. Also, a high processing temperature is undesirable. When 2 materials with different thermal expansion coefficients are bonded at high temperature, bonded samples may crack due to different shrinkage rates during cooling. Typically, the desired curing temperature is between room temperature and 450°C [23]. Several polymers have been proposed such as thermoplastic adhesives (e.g. polymethylmeth acrylate(PMMA)) [24, 25] and thermosetting polymers such as B-stage polymers (e.g. benzocyclobutene, SU8) [14, 21, 26]. Each material has its own advantages and disadvantages de-

Detail	Surface tension (J/m^2)	Dispersive (J/m^2)	Polar (J/m^2)	Polar/ Dispersive	Contact angle with water (degrees)
Oxide on SOI +acetone+IPA	60.98	21.43	39.55	1.845544	33
Oxide on SOI +RCA	58.33	21.44	36.89	1.720616	37.28
Oxide on InP	68.99	18.93	50.06	2.64448	60.31333
SiN on InP	45.28	27.8	17.48	0.628777	60.5525
p-i-n epitaxy	38.8	24.58	14.21	0.578112	68
p-i-n epitaxy +removed InAsSb layer	58	20.99	37.02	1.763697	36.84
GaSb+acetone +IPA	28.47	19.28	9.2	0.477178	80.91
InAs+acetone +IPA	24.98	20.74	4.25	0.204918	90.78
InAs	27.88	22.31	5.57	0.249664	86.43
SOI+RCA	59.02	20.83	38.19	1.833413	35.90667
SOI+acetone +IPA	41.53	21.07	20.45	0.970574	61.44667
SOI (1.5μm +acetone+IPA	41.45	37.11	4.35	0.117219	70.8
SOI (imec9) +acetone+IPA	47.22	19.7	27.52	1.396954	50
DVS-BCB fully cured	31.91	29.76	2.15	0.072245	91.1
DVS-BCB at 150°C (30min)	33.22	28.71	4.5	0.15674	84.48
DVS-BCB at 190°C (30min)	31.94	23.96	7.98	0.333055	80.09
DVS-BCB at 210°C (30min)	32.56	28.44	4.12	0.144866	85.78667

Table 3.1: Surface tension measured from several substrates used in this thesis
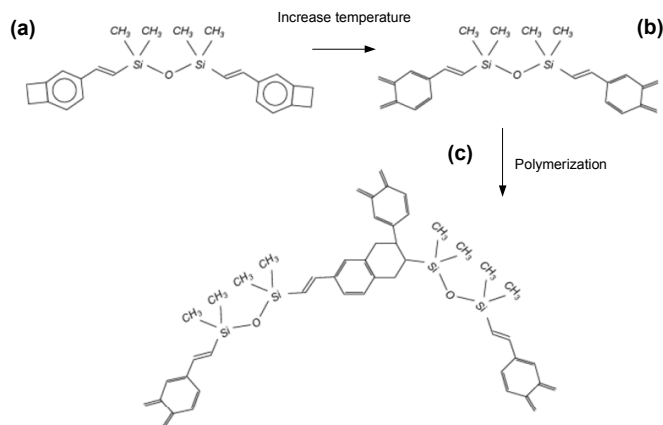
*Figure 3.3: Chemical structure of DVS-BCB at different stages a) B-stage monomer b)
Opening of benzocyclobutene ring c) Diels-Alder reaction creating polymerization
(reproduced from [28])*

pending on the bonding purposes and the material which has to be bonded. Thermoplastic adhesives are typically limited to low temperatures. A thermoplastic adhesive has relatively poor creep resistance and good peel strength [14]. Thermosetting polymers are more rigid than thermoplastics. They offer higher operating temperatures, up to 400°C, which is important for further semiconductor processing. Therefore, a thermosetting polymer (DVS-BCB) is selected for this thesis.

Chemically, DVS-BCB is a monomer molecule. Its full IUPAC name is 1,3-divinyl-1,1,3,3-tetramethyldisyloxane-bisbenzocyclobutene. The chemical structure is illustrated in Fig. 3.3a. It consists of a siloxane backbone, terminated by two benzocuclobutene rings via two vinyl groups. The polymer is typically available in B-stage bisbenzocyclobutene monomer form, i.e partially cured to form an oligomer which is dissolved in mesitylene [27]. Upon curing, the benzocyclobutene rings open, forming a highly reactive o-quinodimethene group [28] (see Fig. 3.3b). Following the Diels-Alder reaction between the o-quinodimethene group and the adjacent vinyl group, a fully polymerized 3-dimensional network structure is formed (Fig. 3.3c).

Adhesive bonding using DVS-BCB as bonding agent is commonly considered as an alternative strategy for bonding at low temperatures (250°C). It has been used in microelectronic industry since the 1980s [29]. The first intensive study for wafer bonding was conducted in 2002 [14]. Apart from being a low temperature process, DVS-BCB bonding gives superior adhesion between a wide range of materials. It does not release by-products during the curing process [27]. This makes DVS-BCB an ideal adhesive for integrated circuits operating in SWIR.

Property	3022-35 DVS-BCB
Curing temperature($°$C)	200-300
Layer thickness for single spin coat (μm)	1.0-2.6
Glass transiton temperature($°$C)	$>$350
Thermal conductivity (W/m.K)	0.29 at 24$°$C
Young's modulus(GPa)	2.9+/-0.2
Tensile strength (MPa)	87+/-7
Coefficient of thermal expansion (CTE) (ppm/$°$C)	42
Elongation(%)	8+/-2.5
Dielectric constant(kHz)	2.65-2.5 at 1-20 GHz
Dissipation factor (kHz)	0.0008-0.002 at 1-20 GHz
Breakdown voltage (V/cm)	5.3×10^6

Table 3.2: The thermal, electrical and mechanical properties of CYCLOTENE 3000 series resins (DVS-BCB) (reproduced from [27])

Table 3.2 [27] lists the thermal, electrical and mechanical properties of DVS-BCB. The glass transition temperature T_g is the temperature at which links in a polymer start to weaken. For DVS-BCB, T_g equals 350$°$C which is sufficiently high for subsequent processes. The degree of polymerisation of DVS-BCB versus curing time and temperature is shown in Fig. 3.4 [27]. The standard curing temperature is 250$°$C for 1 hr. The viscosity of DVS-BCB at different temperatures is shown in Fig. 3.5 [23]. The viscosity is minimal at 150$°$C, where the polymer can conform itself optimally to the substrate surface. Bonding performed at 150$°$C is, therefore, considered as the best condition. Although the conformity is high, uniformity is an issue because of the low viscosity. Uniformity is determined by measuring the variation of DVS-BCB thickness across the bonded area. Typically, in a die to wafer bonding process, the pressure applied onto the epitaxial die is nonuniform across the bonded area due to the small size of the epitaxial die. This results in nonuniformity of the bonding layer. To solve this problem, partial curing of the DVS-BCB can be used where the bonding temperature is shifted from 150$°$C to 190$°$C. This increases the amount of cross-linked states from 34% to 43% before it is used for bonding. The nonuniformity also improves dramatically from 17% to less than 1% [23]. Different bonding procedures will be discussed in the next section.

The thickness of the DVS-BCB layer can be controlled by diluting the solution with mesitylene. The DVS-BCB is applied on the sample using a spin coater. The bonding thickness is determined by the volume ratio between DVS-BCB and mesitylene, spinning speed, spinning time and the topography of the substrate. The thickness of the DVS-BCB as a function of volume ratio between DVS-BCB and mesitylene, spin coated on a flat Si substrate at different spinning speeds is shown in Fig. 3.6. The spinning time is kept at 40sec.
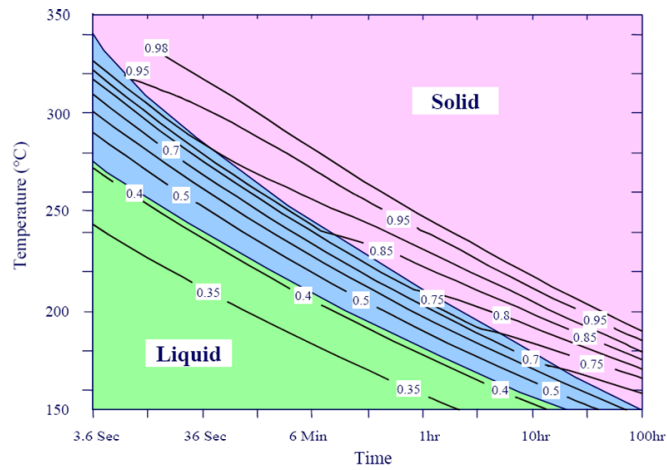
Figure 3.4: The degree of polymerisation of DVS-BCB versus curing time and temperature (reproduced from [27])
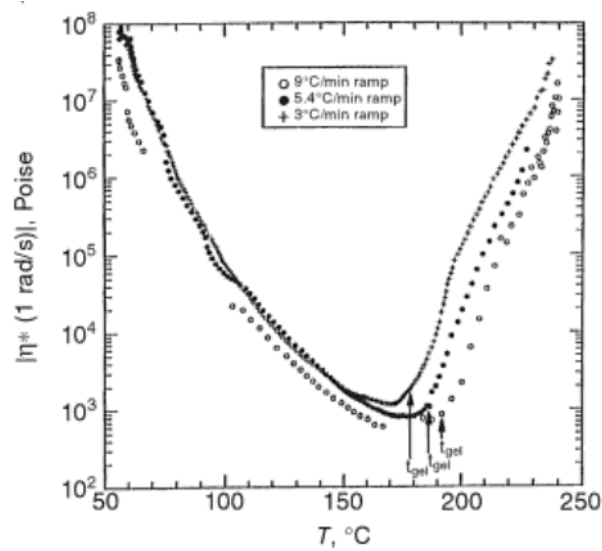
Figure 3.5: The viscosity of DVS-BCB versus curing temperature (reproduced from [23])
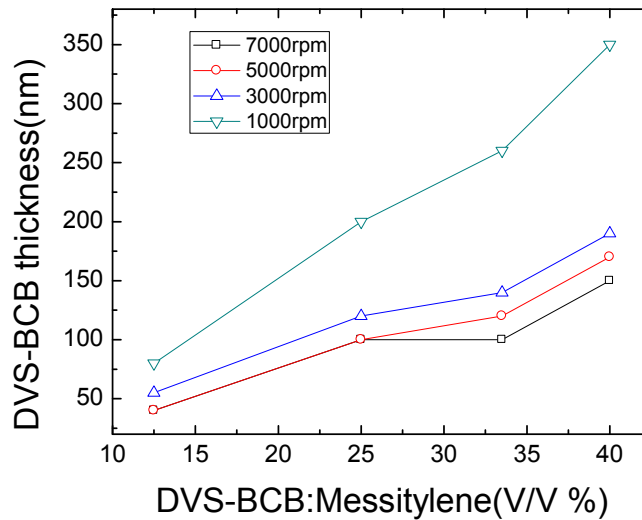
Figure 3.6: The thickness of DVS-BCB as a function of volume ratio between DVS-BCB and mesitylene, at different spinning speeds (reproduced from [21])

3.2.4 Bonding Process

Prior to the integration process, the epitaxial die and carrier wafer/SOI sample are cleaned using acetone and isopropanol. However, if the SOI sample is processed in house (i.e. for forming the waveguides, see Chapter 6), the SOI sample is cleaned using RCA solution ($NH_4OH:H_2O_2:H_2O$ 1:1:5 v/v) for 15 minutes at 80°C, followed by rinsing with DI water. The SOI sample is baked at 150°C for 5 minutes to ensure evaporation of water and solvent. An adhesion promoter (AP3000) is spin coated on the SOI wafer (3000rpm, 40sec) to enhance adhesion. DVS-BCB is spin coated on the SOI wafer simultaneously. The thickness of the DVS-BCB layer can be adjusted by controlling rotation speed, spinning time and diluting the commercially available solution with mesitylene according to Fig. 3.6.

3.2.4.1 Manual bonding

After spin coating, the sample is baked at 150°C for 3 minutes to remove the mesitylene. The epitaxial die is then transferred onto a carrier wafer (with DVS-BCB) using tweezers. The epitaxial die is pressed with a small force. The sample is then loaded into an oven and cured at 250°C for 1 hr. This is carried out under a nitrogen environment to avoid oxidation of the DVS-BCB. The temperature profile for curing is plotted in Fig. 3.7. Using this process, it is possible to achieve bonding thicknesses down to 100nm depending on the dilution ratio of DVS-BCB
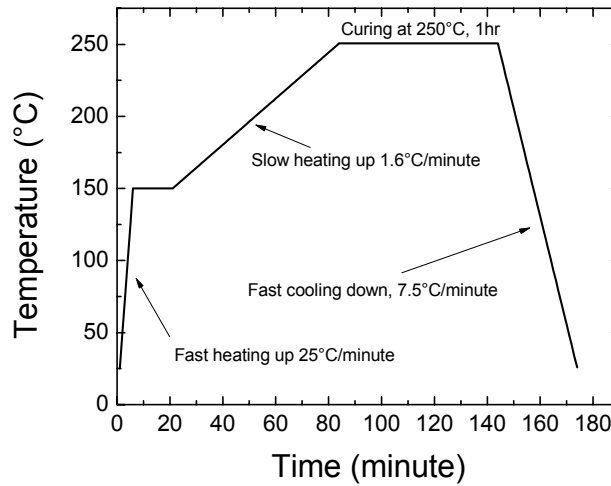
Figure 3.7: Temperature profile for the DVS-BCB curing programmed for the oven

and mesitylene. However, since the applied force is usually not uniform across the sample, the bonding layer thickness is nonuniform.

3.2.4.2 Machine bonding

Machine bonding is employed to control the pressure applied on the sample, resulting in an improvement of thickness uniformity of the bonding layer. The Suss MicroTec ELAN CB6/8L wafer bonding machine (Fig. 3.8a) is used for this work. Fig. 3.8b shows the fixture where the sample is mounted between 2 pyrex glass plates. Fig. 3.9 shows the interior of the bonding machine, where a pressure head is used to apply force. The machine is designed for wafer bonding with a bonding head area (A_{bh}) of 222cm^2 [30]. For machine bonding, after spin-coating DVS-BCB on the carrier sample (InP/SOI), the sample is baked at 150°C for 10min to remove mesitylene. The temperature is then decreased gradually to 90°C. Afterwards, the epitaxial die is transferred onto the carrier without applying force. The sample is mounted between 2 pyrex glass plates and then loaded into the bonding chamber. The typical temperature profile used for curing is shown in Fig. 3.10a. The temperature is ramped quickly from room temperature to 150°C and stays constant for 15 minutes to evaporate the remaining solvent and apply pressure onto the sample. The temperature ramps again slowly to 180°C while the force is kept constant. After 15 minutes, the force is removed. The temperature starts to ramp up with a slow rate of 1.6°C/minute until it reaches 250°C. DVS-BCB is cured at 250°C for 1 hr in N$_2$ environment. A typical force profile is shown in Fig. 3.10b. Note that the bonding chamber is kept under vacuum with a cham-
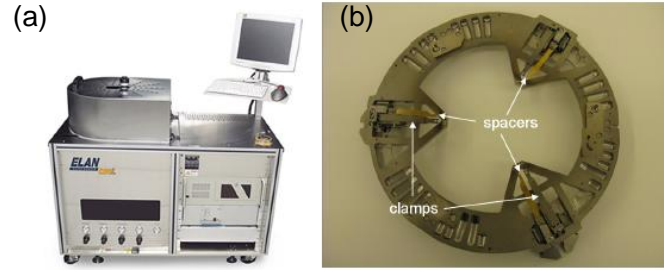
Figure 3.8: a) Suss MicroTec ELAN CB6L b) the fixture for mounting the sample (reproduced from [21])

ber pressure of 0.4μBar until the temperature reaches $250°$C. The chamber is then purged with N_2. The tool pressure (P_{tool}) is set at 10mBar corresponding to a bonding force of 22.2N which is the product of P_{tool} and A_{bh}. This pressure setting is actually lower than the limit of the bonding machine: e.g. the operating range is typically between 100-3600mBar [30]. Therefore, the machine is unable to keep the pressure constant at 10mBar. During the experiment, the applied force fluctuates between 55-60N as shown in Fig. 3.10b. The pressure on the sample (P_{die}[N/cm^2]) as expressed in Equation 3.6 [30] changes according to the ratio between A_{bh} and the area of the die (A_{die}), which is only 0.25cm^2 in this case. Therefore, P_{die} is in the range of 220-240N/cm^2. This high pressure ensures intimate contact between the die and the substrate while it does not cause damage to the sample.

$$P_{die} = \frac{F}{A_{die}} = \frac{A_{bh}}{A_{die}}.P_{tool} \tag{3.6}$$

3.2.5 Bonding quality assessment

After the bonding process, the substrate is removed using a combination of grinding and wet etching (discussed in Section 3.3.3.1). The successful bonding and substrate removal process leaves the thin membrane of epitaxy on the substrate as shown in Fig. 3.11a. Fig. 3.11b shows a zoom picture of the bonded epitaxy after substrate removal representing a clean surface without defects.

Nevertheless, an epitaxial film that by the eye looks well bonded to a substrate does not guarantee sufficiently good adhesion such that it can withstand following fabrication steps. Several techniques can be employed to assess adhesion properties in both destructive (tensile and shear load test, crack opening, blister test) [19] and non-destructive (optical microscope, scanning electron microscope (SEM)) manner [31, 32]. Several works on the adhesion assessment of DVS-BCB with
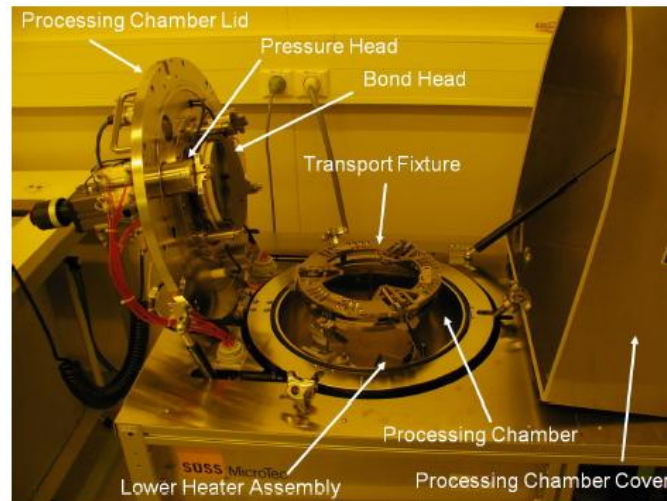
Figure 3.9: The interior of the bonding machine MicroTec ELAN CB6L (reproduced from [21])
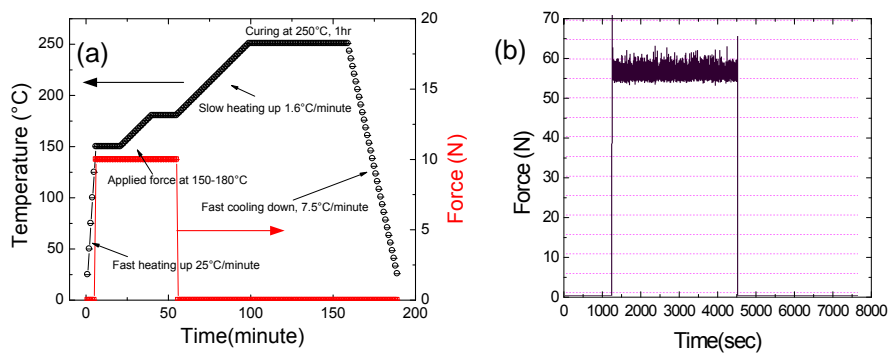
Figure 3.10: a) Temperature profile used for curing DVS-BCB b) force profile exerted on the epitaxial die during machine bonding process
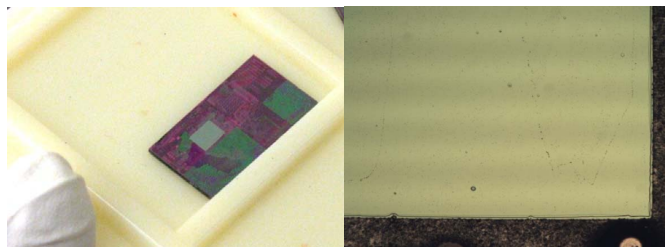
Figure 3.11: a) Photograph of the bonded sample b) Zoom on the die surface
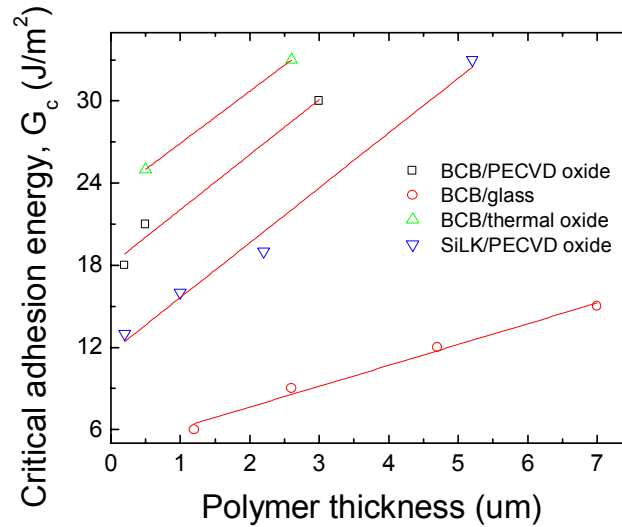
Figure 3.12: Critical adhesion energy as a function of DVS-BCB thickness (reproduced from [18])

different substrates are reported. The most extensive works are performed using SOI and InP [23, 26]. Roelkens et al. reported very high critical adhesion energy ($14 \, J/m^2$) on SOI and DVS-BCB [26]. Kwan et al. reported $>18 \, J/m^2$ [18]. These experiments support the feasibility of the use of DVS-BCB as a bonding material. Kwon also showed experimentally that the thickness of DVS-BCB affects critical adhesion energy linearly, corresponding to plastic dissipation energy. Thinner DVS-BCB exhibits lower adhesion strength. Fig. 3.12 shows the results from reference [18]. These results indicate that DVS-BCB bonding is a good bonding platform.

In this thesis, only non-destructive optical inspection is used. The inspection is performed only after the substrate removal process to assess bonding quality. Typical defects found on bonded films are blisters or detachment of the die; see Fig. 3.2c, d, respectively. Blisters are mostly related to the cleanliness of the substrate and the die. If there are any particles on the surface, no intimate contact is formed locally, resulting in a blister. The detachment of the film is caused by mismatch of surface energy of both die and wafer and particle contamination, leading to a non-contacted area. From the results in Table 3.1, after removing the sacrificial layer (InAsSb) of the p-i-n InGaAsSb epitaxy, the surface energy (in particular the polar component) increased significantly. This results in lower adhesion strength as discussed in Section 3.2.1, thereby causing detachment of the die. As a consequence, keeping the InAsSb sacrificial layer improves the bonding yield significantly. An-
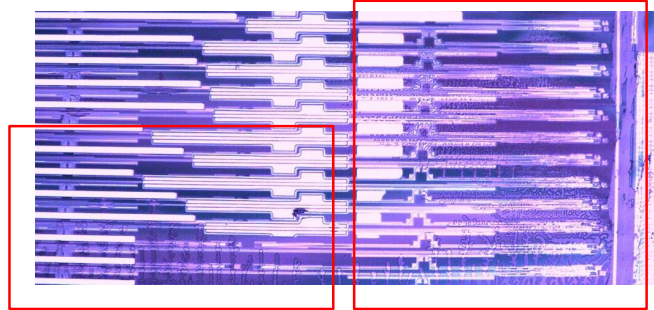
Figure 3.13: Optical image of a sample where not all trenches are filled completely with DVS-BCB

other common problem found in patterned SOI substrates is when the DVS-BCB does not fill all the trenches, as shown in Fig 3.13. This results in bonding defects which allow penetration of the etching solution and consequently detachment of the die. Unfilled trenches mostly occur because the available volume of DVS-BCB is not enough to fill the trenches and planarize the substrates. In most cases, the problem is solved by increasing the DVS-BCB thickness. Alternatively, the SOI pattern can be planarized using DVS-BCB and cured up to 210°C for 30 minutes before bonding. Then another DVS-BCB layer is applied as interfacial adhesive layer. This approach reduces topography of the substrate as well as maintains good adhesion between epitaxial die and polymer.

3.3　Fabrication process

3.3.1　General fabrication procedure

After the bonding process, the substrate of the epitaxy is removed using a combination of mechanical grinding and wet etching. Then, depending on the component, different III-V processing steps are carried out. The generic process diagram is shown in Fig. 3.14 which is valid for both photodetectors and lasers. The process starts from the substrate removal. Subsequently, the p-contact is deposited on the p-doped layer. The mesa is etched by both wet and dry etching until the n-contact layer is reached. Metal is then deposited on the n-doped layer. The device is planarized. The metal vias are then opened using Reactive-Ion Etching (RIE). Finally, metal is deposited for probing. Detailed discussions on each processing step are presented in the following sections.

GaSb substrate
QW
Si
Si substrate

(1) After Bonding

(2) After substrate removal

(3) n-contact deposition

(4) Forming mesa by Dry etching

(5) p-contact deposition

(6) Island definition

(7) BCB passivation

(8) BCB opening and Contact deposition
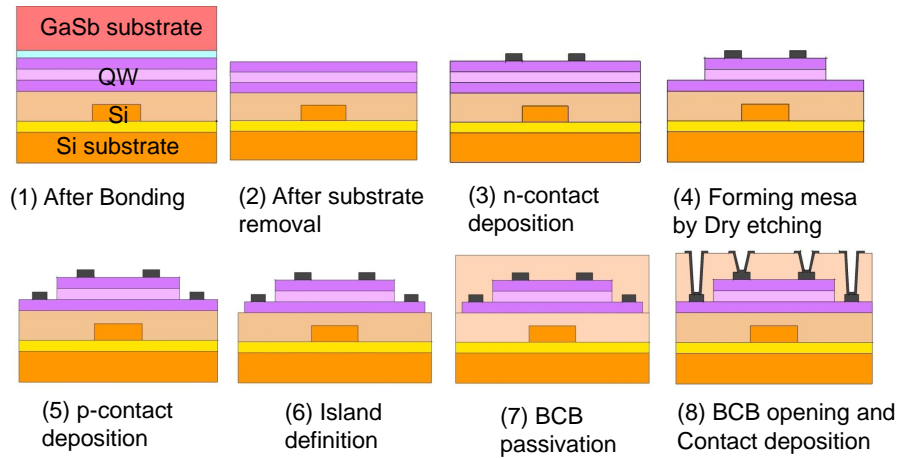
Figure 3.14: A generic fabrication process flow for both detectors and lasers

(a)

(b)

Thickness meter
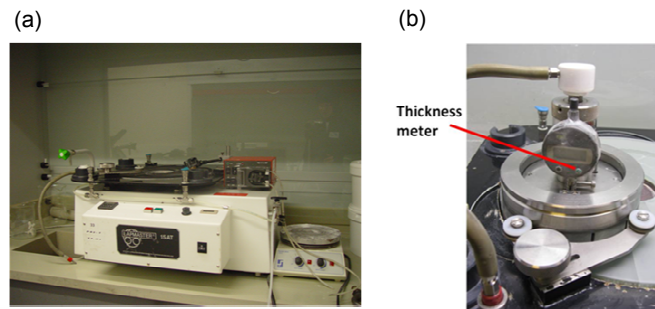
Figure 3.15: a) photograph of the lapmaster used for this work b) pressure head mounted on the grinding plate during grinding

3.3.2 Substrate removal

Before removing the GaSb substrate, a wax (CrystalBond 509) [33] is applied around the die and areas of interest to protect them during the etching process. CrystalBond 509 can be dissolved in acetone. Its melting point is at $121°C$ and its softening point is at $71°C$. The glue exhibits strong adhesion and high chemical resistance towards HF which makes it suitable for side wall protection during the substrate removal process.

The substrate is removed by using a combination of mechanical grinding and wet etching. The grinding machine shown in Fig. 3.15a is used to reduce the GaSb substrate from $500\mu m$ thickness down to approximately $50\mu m$ thickness. Fig. 3.16a presents the setup of mechanical grinding process. This consists of the
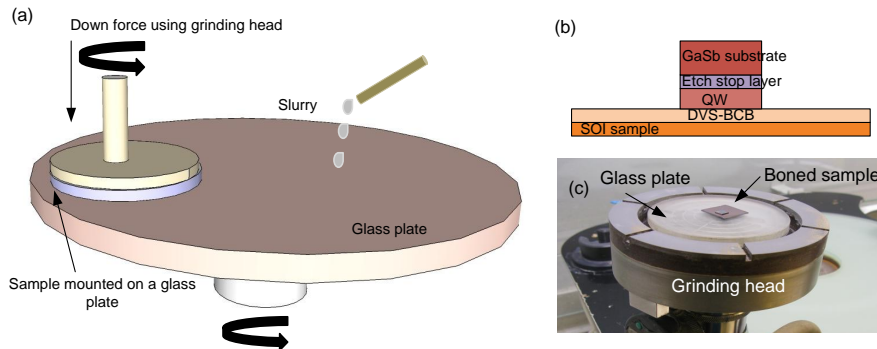
Figure 3.16: a)the schematic representing grinding element and it mechanism b)drawing of the bonded III/V on SOI c) a photograph of the bonded sample glued on a glass plate which is mounted on a grinding head

grinding head to exert a downward force, a glass plate for mounting the sample and a glass grinding plate for abrasion. The abrasive slurry is fed continuously on to the grinding plate for homogenous abrasion. Fig. 3.16b presents a typical structure of the bonded sample indicating the GaSb substrate. Fig. 3.16c presents a photograph of the sample glued on a glass plate mounted on the grinding head. Minimum thickness of the GaSb substrate after this process is desirable in order to minimize the time required for wet etching, since the wet etching solution used to remove the GaSb substrate also etches Si and oxide. A glass plate is used as a grinding plate. The force applied during grinding is controlled by the pressure head which is illustrated in Fig. 3.15b. The grinding time to remove 450μm of GaSb is approximately 15 minutes. Alumina oxide powder (12.5μm diameter) mixed with water is used as the grinding slurry. The roughness of the surface after grinding is expected to be approximately 12.5μm corresponding to the abrasive grain diameter. However, due to the non-uniform force applied on the sample during grinding, a thickness variation of the grinded sample in the range of 20μm is obtained. Common problems in this step are the development of cracks and significant variation in overall topography. The cracks are mostly caused by non optimum force and rotation speed of the grinder (too high force and too fast rotation speed). The variation in topography can be a result of the usage of an excess amount of glue to mount the sample onto the glass substrate. The problem is solved by using a low amount of glue with low viscosity. The force must be applied equally on 2 corners of the sample at the same time to achieve intimate flat contact between the sample and the glass plate.

A chrome acid based solution (CrO_3:HF:H_2O (1:1:3 v/v)) is used to remove the rest of the substrate. Details about this etchant are discussed in Section 3.3.3.1. The CrystalBond glue is removed using acetone at room temperature followed

by isopropanol and a DI water rinse. The sample is then baked at 120°C for 3 minutes to evaporate residual solvent and water. After this processing step, the bonding quality is assessed under an optical microscope.

3.3.3 Wet etching

Wet etching is a common process used in a typical opto-electronic device fabrication process. It is cheap and can be material-selective. The etching mechanism typically consists of the oxidation of the etched material and dissolution of the oxidized products. Oxidizers such as H_2O_2 are added to break covalent bonds of III-V material. Acids or bases such as HCl or HF are added to dissolve the oxidized compounds. In some cases, complex agents such as citric acid and NaK tartrate are added to form stable ions [34].

In this section a study of different etchants used on different GaSb compounds is carried out. Table 3.3 is a summary of the etchants used in this thesis. Table 3.4 summarizes the etch rate of the etching solutions on different materials. Etching profiles of GaSb and InAs substrates obtained by using different etchants are shown in Fig. 3.17. The main etching solutions used in this work are discussed next.

3.3.3.1 Chrome based acid

Chrome based acid is a mixture of CrO_3:HF:H_2O (1:1:3 v/v). This solution was originally proposed by J. Van de Ven in 1986 [35] for etching GaAs. The mixture consists of $Cr_2O_7^{-2}$ as an oxidizing agent. The solution etches GaSb leaving a very smooth surface as shown in Fig. 3.17. The etch rate is 9.4μm/min and 500nm/min for GaSb and InAs respectively at room temperature. The etching is isotropic, and the side wall profile is smooth both for GaSb and InAs substrates. This implies that for both materials the solution is a good choice for mesa etching. The study of this solution at different ratios of CrO_3 and HF confirms that the etch rate of GaSb is 100 times faster than that of $InAs_{0.91}Sb_{0.09}$ [36]. This property indicates that the solution is the best candidate for substrate removal. The etching is diffusion limited (i.e. the etching rate is sensitive to diffusion of the etchant). Therefore, agitation is required to ensure a stable etch rate. Without agitation, a non-soluble, black-colored oxide is formed on the sample surface, preventing further etching.

3.3.3.2 Citric based acid

Citric based acid is a mixture of $C_6H_8O_7$:H_2O_2 (2:1 v/v) [37]. The solution is reaction limited with an etch rate depending on the reaction of the etchant and semiconductor [38]. The etch rate is sensitive to temperature [39]. The solution produces very smooth etched surfaces on InAs and GaSb as shown in Fig.

GaSb   InAs

Chrome based acid

Phosphoric based acid

NaK Tartrate based acid

Citric based acid
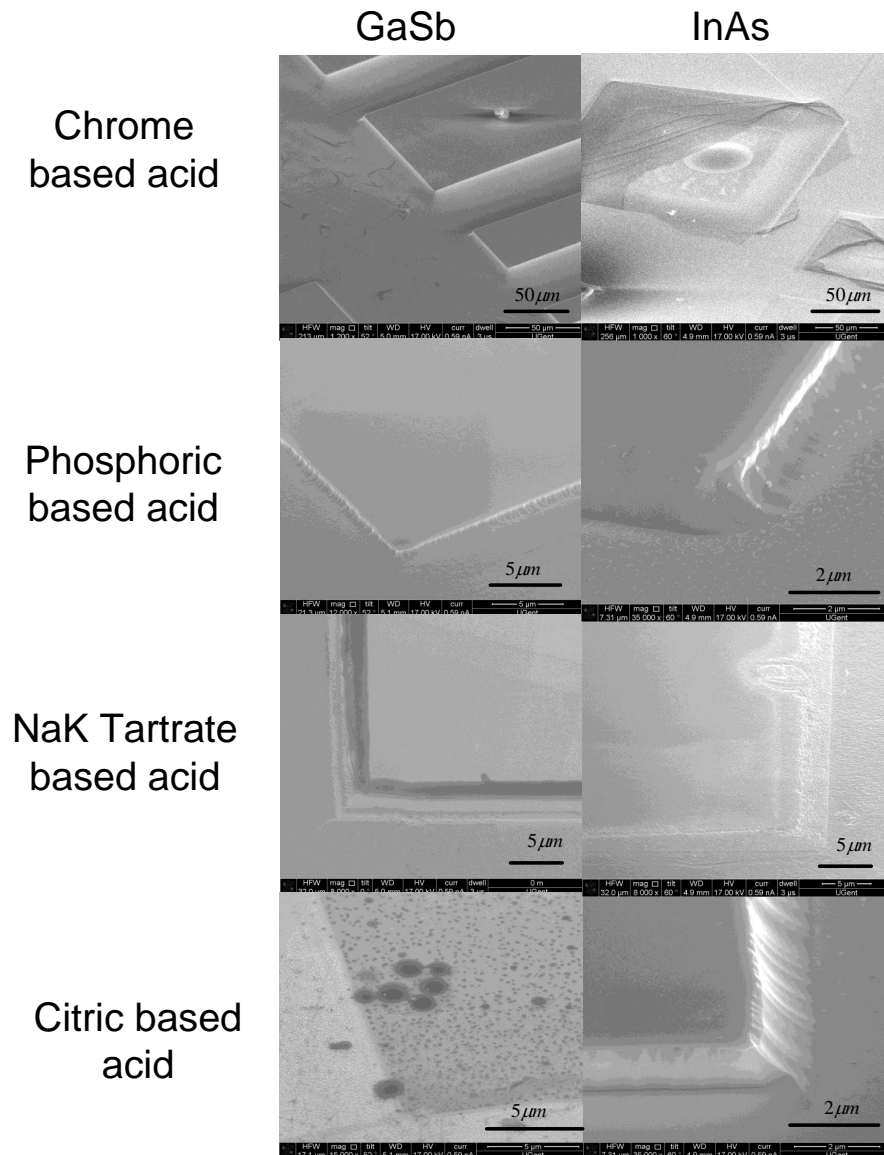
Figure 3.17: SEM images of a GaSb and InAs substrate etched with different etching solutions

Figure 3.18: Schematic of the crystallography of a crystalline semiconductor (reproduced from [42])

3.17. However, etched sidewalls show slight roughness. The solution gives an etch rate of 100nm/min for InAs and almost does not etch GaSb at room temperature. Therefore, the solution is suitable for etching InAsSb with GaSb as an etch stop layer.

3.3.3.3 Phosphoric based acid

The solution consists of Citric acid: H_2O_2:H_3PO_4:H_2O (55:5:3:220 v/v) [40]. The detailed analysis of its chemistry is discussed in [41]. The solution employs H_2O_2 as an oxidizing agent. Citric acid is used here as a complex agent to remove oxidized material, resulting in a smooth surface [41]. The etch rate is 34nm/min and 84nm/min for GaSb and InAs respectively. From the etch rate, one can see that, the solution can etch InGaAsSb compounds with low selectivity. Therefore, it is suitable for etching several layers with different material composition such as quantum wells and separate confinement layers. However, it should be noted that the side wall roughness is quite high on InAs and GaSb as shown in Fig. 3.17. According to Chaghi et al. [41], NaClO can be used to obtain better smoothness of the side walls. In this thesis, this solution is used for mesa etching.

3.3.3.4 NaK Tartrate based acid

NaK tartrate based acid is a mixture of NaK tartrate:H_2O:HCl:H_2O_2 (5g:70:60:5 v/v) [37]. H_2O_2 is used as an oxidizer, resulting in the insoluble compound (S_2O_5). NaK tartrate is added to make the oxidized compound soluble [43]. The etching is

diffusion limited. Therefore, it requires regular agitation in order to obtain a stable etching rate. Note that during the mixing process, the mixing of HCl and water creates an exothermic reaction which increases the temperature of the solution by approximately 9°C. Therefore, before use, the solution is cooled down to 20°C using surrounded water in order to obtain a stable etching rate. H_2O_2 is added before just before starting the etching process. The solution etches GaSb and InAs with etch rates of 210nm/min and 63nm/min at room temperature. The solution gives smoothly etched surfaces on GaSb substrate, but not on InAs (Fig. 3.17). The NaK Tartrate solution is reported as an alternative solution for substrate removal [37]. However, our experiments show that etch rate of InAs and GaSb is quite similar. Therefore, this solution is used only for the island definition step to remove the rest of the GaSb n-contact layer.

3.3.3.5 HCl based acid

The solution consists of $HCl:H_2O:H_2O_2$ (50:100:1 v/v). The HCl based solution is commonly used to etch semiconductor compounds which contain an Al-fraction higher than 30% [44, 45]. H_2O_2 is added to accelerate the oxidation process. The etching process is diffusion limited and therefore, requires agitation. Similarly to Section 3.3.3.4, the solution is cooled down to 20°C before use. H_2O_2 is added just before starting the etching process. Fig. 3.18 schematizes the crystallographic orientation of a GaSb wafer indicating typical OF(the primary long flat cut) and IF (the secondary flat cut) flat cut location [42]. The etch rate perpendicular to the (100) plane is 1.5μm/min for $Al_{0.9}GaAsSb$ and 20nm/min for GaSb and there is no observation of etching of $Al_{0.3}GaAsSb$ for 1 minute, at room temperature. The etch rate strongly depends on the crystal orientation. The etch rate perpendicular to the IF flat and OF flat (011 plane) is 2 times faster than that on the (100) plane. Fig. 3.19a and b shows a typical cross-section with etching profiles perpendicular to the IF and OF flat respectively. The epitaxial structure used in this experiment is summarized in Table 6.1. Since, the solution etches $Al_{0.9}GaAsSb$ layer much faster than $Al_{0.3}GaAsSb$, this etchant is selected for etching the cladding of the laser epitaxy.

3.3.4 Dry etching

Dry etching is an alternative method to form photodiodes or laser mesas. It uses a plasma and its radicals. Plasma is an ionized gas containing an equal number of positive (ions) and negative (electrons) charges, generated by coupling a strong electromagnetic field to the gas to start the ionization process. The electrons collide with neutral gas molecules and generate radicals. A radical is a neutral gas atom or molecule that is in a state of incomplete chemical bonding. Radicals are highly chemically reactive. Dry etching is a combination of chemical and me-
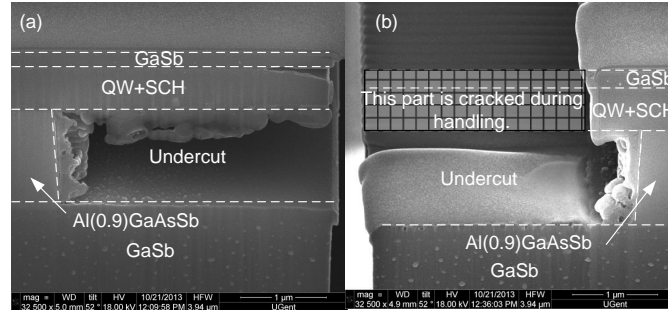
Figure 3.19: SEM of the cross section of the etching profile a) perpendicular to the IF flat b) perpendicular to the OF flat

Name	Description	Ratio
Citric acid	$C_6H_8O_7$:H_2O	1g:1ml
Chrome based acid	CrO_3:HF:H_2O	1:1:3 v/v
NaK Tartrate based acid	tartrate:H_2O:HCl:H_2O_2	5:70:60:5 v/v
Phosphoric based acid	Citric acid:H_2O_2:H_3PO_4:H_2O	55:5:3:220 v/v
Citric based acid	Citric acid:H_2O_2	2:1 v/v
RCA cleaning	NH_4OH:H_2O_2:H_2O	1:1:5 v/v
HCL based acid	HCl:H_2O:H_2O_2	50:100:1 v/v

Table 3.3: Summary of all chemicals used in this thesis

Etchants/ Materials	Chromic based acid (nm/min)	Phosphoric based acid (nm/min)	Citric based acid (nm/min)	NaK Tartrate based acid (nm/min)	HCl based acid (nm/min)
InAs	500	83	100	63	-
GaSb	9600	34	negligible	210	20
$Ga_{0.79}In_{0.21}As_{0.19}Sb_{0.81}$	-	61	-	-	-
$Al_{0.9}Ga_{0.1}As_{0.07}Sb_{0.93}$	-	60	-	-	1500
$Al_{0.25}Ga_{0.75}As_{0.02}Sb_{0.98}$	-	30	-	-	negligible

Table 3.4: Summary of all chemicals used in this thesis and the etch rate of different materials perpendicular to the 100 plane

chanical etching. The radicals chemically etch the material by adsorbing at and desorbing from the material as volatile agents. Ions, on the other hand, are accelerated towards the material under applied DC bias. As a result material is also removed mechanically by ion bombardment. The ratio of chemical and mechanical reaction is controlled by chamber parameters such as pressure and DC bias. Details on dry etching can be found in [46]. Generally there are two methods: The first is reactive ion etching (RIE) where plasma concentration and acceleration are coupled. The other is inductively coupled plasma (ICP - RIE) where the control of the plasma density and ion acceleration are separated. Both systems are employed in this work.

3.3.4.1 Inductively coupled plasma - reactive ion etching (ICP-RIE)

The PlasmaPro 100 from Oxford Instruments is used to etch GaSb, InAs and In-GaAsSb. A gas mixture of CH_4 and H_2 is selected for etching. CH_3 and H radicals are responsible for chemical etching of the semiconductor. H_2 contributes to increase the concentration of the radical H, thereby increasing the plasma density. Moreover, the presence of H_2 reduces the amount of gas phase polymerization of the hydrocarbon compound [47]. Several groups have reported smooth etched surfaces and sidewalls with a CH_4-H_2 mixture [48, 49]. An extensive study on the use of this gas mixture on Ga based materials can be found in [48, 49]. The recipes for etching GaSb and InAs reported in literature are summarized in Table 3.5.

In this thesis, the ratio of CH_4:H_2 is 15:40 sccm. The system pressure is 20mTorr. RF power is 200W and ICP plasma power is 100W. Ti is used as a hard mask. The etch rate is 3.6nm/min and 8.5nm/min for GaSb and InAs, respectively. The side wall profiles for both GaSb and InAs are shown in Fig. 3.20.

3.3.4.2 Reactive ion etching (RIE)

The system used for this work is the Vision 320 from Advanced Vacuum. It is used to etch DVS-BCB in order to open the metal vias. Polymer waveguides are also formed during the same process. The gas mixture consists of SF_6 (5%)and O_2 (50%). An RF power of 150V is used. The DVS-BCB etch rate is 320nm/min. Si waveguides are also formed by RIE. A gas mixture consist of SF_6 (38%)and O_2 (27%), using an RF power of 100W. The etch rate is 300nm/min. A SEM image of the etched Si is shown in Fig. 3.21.

3.3.5 Metallization

Metallization is one of the most critical steps for laser fabrication. This process creates the interface between metal and semiconductor. A good ohmic contact is
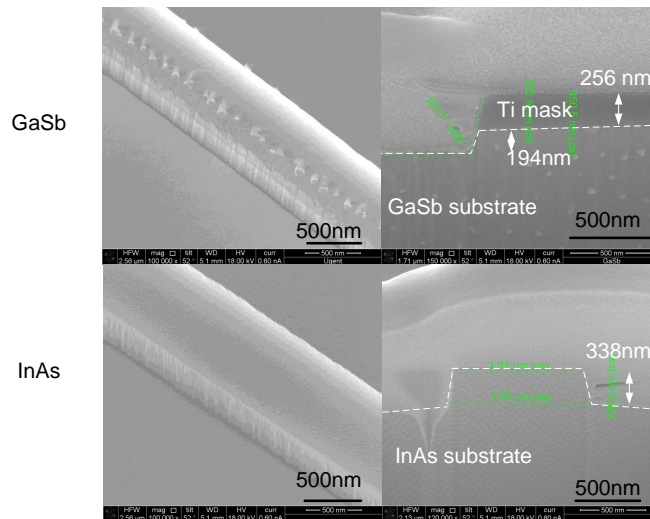
Figure 3.20: SEM image of GaSb and InAs substrate etched with an ICP-RIE system using CH$_4$ and H$_2$
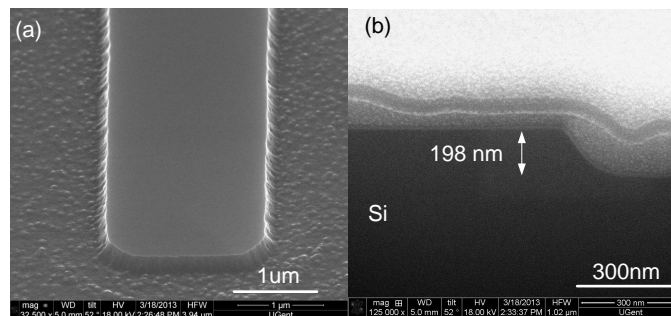
Figure 3.21: a) SEM image of a Si substrate etched with an RIE system, using SF$_6$ and O$_2$ b) cross section image of the Si waveguide

Gas	Material	Source	Hard Mask	Pressure (mTorr)	Flow rate (SCCM)	RF power (W)	DC bias (V)	Etch rate (GaSb) (nm/min)	(ICP) Plasma power (W)
$CH_4/H_2/Ar$ [49]	GaSb	RIE/ECR	SiO_2	2	4:16:7.6	100	not speci-fied	40-45	100
$Cl_2/BCl_3/$ $CH_4/Ar/H_2$ [50]	GaSb	ECR	Photoresist	1.3	2:1:2: 6:12	500	not speci-fied	560	400
BCl_3 [51]	GaSb/ GaInAsSb/ AlGaAsSb	ICP	AZ4330	2.5	40	not speci-fied	350	270-300	500
BCl_3/Ar [52]	GaSb, GaInAsSb, AlGaAsSb	ICP	AZ6809	4	6:4	30-100	150	490, 210, 510	150
Cl_2/Ar [50]	GaSb	ECR	Photoresist	1.5	1:6	100	not speci-fied	135	300
CH_4/H_2 [UGent]	InP	ICP	Ti, SiO_2	20	15:40	200	not speci-fied	6	100
$CH_4/H_2/Ar$ [48]	GaSb, GaAs, AlGaAs, GaP	ICP	AZ5109E/ SiO_2	2	5:15:10	350	37.5, 50,12.5, 75	120	500

Table 3.5: Summary of ICP and ECR etching recipes used for GaSb and its compounds

highly desirable in order to avoid excessive heating of the device at high current injection. A good ohmic contact typically refers to the specific contact resistance (ρ_c) which is expressed as a function of voltage (V) and current density (J) as follows:

$$\rho_c = \frac{dV}{dJ} \tag{3.7}$$

where dV is the voltage dropped across the metal-semiconductor contact and dJ is the current density. The metal-semiconductor contact behaviour is described using Schottky-Mott theory [53], in the ideal case i.e. when anomalies and surface states are not considered. The formation of a potential barrier occurs when semiconductor material comes in contact with metal. The fermi level of semiconductor is lower by an amount equal to the difference of work function of metal (Φ_m) and work function of semiconductor (Φ_s) forming a potential barrier. This potential barrier is defined in Equation 3.8 for n-doped semiconductor and Equation 3.9 for p-doped semiconductor:

$$q\Phi_{bn} = q(\Phi_m - \chi) \tag{3.8}$$

$$q\Phi_{bp} = E_g - q(\Phi_m - \chi) \tag{3.9}$$

where
Φ_{bn} is the potential barrier at a n-type contact
Φ_{bp} is the potential barrier at a p-type contact
Φ_m is the work function of metal
χ is the electron affinity of the semiconductor
E_g is the band gap of the semiconductor
q is the electron charge.

Fig. 3.22 presents the diagram of a metal-semiconductor barrier before and after making a contact for both p and n-doped semiconductors. Fig. 3.22b shows that an ohmic contact is formed for n-type if Φ_m is lower than χ, otherwise a Schottky contact is formed as shown in Fig. 3.22a. Similarly in p-type contacts, an ohmic contact is obtained when Φ_m is higher than Φ_{sc} as shown in Fig. 3.22c. Otherwise, a Schottky contact is obtained as shown in Fig. 3.22d.

Although these relations serve as a guideline to select a metal for different semiconductor materials, often there is a large discrepancy with experimental results. This is because several additional parameters affect the behaviour of the contact, such as surface states, the cleanliness of the surface, surface treatment prior metal deposition and the annealing procedure. For p-doped GaSb, it is easy to obtain a good ohmic contact because Φ_m for most metals is higher than the summation of χ and E_g. Several studies on ohmic contact formation on p-doped GaSb were conducted in the mid 90s. The summary of metal composition and specific resistivity is shown in Table 3.6. Tadayon et al. [55] reported a ρ_c of $1x10^{-6}$
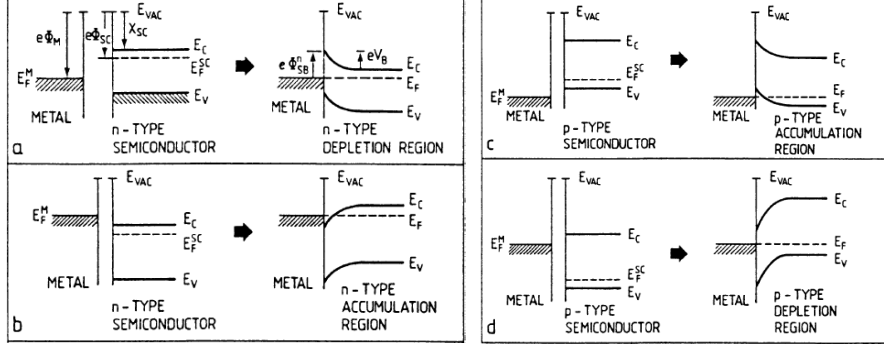
Figure 3.22: Schematic of band bending before and after metal-semiconductor contact a)
n-type semiconductor with high Φ_m b) n-type semiconductor with low Φ_m c) p-type
semiconductor with high Φ_m d) p-type semiconductor with low Φ_m (reproduced
from [54])

$\Omega.cm^2$ with Ti/Pt/Au, with or without alloying. This result is also consistent with
Vogt, et al. [56].

On the other hand, ohmic contacts on n-doped GaSb are generally difficult
to achieve because ϕ_m in general is higher than χ. Several efforts of achieving
ohmic contacts on n-doped GaSb are summarized in Table 3.7. The minimum
ρ_c (1.4x10^{-6} $\Omega.cm^2$) is obtained with metal combination of Pd/Ge/Pd/In/Pd after
alloying at 350°C for 60sec [58].

The quality of the contact is typically assessed by measuring ρ_c. ρ_c is obtained
using the transmission line method (TLM). A detailed analysis can be found in
[66, 67]. This technique involves the measurement of the total resistance (R$_T$)
between 2 contact pads with width (W), length (l) and distance between contact
pads (L). The measurement is conducted in a a series of adjacent contact pads
varying in distance; see Fig. 3.23a.

Fig. 3.23b represents the the current flow between contact pads indicating the
resistances. The total measured resistance can be plotted linearly as a function
of L (Fig. 3.23c). The relationship of R$_T$ and L provide an estimation of ρ_c as
follows [66, 67]:

$$R_T(L) = \frac{2R_{SK}L_T}{W} + \frac{R_{SH}L}{W} \tag{3.10}$$

where R$_{SK}$ is the sheet resistance of the semiconductor layer directly under the
contact, R$_{SH}$ is the sheet resistance of semiconductor layer outside the contact and

Metal(nm)	Doping(cm^{-3})	Surface treatment	Annealing	ρ_c ($\Omega.cm^2$)
Au/Zn/Au (200/300/3400) [57]	10^{17}-10^{18}	not specified	430°C, 5s	10^{-5}
Cr/Au (100/2500) [55]	4×10^{17}	HCl:H_2O, BHF:H_2O	300°C, 60s	10^{-5}
Ti/Pt/Au (500/500/3000) [55]	4×10^{17}	HCl:H_2O, BHF:H_2O	320°C, 60s	10^{-6}
Au (2500) [55]	4×10^{17}	HCl:H_2O, BHF:H_2O	200°, 60s	1.4-7.8x10^{-8}, degraded to 10^{-6} when annealed at 250°C
Ti/Pt/Au (300/1000/1000) [56]	7.9×10^{17}-1.2×10^{18}	HCl:H_2O, BHF:H_2O	not required	5.8×10^{-6}
Pd/Ge/Pd (100/300/1000) [56]	7.9×10^{17}-1.2×10^{18}	HCl:H_2O, BHF:H_2O	550°C, 40s	3×10^{-4}

Table 3.6: Summary of metals used for p-doped GaSb in literature

L_T is the transfer length which is defined as a distance where most of the current transfers from contact to semiconductor as shown in Fig. 3.23b. From Equation 3.10, at R=0, by assuming that R_{SK} and R_{SH} are equal, L_x is equal to $2L_T$. R_{SH} is obtained at L = 0 as follows:

$$R(L = 0) = 2R_c = \frac{2R_{SH}L_T}{W} \rightarrow R_{SH} = \frac{R_cW}{L_T} \qquad (3.11)$$

This yields the specific contact resistance as:

$$\rho_c = R_{SH}.L_T^2 = R_c.W.L_T \qquad (3.12)$$

In this work, a thermal evaporator (Univex) is used for AuGe (Ge 18%), Au and Ti evaporation. Electron beam evaporation (Leybold) is used for Pt, Ti and Au. For the p-contact on GaSb, Ti/Pt/Au(2/35/100nm) [68] is used as a contact. The contact is characterized using TLM. It gives a contact resistance of 4.7×10^{-5} $\Omega.cm^2$ on (1×10^{19} cm^{-3}) p-doped GaSb as shown in Fig. 3.24a. For n-doped GaSb (2×10^{18} cm^{-3}), GeAu(150nm)Ni(50nm)Au(100nm) is used as a contact. A contact resistance of $3.8 \times 10^{-4} \Omega.cm^2$ is measured as shown in Fig. 3.24b. It is important to note that AuGe diffuses strongly into n-GaSb as shown in Fig. 3.25.
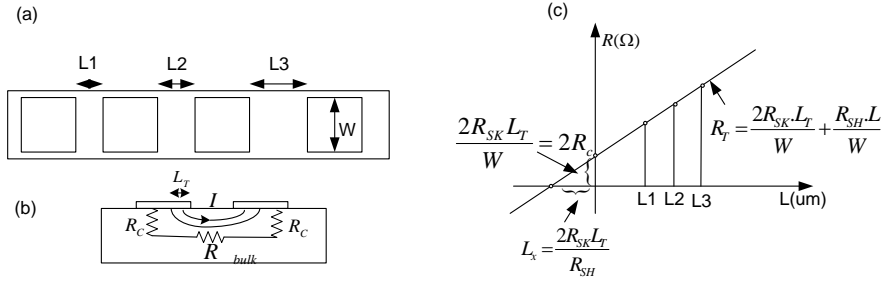
Figure 3.23: a) schematic representing TLM b) a cross section between contact pads presenting current flow, resistance and transfer length c) an example of a plot obtained from TLM where ρ_c is extracted.
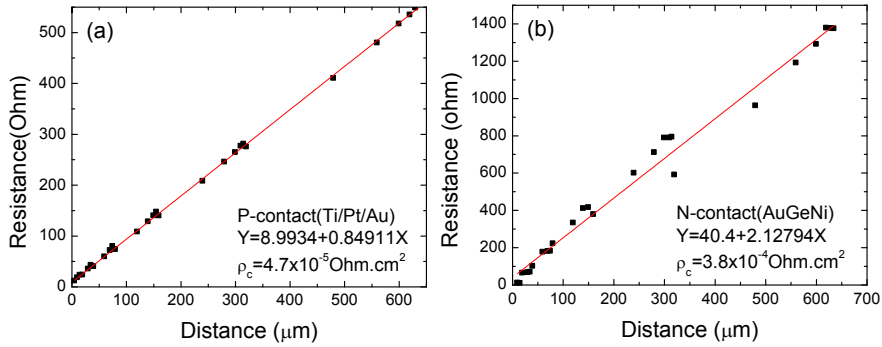
Figure 3.24: The measured resistance between contact pads as a function of their distances a) for a p-GaSb contact with Ti/Pt/Au as metal b) for a n-GaSb contact with GeAuNi as metal

Therefore, Ti/Pt/Au is used as a contact instead of AuGe for integrated photodiodes since the n-contact is on top of the photodetector mesa. Further optimization for both contacts would yield lower resistivity. Literature suggests that Pd based contacts would decrease specific contact resistance [62–65]. Moreover, surface treatment using HCl and HF is recommended to remove native oxide before metal deposition, resulting in a further decrease of ρ_c [60].

3.4   Conclusion

In this chapter, I discussed various experimental aspects of adhesive bonding techniques using DVS-BCB as a bonding agent and the integration of GaSb compound materials on SOI. An optimized bonding process is developed to obtain well bonded epitaxy. Further, I present our study on fabrication processes for both
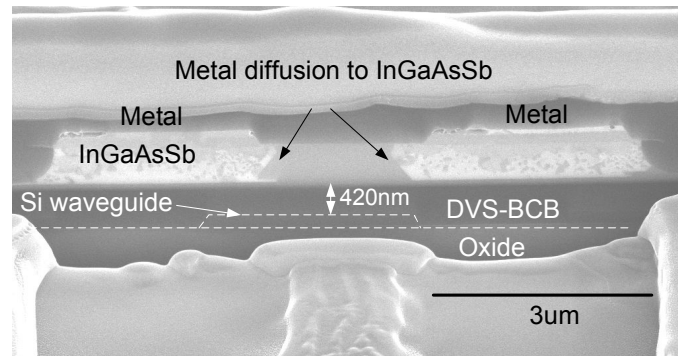
Figure 3.25: *SEM of the cross section of a InGaAsSb p-i-n representing Au diffusion from the n-doped contact*

integrated photodiodes and lasers. The discussion includes mesa etching and metallization. Based on the work in this chapter, I can develop optimized fabrication processes for specific devices. In the following chapters, I present the results of integrated GaSb-based photodetectors (Chapter 4) and integrated GaSb-based lasers (Chapter 5 and 6) as an outcome of the process development described in this chapter.

Metal(nm)	Doping(cm^{-3})	Surface treatment	Annealing	ρ_c ($\Omega.cm^2$)
AuGeNi [59]	1-5x10^{17}	not specified	400°, 2min	2x10^{-4}
Ag/AuGeNi [59]	1-5x10^{17}	not specified	400°, 2min	8x10^{-4}
Pd/Te/Pd/In/Au (75/50/75/500/2000) [60]	Te:10^{18}	HCl:H$_2$O,BOE:H$_2$O	250°C, 120s	< 10^{-6}
Pd/Ge(500/800) [61]	Te:8x10^{17}	C$_4$H$_6$O$_6$:HF:H$_2$O$_2$	300°C, 300min	4.5,10^{-3}
Sb/Pd/Ge (100/500/1250) [61]	Te:8x10^{17}	C$_4$H$_6$O$_6$:HF:H$_2$O$_2$	300°C, 300min	<10^{-2}
Pd (1000) [61]	Te:8x10^{17}	C$_4$H$_6$O$_6$:HF:H$_2$O$_2$	350°, 30 min	4.5x10^{-3}
Sb/Pd (120/1000) [61]	Te:8x10^{17}	C$_4$H$_6$O$_6$:HF:H$_2$O$_2$	300°C, 300min	~10^{-4}
Pd/Ge/Au/Pd/Au (130/400/100/789/577) [62] [63]	9.9x10^{17}	HCl:H$_2$O/HF	300°C, 60s	4.2x10^{-5}
Pd/Ge/Au/Pt/Au (87/560/233/476/1056) [64]	2x10^{18}	HCl:H$_2$O	300°C, 45s	8.3x10^{-6}
Pd/Ge/Au/Pt/Au (70/560/230/480/2000) [65]	1.2x10^{18}	not specified	270-280°C, 60s	1.0x10^{-5}
Pd/Ge/Pd/In/Pd [58]	Te:5.6x10^{17}	not specified	300°C, 60s	1.2x10^{-6}
Pd/Ge/Pd [58]	Te:1.8x10^{18}	not specified	400°C, 60s	3.8x10^{-6}
Pd (500) [64]	2x10^{18}	HCl:H$_2$O	350°C, 10min	4.1x10^{-5}
Pd/Pt/Au (120/350/600) [64]	2x10^{18}	HCl:H$_2$O	350°C, 10min	1.7x10^{-5}
Pd/In/Pd/Pt/Au (40/403/57/500/1000) [64]	2x10^{18}	HCl:H$_2$O	125°C, 120min + 350°C, 10min	2.4x10^{-6}

Table 3.7: Summary of metals used for n-doped GaSb in literature

References

[1] L. Cerutti, J. B. Rodriguez, and E. Tournie. *GaSb-Based Laser, Monolithically Grown on Silicon Substrate, Emitting at 1.55μm at Room Temperature.* IEEE Photonics Technol. Lett., 22(8):553–555, 2010.

[2] J. B. Rodriguez, L. Cerutti, P. Grech, and E. Tournie. *Room-temperature operation of a 2.25μm electrically pumped laser fabricated on a silicon substrate.* Appl. Phys. Lett., 94(6):061124, 2009.

[3] J. Liu, X. Sun, R. Camacho-Aguilera, L. C. Kimerling, and J. Michel. *Ge-on-Si laser operating at room temperature.* Opt. Lett., 35(5):679–81, March 2010.

[4] E. Kasper, M. Oehme, T. Arguirov, J. Werner, M. Kittler, and J. Schulze. *Room Temperature Direct Band Gap Emission from Ge p-i-n Heterojunction Photodiodes.* Adv. Optoelectron., 2012(100):1–4, 2012.

[5] O. Jambois, Y. Berencen, K. Hijazi, M. Wojdak, a. J. Kenyon, F. Gourbilleau, R. Rizk, and B. Garrido. *Current transport and electroluminescence mechanisms in thin SiO_2 films containing Si nanocluster-sensitized erbium ions.* J. Appl. Phys., 106(6):063526, 2009.

[6] O. Jambois, F. Gourbilleau, a. J. Kenyon, J. Montserrat, R. Rizk, and B. Garrido. *Towards population inversion of electrically pumped Er ions sensitized by Si nanoclusters.* Opt. Express, 18(3):2230–5, February 2010.

[7] R. Claps, D. Dimitropoulos, V. Raghunathan, Y. Han, and B. Jalali. *Observation of stimulated Raman amplification in silicon waveguides.* Opt. Express, 11(15):1731–9, July 2003.

[8] P. Ramm, J. Jian-Qiang, and M. M. V. Taklo. *Handbook of Wafer Bonding.* Jonhn Wiley& Sons, 1 edition, 2012.

[9] S. Stankovic, R. Jones, M. N. Sysak, J. M. Heck, G. Roelkens, and D. V. Thourhout. *Hybrid III-V/Si Distributed-Feedback Laser.* IEEE Photonics Technol. Lett., 24(23):2155–2158, 2012.

[10] A. W.-L. Fang. *Silicon Evanescent Lasers.* PhD thesis, University of California, Santa Barbara, 2008.

[11] M. Lackner. *Gas sensing in industry by tunable diode laser spectroscopy (TDLS).* ProcessEng Engineering GmbH, 2008.

[12] F. F. Shi, K.-L. Chang, and K. C. Hsieh. *Interfacial and mechanical characterization of wafer-bonded GaSb/amorphous α-(Ga,As)/GaAs structure for*

GaSb-on-insulator applications. J. Phys. D. Appl. Phys., 40(24):7694–7697, December 2007.

[13] C. A. Wang, D. A. Shiau, P. G. Murphy, P. W. O. Brien, R. K. Huang, M. K. Connors, A. C. Anderson, D. Donetsky, S. Anikeev, G. Belenky, D. M. Depoy, and G. Nichols. *Wafer Bonding and Epitaxial Transfer of GaSb-Based Epitaxy to GaAs for Monolithic Interconnection of Thermophotovoltaic Devices*. J. Electron. Mater., 33(3):213–217, 2004.

[14] F. Niklaus. *Adhesive Wafer Bonding for Microelectronic and Microelectromechanical Systems*. PhD thesis, Royal Institute of Technology, 2002.

[15] T. Suni. *Direct wafer bonding for MEMS and microelectronics*. PhD thesis, Helsinki University of Technology, 2006.

[16] Z. Zhu, S. Member, F. E. Ejeckam, S. Member, Y. Qian, J. Zhang, Z. Zhang, G. L. Christenson, and Y. H. Lo. *Wafer Bonding Technology and Its Applications in Optoelectronic Devices and Materials*. IEEE J. Sel. Top. Quantum Electron., 3(3):927–936, 1997.

[17] M. Jenkins, J. Snodgrass, A. Chesterman, G. Devries, H. Reinhold, and J. C. Bravman. *Adhesion Mechanism of Silane Adhesion Promoters in Microelectronic Packaging*. MRS Proc., 682(1):1–6, 2001.

[18] Y. Kwon, J. Seok, J.-Q. Lu, T. S. Cale, and R. J. Gutmann. *Critical Adhesion Energy at the Interface Between Benzocyclobutene and Silicon Nitride Layers*. J. Electrochem. Soc., 154(6):H460, 2007.

[19] M. C. Pocius, A. V. *Adhesion Science and Engineering: Surfaces, Chemistry and Applications (Annals of Discrete Mathematics)*. Elsevier Science B. V., 1 edition, 2002.

[20] KRÜSS, *KRÜSS Contact Angle*, *http://www.kruss.de/en/theory/measurements/surface-tension.html*.

[21] S. Stankovic. *Hybrid III-V/Si DFB lasers based on Polymer Bonding Technology*. PhD thesis, Ghent University, 2013.

[22] A. Tarraf, J. Daleiden, S. Irmer, D. Prasai, and H. Hillmer. *Stress investigation of PECVD dielectric layers for advanced optical MEMS*. J. Micromechanics Microengineering, 14(3):317–323, March 2004.

[23] F. Niklaus, R. J. Kumar, J. J. McMahon, J. Yu, J.-Q. Lu, T. S. Cale, and R. J. Gutmann. *Adhesive Wafer Bonding Using Partially Cured Benzocyclobutene for Three-Dimensional Integration*. J. Electrochem. Soc., 153(4):G291, 2006.

[24] G. Spierings, J. Haisma, F. V. D. Kruis, R. Soref, J. g. A. C. M. Spierings, Haisma, and V. D. Kruis. *Direct Bonding of Organic Polymeric Materials*. Philips J. Res., 49(I):139–149, August 1995.

[25] W. P. E. Smith and S. H. Risbud. *Silicon wafer-to-wafer bonding at Temperature below 200°C with polymethylmethacrylate*. Appl. Phys. Lett., 65(4):439–441, 1994.

[26] G. Roelkens. *Heterogeneous III/V Silicon Photonics: Bonding Technology and Integrated Devices*. PhD thesis, Ghent University, 2006.

[27] Dow chemical Company, *CYCLOTENE 3000 Series Advanced Electronic Resins*, *http://www.dow.com/cyclotene/prod/302235.htm*. 2005.

[28] G. Roelkens, L. Liu, D. Liang, R. Jones, A. Fang, B. Koch, and J. Bowers. *III-V/silicon photonics for on-chip and intra-chip optical interconnects*. Laser Photon. Rev., 4(6):751–779, November 2010.

[29] Y.-H. So, P. Garrou, J.-H. Im, and D. M. Scheck. *Benzocyclobutene-based polymers for microelectronics*. Chem. Innov., 2001.

[30] *CB6 8L, SUSS MicroTec*, *http://www.suss.com/en.html*.

[31] D. van Krevelen and K. te Nijenhuis. *Properties of polymers*. Elsevier, 4 edition, 2009.

[32] A. Pizzi and K. L. Mittal. *Handbook of Adhesive Technology*. Taylor&Francis Group, LLC, 2 edition, 2003.

[33] S. Supplies, *Crystalbond and Wafer-mount Washaway Mounting Adhesives*, *http://www.crystalbond.com/*.

[34] E. Paris-Olakowska. *Surface Treatments of GaSb and Related Materials for the processing of Mid-Infrared Semiconductor Devices*. Electron Technol. - Internet J., 37(38):1–34, 2006.

[35] J. van de Ven and J. L. Weyher. *Kinetics and Morphology of GaAs Etching in Aqueous CrO$_3$-HF Solutions*. J. Electrochem. Soc., 133(4):799–805, 1986.

[36] M. Grzesik, S. R. Vangala, and W. D. Goodhue. *Indirect Wafer Bonding and Epitaxial Transfer of GaSb-Based Materials*. J. Electron. Mater., 42(4):679–683, January 2013.

[37] O. Dier, C. Lin, M. Grau, and M.-C. Amann. *Selective and non-selective wet-chemical etchants for GaSb-based materials*. Semicond. Sci. Technol., 19(11):1250–1253, November 2004.

[38] G. C. DeSalvo, R. Kaspi, and C. A. Bozada. *Citric Acid Etching of GaAs$_{1x}$Sb$_x$, Al$_{0.5}$Ga$_{0.5}$Sb, and InAs for Heterostructure Device Fabrication.* J. Electrochem. Soc., 141(12):3526, 1994.

[39] D. Sanchez, L. Cerutti, and E. Tournié. *Selective lateral etching of InAs/GaSb tunnel junctions for mid-infrared photonics.* Semicond. Sci. Technol., 27(8):085011, August 2012.

[40] J. P. Prineas, M. Reddy, J. T. Olesberg, C. Cao, S. Veerasamy, M. E. Flatte, E. Koerperick, T. F. Boggess, M. R. Santilli, and L. J. Olafsen. *Quaternary GaInAsSb 2.0-2.5 micron back-illuminated focal plane array for blood glucose monitoring.* Proc. SPIE, 5726:113–121, 2005.

[41] R. Chaghi, C. Cervera, H. Aït-Kaci, P. Grech, J. B. Rodriguez, and P. Christol. *Wet etching and chemical polishing of InAs/GaSb superlattice photodiodes.* Semicond. Sci. Technol., 24(6):065010, June 2009.

[42] *Categories of Off-Orientation, Galaxy Compound Semiconductors, http://www.iqep.com/galaxy/products/categories-of-off-orientation/.*

[43] J. G. Buglass, T. D. McLean, and D. G. Parker. *A Controllable Etchant for Fabrication of GaSb Devices.* J. Electrochem. Soc., 133(12):2565–2567, 1986.

[44] W. P. Dumke, J. M. Woodall, and V. L. Rideout. *GaAs-GaAlAs Heterojunction Transistor for high frequency operation.* Solid. State. Electron., 15:1339–1343, 1972.

[45] L. P. R. Srnfinek, S. Nemeth, j. Kovac, S. Kicin, B. Grietens b, G. Borghs, J. Novak, V. Sestakova. *Classification of morphological defects on GaAs / A1AsSb / GaSb structures prepared by MBE.* J. Cryst. Growth, 165(96):156–158, 1996.

[46] M. Kohler. *Etching in Microsystem Technology.* Wiley-VCH, 1 edition, 1999.

[47] H.-y. Chen. *Inductively Coupled Plasma Etching of InP.* Master thesis, University of Toronto, 2000.

[48] J. W. Lee, C. R. Abernathy, S. J. Pearton, C. Constantine, S. R. J., and W. S. Hobson. *Etching of Ga-based III-V semiconductors in inductively coupled Ar and CH$_4$/H$_2$-based plasma chemistries.* Plasma Sources Sci. Technol., 6:499–507, 1997.

[49] F. M. Mohammedy, Z. L. Peng, D. a. Thompson, and M. J. Deen. *RIE of GaSb with an ECR Source Using Methane/Hydrogen Chemistry in an Argon Plasma.* J. Electrochem. Soc., 154(2):H127, 2007.

[50] V. Bhagwat, J. P. Langer, I. Bhat, P. S. Dutta, T. Refaat, and M. N. Abedin. *A Comparison of Dry Plasma and Wet Chemical Etching of GaSb Photodiodes*. J. Electrochem. Soc., 151(5):A728, 2004.

[51] G. M. Peake, R. J. Shul, C. I. H. Ashby, J. G. Cederberg, M. J. Hafich, R. M. Biefeld, and P. M. N. *Inductively coupled plasma reactive ion etching of GaInAsSb and AlGaAsSb for quaternary antimonide multiple interconnected module thermophotovoltaics*. J. Vac. Sci. Technol. B, 21(2):843–847, 2003.

[52] T. Hong, Y. G. Zhang, T. D. Liu, and Y. L. Zheng. *BCl$_3$/Ar ICP Etching of GaSb and Related Materials for Quaternary Antimonide Laser Diodes*. J. Electrochem. Soc., 152(5):G372, 2005.

[53] S. M. Sze and K. K. NG. *Physics of Semiconductor Devices*. John Wiley & Sons, Inc., 3 edition, 2007.

[54] H. Luth. *Solid Surfaces, Interfaces and Thin Films*. Springer, 2010.

[55] B. Tadayon, C. S. Kyono, M. Fatemi, S. Tadayon, and J. A. Mittereder. *Extremely low specific contact resistivities for p-type GaSb, grown by molecular beam epitaxy*. J. Vac. Sci. Technol. B, 13(1):1, January 1995.

[56] A. Vogt, H. Hartnagel, G. Miehe, H. Fuess, and J. Schmitz. *Electrical and microstructure analysis of ohmic contacts to p- and n-type GaSb, grown by molecular beam epitaxy*. J. Vac. Sci. Technol. B, 14(6):3514, November 1996.

[57] E. Villemain, S. Gaillard, M. Rolland, and A. Joullie. *Characterization of ohmic contacts on n- and p- type GaSb*. Mater. Sci. Eng., 20:162–164, 1993.

[58] K. Ikossi, M. Goldenberg, and J. Mittereder. *Metallization options and annealing temperatures for low contact resistance ohmic contacts to n-type GaSb*. Semicond. Sci. Technol., 46:1627–1631, 2002.

[59] Y. K. Su, F. S. Juang, and K. J. Gan. *Ohmic Contacts of AuGeNi and Ag/AuGeNi to n-GaSb with Various Sintering Temperatures*. Jpn. J. Appl. Phys., 30(5):914–916, 1991.

[60] Z. Yang, P. Hao, and L. Wang. *Au/In/Pd/Te/Pd ohmic contact to n-GaSb*. Electron. Lett., 32(25):2348–2349, 1996.

[61] K. Varblianska, K. Tzenev, and T. Kotsinov. *Pd-based ohmic contacts to n-GaSb*. Phys. Status Solidi, 163:387–393, 1997.

[62] A. Vogt, A. Simon, H. Hartnagel, J. Schikora, V. Buschmann, M. Rodewald, H. Fuess, S. Fascko, C. Koerdt, and H. Kurz. *Ohmic contact formation mechanism of the PdGeAu system on n-type GaSb grown by molecular beam epitaxy*. J. Appl. Phys., 83(12):7715–7719, 1998.

[63] J. Sigmund, M. Saglam, A. Vogt, H. Hartnagel, V. Buschmann, T. Wieder, and H. Fuess. *Microstructure analysis of ohmic contacts on MBE grown n-GaSb and investigation of sub-micron contacts*. J. Cryst. Growth, 228:625–629, 2001.

[64] J. A. Robinson and S. E. Mohney. *Characterization of sulfur passivated n-GaSb using transmission electron microscopy and the influence of passivation on ohmic contact resistance*. J. Appl. Phys., 96(5):2684, 2004.

[65] R. K. Huang, C. A. Wang, C. T. C. Harris, M. K. Connors, and D. A. D. Shiau. *Ohmic Contacts to n-Type GaSb and n-Type GaInAsSb*. J. Electron. Mater., 33(11), 2004.

[66] H. H. Berger. *Contact Resistance and Contact Resistivity*. J. Electrochem. Soc., 119(4):507–514, 1972.

[67] G. K. Reeves and H. B. Harrison. *Obtaining the specific contact resistance from Transmission Line Model Measurements*. IEEE Electron Device Lett., EDL-3(5):111–113, 1982.

[68] K. Vizbaras, M. Törpe, S. Arafin, and M.-C. Amann. *Ultra-low resistive GaSb/InAs tunnel junctions*. Semicond. Sci. Technol., 26(7):075021, July 2011.

4

Integration of GaSb-based Photodiodes on SOI Waveguide Circuits for the short-wave infrared

In this chapter, the integration of III-V SWIR photodiodes on an SOI waveguide circuit is discussed. This includes the design of the epitaxy and the optical coupling between the Si waveguide and the III-V photodetector, the fabrication and characterization. The chapter ends with measurement results and discussions on the fabricated devices. The work presented in this chapter was carried out in collaboration with dr. Alban Gassenq who has contributed to the fabrication process for grating assisted photodiodes and to the study of the detector leakage mechanism.

4.1   Introduction

An integrated photodiode is one of the basic components required in an integrated spectroscopic system. The general requirements of such photodiodes are room temperature operation, low noise and high responsivity. Coupling light from a Si waveguide circuit into an integrated photodiode poses an additional challenge. In this chapter, I demonstrate integrated GaSb and InGaAsSb photodiodes on an SOI waveguide circuit. The integrated GaSb photodiode serves as a proof of concept (the first generation) where the design, integration and fabrication process are de-

veloped. The integrated InGaAsSb photodiode is then further developed to operate
in the SWIR. Two different coupling mechanisms, namely, evanescent coupling
(the second generation) and grating assisted coupling (the third generation) from
SOI waveguide into the photodiode are investigated. I also discuss several param-
eters affecting coupling efficiency such as the thickness of the DVS-BCB layer
and the intrinsic InGaAsSb layer. The fabrication process that I have developed
and that is presented here defines an optimum process for the realization of GaSb-
based photodetectors on Si based photonic circuits. The measurement results of
the three generations of photodiodes are also presented here. The devices operate
at room temperature and show good responsivity. These results present an excit-
ing opportunity for high density integrated spectrometers. This chapter ends with
a discussion and outlook on how to improve the device performance.

4.2   Basic Photodiode Characteristics

A semiconductor photodiode is a device, which is used to convert optical power
to electrical current. A typical photodiode consists of a p-i-n junction. If the
photon energy E[eV]=$\frac{1.24}{\lambda}$[μm] [1] is higher than the material band gap in the
intrinsic region, the photon is absorbed by the material. An electron is excited and
jumps from the valence band to the conduction band. This transition generates
charge carriers (electrons and holes), which travel to electrodes under applied bias
voltage, resulting in a photocurrent (I$_p$). Typically (I$_p$) is defined as [1]:

$$I_p = q\frac{collected\ electron - hole\ pairs}{\Delta T} = \eta.q\frac{P_{incident}}{hv} = \eta\frac{\lambda}{1.24}P_{incident}$$

$$(4.1)$$

where q is the electron charge, λ is the wavelength of the incident photon in μm,
h is Planck's constant, v is the frequency of the light, ΔT is the time duration,
P$_{incident}$ is the optical power and η is the quantum efficiency of the photodiode.

4.2.1   Quantum efficiency and responsivity

The quantum efficiency (η) describes the number of generated electron-hole pairs
that eventually contribute to the photocurrent per incident photon. This figure of
merit is very important to quantify both the photodiode material stack as well as
the optical coupling design. It is defined as [1]:

$$\eta = \frac{collected\ electron - hole\ pairs}{incident\ photon} = \frac{I_p}{P_{incident}}\frac{1.24}{\lambda} \qquad (4.2)$$

Alternatively, it is also possible to calculate η from the thickness of the absorbing
layer and absorption coefficient omitting the non-absorbing p and n-doped layers

and when an AR-coating is applied to the surface [1]:

$$\eta = (1 - e^{-\alpha L}) \tag{4.3}$$

where α is the absorption coefficient of the material and L is the absorption length. η also relates to the responsivity ($\Re$), another figure of merit. $\Re$ is defined as the ratio of the generated photocurrent in Ampere (A) and incident optical power in Watt (W) [1]:

$$\Re = \frac{I_p}{P_{incident}}[A/W] \tag{4.4}$$

where I_p is the photo-generated current and $P_{incident}$ is the incident power. Therefore, η can be expressed in terms of $\Re$ as:

$$\eta = \Re\frac{1.24}{\lambda} \tag{4.5}$$

From Equation 4.5, one can see that $\Re$ increases linearly with the wavelength when we assume that η is a constant. For the ideal photodiode, η is equal to 1. Commercial devices [2, 3], using InGaAsSb as an intrinsic layer with top or bottom illumination have η in the range of 0.3 to 0.6, at peak wavelength (1.9 to 2.1μm). These values depend largely on the epitaxy and the light coupling design. A typical $\Re$ for InGaAsSb photodiodes is 0.6-1A/W for basic top illumination [2, 3].

4.2.2 Noise Performance

The noise level of a photodiode is another important figure of merit. Noise refers to random fluctuation of current due to random motion of electrons that pass through the photodiode. The noise current determines the minimal signal level that can be detected by the photodiode [4]. Understanding the noise current helps us to estimate the power budget for a spectroscopic sensing system. The photodiode noise current has two main sources: thermal noise (Johnson-Nyquist noise)(i_j) and shot noise(i_s) [5]. Fig. 4.1 presents the photodetection process indicating the noise sources. The typical optical input consist of background radiation and the input signal. The currents that are generated include the photocurrent (I_p) due to the optical input signal, the current due to background radiation (I_B) and dark current (I_d) which is a leakage current attributed to intrinsic properties of the photodetector material and the fabrication process. Since the generation and the motion of the carriers are random processes, a fluctuation of the generated current is introduced to the total current (I_p+I_B+I_d) as shot noise. The mean square of the shot noise current $<i^2{}_s>$ is given by [5]:

$$< i_s^2 >= 2q(I_d + I_p + I_B)B \tag{4.6}$$
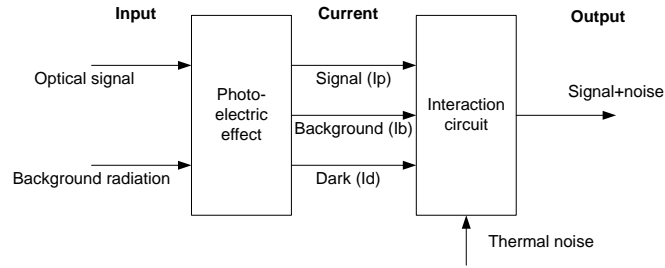
Figure 4.1: Schematic presenting the photodetection process indicating noise sources (reproduced from [6])

where B is the noise bandwidth in Hz. q is electron charge. Johnson noise (i_j) is further added to the output signal as shown in Fig. 4.1. Johnson noise is the result of random motion of electrons due to thermal fluctuation in conductive material. The mean square of Johnson noise $<i_j{}^2>$ is given by [5]:

$$<i_j^2> = \frac{4kTB}{R_{sh}} \tag{4.7}$$

where k is Boltzmann's constant(1.38×10^{-23}J/K), T is the temperature of the photodiode in Kelvin. R_{sh} is shunt resistance in ohm.

Finally, the root mean square (RMS) value of the total noise current($<i_n>$) is a summation of the mean square of thermal and shot noise, as given by [5]:

$$<i_n> = \sqrt{<i_j^2> + <i_s^2>} \tag{4.8}$$

Typically at low bias voltage, i_s is less significant compared to i_j due to a very low I_d (μA range for InGaAsSb). However, i_s becomes dominant at higher bias voltage due to an increase of I_d. At normal operation, i_s is dominant due to an increase in I_p.

The photodiode noise performance can also be expressed as the signal power required to generate a photocurrent I_p such that it is equal to i_n. This figure of merit is called Noise Equivalent Power (NEP) and can be expressed as [5]:

$$NEP = \frac{i_n}{\Re} \left[W/Hz^{1/2} \right] \tag{4.9}$$

For InGaAsSb photodiodes, NEP values are in the range of 10^{-12} W/Hz$^{1/2}$ [7]. However, this value depends on the size of photodiode mesa. Therefore, it is not convenient to use this parameter to compare different photodiodes.

Noise performance of photodiodes can also be expressed in the form of a specific detectivity (D*). The specific detectivity (D*) is inversely proportional to the

NEP and is independent of the photodiode area and the bandwidth. The value of D^* is expressed as [1].

$$D^* = \frac{\sqrt{A_{det}}}{NEP} \left[cmHz^{1/2}/W \right] \tag{4.10}$$

where A_{det} is the photodiode area. Since D^* is independent of the diode area and the bandwidth, it is a useful parameter for comparing different types of photodiodes. Typical values of D^* for InGaAsSb photodiodes are in the range of 10^{10} cmHz$^{1/2}$/W [3, 7, 8]. When considering a photodiode which is limited only by Johnson noise, Equation 4.10 is derived to:

$$D_j^* = \frac{\sqrt{A_{det}R_{sh}}}{4kT} \left[cmHz^{1/2}/W \right] \tag{4.11}$$

where the area-resistance product $A.R_{sh}$ or $R_0.A$ is another useful figure of merit which is used to assess photodiode characteristics including leakage current, electrical properties and noise level, regardless of the size of photodiode mesa. R_0 or R_{sh} (Ω) is measured at zero bias which is typically relatively high for InGaASSb photodiode. Consequently this results in a typical value of $R_0.A = \sim 10\text{-}90\Omega.cm^2$ [8, 9] depending on the operating temperature.

4.3   Design and Simulation

The design of the integrated photodiode is divided into 2 parts: epitaxial design and optical coupling design. In the first part, the epitaxy is designed where lattice-matched semiconductor compounds are selected according to the cut-off wavelength requirement. In the second part, the quantum efficiency (η) of the integrated photodiode is optimized by optimizing the light coupling. To achieve this, different coupling techniques are investigated.

4.3.1   Epitaxy design

In this section, all photodiode epitaxies are grown by molecular beam epitaxy (MBE) at the university of Montpellier 2. A simple GaSb p-i-n epitaxy is chosen for the first generation device. The study focuses on the feasibility of the integration of GaSb photodiodes on an SOI waveguide circuit. The details of the epitaxy are shown in Table 4.1. The structure consists of a 75nm thick InAsSb etch stop layer, a 50nm thick n-doped GaSb n-contact layer, a 150nm thick intrinsic GaSb absorbing layer and a 50nm p-doped GaSb p-contact layer.

For the second generation devices, the intrinsic layer is changed from GaSb to $Ga_{0.79}In_{0.21}As_{0.19}Sb_{0.81}$ to increase the cut-off wavelength from 1.7μm to

Layer	Material	Thickness (nm)	Doping	Refractive index (n_i) [10]	Absorption coefficient (cm^{-1}) at $1.55\mu m$ [10]
p-contact	p-GaSb	50	$1x10^{18}$	4.02	10000
intrinsic	GaSb	150	$1x10^{16}$	4.02	10000
n-contact	n-GaSb	50	$1x10^{18}$	4.02	10000
etch stop layer	InAsSb	75			
substrate	GaSb				

Table 4.1: Epitaxial structure and its optical properties at 1.55μm wavelength for the first generation GaSb p-i-n integrated photodiode

$2.5\mu m$. According to the simulation results in Fig. 4.5 for the evanescent coupling design which will be discussed in the following section, a 500nm thick intrinsic region provides phase matching between the Si waveguide and the photodiode waveguide with a high absorbed power fraction (80%) over a range of DVS-BCB thicknesses. Therefore, a 500nm thick intrinsic layer is selected to obtain optimum coupling efficiency. While the epitaxial structure is designed to obtain optimum results for evanescent coupling, the same epitaxial structure is used for the grating assisted devices. The epitaxial structure for the second and the third generation device is shown in Table 4.2. The epitaxial stack consists of 50nm p-doped ($1.0x10^{18}cm^{-3}$) GaSb and a 50nm p-doped ($1.0x10^{18}cm^{-3}$) $Ga_{0.79}In_{0.21}As_{0.19}Sb_{0.81}$ layer as the p-zone of the p-i-n layer stack. An unintentionally doped 500nm thick $Ga_{0.79}In_{0.21}As_{0.19}Sb_{0.81}$ layer is used for the intrinsic absorbing region which is indicated as the optimum point from the simulation in Fig. 4.5. The n-type region consists of 50nm $Ga_{0.79}In_{0.21}As_{0.19}Sb_{0.81}$ and 50nm $InAs_{0.91}Sb_{0.09}$. Both are doped to $1.0x10^{18}cm^{-3}$. An $InAs_{0.91}Sb_{0.09}$ layer is chosen as n-contact because of its lower bandgap (0.35eV) [11] and hence, low contact resistance ($3.3x10^{-6}$ Ohm.cm^2) [12]. A 100nm cap layer of InAsSb is used which will be removed before the integration process. This is to ensure a clean surface prior to bonding. $InAs_{0.91}Sb_{0.09}$ etch stop layer is used to stop the etchant (chromic based acid, Section 3.3.3.1) from completely etching the epitaxial stack during the substrate removal process. However, the grinding process typically results in a slope across the die due to levelling inaccuracy, leading to inhomogeneous thickness of $InAs_{0.91}Sb_{0.09}$ after wet etching. Hence, GaSb etch stop layer is inserted as a second etch stop layer to restore the flatness of the bonded epitaxy surface.

The energy band diagram is presented in Fig. 4.2. The band diagram is calculated using Silvaco which is based on 2D numerical modelling using the finite element method [13]. The diffusion of minority carriers is prevented on the p-type
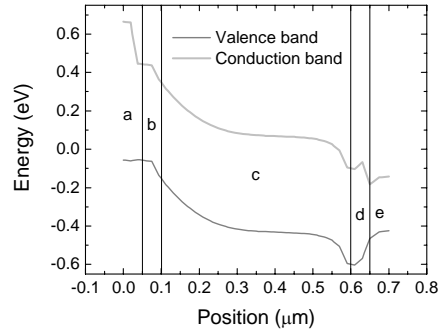
Figure 4.2: Energy band diagram of the integrated photodetector indicating region a) as GaSb p-doped, b) c) d) as p-i-n GaInAsSb respectively and e) as InAsSb n-doped

Layer	Material	Thickness (nm)	Doping (cm^{-3})	Refractive index (n$_i$)	absorption coefficient (cm^{-1}) at 2.2μm
cap layer	InAs$_{0.91}$Sb$_{0.09}$	100		3.85	8000
p-contact	GaSb	50	1x10^{18}	3.93	9
p-doped	Ga$_{0.79}$In$_{0.21}$As$_{0.19}$Sb$_{0.81}$	50	1x10^{18}	3.75	5000
intrinsic	Ga$_{0.79}$In$_{0.21}$As$_{0.19}$Sb$_{0.81}$	500	1x10^{16}	3.75	5000
n-doped	Ga$_{0.79}$In$_{0.21}$As$_{0.19}$Sb$_{0.81}$	50	1x10^{18}	3.75	5000
n-contact	InAs$_{0.91}$Sb$_{0.09}$	50	1x10^{18}	3.85	8000
etch stop layer	GaSb	100		3.9	
etch stop layer	InAs$_{0.91}$Sb$_{0.09}$	100		3.85	
substrate	GaSb				

Table 4.2: Epitaxial structure and its optical properties at 2.2μm wavelength for the second and the third generation integrated p-i-n InGaAsSb photodiode [14]

side by the use of a wide bandgap GaSb layer. The cut-off wavelength of this epitaxial stack is estimated to be 2.5μm.

4.3.2 Optical design

The coupling technique plays a major role in the design of the photodiode structure and coupling efficiency, which eventually determines the sensitivity of the device. Several techniques to couple light from Si waveguides into integrated photodiodes have been reported. These include butt coupling [15], grating assisted coupling [16] and evanescent coupling [17]. A schematic of different coupling approaches
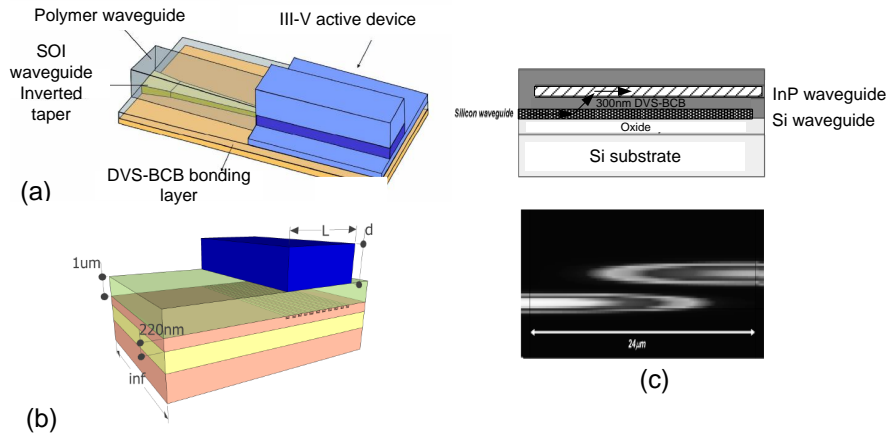
Figure 4.3: Summary of common coupling schemes a) Butt coupling [15] b) Grating assisted coupling [16] c) Evanescent coupling [18]

is depicted in Fig. 4.3. Most of these investigations have been carried out for InP-based devices at telecommunication wavelengths.

Butt coupling is based on an inverted taper which adiabatically transforms the Si waveguide mode to a polymer waveguide mode which is formed on top of the inverted taper and butt coupled to the photodetector as shown in Fig. 4.3a. This coupling technique shows high coupling efficiency and permits wide wavelength operation. However, high accuracy alignment is required for maximum coupling efficiency, which leads to an increase in complexity of fabrication. On the other hand, grating couplers on the Si waveguide layer can be fabricated at the same time as the passive circuits as depicted in Fig. 4.3b, which eases fabrication. It allows an easy way to couple light in and out the chip with high coupling efficiency [19, 20]. Coupling efficiency and polarization can be controlled by design [21]. Despite its fabrication advantages, grating assisted couplers are wavelength and polarization dependent [22]. Each design is limited to a certain bandwidth [22]. This hinders its use in applications where broadband operation is required, such as spectroscopy. Alternatively, evanescent coupling, where light is evanescently coupled from the Si waveguide to the III-V membrane as depicted in Fig. 4.3c, provides good coupling efficiency and broadband operation. However, the design requires a more complex fabrication technique compared to the grating assisted coupler. This is due to the requirement of intimate contact between the photodetector and the waveguide [23]. In this thesis, I have investigated both coupling techniques to a GaSb compound photodiode.

4.3.2.1 Simulation tool

CAMFR [24], which is based on a frequency-domain eigenmode expansion technique, is used for this simulation. This software allows accurate but simplified 2D optical mode calculation and propagation calculation. The TE-polarized fundamental mode is excited in the Si waveguide. The optical mode then propagates along the photodiode slab depending on the coupling scheme. Lateral dimensions and metals are not included in the simulation. The parameters used for this simulation are listed in Table 4.2. The absorbed power is calculated using the following equation [16]:

$$P_{abs} = -2k\sqrt{\frac{\epsilon_0}{\mu_0}} \iint n_r n_i \left| E \right|^2 dA \qquad (4.12)$$

where k=$\frac{2\pi}{\lambda_0}$, n_r and n_i is the real and imaginary part of the absorbing material respectively. $\left| E \right|^2$ is the modulus of the electric field. The double integration is performed over the area of the absorbing region (A).

Another choice of simulation tool is Fimmwave [25]. Fimmwave is a fully vectorial mode solver. The solver allows 2D and 3D propagation modeling which gives more accurate simulation results. Naturally this requires more hardware resources and CPU time. Therefore, in this chapter the simulation results are based on CAMFR only. Fimmwave is used only to visualize the mode propagation.

4.3.2.2 Evanescent coupling

Fig. 4.4a shows a schematic of the overall structure of the integrated photodiode on SOI waveguide. It consists of a semiconductor photodiode bonded on top of a Si waveguide using DVS-BCB as an adhesive bonding layer. Light is coupled from single mode fiber (SMF) to the Si waveguide through a grating coupler. Light is then coupled evanescently from the SOI waveguide into the photodiode membrane, which happens over the shortest length scale when phase matching occurs. With such a design, only a thin epitaxial membrane is required. A high quality thick epitaxy of InGaAsSb ($>$ 100nm) with high stress to cover a wide range of wavelengths in the SWIR is difficult to obtain because the instability of the alloy during epitaxial growth causes the layer to degrade with increasing thickness [26]. Hence, the thin epitaxial membrane would ease epitaxial growth. Moreover, the coupling efficiency depends weakly on wavelength since the coupling mechanism employs phase matching is not strongly wavelength dependent. Fig. 4.4b shows a schematic of the device (not-to-scale) across a section in the YZ plane. The Si waveguide thickness is 220nm. The waveguide is 3μm wide.

The simulation shown in Fig.4.5 is performed using InGaAsSb as intrinsic layer (the second generation device, with epitaxial structure as shown in Table 4.2). Fig. 4.5a represents the fraction of absorbed power in the photodiode depending
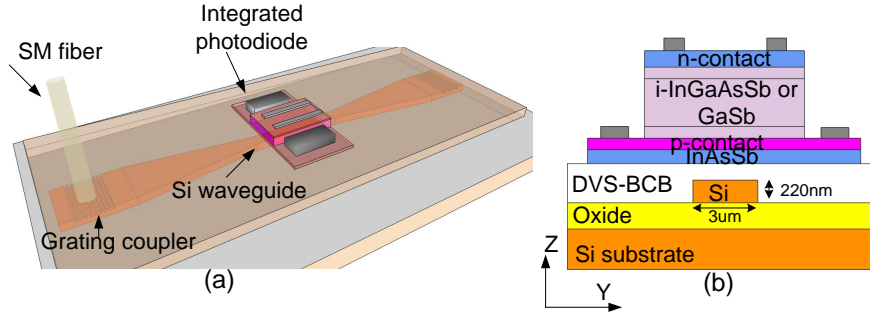
Figure 4.4: a) Structure of the photodiode bonded on a Si waveguide (not-to-scale). Light is coupled into the Si waveguide through a grating coupler b) Cross section of the YZ plane of the integrated photodiode.

on the intrinsic region thickness of the photodiode and the DVS-BCB bonding thickness. The wavelength is set at 2.2μm for this simulation. The oscillation is a result of the phase-matching between Si and III-V waveguide. A 20μm absorption length is used for this simulation. The impact of the intrinsic region thickness and DVS-BCB bonding thickness on the absorbed power fraction also depends on the refractive index of the intrinsic material (n_i).

Fig. 4.5b shows an example of the optical mode propagating through the Si and the photodiode. Due to the phase matching between the photodiode and the Si waveguide, the optical field couples between the waveguides and is absorbed along the detector length. This simulation is carried out using Fimmwave [25]. Simulation results indicate that this approach allows high $\Re$ using a thin absorbing layer with long absorption length.

In the first generation device (GaSb photodiode), a 150nm thick intrinsic GaSb layer is used. The thickness of the DVS-BCB bonding layer is 265nm. For the second generation device (InGaAsSb photodiode), a 500nm thick intrinsic region is selected according to the simulation in Fig. 4.5a. The DVS-BCB thickness is 258nm.

4.3.2.3 Grating assisted coupling

Another technique to couple light from a Si waveguide into a photodiode is via a grating coupler. Similar to the conventional top illumination photodiode, this approach allows a relaxed control of the DVS-BCB thickness thereby simplifying the bonding process. Fig. 4.6a presents the overall structure of the device. The photodiode is bonded on top of the grating coupler. As a result, light from the Si waveguide is diffracted and coupled to the photodiode directly via the grating
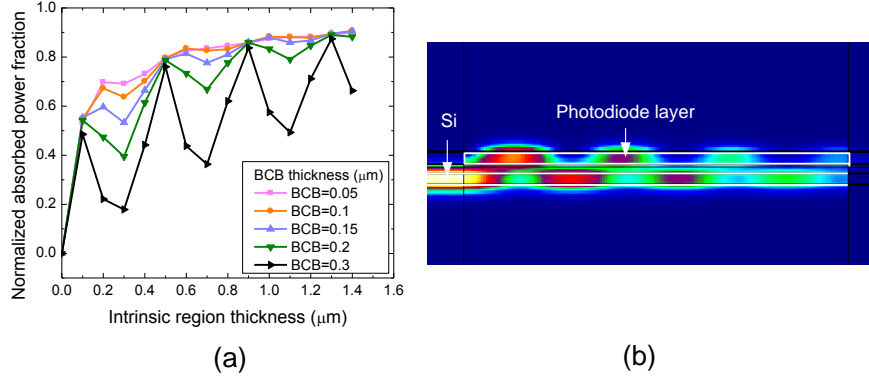
Figure 4.5: a) Simulation of absorbed power fraction as a function of InGaAsSb intrinsic region and DVS-BCB thickness at 2.2µm wavelength b) Example of the fundamental TE-polarized optical mode propagation along the waveguide structure
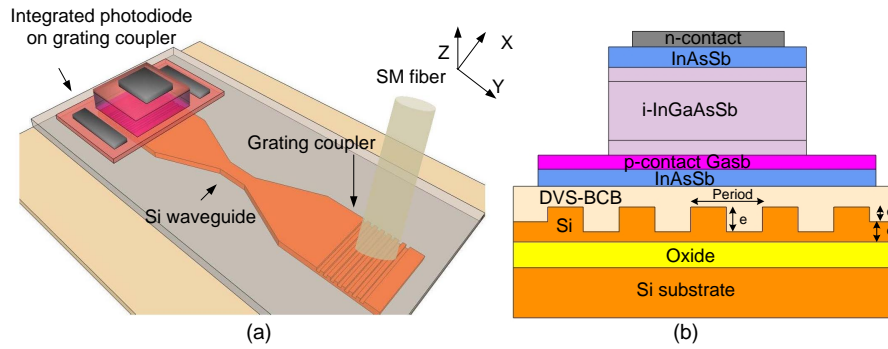
Figure 4.6: a) Schematic of photodiode bonded on a Si grating coupler (not-to-scale) b) Cross section in the YZ plane of the integrated photodiode.

coupler. Fig. 4.6b shows a cross section schematic in the YZ plane illustrating important parameters for the grating design. For this demonstration, a standard grating coupler is selected such that it is compatible with fabrication in the ePIXfab multi-project wafer scheme [27]. The detailed analysis of this type of grating coupler and experimental results can be found in Section 2.3.

The absorbed power fraction as a function of intrinsic layer and DVS-BCB thickness is shown in Fig. 4.7a. In this simulation, the following grating parameters are used: period=1.3µm, d=0.15µm, e=0.15µm and o=0µm with 20 periods at 2.2µm wavelength. An example of the optical field profile of the device is plotted in Fig. 4.7b, with a DVS-BCB thickness of 200nm. Similar to the evanescent coupling approach, the absorption is strongly dependent on the thicknesses of the
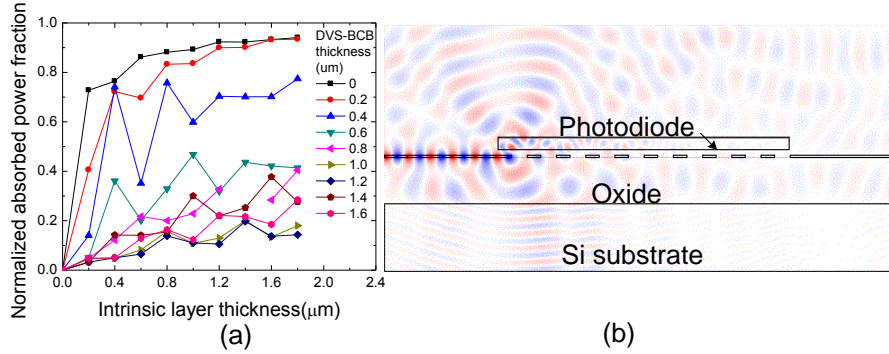
Figure 4.7: a) Absorbed power fraction as a function of intrinsic layer and DVS-BCB thickness b) An example of the field plot of the simulated device

InGaAsSb intrinsic layer and the DVS-BCB layer. With an intrinsic InGaAsSb layer >0.8 μm and a very thin DVS-BCB layer (<400nm), an absorbed power fraction of > ~90% is achieved because of the combination of evanescent and grating assisted coupling. However, for thicker DVS-BCB layers (>400nm), the fraction of absorbed power is relatively low (~40%) even with a thick intrinsic layer (1.6μm). This is because now only diffraction plays a role in the coupling between Si and III-V. The diffraction efficiency largely depends on the directivity of the grating coupler. By optimizing the grating assisted coupler, including an anti-reflective layer at the interface of III-V and DVS-BCB, it is possible to achieve a high efficiency integrated photodiode [28]

Fig. 4.8 presents the absorbed power fraction as a function of photodiode length (Grating period is 1.05μm. Fill factor is 0.5.). This indicates that the optimum length of the photodiode can be as low as 10μm. The result implies the potential use of this grating coupler in a compact integrated photonic circuit.

Fig. 4.9 shows a comparison of the evanescent (with 20μm absorption length) and grating assisted coupling (with 36μm absorption length) approach using the epitaxy stack described in Table 4.2 with 500nm intrinsic layer thickness and an optimized grating assisted coupler. The optimized grating coupler is designed so that the coupling efficiency of the grating coupler to the thin film photodiode is maximized. This results in grating parameters of period=0.95μm, d=0.21μm and e=o=0.312μm with 12 periods, and adding an anti-reflection coating between the III-V structure and the DVS-BCB layer (thickness=0.227μm, n=2.42 for TiO$_2$). The results show that in all designs, maximum coupling efficiency is achieved with a very thin (<0.3μm) bonding layer. The efficiency of both evanescent and grating assisted coupling decreases significantly with an increase in bonding layer thickness. With a thick (>0.6μm) bonding layer, while evanescent coupling is
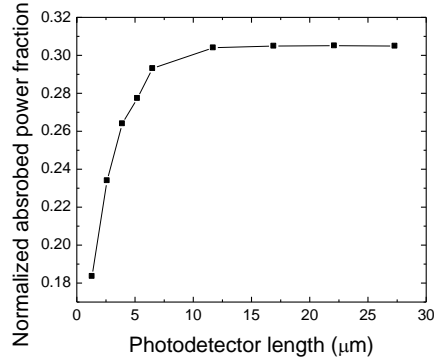
Figure 4.8: The absorbed power fraction as a function of photodiode length
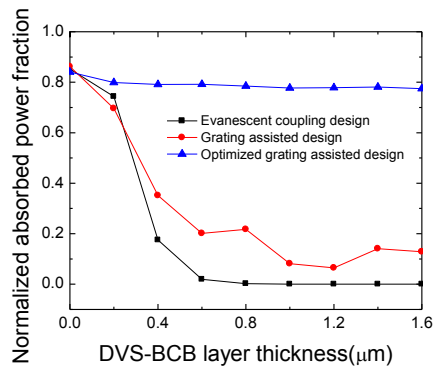
Figure 4.9: A comparison of absorbed power fraction as a function of DVS-BCB layer thickness between 3 different designs: evanescent coupling, grating assisted coupling and optimized grating assisted coupling

no longer feasible, both grating assisted designs are still feasible. This leads to an easier integration process and therefore, higher fabrication yield in view of the realization of large detector arrays on integrated SOI spectrometers. For standard grating couplers, the fraction of absorbed power is limited by the directivity of the grating coupler. In contrast, the optimized grating assisted design provides nearly 90% directivity. However, it requires a relatively thick intrinsic layer to maintain the efficiency of the integrated photodiode at 80%. Although a high efficiency device is achievable with this optimized design, increasing the thickness of the intrinsic region poses difficulties in epitaxy growth [29]. Optimized grating structures also result in a complex Si waveguide fabrication process [20].

4.4   Integration and Fabrication Technology

In Chapter 3, I discussed the integration technology used in this thesis. Details of each fabrication process step including chemical recipes are also presented. In this section the specific integration and fabrication processes, optimized for each photodiode generation, are described. The processing steps are also discussed.

4.4.1   Heterogeneous integration of III-V and SOI

The SOI chip and epitaxial die are first cleaned using acetone and isopropanol. The sample is then dried on a hot plate at $150°$C for 5 minutes. The DVS-BCB is spin coated on the SOI chip. The spinning speed and time is selected according to the required DVS-BCB thicknesses (Fig. 3.6). The epitaxial die is then transferred to the SOI chip manually at $150°$C on a hotplate in air. The sample is baked at $250°$C for 1hr in nitrogen environment to avoid oxidation of the DVS-BCB. The details of the bonding process can be found in Section 3.2.4.1. After the bonding process, the side wall of the epitaxial die is protected using CrystalBond glue [30] to prevent lateral etching during the wet etching process before mechanical grinding. Grinding is performed on a glass plate using a Lapmaster. 12.5μm diameter Aluminium oxide powder is mixed with water and used as abrasive. The GaSb substrate is grinded down to 50-100μm thickness. Wet etching (Chromic acid based solution, CrO_3:HF:H_2O (1:1:3 v/v), Section 3.3.3.1) is then used to remove the rest of the substrate. The details about substrate removal can be found in Section 3.3.2. InAs$_{0.91}$Sb$_{0.09}$ etch stop layer is removed using Citric based acid ($C_6H_8O_7$:H_2O_2 (2:1 v/v), Section 3.3.3.2). Subsequently, GaSb etch stop layer is removed using NaK Tartrate based acid (NaK tartrate:H_2O:HCl:H_2O_2 (5g:70:60:5 v/v), Section 3.3.3.4).

The same integration process is employed for all photodiode generations illustrating the flexibility of the process (different DVS-BCB thickness and III-V structure). In the next section, the fabrication process selected for each of the photodiode generations is described. The generic fabrication process is presented in Fig. 4.10.

4.4.2   GaSb p-i-n photodiode integrated on SOI waveguide

After the bonding process, which leaves the epitaxy attached upside down to the silicon waveguide circuit, AuGe(150nm)Ni(50nm)Au(100nm) is deposited on the n-doped GaSb layer to form an n-contact. The photodiode mesa is then formed using ICP-RIE using a CH_4 and H_2 gas mixture (Section 3.3.4.1). After mesa formation, Ti(10nm)/Au(100nm) is deposited on the p-doped GaSb as a p-contact. The photodiodes are then isolated by using wet etching in a NaK tartrate based
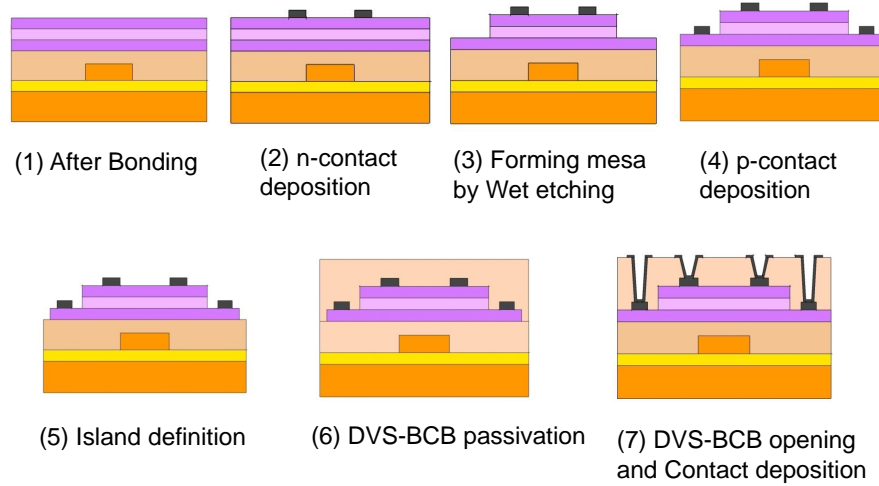
Figure 4.10: The fabrication process flow for integrated GaSb-based photodiodes

solution (Section 3.3.3.4). DVS-BCB is used for device passivation to reduce photodetector dark current. A top view image of the device from an optical microscope is shown in Fig. 4.11a. The total footprint of the device is $\sim$37x50μm^2.

Fig. 4.11b shows a cross section image of the realized device. The bonding thickness of the device is $\sim$265nm. The Si waveguide seen in this image is located adjacent to the one actually used for light coupling.

4.4.3 InGaAsSb p-i-n photodiode integrated on SOI waveguide

To process InGaAsSb p-i-n photodiodes with evanescent coupling, the mesa etching was optimized by changing from a complete dry etching to a combination of dry and wet etching to minimize mesa side wall damage, resulting in a lower dark current. The dry etch rate is well controlled so as to be able to stop when reaching the n-contact layer. This technique allows a good control of mesa etching due to the different etch rate of InGaAsSb and GaSb during dry etching (Section 3.3.4.1). The mesa is first etched 300nm using a phosphoric acid based solution (Citric acid:H_2O_2:H_3PO_4:H_2O (55:5:3:220 v/v), Section 3.3.3.3). This is followed by dry etching using a CH_4 and H_2 gas mixture (Section 3.3.4.1). Fig. 4.12b shows a SEM image of the cross section of the realized evanescent InGaAsSb photodiode. Ti/Pt/Au (2/35/100nm) is used as the hard mask. A bonding thickness of 258nm is achieved.

The original process scheme included the removal of the InAsSb cap layer using a citric acid based solution ($C_6H_8O_7$:H_2O_2 (2:1 v/v), Section 3.3.3.2) to obtain
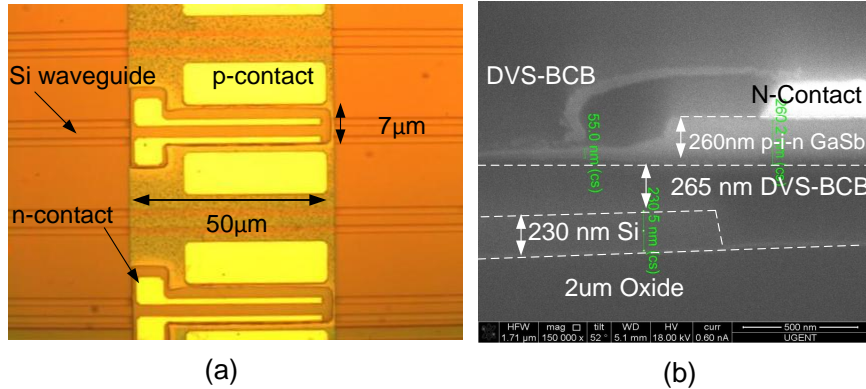
Figure 4.11: a) Optical image of the integrated GaSb photodiode b) SEM cross section of the device (note that the Si waveguide seen in the figure is the Si waveguide located next to the one used for light coupling)
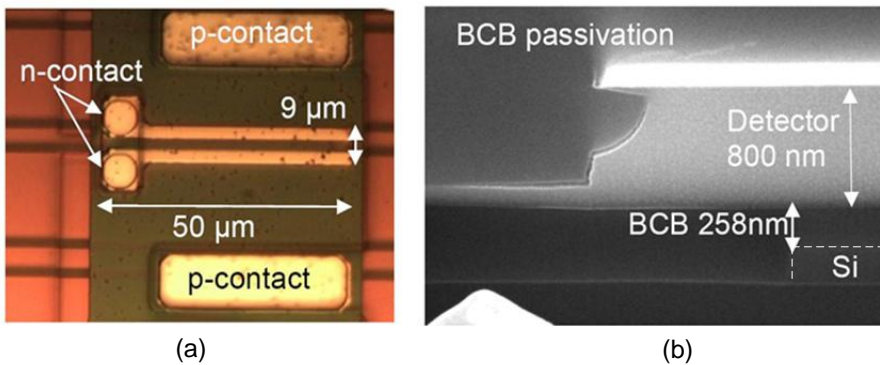
Figure 4.12: a) Optical image of the InGaAsSb evanescent coupling device with a foot print of $72x50\mu m^2$ b) SEM image of the cross section of the realized device

a clean surface before the integration process. However, this creates a hydrophilic surface as the contact angle with water decreases from 68° to 37° as listed in Table 3.1. This prevented good bonding with DVS-BCB. Therefore, the InAsSb cap layer is kept in this experiment. The mesa is $9\mu m$ wide and $50\mu m$ long. The optical image of the realized device is shown in Fig. 4.12a. The contacts were optimized for this experiment (Section 3.3.5). Ti(2nm)/Pt(35nm)/Au(100nm) is used for both n and p contacts.

For the integrated InGaAsSb p-i-n photodiode on grating coupler, the process is further optimized by using full wet etching. This provides a very small sidewall damage. The etching solution is a phosphoric acid based solution (Section

(a)   (b)
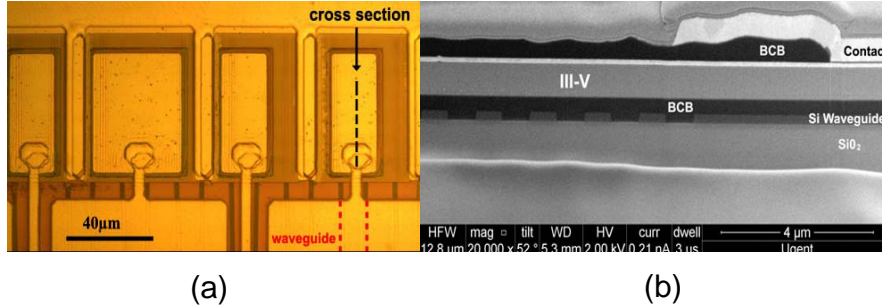
Figure 4.13: a) Optical image of the integrated InGaAsSb p-i-n photodiode on a grating coupler b) SEM image of the cross section of the device

3.3.3.3). The solution has very limited selectivity between InGaAsSb and GaSb (2:1, see Table 3.4). Therefore, precise timing is necessary to stop at the p-doped contact layer. An optical image of the realized device is shown in Fig. 4.13a. The photodiode mesa is 50μm long and 20μm wide which corresponds to the grating coupler size. A SEM image of the cross section of the realized device is shown in Fig. 4.13b.

4.5   Measurement results

Characterization is carried out using a standard single mode fiber (SMF-28) which is mounted on a translation stage for aligning purposes. The photoresponse of the device is measured by coupling light into the SOI waveguide using a diffractive grating coupler. The fiber is tilted 10°. An optical spectrum analyzer (Yokogawa AQ6375) is used to measure the input power before injecting the light into the photodiode. A continuous wave mid-infrared tunable laser (IPG Cr:ZnSe tunable laser) is used as a light source for the 2-2.5μm wavelength range. A tunable laser (Agilent 81980A) is used as a light source for 1.55μm wavelength. Needle-probes are connected to a voltage/current source and meter (2400 sourcemeter from Keithley) which is used to apply a voltage to the photodiode and measure current from photodiode. A thermo-electric cooling stage is used for controlling temperature. A reference waveguide fabricated in the same fabrication batch is used to normalize the photoresponse to the optical power propagating through the waveguide. Fig. 4.14 shows the measurement setup for the photodiode characterization.

4.5.1   GaSb p-i-n photodiode (Generation 1)

The measurement is carried out at 1.57μm wavelength at room temperature. No characterization close to the bandgap wavelength could be carried out due to a lack
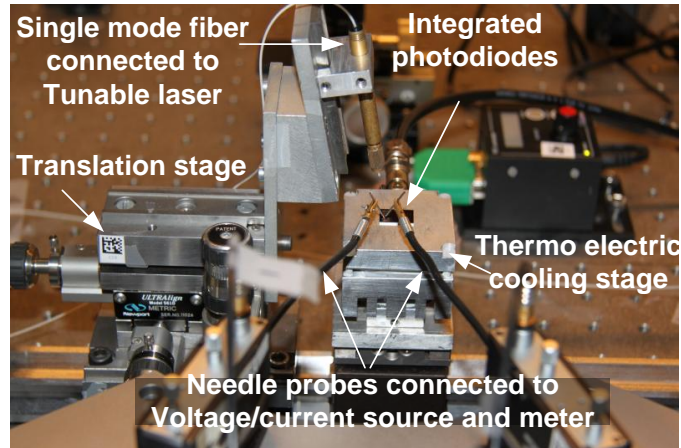
Figure 4.14: Measurement setup for photodiode characterization

of a laser source at 1.7μm at the time of the experiment. The I-V characteristic of the device is shown in Fig. 4.15, for various optical power levels without taking the large fiber-chip coupling loss into account. A grating coupling efficiency of 10% is assumed here [22]. The high leakage current is likely caused by ICP etching, which causes significant damages to the mesa sidewall as will be discussed in Section 4.6. Nevertheless, the device shows good photoresponse (∼0.14A/W) at -1V.
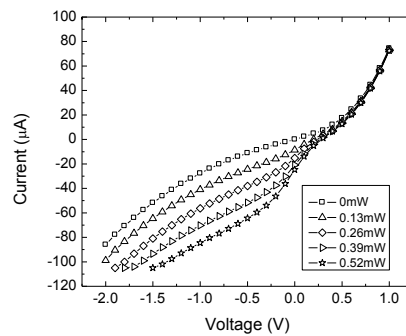
Figure 4.15: The photoresponse of the integrated GaSb photodiode at different on-chip input powers
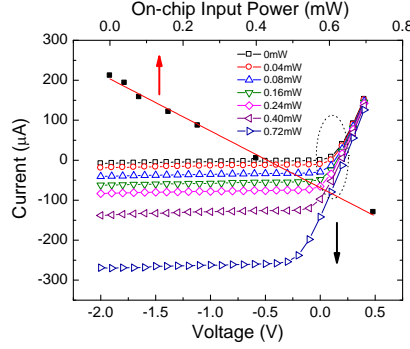
Figure 4.16: I-V characteristics at different on-chip input power levels measured at 2.25μm wavelength. (■)Photocurrent measured at -0.1V with different input powers showing good linearity

4.5.2 InGaAsSb p-i-n photodiode

4.5.2.1 Evanescent coupling photodiode (Generation 2)

For the InGaAsSb p-i-n photodiode, the characterization is performed at a wavelength of 2.27μm. The gratings have approximately -9 dB peak coupling efficiency at 2.27μm with 200nm 3dB-bandwidth, as shown in Section 2.3. The distance between the grating coupler and the device is designed to be only 400μm. Typically, the loss in the Si waveguide is 0.6dB/cm [20]. Therefore, the loss due to the propagation in the waveguide can be neglected. The reference signal before injecting into chip is measured using the Yokogawa AQ6375 optical spectrum analyzer.

The photoresponse measured at 2.25μm wavelength at different input power levels is shown in Fig. 4.16. The photocurrent increases linearly as a function of input power over a 12dB input power range as shown in Fig. 4.16.

In this measurement, a system $\Re$ (i.e. the ratio of input power at the fiber and the measured current I_p) of 0.06A/W at 2.29μm is obtained. Therefore, a maximum intrinsic $\Re$ (i.e. the ratio of the on-chip input power and the measured current I_p) of 0.44 A/W is deduced resulting in 24% quantum efficiency. An average value of $\Re$ of 0.33A/W is obtained. This low $\Re$ comparing to simulation ($\Re$ = 1.45A/W, where the simulated η=0.8 is obtained from Fig. 4.5a) is attributed to a misalignment between the Si waveguide and the photodiode waveguide during the first processing run [31].

In the second processing run, the fabrication process is further improved. A $\Re$ of 1.4A/W is obtained at 2.3μm, measured at room temperature. The system $\Re$ as a function of wavelength is plotted in Fig. 4.17a. The intrinsic $\Re$, which is deduced corresponding to the grating coupler efficiency plotted in Fig. 4.17b, is plotted
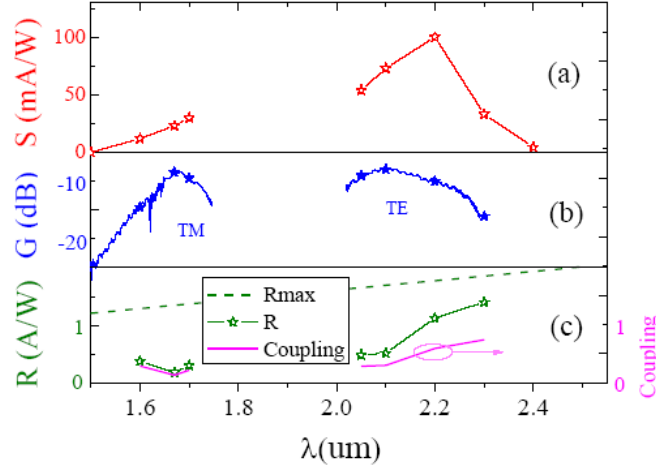
Figure 4.17: a) System responsivity (S=I_p/P_{fiber} b) Grating coupler efficiency c) deduced intrinsic photodiode responsivity and minimum coupling efficiency as a function of wavelength

in Fig. 4.17c. The intrinsic maximum value $\Re_{max}$ = q/hv and the corresponding minimum waveguide to detector coupling efficiency are depicted in Fig. 4.17c. As can be seen, the grating coupler supports both TM-polarization at $\sim 1.6\mu$m and TE-polarization at $\sim 2.2\mu$m. The responsivity is only 0.3A/W at $\sim 1.6\mu$m because of the limited responsivity of this grating coupler at shorter wavelength. Nevertheless, these results show the possibility of utilizing this system as a broadband integrated circuit operating from 1.6 to 2.4μm using InGaAsSb as an intrinsic absorbing layer.

The sensitivity of the photodiode is limited by the dark current I_d. I_d is measured at 1.13μA at room temperature using -0.1V bias. This corresponds to a dark current density J_d of 251mA/cm^2 using a photodiode mesa size of (9x50μm^2). This is relatively high (around 20 times higher) compared to literature [32, 33]. This high I_d is attributed to high sidewall leakage current. To confirm that sidewall leakage is the limiting factor, the R_0.A product is measured at room temperature. R_0 is obtained from the I-V characteristics at zero bias voltage. A is the area of the photodiode. I obtain R_0.A values ranging from 1.6 to 0.53Ω.cm^2 for the devices with an area of 180x180 and 60x60μm^2 respectively. In the second processing run, a R_0.A value of 0.1Ω.cm^2 is obtained for a photodiode mesa of 10x60μm^2. It shows a strong dependence of R_0.A on the detector area, suggesting that side wall leakage is the limiting factor. Typical values for R_0.A from literature are $\sim$10-90Ω.cm^2 depending on operating temperature [9]. The characteristics of the photodiode at low temperature is assessed and presented in Fig. 4.18a. Dark cur-
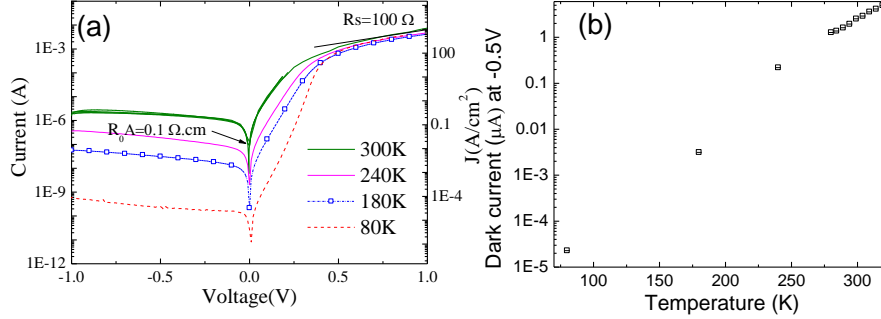
Figure 4.18: a) I-V characteristic at different temperatures b) Dark current at -0.5V at different temperatures
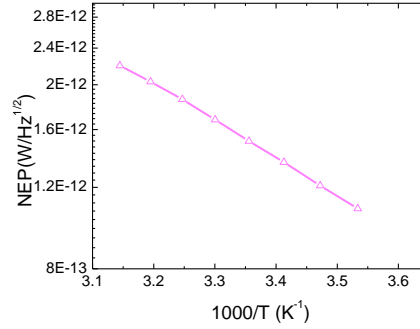
Figure 4.19: Johnson noise limited NEP as a function of temperature

rent density (J_d) is reduced significantly down to $60\mu A/cm^2$ at 80K. As seen in Fig. 4.18b, I_d at -0.5V increases exponentially as a function of temperature. This result agrees well with the work of Prineas et al. where the leakage current is strongly dependent on the temperature and becomes dominant at high temperature [8]. The detailed study on the leakage current can be found in Section 4.6.

The Johnson noise limited NEP at 0V bias is calculated as a function of the temperature and plotted in Fig.4.19b. It decreases gradually due to the increase of shunt resistance R_{sh} (Fig. 4.19) when the temperature decreases. From Fig.4.19, the Johnson-noise limited NEP is calculated to be $1.51 \times 10^{-12} W/Hz^{1/2}$ at 25°C using a $\Re$ of 0.44 A/W. This represents a Johnson noise limited detectivity D* of $1.63 \times 10^9 cmHz^{1/2}/W$. An $R_0.A$ of 0.25 $\Omega.cm^2$ is measured on these devices.

In conclusion, the integrated device operates at room temperature with good intrinsic $\Re$ (0.44A/W) which is improved further to 1.4A/W with better alignment of the Si and photodiode waveguides during the fabrication process. The noise performance of this device is not as good as the previous reports on stand-alone,
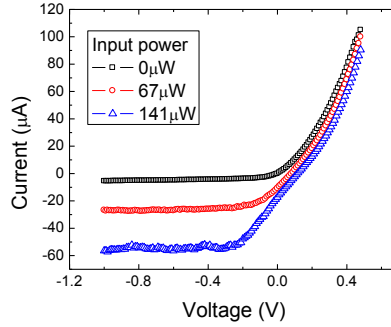
Figure 4.20: Photoresponse at different input power levels of the integrated photodiodes on grating couplers

non-integrated devices [8, 9]. However, process optimization can alleviate this performance degradation. This is further discussed in Section 4.6.

4.5.2.2   Grating-assisted coupling photodiode (Generation 3)

Given the advantages of grating-based photodetectors, both in terms of a more tolerant integration process and its potentially smaller footprint, the first demonstration of a grating-assisted photodiode at 2.2μm wavelength using a grating coupler as a coupling element between the waveguide and the photodiode is presented in this section. The photodiode mesa is 50μm long and 20μm wide in order to cover the grating coupler area used in this experiment. However, the device footprint can be substantially reduced, as illustrated in Fig. 4.8, down to a length $\sim 10\mu$m. Fig. 4.20 shows the photoresponse of the integrated photodiode at different on-chip input powers. The photodiode has a dark current of -4μA at -1V corresponding to a dark current density of 0.4A/cm^2 at room temperature. The system responsivity is 25mA/W. Given the measured input grating coupler efficiency of -12dB at 2.2μm, an intrinsic $\Re$ of about 0.3A/W is deduced. This value is lower than the evanescently coupled device due to the thin intrinsic absorption region, which is not sufficiently thick for surface illuminating operation. However, this design can operate with thicker DVS-BCB as illustrated in Fig. 4.9. This would lead to a more relaxed fabrication process, thereby improving fabrication yield.

4.6   Leakage current study

The surface leakage current is one of the most important parameters defining photodetector performance. High surface leakage contributes to an increase in I$_d$,

thereby generating high shot noise, as defined in Equation 4.6. This limits the sensitivity of the photodiode. The source of surface leakage is largely attributed to the presence of surface states [8]. The surface states are interfacial traps, which are created by the attachment of contamination or byproducts to dangling bonds [5]. When a large number of surface states exist between the band gap, the Fermi level gets pinned [5]. This leads to several effects such as trap assisted tunneling dark current contributing to the excess leakage current [34]. The leakage current depends largely on the quality of the side wall profile and damage [34]. By wet etching, the side-wall damage is reduced. However, the undercut and concave shape of the etched mesa arises as a problem. This can be alleviated by using dry etching, as discussed in Section 3.3.4. Nevertheless, dry etching creates different problems which increase side-wall roughness/damage significantly [35]. Passivation is as important as the etching mechanism. By applying the right passivation, the surface state density can be reduced [36, 37], thereby reducing the leakage current. The total dark current density J_{total} is given by:

$$J_{total} = J_{bulk} + J_{leakage} \frac{P}{A} \tag{4.13}$$

where J_{bulk} is the intrinsic current density through the bulk material. $J_{leakage}$ is the surface leakage current density. P is the perimeter of the diode and A is the area of the diode.

Fig. 4.21 presents J_d at -1V at room temperature as a function of perimeter to surface ratio (P/A) of the photodiode mesa. Two fabrication processes with the same bonded epitaxial stack are compared. On the left side of the graph, the results of the first process with different mesa sizes with and without DVS-BCB passivation are shown. The results show that DVS-BCB passivation clearly improves the side-wall surface termination, thereby reducing dark current. On the right side of the graph, the J_d of the integrated photodiodes with DVS-BCB passivation are plotted, giving an agreement with results of the first fabrication run. By fitting the graph, there is a clear indication that dark current is dominated by the surface leakage current. While the leakage current related to intrinsic material properties is found to be 10mA/cm^2, the rest is attributed to the side wall leakage. Side wall passivation and mesa shape therefore require further optimization in order to enhance photodiode sensitivity.

Table 4.3 shows the summary of the passivation materials in literature. The most common technique is based on the use of ammonium sulfide as a passivation material. However, ammonium sulfide does not seem to provide reproducibility and long term stability. CdS shows a promising result with an order of magnitude reduction in dark current and long term stability (3 months) [38, 39]. Mohammedy et al. [40] reviews the use of SiN_x, SiO_2 and polyimide. The results show that SiN_x yields good results. However, SiN_x is undesirable since the high temperature processing required results in desorption of sulfur from the surface leading to
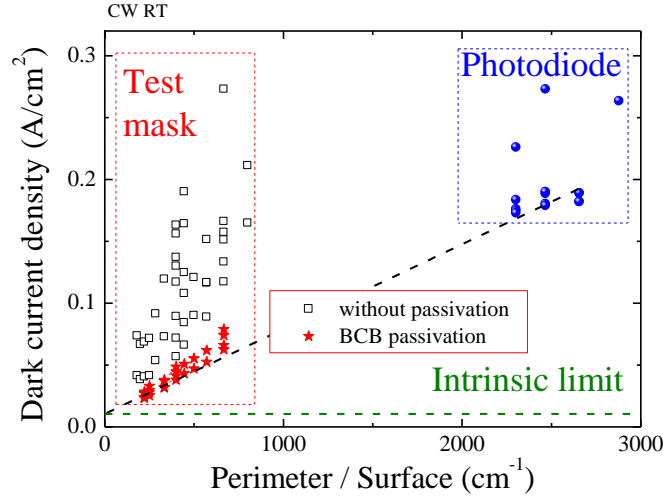
Figure 4.21: Dark current density (A/cm^2) at -0.1V as a function of perimeter to surface area ratio(cm^{-1}) of the bonded device structures

degradation over time. Polyimide improves the suppression of the surface leakage due to less charge accumulation at the side wall [41]. SiO$_2$ passivation may contain fixed charges, resulting in charge accumulation at the surface. This typically results in marginally worse performance than unpassivated device [40, 41]. SU-8 is reported as a good passivation material with 4 orders of magnitude lower dark current density than that of unpassivated devices [42]. NaClO is reported as a smooth side wall etchant after mesa etching process. This reduces the dark current [43].

Alternatively, epitaxial overgrowth of wide band gap materials such as AlGaAsSb has been demonstrated as an ideal passivation technique [44]. This involves adjusting Fermi level and depletion region at the interface, resulting in reduction of the surface tunnelling current. The result yields a complete suppression of the surface leakage current. However, this technique is not applicable for our approach as it is not desirable to load the sample back to MBE chamber after the bonding process.

4.7   Summary and outlook

In this chapter, I have presented the results on InGaAsSb photodiodes integrated on an SOI waveguide circuit. Three generations of integrated devices are discussed. This includes integrated GaSb p-i-n photodiodes with evanescent coupling, integrated InGaAsSb p-i-n photodiodes with evanescent coupling and integrated In-

Passivation material	Material	R_0A (ohm.cm^2)	Dark Current Density (J_d A/cm^2)
Alkali (NH$_4$)$_2$S (Ph=11) [32]	InGaAsSb	-	490 μA/cm^2
Neutralized (NH$_4$)$_2$S (Ph=7) [32]	InGaAsSb	-	87 μA/cm^2
(NH$_4$)$_2$S, ph =9.5, Polyimide [45]	InGaAsSb	36$\pm$6	-
CdS [38, 39]	GaSb	50	-
Silicon Nitride [40]	GaInAsSb	123$\pm$25	-
NaClO [43]	InAs/GaSb	4.7x10^5 at 77K	-
SU-8 [42]	InAs/GaSb	-	0.5 μA/cm^2 at 77K
Na$_2$S/SiO$_2$ [40]	GaInAsSb	2.8x10^{-2} at 77K	-
SiO$_2$ [40]	GaInAsSb	16	-
(NH$_4$)$_2$S [46]	GaSb	-	improvement observed
Overgrowth [44]	GaInSb/InAs	Reaching bulk limit	-

Table 4.3: Summary of passivation material in literature

GaAsSb p-i-n photodiodes with grating assisted coupling. The devices perform with good responsivity (0.13A/W [47], 0.44-1.4A/W [23, 31], 0.3A/W [31] for the 3 generations, respectively) at room temperature. The InGaAsSb p-i-n photodiodes exhibit good noise performance (D* =1.63x10^{9}cmHz$^{1/2}$/W). Moreover, the leakage current study indicates that the side-wall leakage current limits the overall device performance. This can be improved further in fabrication processes, including different etching recipes and passivation materials such as ammonia sulfide to lower the dark current [38, 46].

Table 4.4 represents a comparison of the devices fabricated in this thesis with state-of-the-art commercial photodiodes on GaSb and on competitor material (strained InGaAs). Fig. 4.22 presents a comparison of NEP of the photodiodes as a function of device area. For the same material (InGaAsSb), it is clearly shown that the device fabricated in this thesis performs well compared to the state of the art in terms of $\Re$. However, D* is an order of magnitude lower. As discussed above, this can be improved. When comparing our device with strained InGaAs, the latter performs better due to advantages of the fabrication process of InP based compounds. However, InGaAs is reaching its limit due to strain mismatch [11]while InGaAsSb has the potential to extend its operating wavelength up to 4.9μm [29]. Therefore, for long wavelengths in the mid-wave infrared, the InGaAsSb photodiode is a very promising alternative and holds exciting technological opportunities.
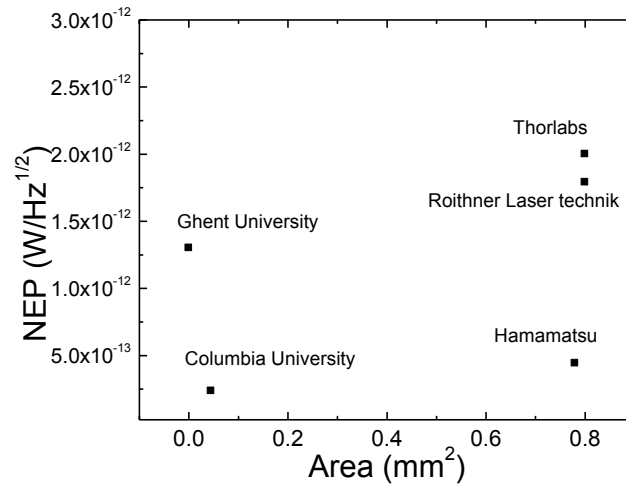
Figure 4.22: A comparison of NEP of the device fabricated in this thesis, by Columbia University and state-of the art commercial photodetectors as a function of device area.

Institute/Company	Material	$\Re$(A/W)	D^* (cmHz$^{1/2}$/W)	NEP (W/Hz$^{1/2}$)	cut-off wavelength (μm)	Area (mm^2)	$I_d(\mu A)$
Columbia University [9]	InGaAsSb	1.18	9×10^{10}	2.36×10^{-13}	2.57	0.045	1.8
Ghent University [23] [31]	InGaAsSb	1	1.63×10^{9}	1.51×10^{-12}	2.4	45×10^{-5}	2-4
Roithner Lasertechnik [3]	InGaAsSb	1	5×10^{10}	1.8×10^{-12}	2.4	0.8	not specified
Nanoplus [2]	InGaAsSb	0.6	not specified	not specified	2.6	0.78-7	1000
Thorlabs [48]	Strained InGaAs	1.1	not specified	2.0×10^{-12}	2.6	0.8	not specified
Hamamatsu [49]	Strained InGaAs	1.3	2×10^{11}	4.4×10^{-13}	2.6	0.78-7	3-10

Table 4.4: Comparison of state-of-the-art and the device fabricated in this thesis

References

[1] F. Trager. *Handbook of lasers and optics*. Springer Science+Business Media, 1 edition, 2007.

[2] *Welcome to Nanoplus*, *http://www.nanoplus.com/*.

[3] *Roithner Lasertechnik*, *http://www.roithner-laser.com/*.

[4] R. F. Potter and W. L. Eisenman. *Infrared Photodetectors : A Review of Operational Detectors*. Appl. Opt., 1(5):567–574, 1962.

[5] S. M. Sze and K. K. NG. *Physics of Semiconductor Devices*. John Wiley & Sons, Inc., 3 edition, 2007.

[6] M. Fukuda. *Optical Semiconductor Devices*. Wiley, 1999.

[7] A. P. Astakhova, B. E. Zhurtanov, A. N. Imenkov, M. P. Mikhailova, M. A. Sipovskaya, N. D. Stoyanov, and Y. P. Yakovlev. *Long-wavelength photodiodes based on n-GaSb/n-GaInAsSb/p-AlGaAsSb heterostructures*. Tech. Phys. Lett., 33(1):11–13, January 2007.

[8] J. P. Prineas, J. Yager, S. Seyedmohamadi, and J. T. Olesberg. *Leakage mechanisms and potential performance of molecular-beam epitaxially grown GaInAsSb 2.4 µm photodiode detectors*. J. Appl. Phys., 103:104511, 2008.

[9] H. Shao, a. Torfi, W. Li, D. Moscicka, and W. Wang. *High detectivity AlGaAsSb/InGaAsSb photodetectors grown by molecular beam epitaxy with cutoff wavelength up to 2.6µm*. J. Cryst. Growth, 311(7):1893–1896, March 2009.

[10] M. Munuz, K. Wei, F. H. Pollak, J. L. Freeouf, and G. W. Charache. *Spectral ellipsometry of GaSb: Experiment and modeling*. Phys. Rev. B, 60(11):8105–8110, 1999.

[11] I. Vurgaftman, J. R. Meyer, and L. R. Ram-Mohan. *Band parameters for III-V compound semiconductors and their alloys*. J. Appl. Phys., 89(11):5815, 2001.

[12] C. Lauer, O. Dier, and M.-C. Amann. *Low-resistive metal/n+InAsSb/n-GaSb contacts*. Semicond. Sci. Technol., 21(9):1274–1277, September 2006.

[13] Silvaco, *Silvaco*, *http://www.silvaco.com/*.

[14] S. Adachi. *Band gaps and refractive indices of AlGaAsSb, GaInAsSb and InPAsSb: Key properties for a variety of the 2-4µm optoelectronics device application*. J. Appl. Phys., 1987.

[15] G. Roelkens, D. Van Thourhout, R. Baets, R. Nötzel, and M. Smit. *Laser emission and photodetection in an InP/InGaAsP layer integrated on and coupled to a Silicon-on-Insulator waveguide circuit.* Opt. Express, 14(18):8154–9, September 2006.

[16] J. Brouckaert. *Heterogeneous integration of photodetectors on silicon photonic ICs.* PhD thesis, Ghent University, 2010.

[17] Z. Sheng, L. Liu, J. Brouckaert, S. He, and D. Van Thourhout. *InGaAs PIN photodetectors integrated on silicon-on-insulator waveguides.* Opt. Express, 18(2):1756–61, January 2010.

[18] G. Roelkens, J. Brouckaert, D. Taillaert, P. Dumon, W. Bogaerts, D. Van Thourhout, R. Baets, R. Nötzel, and M. Smit. *Integration of InP/InGaAsP photodetectors onto silicon-on-insulator waveguide circuits.* Opt. Express, 13(25):10102–8, December 2005.

[19] D. Vermeulen, S. Selvaraja, P. Verheyen, G. Lepage, W. Bogaerts, P. Absil, D. Van Thourhout, and G. Roelkens. *High-efficiency fiber-to-chip grating couplers realized using an advanced CMOS-compatible silicon-on-insulator platform.* Opt. Express, 18(17):18278–83, August 2010.

[20] N. Hattasan, B. Kuyken, F. Leo, E. M. P. Ryckeboer, D. Vermeulen, and G. Roelkens. *High-Efficiency SOI Fiber-to-Chip Grating for the Short-Wave Infrared.* IEEE Photonics Technol. Lett., 24(17):1536–1538, 2012.

[21] X. Chen and H. K. Tsang. *Polarization-independent grating couplers for silicon-on-insulator nanophotonic waveguides.* Opt. Lett., 36(6):796–8, March 2011.

[22] D. Taillaert. *Grating couplers as Interface between Optical Fibres and Nanophotonic Waveguides.* PhD thesis, Ghent University, 2005.

[23] N. Hattasan, A. Gassenq, L. Cerutti, J.-b. Rodriguez, E. Tournié, and G. Roelkens. *Heterogeneous Integration of GaInAsSb p-i-n Photodiodes on a Silicon-on-Insulator Waveguide Circuit.* Photonics Technol. Lett. IEEE, 23(23):1760–1762, 2011.

[24] *CAMFR, http://camfr.sourceforge.net/.* 2013.

[25] *Mode Solvers Waveguide CAD Software FIMMWAVE, http://www.photond.com/products/fimmwave.htm.*

[26] A. N. Semenov, Y. V. Terentev, B. Y. Meltser, V. A. Solovev, T. V. Popova, a. V. Nashchekin, I. a. Andreev, E. V. Kunitsyna, A. A. Usikova, Y. P. Yakovlev, and S. V. Ivanov. *Molecular beam epitaxy of thermodynamically*

metastable GaInAsSb alloys for medium IR-range photodetectors. Semiconductors, 44(5):672–677, May 2010.

[27] *ePIXfab, http://www.epixfab.eu/.*

[28] G. Roelkens. *Heterogeneous III/V Silicon Photonics: Bonding Technology and Integrated Devices.* PhD thesis, Ghent University, 2006.

[29] J. P. Prineas. *Antimonide Optoelectronics for Infrared Chemical Sensing.* Adavnce Photonics Congr., pages 7–9, 2013.

[30] S. Supplies, *Crystalbond and Wafer-mount Washaway Mounting Adhesives, http://www.crystalbond.com/.*

[31] A. Gassenq, N. Hattasan, L. Cerutti, J. B. Rodriguez, E. Tournié, and G. Roelkens. *Study of evanescently-coupled and grating-assisted GaInAsSb photodiodes integrated on a silicon photonic chip.* Opt. Express, 20(11):11665–72, May 2012.

[32] X. Zhang. *The effects of (NH4)2S passivation treatments on the dark current-voltage characteristics of InGaAsSb PIN detectors.* J. Cryst. Growth, 251(1-4):782–786, April 2003.

[33] J. P. Prineas, M. Reddy, J. T. Olesberg, C. Cao, S. Veerasamy, M. E. Flatte, E. Koerperick, T. F. Boggess, M. R. Santilli, and L. J. Olafsen. *Quaternary GaInAsSb 2.0-2.5 micron back-illuminated focal plane array for blood glucose monitoring.* Proc. SPIE, 5726:113–121, 2005.

[34] C. Jagadish, S. D. Gunapala, and D. R. Rhiger. *Adavances in infrared Photodetectors.* Academic press, 2011.

[35] S. K. Kutty, M. N.; Plis, E.; Khoshakhlagh, A.; Myers, S.; Gautam, N.; Smolev, S.; Sharma, Y. D.; Dawson, R.; Krishna, S.; Lee, S. J.; Noh. *Study of Surface Treatments on InAs GaSb Superlattice LWIR Detectors.* J. Electron. Mater., 39:2203–2209, 2010.

[36] J. A. Robinson and S. E. Mohney. *Characterization of sulfur passivated n-GaSb using transmission electron microscopy and the influence of passivation on ohmic contact resistance.* J. Appl. Phys., 96(5):2684, 2004.

[37] E. Paris-Olakowska. *Surface Treatments of GaSb and Related Materials for the processing of Mid-Infrared Semiconductor Devices.* Electron Technol. - Internet J., 37(38):1–34, 2006.

[38] S. Sridaran, a. Chavan, and P. Dutta. *Fabrication and passivation of GaSb photodiodes.* J. Cryst. Growth, 310(7-9):1590–1594, April 2008.

[39] A. Chavan, A. Chandola, S. Sridaran, and P. Dutta. *Surface passivation and capping of GaSb photodiode by chemical bath deposition of CdS*. J. Appl. Phys., 100(6):064512, 2006.

[40] F. M. Mohammedy and M. Jamal Deen. *Growth and fabrication issues of GaSb-based detectors*. J. Mater. Sci. Mater. Electron., 20(11):1039–1058, June 2009.

[41] P.-Y. Delaunay, A. Hood, B. M. Nguyen, D. Hoffman, Y. Wei, and M. Razeghi. *Passivation of type-II InAsGaSb double heterostructure*. Appl. Phys. Lett., 91(9):091112, 2007.

[42] H. S. Kim, E. Plis, a. Khoshakhlagh, S. Myers, N. Gautam, Y. D. Sharma, L. R. Dawson, S. Krishna, S. J. Lee, and S. K. Noh. *Performance improvement of InAs/GaSb strained layer superlattice detectors by reducing surface leakage currents with SU-8 passivation*. Appl. Phys. Lett., 96(3):033502, 2010.

[43] R. Chaghi, C. Cervera, H. Aït-Kaci, P. Grech, J. B. Rodriguez, and P. Christol. *Wet etching and chemical polishing of InAs/GaSb superlattice photodiodes*. Semicond. Sci. Technol., 24(6):065010, June 2009.

[44] R. Rehm, M. Walther, F. Fuchs, J. Schmitz, and J. Fleissner. *Passivation of InAs(GaIn)Sb short-period superlattice photodiodes with 10μm cutoff wavelength by epitaxial overgrowth with $Al_xGa_{1x}As_ySb_{1y}$*. Appl. Phys. Lett., 86(17):173501, 20.

[45] Z. Y. Liu, D. a. Saulys, and T. F. Kuech. *Improved characteristics for AunGaSb Schottky contacts through the use of a nonaqueous sulfide-based passivation*. Appl. Phys. Lett., 85(19):4391, 2004.

[46] P. Dutta, J. Langer, V. Bhagwat, and J. Juneja. *Dry etching, surface passivation and capping processes for antimonide based photodetectors*. Proc. SPIE, 5783:98–105, 2005.

[47] N. Hattasan, L. Cerutti, J. Rodriguez, E. Tournié, D. V. Thourhout, and G. Roelkens. *Heterogeneous Integration of GaSb-based epitaxy on silicon-on-insulator: towards mid-infrared photonic integrated circuits for environmental and bio-medical applications*. 10th Int. Conf. Mid-Infrared Optoelectron. Mater. Device, pages 90–91, 2010.

[48] Thorlab, *Thorlabs*, *http://www.thorlabs.de/index.cfm?*

[49] *Hamamatsu Photonics*, *http://www.hamamatsu.com/jp/en/index.html*. 2013.

5

Integration of Fabry-Perot MQW-InGaAsSb Lasers on Silicon-on-insulator waveguide circuits Emitting at 2.01μm

5.1 Introduction

In Chapter 4, the integration of the first InGaAsSb photodiode on an SOI waveguide circuit for SWIR applications was discussed. Eventually, an integrated spectroscopic system is being developed and demonstrated as part of the PhD of Eva Ryckeboer. However, an integrated spectrometer cannot fully operate without a light source. A complete system with both photodiodes, light sources and dispersive elements would enable a variety of applications such as implantable glucose sensors [1] and ultra compact gas sensors [2].

In this chapter, I discuss the integration of a Fabry-Perot (FP) laser on an SOI waveguide circuit. The experimental section is divided into 2 subsections. The first section is focused on a proof of concept device: a thin-film GaSb-based FP laser on an InP substrate. Integration of GaSb epitaxy to the InP substrate is carried out to assess the integration feasibility. The fabrication process for the integrated laser is also developed during this phase. In the second subsection, I employ the same epitaxy design and fabrication process to realize an integrated GaSb-based FP laser on an SOI waveguide circuit. The focus in this part is on the light coupling

from the laser to a Si waveguide. The coupling between these two components is achieved using a polymer waveguide formed on an inverted Si taper.

The chapter starts with the basic operating principle of the laser diode and its design and then subsequently moves to fabrication and measurement results. The design section discusses the design of the epitaxial structure and the coupling mechanism. The laser fabrication process is then discussed in detail. In the measurement part, the results are presented in 2 subsections: integrated GaSb-based FP lasers on an InP substrate as the first generation device and the integrated GaSb-based FP lasers on an SOI waveguide circuit using a polymer waveguide to couple light into the Si waveguide as the second generation device. A thermal analysis of the integrated FP laser is also presented. The chapter ends with a discussion of the results. The work presented in this chapter is carried out in collaboration with dr. Alban Gassenq who has contributed to the design of the epitaxy.

5.1.1   Basic semiconductor laser diode characteristics

A laser consists of a gain medium and a cavity. In semiconductor lasers, the gain is typically provided by a semiconductor material with a direct band gap that is pumped. Pumping is achieved either optically or electrically such that the number of electrons in the conduction band is higher than in the valence band. This is commonly referred to as population inversion, which leads to stimulated emission. The cavity or optical feedback mechanism serves as a light trap to create a resonance. The laser cavity is formed using highly optically reflective components such as mirrors or gratings. The efficiency of a laser diode depends strongly on the efficiency of pumping and the design of the cavity. In this work, an electrically pumped laser is studied and demonstrated. This section discusses the optical and electrical characteristics of the lasers which subsequently will be used to analyse the experimental results.

5.1.1.1   Power-Current characteristic (L-I)

In an electrically injected laser diode, electrons and holes are injected into the gain region to create population inversion. The relationship between emitted optical power and injected current above threshold is given by [3]:

$$P_o(I) = \eta_{ext}\frac{hv}{q}\left(I - I_{th}\right) = \eta_{in}\frac{\alpha_m}{\alpha_i + \alpha_m}\frac{hv}{q}\left(I - I_{th}\right) \tag{5.1}$$

where η_{ext} is the differential quantum efficiency, which describes the output power change (ΔP_o) as a function of the change in injected current (ΔI). η_{ext} depends on injection efficiency (η_{in}), mirror loss (α_m) and internal loss (α_i). I_{th} is the threshold current required to overcome the cavity losses. h is Planck's constant,

v is the photon energy and q is the electron charge. P_o in this equation refers to the output power from both laser facets.

The L-I characteristic is one of the most important characteristics indicating the performance of the laser, i.e. minimum I_{th} and maximum η_{ext} are desirable. I_{th} is proportional to the threshold material gain (g_{th}). It is related to the cavity parameters and confinement factor in the gain region by:

$$\Gamma g_{th} = \alpha_i + \alpha_m = \alpha_i + \frac{1}{2L} ln(\frac{1}{R_1 R_2}) \qquad (5.2)$$

where L is the cavity length, R_1 and R_2 are reflectivity of the laser cavity mirrors on both sides, which depend on the laser cavity design. For the case of FP lasers, the reflectivity (R) of the laser facets is calculated using the Fresnel's equations [3]:

$$R = |r|^2 = \left| \frac{n_i cos\theta_i - n_t cos\theta_t}{n_i cos\theta_i + n_t cos\theta_t} \right|^2 \qquad (5.3)$$

where n_i is refractive index of medium for the incident wave and n_t is the refractive index of the medium for the transmitted wave. θ_i and θ_t are the incident and transmitted angle respectively. A typical value of R is $\sim$0.3 for a GaSb-based FP laser with n_{laser} = 3.5 [4] and n_{air} =1 [5]. Minimum total loss in the cavity is obtained by minimizing internal loss and increasing R. Γ_{act} is the optical mode confinement factor which is defined as the ratio of the mode energy in the active region to the total energy in the optical mode in a 1D approximation as [6]:

$$\Gamma_{act} = \frac{\int_0^{d_{act}} |E(y)|^2 \, dy}{\int_{-\alpha}^{\alpha} |E(y)|^2 \, dy} \qquad (5.4)$$

where E(y) is the electric field across the epitaxial stack and d_{act} is the total quantum well (QW) thickness. Γ_{act} is very important for laser design to ensure a low I_{th}, and thereby, low power consumption. Typical Γ in QWs is approximately 5% for standard edge emitting lasers [7, 8].

For edge emitting FP laser structures, it is often of interest to plot $1/\eta_{ext}$ as a function of the laser cavity length (L).

$$\frac{1}{\eta_{ext}} = \frac{2.\alpha_i}{\eta_i ln(1/R_1 R_2)} L + \frac{1}{\eta_i} \qquad (5.5)$$

From this relation, η_i and α_i can also be extracted (if R_1 and R_2 are known).

5.1.1.2 Current-Voltage characteristics (I-V)

Apart from monitoring output power versus injected current, the relationship of injected current versus applied voltage provides information on the electrical characteristics of the laser diode. The electrical characteristics relate to the electrical

D1 is ideal diode.

(a)   (b)
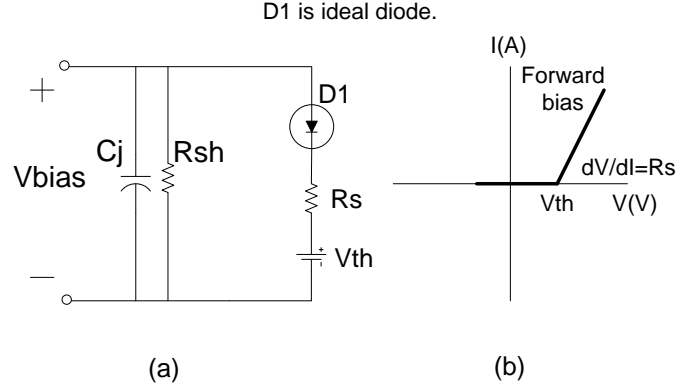
Figure 5.1: The diode equivalent circuit

contact quality. Fig. 5.1a represents the diode equivalent circuit where R_{sh} is the shunt resistance, which relates to the conduction path along the surface of the laser mesa sidewall. R_{sh} can be obtained from the I-V characteristic (Fig. 5.1b) by measuring resistance at zero bias. R_s is the series resistance which relates to the quality of the metal contact for both n-doped and p-doped material. R_s is obtained by linearly fitting the I-V curve when $V > V_{th}$.

5.1.1.3   Thermal characteristics

The investigation of laser characteristics at different temperatures is important for many applications. Some applications require laser diodes with small wavelength drift while, in some applications, such as spectroscopy, it is beneficial to tune the lasing wavelength by changing temperature. Moreover, the performance of semiconductor lasers decreases with an increase of temperature due to the reduction in gain [3]. Therefore, it is useful to understand the thermal characteristics of the laser. The relationship of laser threshold current density (J_{th}) and temperature (T) is given by [9]:

$$J_{th}(T) = J_{th}(T_1)exp[\frac{T - T_1}{T_o}] \qquad (5.6)$$

where T_o is a characteristic temperature which determines the dependence of laser performance on the temperature. Note that a high value of T_o indicates a smaller dependence. $J_{th}(T_1)$ is the threshold current density at temperature T_1. By taking the natural logarithm on both sides, T_o is obtained as :

$$T_o = \frac{\Delta T}{\Delta ln\,(J_{th})} \qquad (5.7)$$

The thermal resistance (R_{th}) is also an important parameter determining the thermal behavior of the laser [10]. R_{th} is defined by the ratio of the change in

device temperature (T_{dev}) and the total heat flux (P) generated per unit length. R_{th} is given by [3]:

$$R_{th} = \frac{T_{dev} - T_0}{P_{heat}}$$ (5.8)

where T_0 is the ambient temperature, i. e. temperature of a heatsink. In practise, R_{th} is obtained by a product of 2 sets of measurements; 1) the change of lasing wavelength (dλ) as a function of the change in ambient temperature (*dT*) (in this case, a thermo-electric cooler is employed.) and 2) the change of lasing wavelength (dλ) as a function of the change in power consumption (*dP*).

$$R_{th} = \frac{\mathrm{d}T}{\mathrm{d}P} \rightarrow \left(\frac{d\lambda}{dP}\right) / \left(\frac{d\lambda}{dT}\right)$$ (5.9)

Note that a small value of R_{th} indicates a smaller dependence of the laser on temperature.

5.2 Design and simulation

Several design parameters need careful tuning when designing integrated laser diodes on an SOI waveguide circuit. These include maximum optical mode overlap with the gain region (high Γ_{act}) and minimum internal loss (α_i), and efficient current injection and light coupling. The design of the integrated GaSb-based FP laser is divided into 2 parts: epitaxy design and optical coupling optimization. In the first design section, epitaxy design is carried out to achieve maximum Γ_{act} and minimum α_{int} by minimizing the mode overlap with lossy material regions such as the n and p-doped cladding. In the second section, the optical coupling is then optimized to couple efficiently from the laser facet to the Si waveguide.

5.2.1 Epitaxy design

The epitaxy design used in this section is restricted to a conventional laser design [11] to reduce unknown parameters related to epitaxy in these first generation devices and to obtain high Γ_{act}. The epitaxy is grown by a solid source molecular beam epitaxy (MBE) on a n-type GaSb substrate at the university of Montpellier 2. The heterostructure consists of 300nm Be-doped GaSb (1×10^{19} cm^{-3}) as p-contact and 300nm Te-doped GaSb (2×10^{18} cm^{-3}) as n-contact. A 1μm thick $Al_{0.9}Ga_{0.1}As_{0.07}Sb_{0.93}$ cladding layer is used on both sides of the active region (2×10^{18} cm^{-3} Be/Te doping, respectively). Composition grading is performed between the contact and cladding layer over 100nm thickness. 360nm thick $Al_{0.25}Ga_{0.75}As_{0.02}Sb_{0.98}$ separate confinement layers (SCH) are used. The active region is made of four 10 nm $In_{0.24}Ga_{0.76}As_{0.01}Sb_{0.99}$ quantum wells separated by three 30nm thick $Al_{0.25}Ga_{0.75}As_{0.02}Sb_{0.98}$ barriers. $InAs_{0.91}Sb_{0.09}$ is

Layer	Material	Thickness (nm)	Doping (cm-3)	Refractive index	loss(cm^{-1} at 2.0μm)
n-contact	GaSb	300	2x10^{18}	3.87	80
n-grading	composition grating	100	2x10^{18}		16
n-cladding	Al$_{0.9}$Ga$_{0.1}$As$_{0.07}$Sb$_{0.93}$	1000	2x10^{18}	3.14	16
SCH	Al$_{0.25}$Ga$_{0.75}$As$_{0.02}$Sb$_{0.98}$	360	undoped	3.69	
MQWs	Ga$_{0.76}$In$_{0.24}$As$_{0.01}$Sb$_{0.99}$	10x4	undoped	3.9	
barriers	Al$_{0.25}$Ga$_{0.75}$As$_{0.02}$Sb$_{0.98}$	30x3	undoped	3.69	
SCH	Al$_{0.25}$Ga$_{0.75}$As$_{0.02}$Sb$_{0.98}$	360	undoped	3.69	
p-cladding	Al$_{0.9}$Ga$_{0.1}$As$_{0.07}$Sb$_{0.93}$	1000	5x10^{17}	3.14	6
p-grading	composition grating	100	5x10^{18}		58
p-contact	GaSb	300	1x10^{19}	3.92	70
etch stop layer	InAs$_{0.91}$Sb$_{0.09}$	150	1x10^{19}	3.5	
substrate	GaSb				

Table 5.1: Epitaxial structure and its optical properties used for this work

used between the GaSb substrate and the GaSb contact layer as etch stop layer for the bonding process. The summary of the epitaxial structure is shown in Table 5.1. Fig. 5.2a represents the band diagram of the epitaxy. The band parameters and compound data are obtained from linear interpolation of the compounds [12]. Details on how to obtain these parameters can be found in Appendix A. The QW (with 1.2% compressive strain) is designed to have its peak emission at 2.05μm. Fig. 5.2b represents the simulation of the refractive index profile and fundamental optical mode profile. The refractive index parameters are obtained from Ref. [13]. The calculated confinement factor in the QWs and in the p-cladding layer is 7.2% and 3%, respectively. The simulated modal loss is 0.8cm^{-1}(details in Appendix A.). The simulation is carried out using a full-vectorial 1D eigenmode expansion method [14].

5.2.2 Optical coupling design

The epitaxy is first bonded on an SOI waveguide circuit. After this, the FP laser is processed. A DVS-BCB polymer waveguide fabricated on Si inverted taper
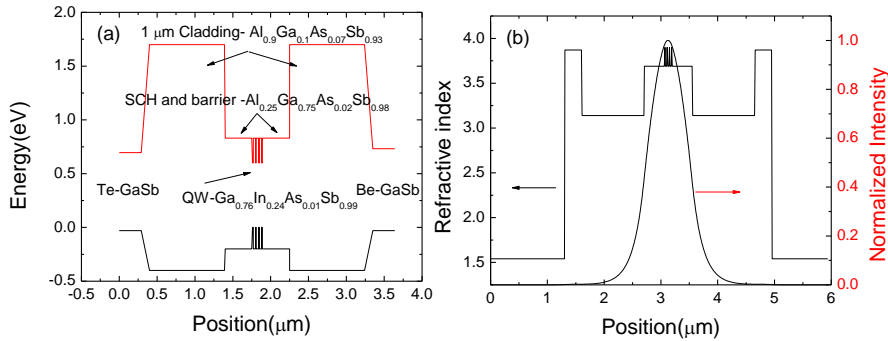
Figure 5.2: a) Energy band diagram of the laser epitaxial structure b) Fundamental optical mode profile

during the laser processing is utilized to couple light from the laser facet to the Si waveguide. Note that, DVS-BCB is selected as a waveguide material due to its transparency in the short-wave infrared as well as the simplicity in its fabrication process. The optical coupling scheme used to couple between the III-V FP laser and the Si waveguide circuit is shown in Fig. 5.3.
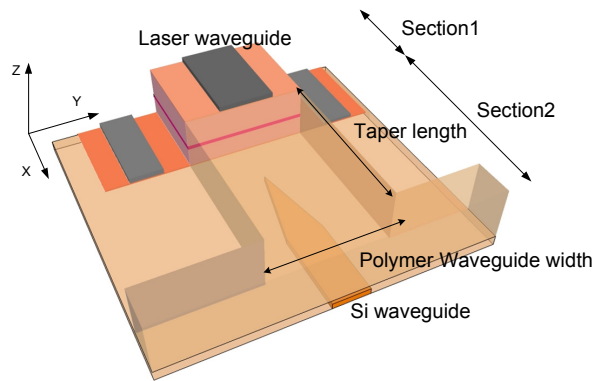
Figure 5.3: Schematic of the integrated laser with polymer waveguide coupled to an inverted Si waveguide

The simulation of the TE-polarized light coupling efficiency from laser facet to Si waveguide is divided into two sections: 1) from laser facet into the polymer waveguide 2) adiabatical coupling from the polymer waveguide to the Si waveguide. In the first section, the optical mode matching between laser waveguide and polymer waveguide is considered. Note that the simulations in this section are

performed at 2.1μm wavelength for TE-polarization using Fimmwave. The parameters which limit transmission from laser facet to polymer waveguide are the reflection at the interface of the polymer and laser facet (in this case, R=16% is obtained where n_{laser}=3.6 simulated using CAMFR [14]and $n_{DVS-BCB}$=1.54 [15]) and the mode matching between the two waveguides. The transmission is normalized to 1-R. The mode mismatch between laser and polymer waveguide depends on the geometry of both laser and polymer waveguide. The simulation is carried out in 3D using a full-vectorial mode solver [16]. The simulation in Fig. 5.4a considers a structure with the same width for both laser and polymer waveguide. The results show that an optimum mode matching is obtained when the minimum waveguide width is 5μm. When changing the thickness (Fig. 5.4b) of the polymer waveguide and keeping the width of the laser waveguide constant at 10μm, there is little change in the coupling efficiency. Note that in Fig. 5.4b, the x-axis represents the thickness which is added onto the thickness of the laser. The mode matching between laser and polymer waveguide can however be enhanced when the n-doped cladding thickness is reduced. The coupling efficiency increases from 0.51 to 0.72 when the n-doped cladding thickness is reduced from 1μm to 0.2μm(assuming the same height for the polymer and laser waveguide) as shown in Fig. 5.4c.

In the second part, the optical mode conversion from polymer to Si waveguide is investigated. The coupling is achieved using an inverted taper formed in the Si waveguide layer which adiabatically transforms the optical mode from the polymer into the Si waveguide. A top view of the inverted taper (*XY* plane) is shown in Fig. 5.5a. An example of the optical field coupled from the laser waveguide to Si waveguide (*XZ* plane) is shown in Fig. 5.5b. The optical modes at different lengths are shown in Fig. 5.5 at 5μm(c), at 21μm(d) and at 150μm(e). As can be seen in Fig. 5.5e, the optical mode is completely coupled into the Si waveguide when the coupling length is 150μm. One important parameter to achieve maximum coupling efficiency is the width of the Si tip: i.e. the smaller the Si tip, the better the matching at the interface from polymer to hybrid polymer/Si waveguide. The simulation in Fig. 5.6a illustrates that coupling efficiency drops significantly when the Si tip is wider than 0.25μm. Another parameter that affects the coupling efficiency is the coupling length. If the coupling length is too short, the fundamental mode will couple to higher order modes, resulting in a lower coupling efficiency to the fundamental mode of the silicon waveguide. However, if the coupling is too long, this will increase the losses due to scattering and due to absorption in the DVS-BCB waveguide (especially at longer wavelength as shown in Fig. 1.10, this loss is not included in our simulation). The simulation in Fig. 5.6b shows that a minimum coupling length (150-250μm) is required to convert the optical mode of the polymer waveguide to the Si waveguide. This minimum coupling length depends on the initial waveguide width or the size of the initial optical mode i.e. the smaller the initial mode size, the faster the mode transformation. The maximum coupling
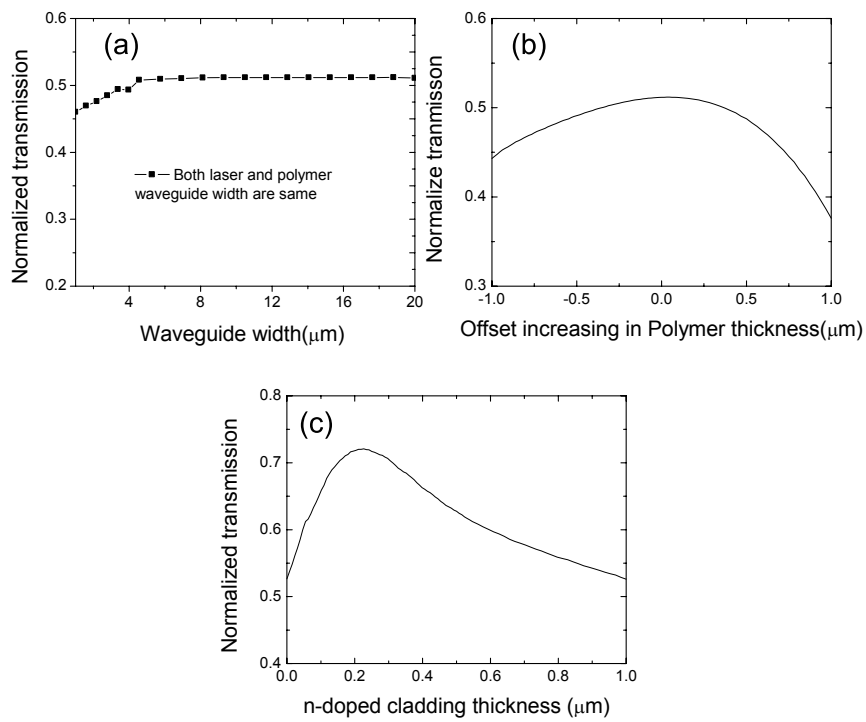
Figure 5.4: Simulation of the normalized transmission as a function of a) waveguide width b) polymer thickness c) n-doped cladding thickness when the polymer and laser height are equal
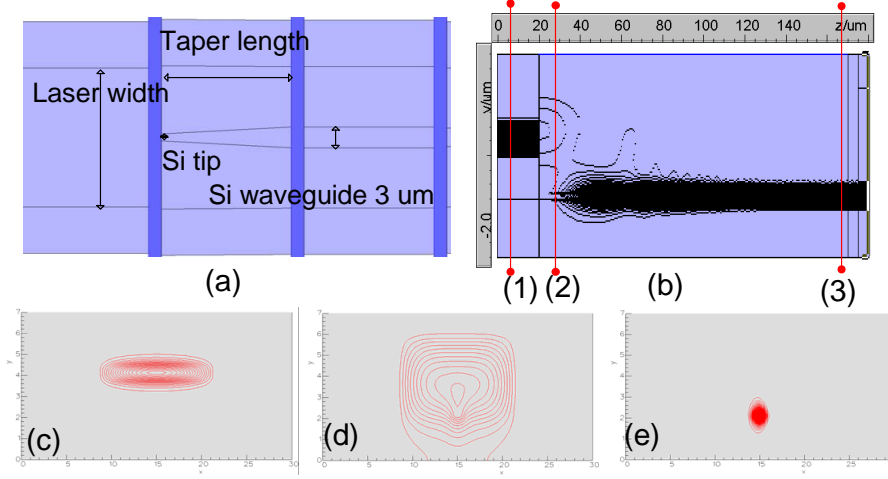
Figure 5.5: a) Top view (XY plane) of the laser structure in Fig. 5.3 b) Example of the field distribution in the adiabatic taper coupler from the laser waveguide to the polymer waveguide. The optical mode profiles at different waveguide positions are shown in (c) at 5µm, (d) at 21µm (e) at 150µm

efficiency obtained for this simulation is only 90% because of the 120nm Si tip (Fig. 5.6), which is compatible with a 193nm deep UV lithography process [17] used for the simulation. Combining the simulation on the mode mismatch and adiabatic taper coupler, a coupling efficiency of $\sim 45\%$ can be expected.

5.2.3 Thermal design

In this section, COMSOL multiphysics engineering software [18] is employed to simulate the thermal properties of the integrated laser for different configurations. The study is conducted in 2D from which, it is possible to obtain the necessary results without employing significant resources and time that 3D simulation requires. The heat source is assumed to be concentrated in the MQW area. Only heat conduction is considered in the simulation, neglecting radiation and convection. Therefore, the heat-transport equation becomes [3]:

$$\vec{q} = -k\nabla T, \nabla.\vec{q} = \begin{cases} Q & , within\ the\ heat\ source \\ 0 & , outside\ the\ heat\ source \end{cases} \tag{5.10}$$

where $\vec{q}$ is the local heat flux density (W/m^2), k is the thermal conductivity of the material (W/m.K), ∇T is the temperature gradient (K/m) and Q is the local heat generation (W/m^3). The temperature is set to 25°C constant at the bottom of the structure as a boundary condition. Insulation is set on both the left, right and top side boundary. The thermal resistance (R_{th}) is then calculated using Equation 5.8.
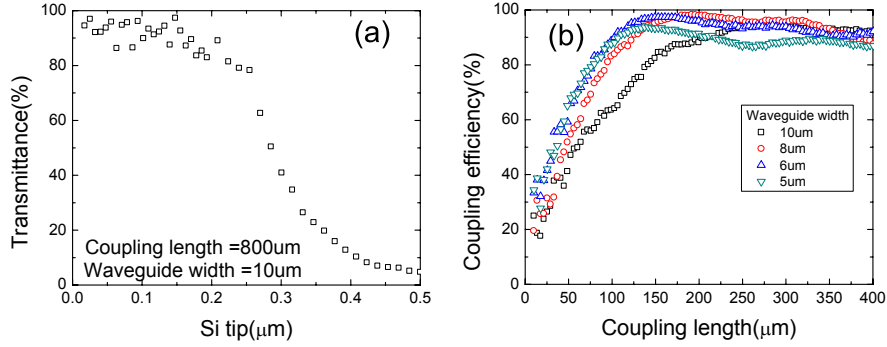
Figure 5.6: a) Coupling efficiency as a function of Si tip with a coupling length of 800μm and a waveguide width of 5μm b) coupling efficiency as a function of coupling length at different waveguide width for wire waveguide structure

Material	Thermal conductivity (W/m.K)
InP	68 [18]
DVS-BCB	0.3 [15]
GaSb	36 [19]
$In_{0.24}Ga_{0.76}As_{0.01}Sb_{0.98}$	3 [19, 20]
$Al_{0.25}Ga_{0.75}As_{0.02}Sb_{0.98}$	10.5 [19, 21]
$Al_{0.9}Ga_{0.1}As_{0.07}Sb_{0.93}$	7.1 [19, 21]

Table 5.2: The thermal conductivities of different materials

The thermal conductivity for different materials used here are presented in Table 5.2.

The integrated laser structure used in this simulation is depicted in Fig. 5.7a. A 18μm wide and 130nm thick heat source is located in the centre between the separate confinement layers (SCH). The heat source is chosen to provide a heat flux per unit length of 3W/cm. The laser mesa is 18μm. The top gold and bottom gold thickness are chosen to be the same as the experiment, which are 600nm and 800nm respectively. The distance between bottom contact and the mesa is 1.5μm. The DVS-BCB is varied between 100nm to 900nm. Fig. 5.7b shows the impact of DVS-BCB thickness on the length-specific thermal resistance (R_{L-th}). As expected, the thicker the DVS-BCB layer, the worse R_{L-th} becomes because the DVS-BCB layer blocks the path for the heat to dissipate through the substrate.

Fig. 5.8 shows the simulation of different integrated laser configurations with 700nm DVS-BCB thickness: a) standard integrated laser, R_{L-th} = 11.8K.cm/W b) standard integrated laser with top gold connection from the laser stack to another epitaxial stack for further heat removal, R_{L-th}=9.1K.cm/W. The distance between the laser epitaxy and heat removal structure is 20μm. The structure used for heat
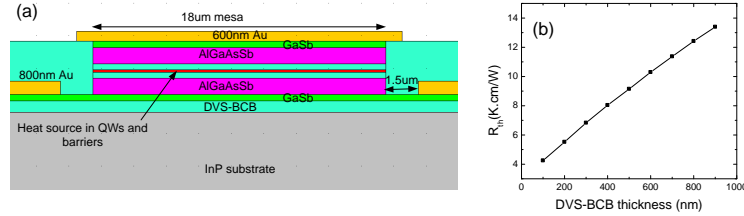
Figure 5.7: The schematic of the standard integrated laser used in this simulation indicating important parameters of the structure b) The simulated R_{L-th} as a function of DVS-BCB layer thickness
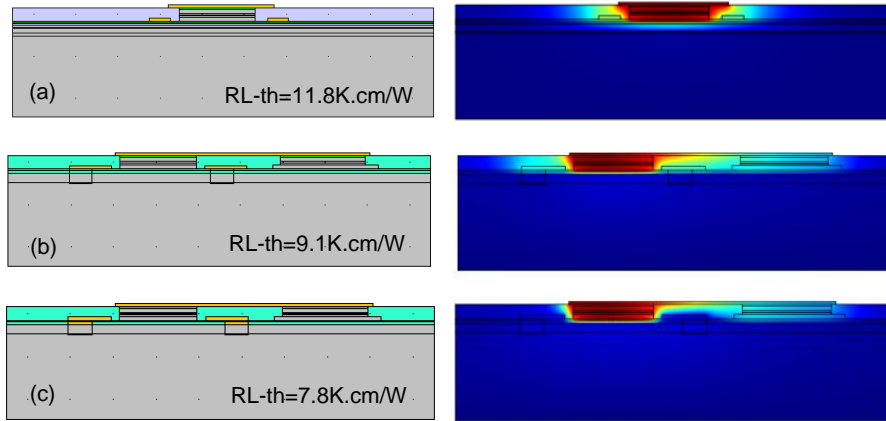
Figure 5.8: The simulated temperature distribution of the integrated laser with different heat removal configuration a) without heat removal structure b) with top heat removal structure c) with top and bottom heat removal structure

removal is also 20μm wide. c) standard integrated laser with both top and bottom gold connection to another epitaxial stack for the top part and to the substrate in the bottom part, R_{L-th}=7.8 K.cm/W. With assistance of a heat removal structure on the top contact, the maximum temperature of the laser is reduced by 23%. This can be improved further by increasing the Au thickness and increasing the width of the heat removal structure. On the other hand, by adding both top and bottom heat removal structures, the improvement is 34%. However, the structure is significantly more complex to fabricate compared to the one with only top heat removal structure. Therefore, the integrated GaSb-based FP laser with top heat removal structure (Fig. 5.8b) is selected for the experiment.

5.3   Integration and Fabrication

The SOI sample/InP sample and epitaxial die are cleaned with acetone and isopropanol. DVS-BCB diluted with mesitylene (2:3 DVS-BCB:Mesitylene) is spin coated on the SOI substrate/InP substrate. The sample is then baked at 150°C for 5 minutes. The epitaxial die is then transferred onto the SOI substrate/InP substrate at 150°C in air. A small force is applied on the die using tweezers to ensure good microscopic contact between the DVS-BCB coated SOI/InP substrate and the epitaxial die. The sample is then baked at 250°C for 1hr (the details can be found in Section 3.2.4.1). A DVS-BCB bonding layer thickness measured from the oxide box layer/InP substrate of ∼560nm/730nm is obtained in this demonstration. The side wall of the epitaxial die is then protected before grinding by using CrystalBond glue [22] to prevent lateral etching during the wet etching process. Grinding is performed on a glass plate using a Lapmaster. A slurry based on water and aluminum powder (12.5μm diameter particles) is used as the abrasive agent. The GaSb substrate is grinded down to 50-100μm thickness. Detail of this process can be found in Section 3.3.2. Wet etching (Chromic acid based solution, CrO_3:HF:H_2O (1:1:3 v/v), Section 3.3.3.1) is then used to remove the rest of the substrate.

After the substrate removal, the etch stop layer (InAsSb) is etched away by wet processing (Citric acid based solution, $C_6H_8O_7$:H_2O_2 (2:1 v/v); see Section 3.3.3.2). Fig. 5.9 presents a summary of the laser fabrication process. The p-doped contact metallization (Ti/Pt/Au 2/35/100nm) is deposited using electron beam evaporation. Next, the laser mesa is formed by wet etching using two lithography steps. First, the GaSb p-doped layer is etched using a phosphoric acid based solution (Citric acid:H_2O_2:H_3PO_4:H_2O, 55:5:3:220 v/v, Section 3.3.3.3). The $Al_{0.9}Ga_{0.1}As_{0.07}Sb_{0.93}$ cladding is then etched using a hydrochloric acid based solution (HCl:H_2O:H_2O_2 (50:100:1 v/v), Section 3.3.3.5). After a second lithography step, which is required to protect the etched mesa from too much undercut, a phosphoric acid based solution (Section 3.3.3.3) is again used to etch the QWs and SCH region. The n-doped cladding is then removed using the HCl-based solution similar to the p-doped cladding (Section 3.3.3.5). AuGe/Ni/Au (150/60/100nm) is deposited as n-contact using a thermal evaporator system. DVS-BCB (3022-46) is then used to planarize and passivate the laser. Next, RIE (Section 3.3.4.2) is used to etch the DVS-BCB for opening the contact vias. 50/500nm Ti/Au is then deposited for probing. Before cleaving the sample, the InP/SOI substrate is grinded down to approximately 150μm for InP and 100μm for SOI to accommodate the cleaving process such that a good facet is obtained. Fig. 5.10a shows a top view optical image of the laser and Fig. 5.10b presents a SEM image of the facet and the cross section of the realized device.
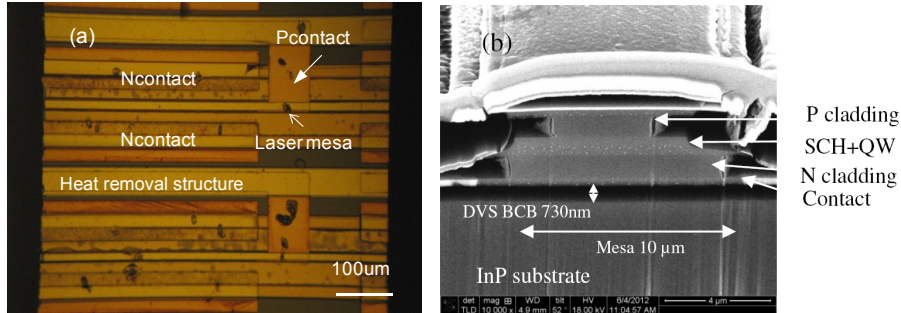
Figure 5.10: a) An optical image of the realized integrated FP laser on InP substrate b) SEM image of the cross section of the mesa of the realized device
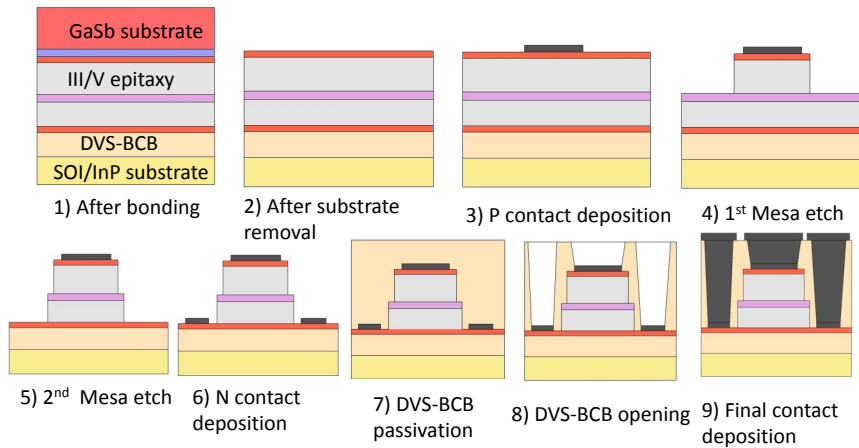
Figure 5.9: Process flow for fabricating an integrated GaSb-based FP laser

5.4 Measurement results

The measurement setup consists of a Keithley 2400 for continuous wave (CW) current injection and a Lightwave LDP-3811 current source for pulsed measurements. A Yokogawa optical spectrum analyzer (AQ6375) is used for spectral analysis. Light is collected using multimode fiber with a 50μm core diameter (M42L01 from Thorlabs). A thermoelectric cooler is used to control the temperature of the substrate. Fig. 5.11 illustrates the setup used for characterizing the integrated GaSb-based FP laser. Laser characteristics are measured and studied in 3 aspects:
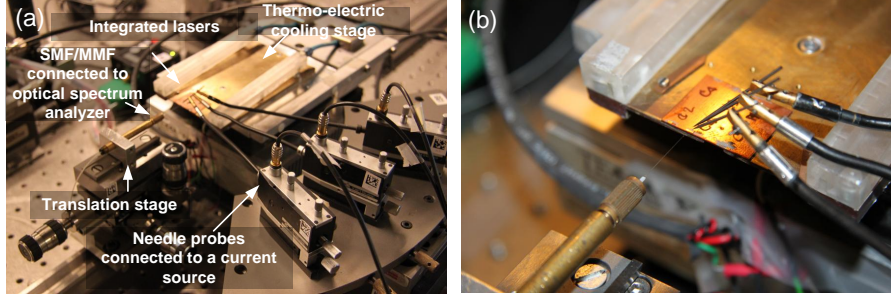
Figure 5.11: a) Measurement setup used for laser characterization. The sample is mounted on a thermo-electric cooler stage. 50µm core multimode fiber is used to coupled light from the laser facet to the OSA. b) zoom of the devices with needle probes and a fiber coupled horizontally to a laser facet

L-I-V curves, optical spectra associated with the L-I-V curves and thermal characteristics.

5.4.1 Proof of concept: Integrated GaSb-based Fabry-Perot lasers on InP substrate

5.4.1.1 Optical characteristics

The measurement of the L-I-V curves is conducted at room temperature. The L-I-V characteristic of a fabricated integrated GaSb-based FP laser is presented in Fig. 5.12a. The laser mesa is 15μm wide and 490μm long. The threshold current is 31mA in pulsed regime and 49.7mA in CW regime, corresponding to a current density of 422 and 676A/cm^2 respectively. These threshold currents confirm that realizing a thin-film GaSb laser is feasible with good laser performance i.e. continuous wave operation at room temperature. The maximum output power is 58μW at 77mA. The optical output power is relatively low compared to literature [11, 23] due to several reasons such as: 1) Low internal efficiency due to a shunt path. R_{sh} can be used to indicate the conductivity of the shunt path at zero bias. Typical R_{sh} is in the order of MΩ [24, 25]. However, in our case, it is $\sim$0.06-0.25kΩ. This indicates high leakage current on our laser structure. 2) The quality of the semiconductor-metal contact or R_s is also of importance. A high value of R_s results in high voltage drop across the diode, thereby increasing heat dissipation, consequently reducing the gain. Typically the value of R_s is lower than 1-5Ω [25]. In our case, the distribution of $R_s.L_{laser}$ is shown in Fig. 5.13. These results indicate a relatively high and large variation of R_s (5-15Ω). The values obtained for R_{sh} imply that current injection efficiency can be improved further by investigating passivation materials to reduce leakage current, thereby increasing shunt resistance. A proper selection of the contact metal reduces R_s further and im-
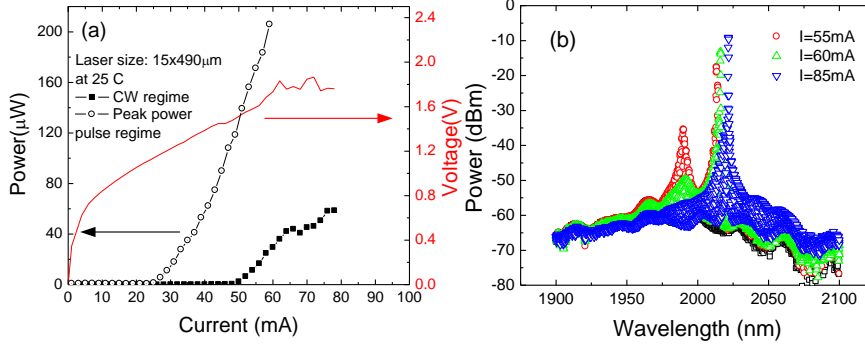
Figure 5.12: The integrated GaSb-based FP laser characteristic (490μm x 15μm device dimensions): a) L-I-V characteristic b) laser spectrum at different bias current
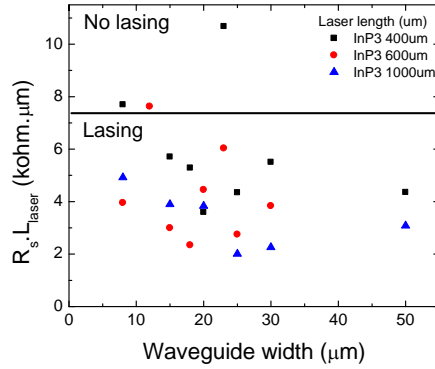
Figure 5.13: Series resistance as a function of laser waveguide widths at different waveguide lengths

prove its stability. Laser spectra at different bias current are shown in Fig. 5.12b. The peak wavelength shifts towards longer wavelengths with the increase of bias current, indicating self-heating.

Fig. 5.14a shows the threshold current density as a function of laser mesa width (laser cavity length: 690μm). The increase of J_{th} at narrow waveguide widths indicates the decrease of the injection efficiency due to surface recombination and current leakage and the increase in optical loss due to scattering of the laser mode at the etched sidewalls [26]. The J_{th} in pulsed operation is plotted as a function of the inverse cavity length in Fig. 5.14b. By linearly fitting the curve and extracting the parameters according to Equation 5.5, I obtain a J_{th} of 223A/cm^2 at infinite length. This J_{th} at infinite length is relatively high compared to standard FP lasers in literature e.g. 150 A/cm^2 [11], 145 A/cm^2 [27]. This is attributed to the low current injection efficiency and high scattering loss in the laser waveguide. The
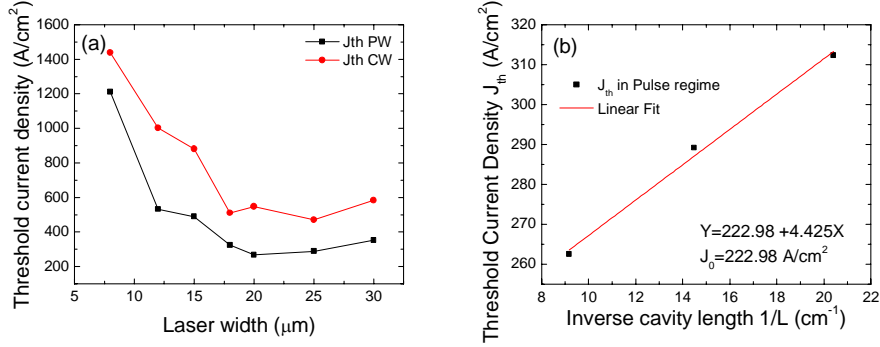
Figure 5.14: Threshold current density as a function of a) laser width (device length 690µm) b) inverse cavity length for a laser width of 25µm

performance of the device would improve by minimizing parasitic shunt paths as well as reducing the scattering loss in the laser waveguide.

5.4.1.2   Thermal characteristics

Fig. 5.15a shows the L-I characteristic as a function of temperature. By fitting the natural logarithm of J_{th} as a function of temperature, as shown in Fig. 5.16, a T_0 of 44K is estimated from Equation 5.7. Fig. 5.17a represents the linear interpolation of wavelength drift as a function of ambient temperature, when the laser is operated in pulsed regime to avoid self-heating. The corresponding optical spectrum are shown in Fig. 5.15b. Fig. 5.17b represents the wavelength drift as a function of power consumption. By using Equation 5.9, the length-specific thermal resistance is estimated as 22K.cm/W. This high thermal resistance, compared to traditional laser fabrication [28] can be attributed to the relatively thick adhesive bonding layer (730nm) used to optically isolate the laser mode from the substrate. Given the low thermal conductivity of the adhesive bonding layer (0.3W/mK [15]) a high thermal resistance can be expected. Therefore, thermal management improvement is required. This is possible to implement by increasing the thickness of the gold contact (The current structure has 600nm and 800nm Au thickness respectively) or employing the laser structure with both top and bottom heat removal path (Section 5.2.3). The experimental R_{L-th} value is also higher than the value obtained from the simulations in Fig. 5.8b. This discrepancy is still unclear. The parameters used in the simulation might be inaccurate due to limited information in literature.
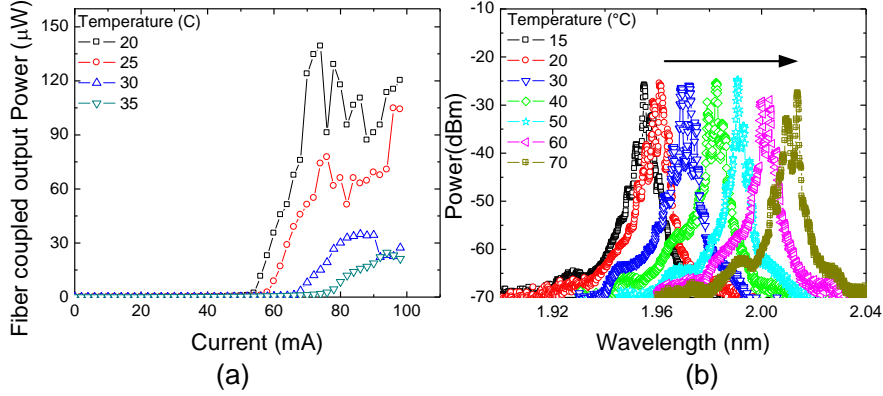
Figure 5.15: Temperature dependent characteristics of the thin-film lasers (18μm wide and 490μm long) a) L-I characteristic at different temperatures b) Optical spectra at different temperatures in pulsed regime
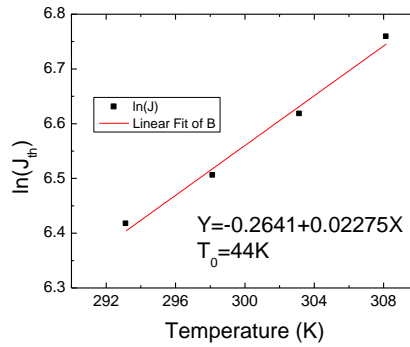
Figure 5.16: Natural logarithm of J_{th} as a function of temperature to determine T_0

5.4.2   Demonstration of integrated GaSb-based laser with polymer waveguide coupling to a silicon waveguide

It is a common goal for integrated waveguide circuits to couple light between active devices and passive waveguide circuits. In this case, an integrated GaSb-based FP laser fabricated on an SOI waveguide circuit is designed to couple its output power to a single mode Si waveguide using a polymer waveguide formed on an inverted Si taper. From the simulation results in Section 5.2.2, a 10μm polymer waveguide is selected while the laser has a top heat removal structure. The polymer waveguide width is kept slightly wider than the mesa to ensure high coupling efficiency. The same epitaxial structure as described in Section 5.4.1,
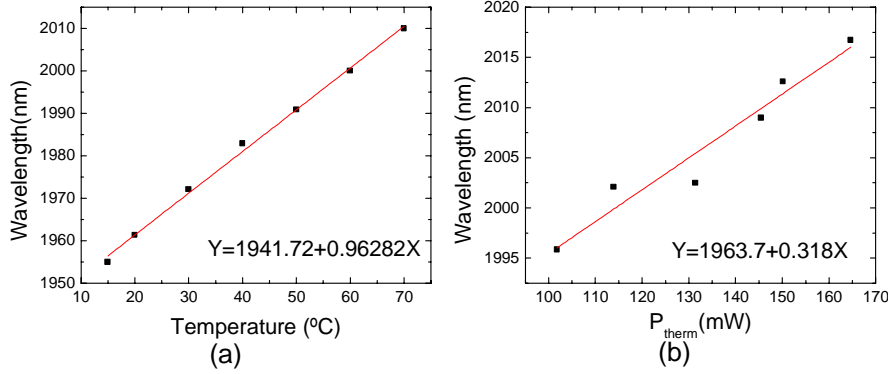
Figure 5.17: Lasing wavelength change as a function of a) carrier temperature (pulsed operation, so no self-heating) b) power consumption

is used for this work. Therefore, the same integration and laser fabrication as discussed in Section 5.3 are employed. The polymer waveguide is formed using RIE etching with a SF_6 and O_2 mixture (Section 3.3.4.2) at the same time with the opening process of the contact vias. Fig. 5.18a shows the optical image of the coupling section. The polymer waveguide streches from the edge of the laser facet to the end of the inverted taper. 200μm is left from the end of the polymer taper to the edge of the cleaved Si waveguide. A coupling length of 400μm is used. The back facet is formed using focused ion beam (FIB) to achieve high reflectivity ($\sim30\%$) due to the fresnel reflection at the semiconductor-air interface. The reflectivity of the front facet formed at the interface between DVS-BCB and the laser is calculated at $R\sim16\%$ ($n_{DVS-BCB}$ = 1.54 [15], n_{laser} = 3.6). Fig. 5.18b shows the cross section of the laser. The laser mesa is 6.5μm wide and the length is 925μm. The bonding thickness is 560nm, measured from the oxide box.

The Si waveguide is cleaved to collect the laser output power horizontally using 50μm core diameter multimode fiber (M42L01 from Thorlabs). The same measurement setup as discussed in Section 5.4 is utilized. Fig. 5.19a shows the L-I characteristic at 5 and 10°C in CW mode. The threshold current is 85mA in pulsed regime and 130mA in CW mode. This corresponds to a J_{th} of 1.4kA/cm² and 2.2kA/cm², for pulsed and CW regime respectively. This high J_{th} is attributed to the small size of the laser mesa. This in turn, gives high R_s and therefore increases the internal temperature. The optical spectrum measured at 10°C is shown in Fig. 5.19b. The lasing wavelength is at $\sim2.01\mu$m at 5°C in CW mode. Fig. 5.19c represents the comparison of the L-I characteristic using multimode fiber and single more fiber (M42L01 and SMF-28 respectively) at 5°C temperature. Multimode fiber gives higher coupling efficiency than single mode fiber. The low output power is attributed to the misalignment between the laser and Si waveguide
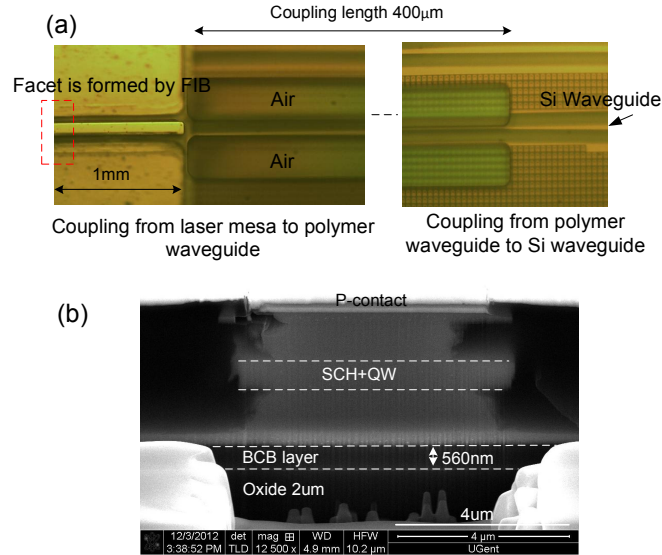
Figure 5.18: a) Optical image of the realized device representing the top view of the laser mesa connected to the polymer waveguide formed on an inverted Si waveguide b) SEM image of the cross section of the laser mesa

as shown in Fig. 5.18.

5.5 Summary and outlook

In summary, the integration and fabrication technique for integrated GaSb-based FP lasers on an SOI waveguide circuit is developed and demonstrated. I developed a simple FP laser fabrication technique employing only wet etching processes which can potentially be used in wafer scale manufacturing. Subsequently, the integration of a GaSb-based FP laser on a InP substrate is demonstrated as a proof of concept to confirm the feasibility of realizing thin-flim GaSb-based FP lasers onto any carrier with good performance. The integrated laser operates at room temperature with low threshold current density($676A/cm^2$ in CW operation). The lasing wavelength is around 2.0μm. Furthermore, the integration of a GaSb-based laser on an SOI waveguide circuit is demonstrated. The integrated FP laser operates in CW mode at temperatures up to 10°C with a J_{th} of $1.4kA/cm^2$ and $2.2kA/cm^2$, for pulsed and CW regime respectively. A polymer waveguide formed on an inverted Si taper is used to couple the light from the laser facet to a single mode Si waveguide. The simulation shows maximum coupling efficiency of 62% with perfect waveguide alignment and optimized epitaxy stack. This coupling design

allows the utilization of a standard epitaxial laser structure with high quantum efficiency to be integrated on an SOI waveguide circuit. Our experiment confirms this possibility.

However, there are some fabrication limitations which may adversely affect the laser performance, for example, misalignment between the laser and Si waveguide, therefore, decreasing coupling efficiency. Another limit of this type of integrated laser is the difficulty to form a highly reflective mirror for the laser cavity. The maximum reflectivity that can be achieved in our design is the reflection at the interface of air and III-V using FIB which is not a wafer scale technique. An alternative is to use dry etching. Moreover, there is always a need for single wavelength lasers.

To solve these problems, in the next chapter, I investigate another type of integrated laser where the design can accommodate a more efficient light coupling into an Si waveguide circuit. The design is improved using a distributed feedback structure formed on the Si waveguide. This structure allows the formation of a high performance single wavelength laser.
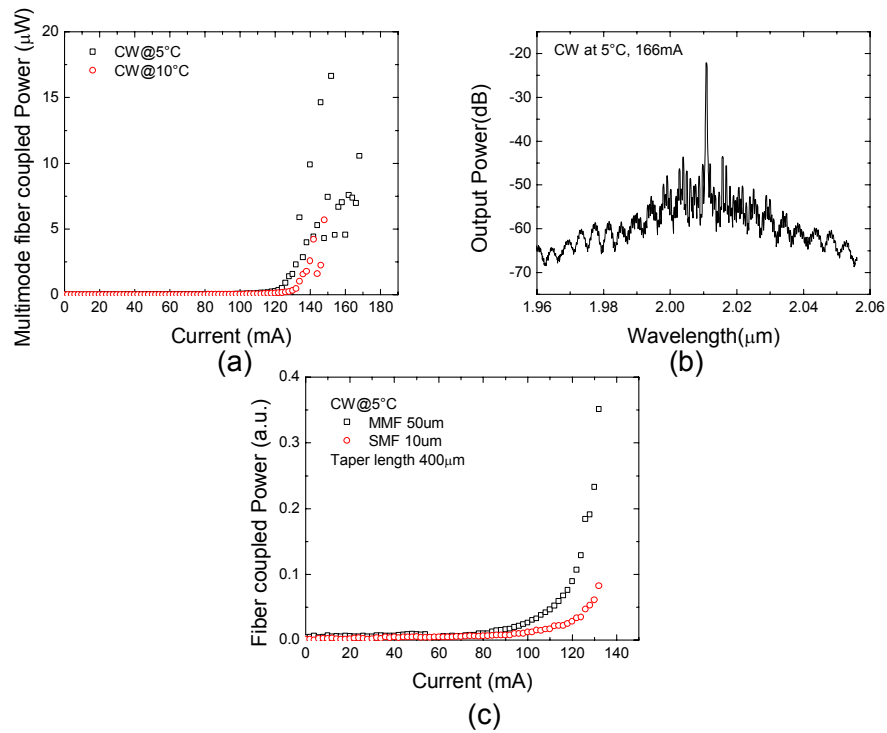
Figure 5.19: Characteristic of the integrated GaSb-based FP laser a) L-I characteristic at 5 and 10°C b) Optical spectrum at 10°C c) A comparison of output power using multimode fiber and single mode fiber

References

[1] Glucosens, *Glucosens*, *http://www.glucosens.be/node/1*.

[2] M. Peach, *Gas sensor based on mid-infrared MEMS design*, *http://optics.org/news/4/2/37*.

[3] J. Piprek. *Semiconductor Optoelectronic Devices*. Elsevier Science B. V., 2003.

[4] C. Alibert, M. Skouri, A. Joullie, M. Benouna, and S. Sadiq. *Refractive indices of AlSb and GaSb-lattice-matched in the transparent wavelength region*. J. Appl. Phys., 69(5):3208–3211, 1991.

[5] E. Hecht. *Optics*. Pearson Education, Inc, 2002.

[6] F. Trager. *Handbook of lasers and optics*. Springer Science+Business Media, 1 edition, 2007.

[7] A. W. Fang, E. Lively, Y.-H. Kuo, D. Liang, and J. E. Bowers. *A distributed feedback silicon evanescent laser*. Opt. Express, 16(7):4413–9, March 2008.

[8] M. Rattunde, J. Schmitz, G. Kaufel, M. Kelemen, J. Weber, and J. Wagner. *GaSb-based 2.X μm quantum-well diode lasers with low beam divergence and high output power*. Appl. Phys. Lett., 88(8):081115, 2006.

[9] L. A. Coldren and S. W. Corzine. *Diode Lasers and Photonics Integrated Circuits*. John Wiley & Sons, Inc., 1 edition, 1995.

[10] M. Leers, K. Boucke, M. Götz, A. Meyer, M. Kelemen, N. Lehmann, and F. Monti di Sopra. *Thermal resistance in dependence of diode laser packages*. Proc. SPIE, 6876:687609–1–11, February 2008.

[11] C. Mermelstein, S. Simanowski, M. Mayer, R. Kiefer, J. Schmitz, M. Walther, and J. Wagner. *Room temperature CW Operation of GaInAsSb/AlGaAsSb Quantum Well Lasers Emitting in the 2.2 to 2.3μm wavelength range*. Appl. Phys. Lett., 77(11):1581–1583, 2000.

[12] I. Vurgaftman, J. R. Meyer, and L. R. Ram-Mohan. *Band parameters for III-V compound semiconductors and their alloys*. J. Appl. Phys., 89(11):5815, 2001.

[13] S. Adachi. *Properties of Semiconductor Alloys : Group-IV , III-V and II-VI Semiconductors*. John wiley & Sons Ltd., 1 edition, 2009.

[14] *CAMFR*, *http://camfr.sourceforge.net/*. 2013.

[15] Dow chemical Company, *CYCLOTENE 3000 Series Advanced Electronic Resins*, *http://www.dow.com/cyclotene/prod/302235.htm*. 2005.

[16] *Mode Solvers Waveguide CAD Software FIMMWAVE*, *http://www.photond.com/products/fimmwave.htm*.

[17] *ePIXfab*, *http://www.epixfab.eu/*.

[18] *COMSOL Multiphysics*, *http://www.comsol.nl/*. 2013.

[19] S. Adachi. *Lattice thermal conductivity of group-IV and III-V semiconductor alloys*. J. Appl. Phys., 102(6):063502, 2007.

[20] S. Arafin. *Electrically - Pumped GaSb-Based Vertical-Cavity Surface-Emitting Lasers*. PhD thesis, Technische Universitat Munchen, 2012.

[21] T. Borca-Tasciuc, D. W. Song, J. R. Meyer, I. Vurgaftman, M.-J. Yang, B. Z. Nosho, L. J. Whitman, H. Lee, R. U. Martinelli, G. W. Turner, M. J. Manfra, and G. Chen. *Thermal conductivity of $AlAs_{0.07}Sb_{0.93}$ and $Al_{0.9}Ga_{0.1}As_{0.07}Sb_{0.93}$ alloys and $(AlAs)_1/(AlSb)_{11}$ digital-alloy superlattices*. J. Appl. Phys., 92(9):4994, 2002.

[22] S. Supplies, *Crystalbond and Wafer-mount Washaway Mounting Adhesives*, *http://www.crystalbond.com/*.

[23] Y. Chen and D. Donetsky. *Optical Mode Parameters of the 2.3um Al(In)GaAsSb/GaSb Ridge-waveguide Laser Diodes and Laser Diode Arrays*. Prog. Electromagn. Res. Symp., pages 577–581, 2008.

[24] S. M. Sze and K. K. NG. *Physics of Semiconductor Devices*. John Wiley & Sons, Inc., 3 edition, 2007.

[25] E. F. Schubert. *Light Emitting Diodes*, volume 12180. Cambridge University Press, 2 edition, 2006.

[26] W. Bewley. *Ridge-width dependence of midinfrared interband cascade laser characteristics*. Opt. Eng., 49(11):111116, November 2010.

[27] M. Garcia, A. Salhi, P. A., Y. Rouillard, C. Sirtori, X. Marcadet, and C. Alibert. *Low Threshold High-Power Room-Temperature Emitting at 2.264μm*. IEEE Photonics Technol. Lett., 16(5):1253–1255, 2004.

[28] G. W. Turner, H. K. Choi, and M. J. Manfra. *AlGaAsSb lasers emitting at 2.05μm*. Appl. Phys. Lett., 72(8):876–878, 1998.

6

Electrically Pumped Hybrid InGaAsSb-Si Laser Emitting at 2.42μm

In this work, I report on an electrically pumped hybrid Fabry-Perot (FP) InGaAsSb-Si laser emitting at 2.42μm wavelength. The device has a threshold current density (J$_0$) of 1.75kA/cm^2 at infinite length at 10°C in pulsed regime. The design, fabrication process and measurement results are discussed. The design of a hybrid InGaAsSb-Si distributed feedback laser is also included.

6.1   Introduction

In the previous chapter, thin-film GaSb-based FP lasers on InP substrate were demonstrated. The results were a proof of principle of the fact that the integration of GaSb-based lasers on an InP substrate operating CW with low threshold current is feasible. The device was further integrated on an SOI waveguide circuit. A polymer waveguide is designed to couple the light output from the laser facet into the Si waveguide circuit. The results bring us a step closer to a fully integrated spectrometer. Nevertheless, the polymer waveguide is not an optimal solution for laser integration on a platform. Moreover, typically there is a need for single wavelength devices instead of FP type lasers.

In this chapter, I propose an electrically pumped hybrid InGaAsSb-Si laser
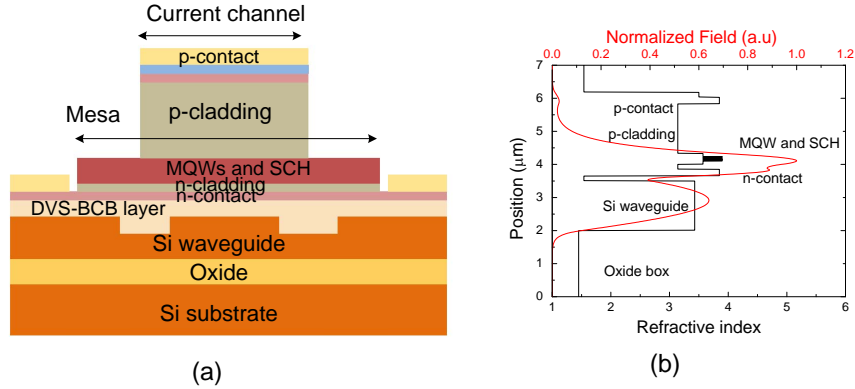
Figure 6.1: a) Not-to-scale device schematic b) optical mode profile ($\lambda = 2.42\mu m$,
TE-polarization)

where the optical mode is designed to be predominantly confined in the Si waveg-uide. The design allows flexible control over the light coupling between laser cavity and Si waveguide. Single mode lasing operation can be achieved by imple-menting a wavelength selective grating in the Si.

The chapter begins with the epitaxial and optical design of the integrated hy-brid laser. It is followed by an explanation of the SOI fabrication process, the III-V on Si integration as well as the laser fabrication. The measurement results of an integrated FP lasers on SOI waveguide are presented. The simulation results on a hybrid distributed feedback (DFB) laser are analysed and discussed. The chapter ends with a summary and an outlook of this work.

6.2 Design and Simulation

The schematic of the proposed device is shown in Fig. 6.1a. The laser structure consists of $In_{0.67}Ga_{0.33}As_{0.12}Sb_{0.88}$ QWs (quantum wells) as a gain region and uses Si as a passive waveguide material. The 1-dimensional optical mode profile along the Y axis is shown in Fig. 6.1b. The device is designed such that the optical mode is divided over the Si waveguide and GaSb laser waveguide. Therefore, a fraction of the optical mode overlaps with the QW active region to provide gain. This approach provides a route towards the efficient coupling of the laser radiation to an adjacent passive Si waveguide circuit. The drawback of this design is the small overlap with the QWs resulting in low modal gain. This leads to an increase in threshold current. The optical mode and confinement factor in the active region can be manipulated by changing the Si waveguide width and thickness and DVS-BCB thickness as will be discussed later.

Layer	Material	Thickness (nm)	Doping	Refractive index	loss at 2.4μm (cm^{-1})
n-contact	GaSb	150	2x10^{18}	3.85	80
n-grading	composition grating	100	2x10^{18}	3.5	22
n-cladding	Al$_{0.9}$Ga$_{0.1}$As$_{0.08}$Sb$_{0.92}$	100	5x10^{17}	3.14	5.6
SCH	Al$_{0.35}$Ga$_{0.65}$As$_{0.03}$Sb$_{0.97}$	100	undoped	3.57	
MQWs	Ga$_{0.67}$In$_{0.33}$As$_{0.12}$Sb$_{0.88}$	10x4	undoped	3.9	
	Al$_{0.35}$Ga$_{0.65}$As$_{0.03}$Sb$_{0.97}$	30x3	undoped	3.57	
SCH	Al$_{0.35}$Ga$_{0.65}$As$_{0.03}$Sb$_{0.97}$	100	undoped	3.57	
p-cladding	Al$_{0.9}$Ga$_{0.1}$As$_{0.08}$Sb$_{0.92}$	500	5x10^{17}	3.14	8
p-cladding	Al$_{0.9}$Ga$_{0.1}$As$_{0.08}$Sb$_{0.92}$	1000	2x10^{18}	3.14	32
p-grading	composition grating	100			32
p-contact	GaSb	100	1x10^{19}	3.9	70
etch stop layer	InAs$_{0.91}$Sb$_{0.09}$	150	1x10^{19}	3.5	
substrate	GaSb				

Table 6.1: Epitaxial structure used for this work

The laser epitaxial structure is grown by MBE (solid source molecular beam epitaxy) at the university of Montpellier 2. The epitaxy is grown on a n-doped (100)GaSb substrate in a reversed stack growth fashion. A highly doped tunnel junction consisting of 150nm n-doped InAsSb(Si-1x10^{19} cm^{-3})/100nm p-doped GaSb(Si-1x10^{19} cm^{-3}) is used as a p-contact with the aim of achieving low contact resistance [1]. 100nm compositional grading between the p-GaSb and Al$_{0.9}$Ga$_{0.1}$As$_{0.07}$Sb$_{0.93}$ p-cladding layer is inserted to reduce the series resistance. 1.5μm of p-doped Al$_{0.9}$Ga$_{0.1}$As$_{0.07}$Sb$_{0.93}$ is used as a p-cladding to keep the optical mode away from the p-contact. The doping is done in 2 steps: Si-1x10^{18} cm^{-3}for 1.0μm and Si-5x10^{17} cm^{-3} for 0.5μm close to the active region to reduce free carrier absorption. The active region consists of 4 QWs of In$_{0.67}$Ga$_{0.33}$As$_{0.12}$Sb$_{0.88}$ with 1.2% compressive strain separated by Al$_{0.35}$Ga$_{0.65}$As$_{0.03}$Sb$_{0.97}$ barriers. The QW active region is surrounded by 100nm thick Al$_{0.35}$Ga$_{0.65}$AS$_{0.03}$Sb$_{0.97}$ separate confinement layers (SCH) on both n and p side. 100nm of 5x10^{17} cm^{-3} Te-doped Al$_{0.9}$Ga$_{0.1}$As$_{0.08}$Sb$_{0.92}$ is used as n-cladding followed by a 100nm compositional grading layer to the highly doped (Te-2x10^{18} cm^{-3}) 100nm thick n-GaSb contact layer. The epitaxial structure is summarized in Table 6.1.

Fig. 6.2a represents the simulation of the confinement factor in Si and QWs as a function of Si thickness, for the fundamental TE mode at 2.42μm. The Si
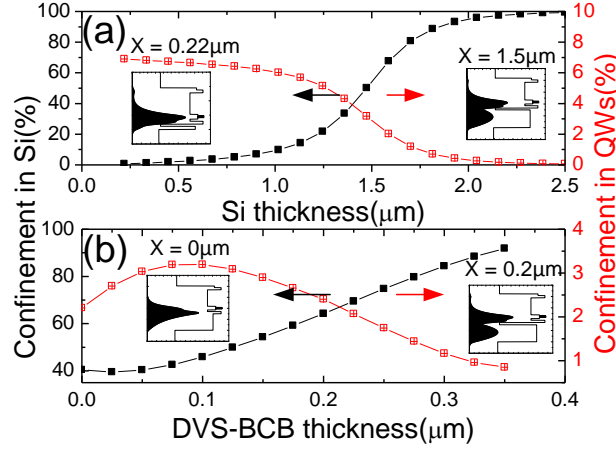
Figure 6.2: Simulation of Si and QW confinement for different a) Si thickness b) DVS-BCB bonding thickness. (λ=2.42μm, TE-polarization) The insets show the optical mode field distribution along the Y-axis (Fig. 6.1) for different parameters of the structure

etch depth and the DVS-BCB thickness between the top of the Si waveguide and the bottom of the epitaxial structure are kept at 150nm for this simulation. The Si waveguide width is 3μm and the mesa width is 21μm. The confinement factor in Si increases significantly in a Si thickness range from 1μm to 1.7μm after which it saturates while the opposite happens for the QW confinement. A Si thickness of 1.5μm is selected for this experiment to obtain a confinement factor of 50% and 3% in the Si and QW region respectively. Fig. 6.2b shows the impact of the bonding layer thickness on the Si and QW confinement factor. All other parameters are kept the same as in Fig. 6.2a. A strong dependence of the mode profile on the DVS-BCB thickness can be seen. In this experiment, 150nm BCB thickness is selected. The simulated modal loss in this waveguide structure is $9.5cm^{-1}$ which is mostly related to the free carrier absorption losses in the n-doped contact layer. In addition, due to the narrow Si waveguide trench in this first design (2μm) additional loss results from the leakage of the optical mode to the Si slab ($42cm^{-1}$) for a 2μm wide Si waveguide. This leakage loss can be eliminated by increasing the trench width from 2 to 6μm

6.3 Integration and device fabrication

The Si waveguide is patterned using i-line contact lithography. The waveguide is formed using RIE (Reactive Ion Etching) using a SF_6-O_2 chemistry etching 150nm deep into the Si device layer (see Section 3.3.4.2). The Si sample is then cleaned using a RCA solution (NH_4OH:H_2O:H_2O_2, 1:5:1 v/v) for 15 minutes at
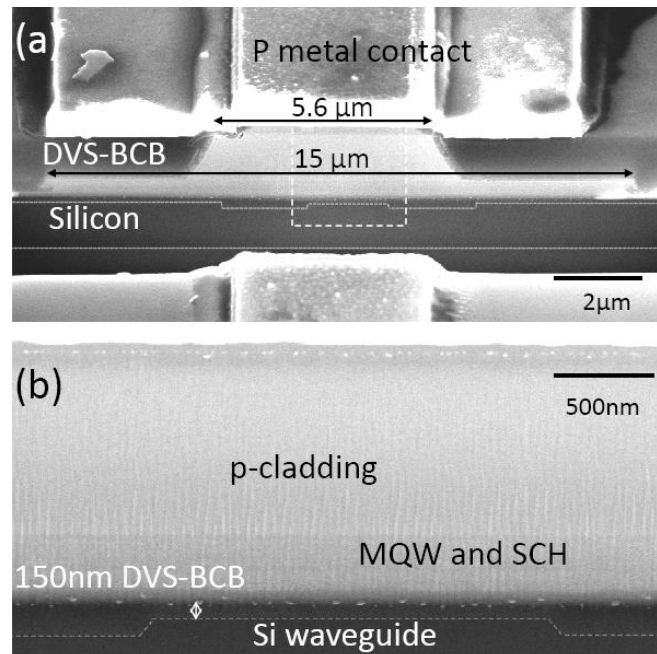
Figure 6.3: SEM image of the realized laser a) overall cross section indicating the current injection channel and mesa b) the inset of Fig. 6.3a representing the bonding interface

80°C. Afterwards, the sample is dried at 150°C for 5 minutes. The integration is performed through a die-to-wafer bonding process utilizing DVS-BCB as a bonding agent. The thickness of the DVS-BCB is controlled by diluting the polymer in mesitylene. The DVS-BCB:mesitylene 1:3 solution is spin coated on the sample for planarization. The sample is then pre-cured at 210°C for 40 minutes. A second layer of DVS-BCB with the same dilution is then spin coated on the sample as bonding layer. The epitaxy is brought in contact with the Si waveguide chip in air after the sample is cooled down to 90°C. The sample is then loaded into the bonding chamber (SUSS Microtec Elan CB6L substrate bonder). The bonding is performed in a vacuum. The DVS-BCB is cured at 250°C for 1hr in a nitrogen environment. The general details of bonding machine and bonding procedure can be found in Section 3.2.4.2. The GaSb substrate is then completely removed by using a combination of lapping (Section 3.3.2) and wet etching (CrO_3:HF:H_2O, 1:1:3 v/v, see Section 3.3.3.1), using 150nm InAsSb as an etch stop layer.

The laser mesa is formed completely by wet etching. The selection of the etching solution depends on the material. For InAsSb, a mixture of citric acid:
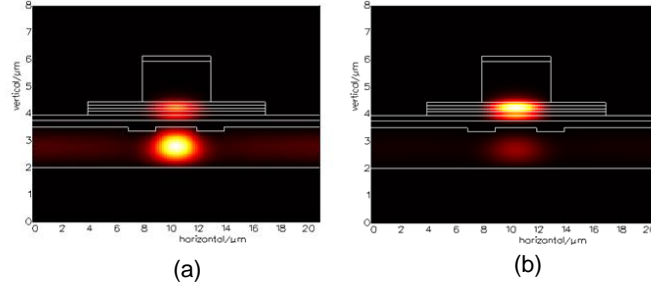
Figure 6.4: Simulated optical mode of the hybrid integrated InGaAsSb-Si laser waveguide a) fundamental mode with DVS-BCB thickness of 250nm b) the second-order mode with DVS-BCB thickness of 250nm. The simulation is performed using a 3μm wide Si waveguide, 5μm wide injection channel, 2μm wide trench

H_2O_2 (2:1 v/v) is used (Section 3.3.3.2). A H_2O_2:HCl:H_2O (1:50:100 v/v) solution is used for etching $Al_{0.9}Ga_{0.1}As_{0.08}Sb_{0.92}$. Finally, QWs, separate confinement layers (SCH) and GaSb layers are etched using a phosphoric acid based solution(citric acid:H_2O_2:H_3PO_4:H_2O 55:5:3:220 v/v). Ti/Pt/Au(2nm/35nm/100nm) and GeAu/Ni/Au(150nm/50nm/100nm) are deposited as p-contact and n-contact respectively. The laser ridge is then passivated with 100nm SiO_2. DVS-BCB (3022-46) is finally used for planarization. The p and n contact vias are then opened using RIE (SF_6-O_2 chemistry), after which 20/500nm Ti/Au is deposited for probing. The Si substrate is lapped down to 100μm to accommodate the cleaving process, after which the laser facets are formed. No facet polishing or high reflection coating is applied. The experiment is performed using 2 different Si waveguide widths (2, 3μm) and varying laser mesa width and cavity length. The current injection window is kept nominally at 5μm. Fig. 6.3 shows a SEM (scanning electron microscope) cross section image of one of the lasers. Fig. 6.3a represents the overall structure of the laser waveguide. The current injection window is 5.6μm wide and the laser mesa is 15μm wide. The bonding interface is shown in Fig. 6.3b. The bonding layer is approximately 150nm thick.

Additionally, the uniformity of the thickness of the DVS-BCB layer is investigated in this structure by performing a FIB cross section at several points on the sample within an area of 1x1mm^2. The thickness of the DVS-BCB layer is found to be between 150nm to 250nm. This thickness variation is most likely caused by the nonuniform force applied on such a small sample. This thickness variation is believed to cause the lasing mode profile to be a combination of the fundamental hybrid mode and the second-order mode which is predominantly confined to the III-V. Fig. 6.4 shows the simulated mode profiles (TE-polarization) of a) the hybrid optical mode in a III-V/Si structure with 250nm DVS-BCB thickness and b) a second-order hybrid mode (250nm DVS-BCB thickness) using the following

parameters: 3μm Si waveguide, 5μm injection channel, 2μm trench. As can be seen, in Fig. 6.4a, for the fundamental mode, the confinement in Si increases as the thickness of DVS-BCB increases. This leads thereby to a reduction of the optical gain and consequently increasing threshold current. The second-order mode is strongly leaking when the DVS-BCB thickness is 150nm. As the thickness of the DVS-BCB increases, the overlap of the optical mode and QWs increases as shown in Fig. 6.4b. At the same time, the modal loss of the second-order mode is reduced, therefore, it is possible for the second-order mode to start lasing when the DVS-BCB thickness is at 250nm. This problem can be solved by increasing the trench width to be wider than 6μm. This suppresses the leakage loss, thereby, maintaining the internal loss of the fundamental mode to be smaller than the second order mode at thick DVS-BCB layer.

6.4 Experimental results and discussion

The lasers are characterized using standard multimode fiber (50μm core) butt-coupled to the laser facet. An optical spectrum analyzer (Yokogawa AQ6375) is used to record the output spectrum and average optical output power from a single facet. Needles probes are used to inject current from a Keithley 2400 source for CW operation and from a Lightwave 3811 current source for pulsed operation. A thermoelectric cooling stage is used for controlling temperature.

6.4.1 Optical Performance

Fig. 6.5 represents the L-I characteristic of a InGaAsSb/Si hybrid laser at $10°$C in pulsed regime. The output spectrum of this device is presented in the inset of Fig. 6.5. The device is 590μm long and has a 5μm wide current injection window, a laser mesa width of 17μm and a Si waveguide width of 3μm. This yields a threshold current density (J_{th}) of 3.78kA/cm^2. The spectrum shows multimode behavior as expected from a FP laser. The threshold current density J_{th} is plotted in Fig. 6.6 as a function of the inverse of the device length for 2μm and 3μm width Si waveguide devices, while the other parameters are kept the same. A transparency threshold current density (J_0) of 1.75kA/cm^2 and 816A/cm^2 is obtained for a Si width of 2μm and 3μm respectively. As discussed earlier, this high J_0 is expected from the high modal loss as well as the small overlap with the gain region. Therefore, this can be improved by reducing the doping level in the n-contact layer to decrease free carrier absorption. Increasing the overlap with the QW active region by using thinner DVS-BCB and/or Si is also possible. In addition, the threshold current density at infinite length J_0 of 2μm Si waveguide structures is higher than that of the 3μm Si waveguide width. This agrees well with the estimation of the optical mode leakage in the 2μm wide Si waveguide as discussed earlier.
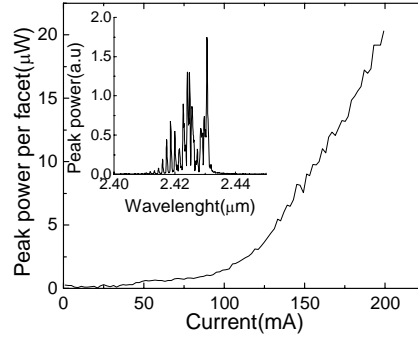
Figure 6.5: L-I characteristic of the laser at 10°C. The current injection window is 5μm wide and the Si waveguide width is 3μm. The laser cavity is 590μm long. The inset represents the emission spectrum at 200mA drive current
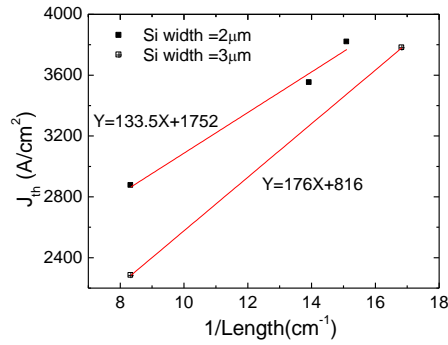
Figure 6.6: J_{th} at 10°C as a function of inverse cavity length resulting in a threshold current density J_0 at infinite length of 1.75kA/cm^2 for a 2μm Si waveguide width and 816A/cm^2 for a 3μm wide Si waveguide.

6.4.2   Thermal Characteristics

Fig. 6.7a represents the L-I characteristic of the hybrid laser at different temperatures. By fitting the natural logarithm of the threshold current density as a function of the stage temperature as shown in Fig. 6.7b, a characteristic temperature (T_0) of 53K is obtained. This value of T_0 is comparable to the value obtained for GaSb lasers on their native substrate with an emission wavelength close to 2.5μm (40-71K) [2, 3].
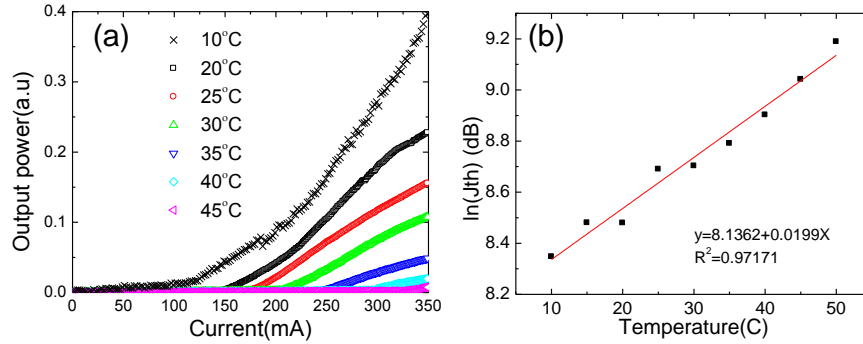
Figure 6.7: a) L-I characteristic at different temperatures b) Natural logarithm of threshold current as a function of stage temperature (3μm Si waveguide width, 5μm wide current injection window, 590μm long laser cavity)
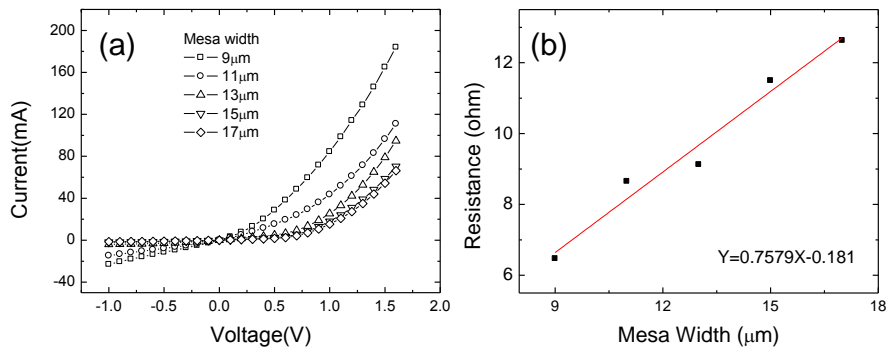
Figure 6.8: a) I-V characteristics and b) series resistance as a function of mesa width (3μm wide Si waveguide, 5μm current injection window, 718μm long laser cavity)

6.4.3   Electrical Characteristics

Fig. 6.8a represents the I-V characteristic of different lasers (3μm Si width, 5μm current injection window and 718μm length) with varying mesa width. Fig. 6.8b shows the series resistance as a function of mesa width. As can be seen, at negative bias, the leakage current increases for narrower mesas, while the series resistance at positive bias increases linearly with the mesa size. This leakage current implies that current injection of these lasers is not very efficient. This is attributed to a leakage current on the surface of the etched mesa. Therefore, it can be improved by increasing the mesa width in exchange for a slight increase in series resistance.
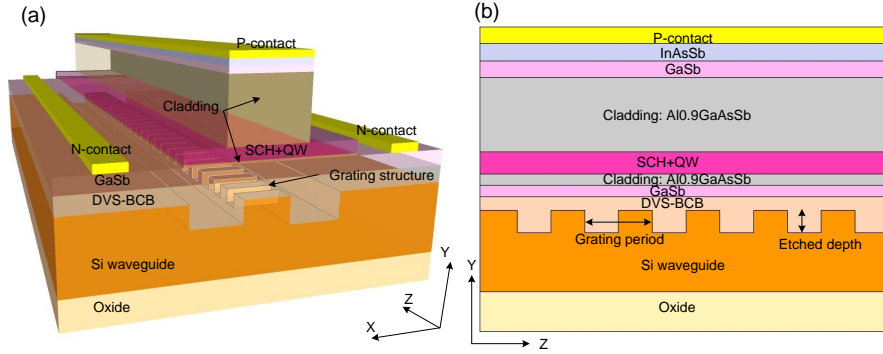
Figure 6.9: a) Schematic of proposed hybrid InGaAsSb-Si DFB laser b) Cross section of a) along YZ representing important parameters for designing hybrid DFB laser

6.5   Towards integrated hybrid InGaAsSb-Si distributed feedback (DFB) laser diodes

FP lasers support many longitudinal modes which is not suitable for several applications such as gas sensing. In order to obtain a single mode laser, a wavelength selective element such as a Bragg grating can be incorporated into the laser cavity. Fig. 6.9a presents the proposed laser structure where the Bragg grating is formed on the Si waveguide. The epitaxial die is bonded on top of SOI waveguide circuit similar to the proposed hybrid FP laser structure as described earlier. A schematic of a cross section of Fig. 6.9a along the YZ is presented in Fig. 6.9b which indicates the critical parameters for this design.

The DFB laser behaviour is determined by the Bragg condition:

$$2 \cdot \Lambda = m \cdot \lambda = m \frac{\lambda_0}{n_{eff}} with \ m = \cdots, -2, -1, 0, 1, 2, \cdots \quad (6.1)$$

where Λ is the grating period, λ is the wavelength of the lasing mode and n_{eff} is an average effective index of the fundamental mode of the etched and unetched waveguide. *m* is the integer representing the order of the grating. Generally, first and second-order gratings are most commonly used. Λ is inversely proportional to the average of the effective refractive indices which depends on the waveguide structure, the duty cycle of the grating and the etch depth as depicted in Fig. 6.9b. The duty cycle is defined as the ratio of the length of the unetched slab (Λ_h) to Λ. In this work, the epitaxial structure is kept the same as for the FP laser. CAMFR [4] is employed to calculate the effective index of the 1D structure as well as the period of the grating. The simulation of the first-order grating period as a function of lasing wavelength is depicted in Fig. 6.10. The period has to be varied from 0.34 to 0.37μm to cover the wavelength from 2.3 to 2.5μm which is already
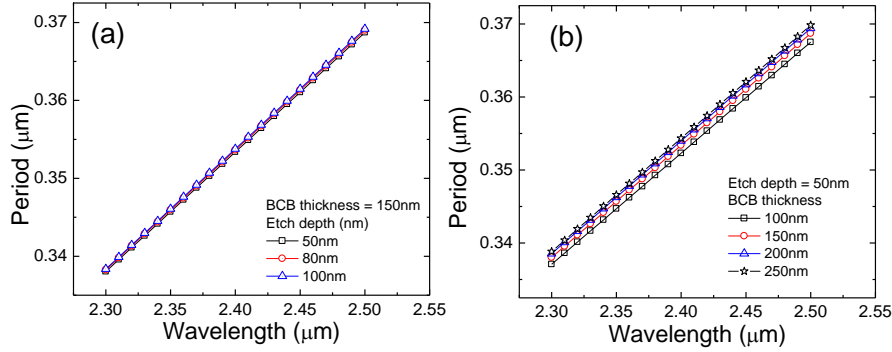
Figure 6.10: The first-order grating period as a function of lasing wavelength assuming a 50% duty cycle a) at different etch depth where the DVS-BCB thickness is 150nm b) at different DVS-BCB thicknesses where the etch depth is 50nm

boarder than the bandwidth of the gain medium. There are small changes in the grating period when the etch depth and the thicknesses of DVS-BCB are varied as shown in Fig. 6.10a and b respectively. However, if the etch depth is large, it is difficult to fill in all trenches using DVS-BCB. Consequently, it leads to poor bonding quality. Therefore, an etch depth of 50nm was selected and used for following simulations. For the first-order grating, a duty cycle of 50% is used for this simulation. From the previous discussion on hybrid FP lasers, we can conclude that the gain peak is located at 2.4μm wavelength. Therefore, 2.4μm is used for the following simulations.

The parameter typically used to design distributed feedback gratings is the coupling coefficient (κ) which represents the reflectivity of the fundamental propagating mode per unit length (cm^{-1}). Assuming a square profile of the grating and using a perturbation approximation, κ is expressed as [5, 6]:

$$\kappa = \frac{2(n_{eff}^h - n_{eff}^l)}{m.\lambda_0}.sin(m.\pi\frac{\Lambda_h}{\Lambda}) \tag{6.2}$$

where n_{eff}^h and n_{eff}^l are the effective indices of the fundamental mode in the unetched and etched slab respectively. *m* is the order of the grating. The maximum value of κ is obtained when 50% duty cycle is used for the first-order grating. From Equation 6.2, one can see that κ depends strongly on the effective indices of the etched and unetched structure i.e. it depends, therefore, on the etch depth and the thickness of DVS-BCB layer. Fig. 6.11 shows the dependence of κ as a function of the thickness of DVS-BCB layer and etch depths. A very high value of κ is not desirable because it leads to a short cavity length, thereby, increasing the self-heating effect. Reducing κ by using thick DVS-BCB layer would also leads to an increment in self-heating effect due to the low thermal conductivity of the DVS-
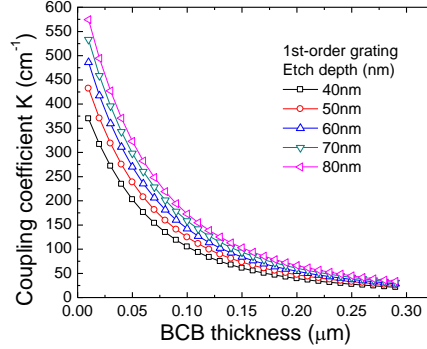
Figure 6.11: Coupling coefficient κ as a function of DVS-BCB thickness at different etched depths

BCB as discussed in Section 5.2.3. A compromise between a reasonable value for the coupling strength κ and bonding yield leads to the selection of a 50nm etch depth and 100nm bonding layer thickness for this work.

In order to decide the length of the grating of DFB lasers (L_g which would provide sufficient reflectivity (R) for laser cavity as well as light output coupling), the product of κ and the grating length (L_g) is normally assessed. The relationship between κ, L_g and R is expressed as [7] (assuming a transparent laser waveguide):

$$R = tanh^2(\kappa \cdot L_g) \rightarrow \kappa \cdot L_g = arctanh(\sqrt{R}) \tag{6.3}$$

A typical value of $\kappa.L_g$ is chosen between 1-3 for a DFB laser. Very high $\kappa.L$ results in spatial hole burning and low output power [8] which is undesirable. Fig. 6.12a and b illustrates $\kappa.L$ as a function of grating length for different DVS-BCB thickness both for a first-order and second-order grating respectively. As expected, thin DVS-BCB layers provide a high $\kappa.L_g$ product for both the first-order grating (assuming a 50% duty cycle) and the second-order grating (assuming a 75% duty cycle). An etch depth of 50nm is used for this simulation. Considering 100nm DVS-BCB thickness, it is possible to obtain a value of $\kappa.L_g$ up to 4 with a L_g of only 300μm. The reflectivity in the second-order grating is weaker compared to the first-order grating at the same DVS-BCB thickness. This results in a longer device in the second-order grating in order to obtain the same $\kappa.L_g$ product as in the first-order grating. Nevertheless, the second-order grating device ($\Lambda \sim 0.7\mu$m) is of interest in this work because it is very challenging to fabricate the first-order grating period of $\sim 0.35\mu$m using electron-beam lithography. By fabricating the second-order grating with a period of 0.75μm, it would relax fabrication process of the grating. Also, using a second-order DFB reduces the thermal resistance of the laser.
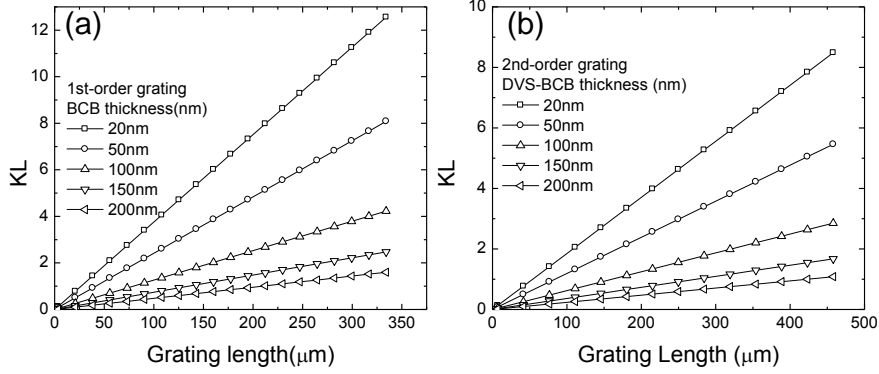
Figure 6.12: $\kappa.L$ as a function of L_g at different thicknesses of DVS-BCB with 50nm corrugation depth a) the first-order grating b) the second-order grating
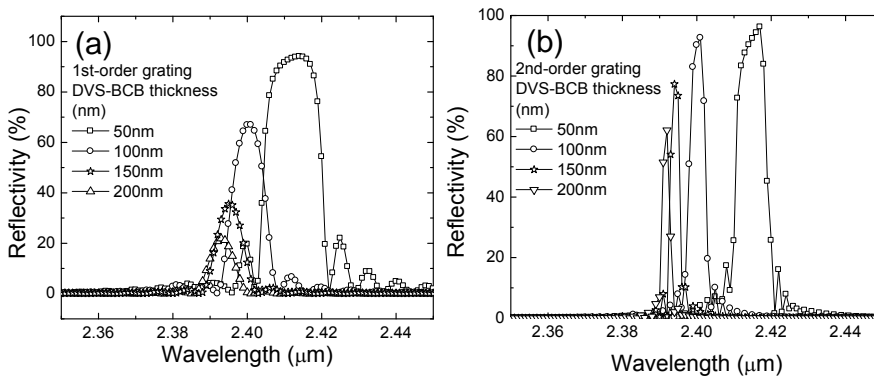
Figure 6.13: Simulated reflectivity of Bragg grating with different DVS-BCB thicknesses a) the first-order grating with $L_g = 105\mu m$ b) the second-order grating with $L_g = 420\mu m$

The impact of the thickness of the DVS-BCB layer on reflectivity and peak wavelength of the grating is investigated. 50nm etch depth and 100nm DVS-BCB thickness are used for the simulation. Λ is set at $0.35\mu m$ for the first order grating and $0.7\mu m$ for the second-order grating to achieve maximum reflectivity at $2.4\mu m$ wavelength. L_g is set at $105\mu m$ and $420\mu m$ for the first and second order grating respectively. The peak wavelength is blue-shifting with increasing DVS-BCB thickness for both the first and second order grating as depicted in Fig. 6.13a and b respectively.

6.6   Conclusion

In conclusion, I have demonstrated hybrid Si-InGaAsSb lasers which emit at 2.42μm. The devices operate at room temperature in pulsed regime. While there is still scope for device performance improvement, this demonstration brings us significantly closer to fully integrated spectroscopic systems on a Si chip. A laser with single wavelength emission using this hybrid structure is proposed. The simulation results shows the potential of this laser structure to realize a hybrid InGaAsSb-Si DFB laser emitting at 2.4μm on an SOI platform.

References

[1] O. Dier, C. Lauer, and M.-C. Amann. *n-InAsSb/p-GaSb tunnel juctions with extremely low resistivity*. Electron. Lett., 42(7):6–8, 2006.

[2] D. Barat, J. Angellier, A. Vicet, Y. Rouillard, L. Le Gratiet, S. Guilet, A. Martinez, and A. Ramdane. *Antimonide-based lasers and DFB laser diodes in the 2-2.7μm wavelength range for absorption spectroscopy*. Appl. Phys. B, 90(2):201–204, December 2007.

[3] J. G. Kim, L. Shterengas, R. U. Martinelli, and G. L. Belenky. *High-power room-temperature continuous wave operation of 2.7 and 2.8μm In(Al)GaAsSb/GaSb diode lasers*. Appl. Phys. Lett., 83(10):1926, 2003.

[4] *CAMFR, http://camfr.sourceforge.net/*. 2013.

[5] K. David, J. Buus, G. Morthier, and R. Baets. *Coupling Coefficients in Gain-Coupled DFB Lasers: Inherent Compromise Between Coupling Strength and Loss*. IEEE Photonics Technol. Lett., 1991.

[6] C. G. F. Woo-Young Choi, Jerry C. Chen. *Evaluation of coupling coefficients for laterally - coupled distributed Feedback lasers*. Jpn. J. Appl. Phys., 35:4654–4659, 1996.

[7] W. Streifer, D. R. Scifres, and R. Burnham. *Coupling coefficients for distributed feedback single- and double-heterostructure diode lasers*. IEEE J. Quantum Electron., 11(11):867–873, 1975.

[8] H. G. Shiraz. *Distributed Feedback Laser Diodes and Optical Tunable Filters*. John wiley & Sons Ltd., 1 edition, 2003.

7
Conclusions

7.1 Conclusions

Interest in sensing liquids and gases such as glucose, CH_4 and CO using SWIR spectroscopy has increased over the past decade due to the low absorption of water in this wavelength region. Conventional spectroscopic techniques, which may offer high accuracy, however, require expensive and bulky sources and detectors. A compact, low-power system is thus strongly desirable for many portable and body-implantable applications. GaSb and its compounds are excellent semiconductor materials for the SWIR. Several room temperature lasers and detectors have thus far been demonstrated using GaSb, underscoring its suitability for integrated active components. Silicon-On-Insulator (SOI), on the other hand, offers mass production of optical circuits with CMOS compatibility. This makes it ideal as a passive integrated optical circuit platform, but without the capability of light emission and detection due to the absence of a direct band gap. Combining SOI and GaSb optoelectronic components could thus yield a compact, efficient spectroscopic detection system.

The work in this thesis deals with the challenges in heterogeneous integration of GaSb based devices on SOI waveguide circuits. The work begins with an investigation of the potential of SOI waveguides as a passive, SWIR platform. Chapter 2 discusses state-of-the-art results for high efficiency fiber-to-chip grating couplers with -3.8dB insertion loss at 2.1μm. In Chapter 3, the integration and fabrication techniques for GaSb-based lasers and detectors are developed. An adhesive inte-

gration technique using DVS-BCB is used in this thesis because of its good bond-
ing properties regardless of the substrate. An assessment of different substrate
surface treatments is performed to optimize the integration process. Depending
on the device components and materials composition, etching processes (wet and
dry) and metallization are assessed and optimized. In Chapter 4, the realization of
integrated InGaAsSb photodiodes on SOI is demonstrated. The design is focused
on two main approaches to couple light from Si to III-V: evanescent and grating-
assisted coupling. The fabricated devices operate at room temperature with high
responsivity. These results prove the feasibility in integrating GaSb-based devices
on the SOI waveguide circuit platform.

In Chapter 5, an integrated Fabry-Perot (FP) laser on an SOI waveguide circuit
is investigated. The first step is to assess the possibilities in integrating lasers on
SOI waveguide circuits in developing a robust fabrication process. Standard laser
epitaxy bonded on a InP substrate is selected as a first test. FP lasers with different
lengths and mesa widths are fabricated and characterized. The minimum threshold
current density achieved at room temperature is 422 and 676A/cm^2 for pulsed and
CW operation, respectively. In the second step, the integration of FP lasers on SOI
waveguides with DVS-BCB polymer waveguides formed on a Si inverted taper to
couple light from the laser to Si waveguide are demonstrated. The lasers operate
in CW mode up to 10°C. The result demonstrates the possibility in integrating a
GaSb-based laser on any carrier. However, this laser design limits light coupling
efficiency from laser to Si waveguide. Therefore, a hybrid InGaAsSb-Si laser is
proposed and designed in Chapter 6. The design of the hybrid laser is focused on
increasing the confinement of the optical mode in the Si waveguide such that only
the evanescent field overlaps with the gain region. The first hybrid InGaAsSb-Si
FP laser emitting at 2.4μm operates up to 10°C in pulsed regime with a threshold
current density of 1.75kA/cm^2 at infinite length. This result opens up possibilities
in designing hybrid InGaAsSb-Si distributed feedback lasers.

7.2   Perspectives and future work

The successful demonstration of both GaSb-based integrated photodiodes and lasers
on the SOI platform opens up new research and development opportunities. The
following subsections lists some of these possible research directions.

Integrated InGaAsSb photodiodes

In Chapter 4, I showed that the sensitivity is greatly affected by sidewall leakage
currents. This is attributed to the sidewall surface states. To improve the sensi-
tivity, attention in reducing surface leakage current is recommended. This can be
implemented by optimizing the sidewall surface treatment using, for example, am-

monia sulfide or changing the passivation material such that the number of surface trap states is reduced. Reducing sidewall roughness/damage by further optimizing the etching recipe would also decrease sidewall leakage.

Integrated InGaAsSb-Si lasers

For integrated InGaAsSb-Si lasers, the results presented in this thesis are preliminary. There are several aspects which can be improved including thermal resistance, laser design in both optical and electrical properties, integration and fabrication technology.

Thermal resistance

As discussed in Chapter 5, the DVS-BCB bonding layer limits the heat conduction from laser to the environment, thereby, increasing thermal resistance and decreasing laser efficiency. Nevertheless, this problem can be overcome by introducing heat removal structures on top and bottom contacts (Section 5.2.3) through which the thermal resistance is reduced by 34%. Increasing the thickness of the Au for the final contact would also allow better heat conduction. Alternatively, reducing DVS-BCB thickness can also improve heat conduction through the Si substrate. However, the latter approach would compromise integration yield as thinner DVS-BCB bonding layers are found to reduce bonding yield. In addition, by flipping the laser onto a better heat conduction material such as SiC would also improve heat conductivity and thus, laser efficiency.

Laser design

In terms of laser design, Chapter 6 demonstrates the possibilities in modifying the GaSb-based epitaxy to accommodate a different optical mode design while maintaining lasing capability. The results in Chapter 6 establish a platform for further design improvement to achieve single wavelength hybrid lasers. This can be implemented by incorporating distributed feedback (DFB) into the laser cavity, as proposed in Section 6.5. Moreover, several types of reflector such as, external Bragg reflector and ring resonators can be incorporated into the laser cavity outside the gain area. With external wavelength selective components, adiabatic tapering is used to couple light from the laser to the Si waveguide. Moreover, GaSb-based material suffers from strong oxidization of AlGaAsSb, which is typically used as claddings of laser waveguides. This makes it difficult in epitaxial regrowth. Therefore, currently, the best technique to create GaSb-based DFB laser is post processing by depositing metal grating. Our technique, through incorporation of Si grating formed on SOI into the GaSb-laser cavity, allows not only integrated photonic circuit in the short-wave infrared but also alternative techniques to form

single wavelength laser without metal grating. In addition, the laser epitaxy can be further optimized to obtain lower modal loss by reducing doping in the n-contact layer.

Integration and Fabrication Technology

GaSb-based materials are considered to be at its early stage in terms of development. Indeed, little information is available in literature on both material properties and integration/fabrication techniques. For integration, yield improvement is considered to be the first priority. With the current fabrication process, the bottleneck is the substrate removal where the etchant (HF) strongly etches GaSb, Si and SiO_2. Thus the SOI substrate is damaged, when the etchant penetrates underneath the bonded die, resulting in detachment. This problem is now minimized by using CrystalBond Glue. However, this problem could be solved completely with a new etchant which can etch only GaSb with good selectivity to the etch stop layer but cannot etch SiO_2 and Si. NaK Tartrate based acid (Section 3.3.3.4) is an example of a research in this direction. However the solution still requires further optimization. Furthermore, GaSb-based material suffers from highly oxidization of AlGaAsSb which is typically used as claddings of laser waveguide. This makes it difficult in epitaxial regrowth. Therefore, currently, the best technique to create GaSb-based DFB laser is done post processing by depositing metal grating. With our technique, by incorporating Si grating formed on SOI into GaSb-laser cavity, it allows not only integrated photonic circuit in the short-wave infrared but also offers alternative technique to form single wavelength laser apart from metal grating. Alternatively, adding an InAsSb layer would also minimize HF etchant penetration because of its slow etch rate. For the mesa etching, by investigating new etchants to improve etching selectivity between materials improved control in the fabrication process could be obtained, and thereby, an enhanced fabrication yield. Further decrease on contact resistance would lower heat generation, thereby increasing laser efficiency.

The short-wave integrated photonic circuit platform

Considering the success in discrete array of integrated photodetectors and lasers in this work, it is reasonable to expect fully functional integrated photodetectors and lasers on SOI spectrometer waveguide circuit in near future. The main challenge remaining includes development of substrate removal process for large area devices.

In conclusion, the successful demonstration of integrated GaSb based lasers and detectors on SOI in this thesis has brought us a significant step closer to a fully integrated photonic circuit for sensing applications in the SWIR. While optimizations in both design and fabrication are still required to reach industrial scale

manufacturing, it is only considered a technology issue. From this work, there is no indication of fundamental limitations in the realization of the integrated GaSb-based devices on the SOI platform. Therefore, with the right technology, efforts in optimization and process engineering, integrated GaSb-based devices on SOI waveguide circuits could definitely become an important technology.

A
Material parameters

A.1   Introduction

In this section, a summary of material properties including refractive indices, absorption coefficients and thermal conductivities of several semiconductor alloys are given.

A.2   Parameter interpolation

An interpolation scheme was first introduced by Adachi et al. [1] to estimate some parameters (including refractive index, absorption coefficient, thermal conductivity) for ternary and quaternary compound semiconductors. The technique is widely used, however, its validity is still open to experimental verification.

Quaternary alloy ($A_x B_{1-x} C_y D_{1-y}$) are a composition of binary compounds (AC, AD, BC and BD), the parameter Q(x,y) of the quaternary alloy is therefore given by [1]:

$$Q\left(x, y\right) = xy B_{AC} + x\left(1 - y\right) B_{AD} + \left(1 - x\right) y B_{BC} + \left(1 - x\right)\left(1 - y\right) B_{BD}$$
(A.1)

If the relationship of ternary alloys is available, the parameter Q can also be extracted. For the full analysis of the interpolation technique, I refer to [1, 2].

For ternary alloys, the parameter T(x) can be approximated using a quadratic function [1]:
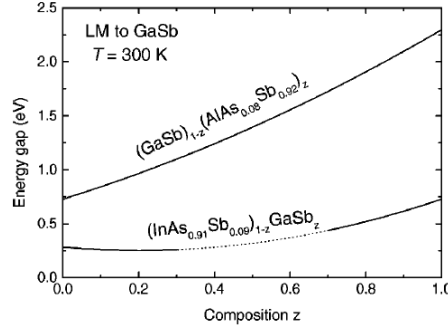
Figure A.1: Energy gaps as a function of composition for $(GaSb)_{1-z}(AlAs_{0.08}Sb_{0.92})_z$ and $(InAs_{0.91}Sb_{0.09})_{1-z}(GaSb)_z$ quaternary alloys, lattice matched to GaSb, at T= 300K. The dotted line is the approximate location of the miscibility gap (reproduced from [4])

$$T_{A(1-x)Bx}(x) = xT_B + (1-x)T_A - x(x-1)C \qquad (A.2)$$

where C is the bowing parameter.

A.3 Quaternary alloy compositions and its band gaps

A.3.1 GaSb

GaSb has a band gap of 0.726eV at 300K [3].

A.3.2 $InAs_xSb_{1-x}$

The bandgap energy of $InAs_xSb_{1-x}$ is obtained using the quadratic interpolation scheme as discussed earlier. As x = 0.91 and the bowing parameter C = 0.67eV [4], an E_g of 0.33eV is obtained.

A.3.3 $Al_xGa_{1-x}As_ySb_{1-y}$/GaSb

$Al_xGa_{1-x}As_ySb_{1-y}$ lattice matched to GaSb is generally used as separate confinement layer and cladding layer for the laser waveguide. Vurgaftman et. al [4] recommends a band gap E_g calculation at 300K as:

$$E_g = [0.727(1-z) + 2.297z - 0.48z(1-z)] \qquad (A.3)$$

Where x=z and y=0.08z. The energy gaps of $Al_xGa_{1-x}As_ySb_{1-y}$ as a function of composition is depicted in Fig. A.1.

A.3.4 $Ga_xIn_{1-x}As_ySb_{1-y}$/GaSb

$Ga_xIn_{1-x}As_ySb_{1-y}$ lattice matched to GaSb is an important material used in the quantum well region of a laser waveguide. The bandgap energy/composition dependence is calculated as [4]:

$$E_g = 0.727\,(1-z) + 0.283z - 0.75z\,(1-z) \qquad (A.4)$$

Where x=z and y=0.08z. The energy gap of $Ga_xIn_{1-x}As_ySb_{1-y}$ as a function of composition is depicted in Fig. A.1.

A.4 Refractive index

A.4.1 GaSb

The refractive index of a material depends on the photon energy, the material composition and the carrier concentration. Fig. A.2a and b present the refractive index of GaSb with n and p-doping, respectively, at different free carrier densities 1) intrinsic material 2) $2x10^{17}$ cm^{-3}, 3) $5x10^{17}$ cm^{-3} 4)$1x10^{18}$ cm^{-3} and 5) $2x10^{18}$ cm^{-3}. The dots are the experimental results for N_h=$1x10^{17}$ cm^{-3} [5].
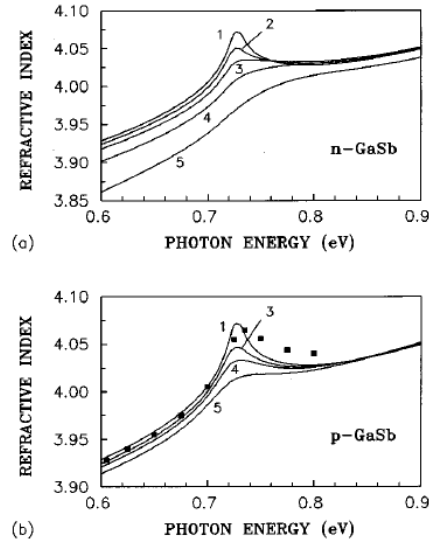

Figure A.2: Refractive index of GaSb with n and p-doping at different free carrier densities 1) intrinsic material 2) $2x10^{17}$ cm^{-3}, 3) $5x10^{17}$ cm^{-3} 4) $1x10^{18}$ cm^{-3} and 5) $2x10^{18}$ cm^{-3}. The dotted line is the experimental result for N_h=$1x10^{17}$ cm^{-3} (reproduced from [5])
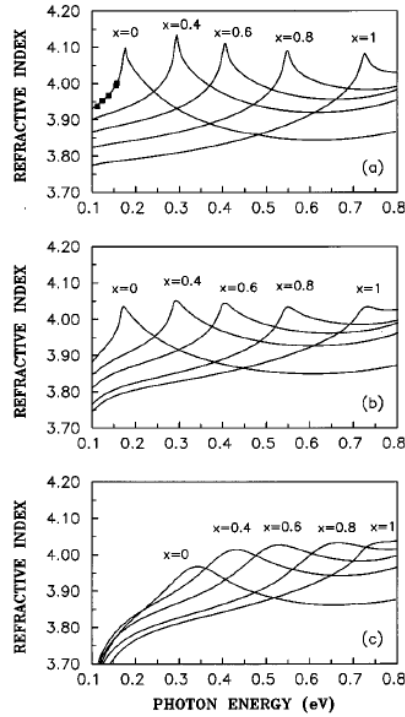
Figure A.3: Refractive index of InAsSb with n and p-doping at different free carrier densities a) intrinsic material b) p-type with $N_h=1x10^{18}$ cm^{-3} c) n-type with $N_e=1x10^{18}$ cm^{-3}. The dotted line indicates the experimental results (reproduced from [5])

A.4.2   InAs$_x$Sb$_{1-x}$

The refractive index of InAsSb is calculated using the same technique as for GaSb [5]. The refractive index as a function of photon energy is plotted for different compositions and carrier densities as shown in Fig. A.3.

A.4.3   Al$_x$Ga$_{1-x}$As$_y$Sb$_{1-y}$/GaSb

Alibert et al. [6] reports the experimental and simulated refractive index of Al$_x$Ga$_{1-x}$As$_y$Sb$_{1-y}$ grown by liquid phase epitaxy measured by reflectometry. The detail calculation can be found in [6]. The simulation and measurement results of the refractive index are shown in Fig. A.4a and b respectively. The results agree well with [7].
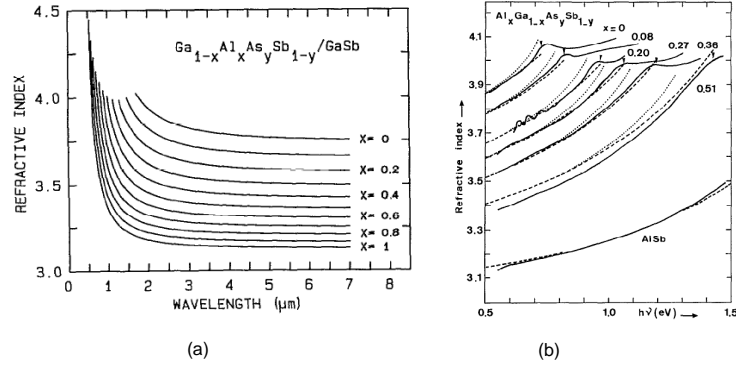
Figure A.4: a) Calculated refractive index as a function of wavelength for different $Al_xGa_{1-x}As_ySb_{1-y}$ compositions (reproduced from [6]) b) comparison between calculated results and experimental results
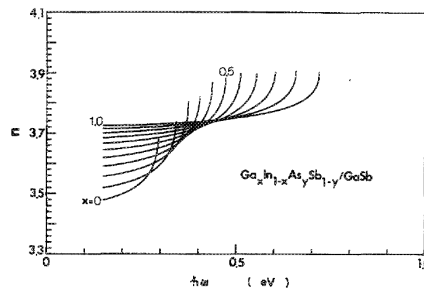
Figure A.5: Calculated refractive index as a function of wavelength for different $Ga_xIn_{1-x}As_ySb_{1-y}$ compositions (reproduced form [1])

A.4.4 $Ga_xIn_{1-x}As_ySb_{1-y}$/GaSb

Adachi et al. [1] have calculated the refractive index of $Ga_xIn_{1-x}As_ySb_{1-y}$ compositions. The results are plotted in Fig. A.5.

A.5   Absorption coefficient

A.5.1   Absorption coefficient: Direct bandgap

The absorption coefficient (α) of a material is important for photodiode simulation. The absorption coefficient of several binary compounds is calculated by Adachi et al. [8].
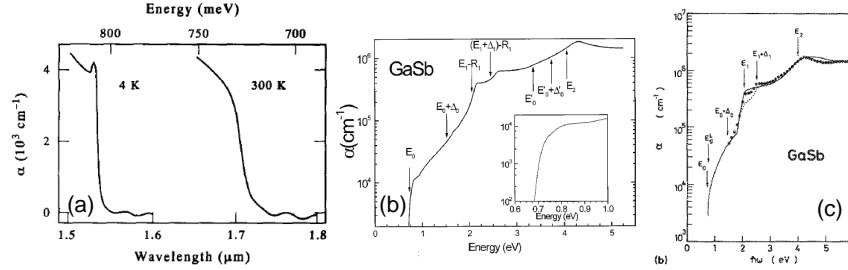
*Figure A.6: Absorption coefficient of intrinsic GaSb at 300K a)reproduced from [9] b) analyzed by Munoz et al. [10] c) analyzed by Adachi et al. [8]*

A.5.1.1   GaSb

An experimental value of α is reported by Milnes et al. [9] as depicted in Fig. A.6a. Munoz et al. employed spectral ellipsometry to analyse and model [10] the absorption coefficient of GaSb. The measurement is depicted in Fig. A.6b. The calculation result for GaSb by Adachi et al. [8] is plotted in Fig. A.6c comparing with experimental results.

A.5.1.2 $InAs_xSb_{1-x}$

In this thesis, the absorption coefficient of InAs is used instead of $InAs_xSb_{1-x}$ because of difficulty in obtaining the data. Moreover, the fraction of Sb is relatively small in our case ($InAs_{0.91}Sb_{0.0.09}$). A similar method as for GaSb is used to model α for InAs [8]. Adachi et al. reports the calculation comparing with experimental results as depicted in Fig. A.7.

A.5.1.3 $Ga_xIn_{1-x}As_ySb_{1-y}$/GaSb

For $Ga_xIn_{1-x}As_ySb_{1-y}$/GaSb, Munoz et al. [11] proposed linear interpolation from binary compounds similar to [8]. The expression is given by:

$$
\begin{aligned}
\alpha_{quat(e,y)}\left(E\right) = {} & xy\alpha_{InAs}\left[E + E_{0,InAs} - E_{0,quat(x,y)}\right] + x\left(1-y\right) \\
& \alpha_{InSb}\left[E + E_{0,InAS} - E_{0,quat(x,y)}\right] + y\left(1-x\right) \\
& \alpha_{GaAs}\left[E + E_{0,GaAs} - E_{0,quat(x,y)}\right] + \left(1-x\right) \\
& \left(1-y\right)\alpha_{GaSb}\left[E + E_{0,GaSb} - E_{0,quat(x,y)}\right]
\end{aligned}
$$

where α_i and $E_{0,i}$ are the absorption coefficient and fundamental band gap of the relevant end-point materials (i=InAs, InSb, GaAs or GaSb) and $E_{0,quat(x,y)}$ is
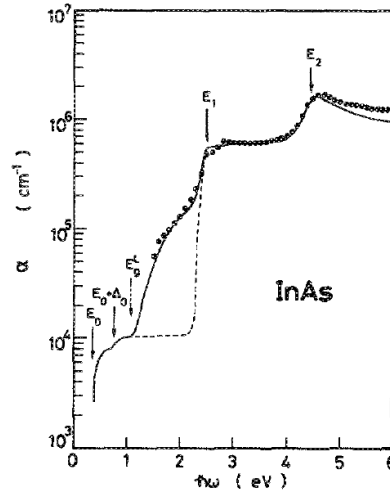
Figure A.7: Absorption coefficient of InAs as a function of photon energy (reproduced from [8])

the fundamental bandgap of the quaternary with composition x, y. The values of α_i and $E_{0,i}$ can be found in [3]. The calculated results comparing with experimental data of α of $Ga_xIn_{1-x}As_ySb_{1-y}$/GaSb are shown in Fig. A.8

A.5.2 Absorption coefficient: Free carrier absorption

The materials in this section are used in a laser waveguide where the fundamental band gap of these materials are larger than the lasing photon energy. Therefore absorption due to band-to-band transition does not occur. However, the materials are doped to reduce resistivity. This results in an absorption of photons by the interaction with free carriers within a band. The absorption coefficient due to free carrier (α_{FC}), is therefore of interest.

A.5.2.1 GaSb

GaSb is used in this thesis as a contact layer which is typically highly doped. In standard laser design, the overlap between the optical mode and contact layers are minimized. This leads to almost no free carrier absorption contribution from doped-GaSb to the modal loss. Therefore, in this case, α_{FC} is not very important to consider. However, with our design in Chapter 6, the contact layer is located between the III-V gain region and the Si passive waveguide. Therefore, a judicious choice of the doping level is required, trading off optical absorption versus resis-
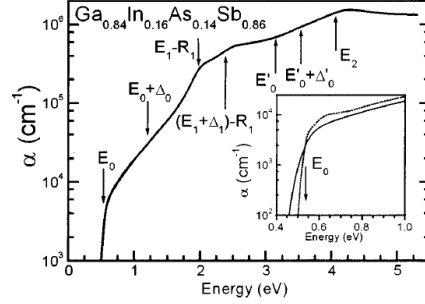
Figure A.8: Experimental values of the absorption coefficient for InGaAsSb. The inset shows the comparison between linear interpolation (dashed line) and experimental result (solid line) in the region near the bandgap. (reproduced from [11])
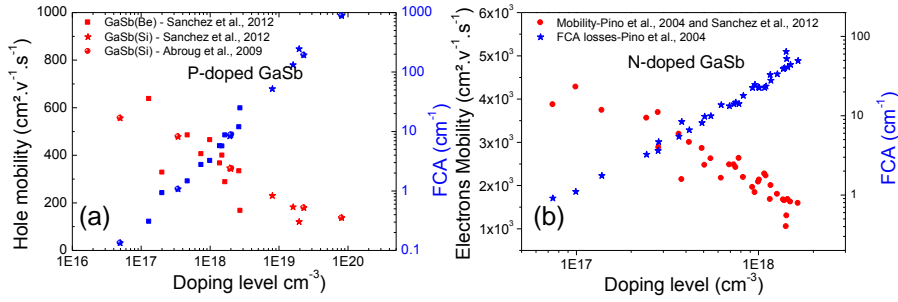

Figure A.9: Absorption coefficient due to free carriers absorption for p and n doped GaSb and hole/electron mobility (reproduced from [12–14])

tivity of the material. The measured values of α_{FC} and majority carrier mobility versus doping concentration for p-doped and n-doped GaSb measured at 2.3μm are shown in Fig. A.9a and b respectively [12–14].

A.5.2.2 $Al_xGa_{1-x}As_ySb_{1-y}$/GaSb

$Al_xGa_{1-x}As_ySb_{1-y}$/GaSb is used in this thesis as a cladding layer in the laser waveguide. The free carrier absorption α_{FC} contributes to modal loss in the laser cavity. α_{FC} of $Al_xGa_{1-x}As_ySb_{1-y}$/GaSb as a function of wavelength is approximated as [15]:

$$\alpha_{FC} = An\lambda^B + Cp\lambda^D \left(cm^{-1} \right) \tag{A.5}$$

where A, B, C and D are constants. λ is the incident wavelength in nm. n/p is the electron/hole concentration in cm^{-3}. For n-type AlSb, A is equal to 1.9×10^{-24}
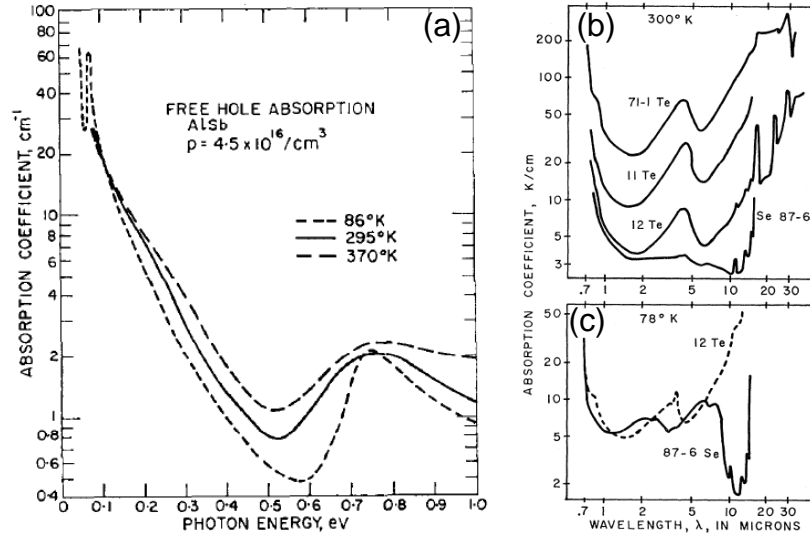
Figure A.10: a) Absorption coefficient of p-doped AlSb as s function of photon energy at different temperatures [17] b) logarithm of absorption coefficient versus logarithm of wavelength at 300K and c) 78K [18]

and B is equal to 2 [15]. For p-type AlSb, the data is very limited. In our case, we use D the same as B for n-type which is 2. C is then calculated from the experimental data in Fig. A.10. This yields C equal to 2.78×10^{-24} at $\lambda = 4\mu$m. This coefficient agrees well with experimental results in [16].

A.6   Thermal conductivity

The thermal conductivity (K) of a material is an important parameter to estimate thermal resistance of opto-electronics devices. K values of binary compounds are listed in Table A.1. Adachi et al. [19] proposes the analysis of K of quaternary compound using a simplified model of the alloy-disorder scattering. The bowing parameters (C) of several binary compounds are reported. This results in the possibility to estimate the thermal conductivity of quaternary compounds using an interpolation method as discussed in Section A.2. For $InAs_{0.91}Sb_{0.09}$, in this thesis, the thermal conductivity of InAs is used for simulation. The thermal conductivity of quaternary compounds used in this thesis are discussed in the following.

Material	K (W/cm K)	$C_{\alpha-\beta}$ (cm K/W)
C (diamond)	22	C_{Si-Ge}=50
Si	1.56	C_{Al-Ga}=32
Ge	0.6	C_{Al-Ga}=32
AlN	3.19	C_{Ga-In}=15
AlP	0.9	C_{N-P}=36
AlAs	0.91	C_{N-As}=12
GaN	1.95	C_{P-As}=15
GaP	0.77	C_{P-Sb}=16
GaAs	0.45	C_{As-Sb}=91
GaSb	0.36	
InP	0.68	
InAs	0.3	
InSb	0.175	

Table A.1: Thermal conductivity (K) of group IV materials and III-V binary compounds with bowing parameters (C) (reproduced from [19])

Composition	Bandgap (eV)	Thermal resistivity W (cm K/W)
$Ga_{0.8}Al_{0.2}Sb_{0.98}As_{0.02}$	0.96	5.8
$Ga_{0.73}Al_{0.27}Sb_{0.97}As_{0.03}$	1.05	9.5
$Ga_{0.49}Al_{0.51}Sb_{0.95}As_{0.05}$	1.3	13.0

Table A.2: The thermal resistivities of AlGaAsSb for different compositions (reproduced from [9])

A.6.1 $Al_xGa_{1-x}As_ySb_{1-y}$/GaSb

According to Adachi et al. [19], the thermal conductivity of $Al_xGa_{1-x}As_ySb_{1-y}$ is plotted as in Fig. A.11a. The results agree well with the data reported by [9] as listed in Table A.2.

A.6.2 $Ga_xIn_{1-x}As_ySb_{1-y}$/GaSb

Thermal conductivity values calculated using linear interpolation [19] are plotted in Fig. A.11b. The results agree well with the report from Milnes et al. [9] as presented in Table A.3. In addition, the simulation of thermal resistivity by [20] is also presented in Fig. A.12.
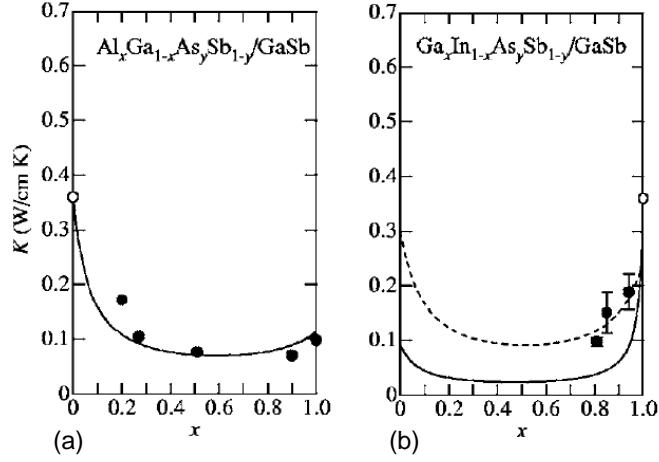
Figure A.11: Thermal conductivity as a function of material composition: a)
$Al_xGa_{1-x}As_ySb_{1-y}$/GaSb b) $Ga_xIn_{1-x}As_ySb_{1-y}$/GaSb (reproduced from [19])

Composition	Bandgap (eV)	Thermal resistivity (cm K/W)
$In_{0.06}Ga_{0.94}Sb_{0.95}As_{0.05}$	0.67	5.5
$In_{0.15}Ga_{0.85}Sb_{0.87}As_{0.13}$	0.59	7.1
$In_{0.19}Ga_{0.81}Sb_{0.83}As_{0.17}$	0.56	10.4

Table A.3: The thermal resistivities of InGaAsSb for different compositions (reproduced
*from [9])*
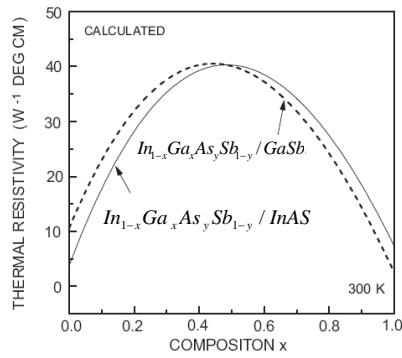
Figure A.12: The calculated thermal resistivity as a function of material composition for
InGaAsSb lattice matched to GaSb (bold) and InAs(dashed) (reproduced from [20])

References

[1] S. Adachi. *Band gaps and refractive indices of AlGaAsSb, GaInAsSb and InPAsSb: Key properties for a variety of the 2-4μm optoelectronics device application*. J. Appl. Phys., 1987.

[2] S. Adachi. *Properties of Semiconductor Alloys : Group-IV , III-V and II-VI Semiconductors*. John wiley & Sons Ltd., 1 edition, 2009.

[3] E. D. Palik. *Handbook of Optical Constants*. Academic press, 1 edition, 1985.

[4] I. Vurgaftman, J. R. Meyer, and L. R. Ram-Mohan. *Band parameters for III-V compound semiconductors and their alloys*. J. Appl. Phys., 89(11):5815, 2001.

[5] P. P. Paskov. *Refractive indices of InSb, InAs, GaSb, $InAs_xSb_{1-x}$, and $In_{1-x}GaSb$: Effects of free carriers*. J. Appl. Phys., 81(February):1890–1898, 1997.

[6] C. Alibert, M. Skouri, A. Joullie, M. Benouna, and S. Sadiq. *Refractive indices of AlSb and GaSb-lattice-matched in the transparent wavelength region*. J. Appl. Phys., 69(5):3208–3211, 1991.

[7] H. Abid, M. Rezki, and H. Aourag. *Electronic structure and optical properties of the quaternary alloy $Ga_{1-x}Al_xAs_ySb_{1-y}$*. Mater. Sci. Eng., 41(96):314–321, 1996.

[8] S. Adachi. *Optical dispersion relations for GaP, GaAs, InP, InAs, InSb, AlGaAs and InGaAsP*. J. Appl. Phys., 66(12):6030, 1989.

[9] A. G. Milnes and A. Y. Polyakov. *Review Gallium Antimonide Device Related Properties*. Solid. State. Electron., 36(6):803–818, 1993.

[10] M. Munuz, K. Wei, F. H. Pollak, J. L. Freeouf, and G. W. Charache. *Spectral ellipsometry of GaSb: Experiment and modeling*. Phys. Rev. B, 60(11):8105–8110, 1999.

[11] M. Munoz, K.Wei, F. H. Pollak, J. L. Freeouf, C. A. Wang, and G. W. Charache. *Optical constants of $Ga_{1-x}In_xAs_ySb_{1-y}$ lattice matched to GaSb(001):Experiment and modelling*. J. Appl. Phys., 87(4):1780–1787, 2000.

[12] D. Sanchez. *Nouveau système de confinement pour le VCSEL GaSb*. PhD thesis, Université Montpellier II, 2012.

[13] R. Pino, Y. Ko, and P. S. Dutta. *Enhancement of infrared transmission in GaSb bulk crystals by carrier compensation*. J. Appl. Phys., 96(2):1064–1067, 2004.

[14] S. Abroug, F. Saadallah, F. Genty, and N. Yacoubi. *Investigation of Electrical and Optothermal Properties of Si-doped GaSb epitaxial layer by the Hall Effect, PL measurement and Photothermal Deflection Spectroscopy*. Phys. Procedia, 2:787–795, 2009.

[15] D. A. Clugston and P. A. Basore. *Modelling Free-carrier Absorption in Solar Cells*. Prog. Photovoltaics Res. Appl., 5:229–236, 1997.

[16] D. Z. Garbuzov, R. U. Martinelli, H. Lee, P. K. York, R. J. Menna, J. C. Connolly, and S. Y. Narayan. *Ultralow-loss broadened-waveguide high-power 2µm AlGaAsSb/InGaAsSb/GaSb separate-confinement quantum-well lasers*. Appl. Phys. Lett., 69(14), 1996.

[17] W. J. Turner and W. E. Reese. *Infrared Absorption in n-Type Aluminum Antimonide*. Phys. Rev., 117(4):1960, 1960.

[18] R. Braunstein and E. O. Kane. *The valence band structure of the III-V compounds*. J. Phys. Chem. Solids, 23:1423–1431, 1962.

[19] S. Adachi. *Lattice thermal conductivity of group-IV and III-V semiconductor alloys*. J. Appl. Phys., 102(6):063502, 2007.

[20] M. Rabah, B. Sahraoui, B. Bouhafs, B. Abbar, and H. Abid. *Theoretical analysis of disorder effects on electronic and optical properties of the quaternary alloy $In_{1-x}Ga_xAs_ySb_{1-y}$ epilayer on GaSb and InAs*. Phys. Status Solidi, 238(1):156–172, July 2003.